Orogenesis from bottom to top – Investigating the geodynamics of mountain building using coupled thermo-mechanical-surface-process models

Sebastian G. Wolf

UNIVERSITY OF BERGEN

Orogenesis from bottom to top – Investigating the geodynamics of mountain building using coupled thermo-mechanical-surface-process models

Sebastian G. Wolf

Thesis for the degree of Philosophiae Doctor (PhD)
at the University of Bergen

Date of defense: 10.03.2021

Year: 2021

Title: Orogenesis from bottom to top – Investigating the geodynamics of mountain building using coupled thermo-mechanical-surface-process models

Name: Sebastian G. Wolf

Print: Skipnes Kommunikasjon / University of Bergen

Preface

This dissertation for the degree of philosophiae doctor (PhD) has been submitted to the Department of Earth Science at the University of Bergen. The research in this thesis was supported by TOTAL, as part of the project "COLORS: Coupling lithosphere deformation and stratigraphy". Research was mainly carried out in the Geodynamics and Basin Studies Research Group at the Department of Earth Science, University of Bergen, under supervision of Prof. Ritske S. Huismans, between September 2016 and December 2020. In August 2018 and August 2019 Prof. Jean Braun hosted the Candidate during research stays at the GFZ Potsdam, section 4.7. Earth Surface process modelling. The candidate received additional financial support as a member of the Norwegian Research School for Dynamics and Evolution of Earth and Planets (DEEP) for participation in the annual DEEP General Assembly and external courses. The candidate furthermore received a mobility grant from the Akademiaavtalen 2019 covering the participation at the EGU General Assembly 2020.

The structure of the dissertation follows the Norwegian guidelines for doctoral dissertations in natural sciences, where the main body of the thesis consists of scientific articles which have either been published in, submitted to, or are in preparation for international peer-reviewed journals. Broadly, the thesis is subdivided into three parts: The first part consists of an introduction to the research topics, an outline of the research questions, and a methods section describing major methodological advancements developed during this thesis. The main research results are presented in the second part of this thesis. Results are presented in the form of 4 articles, where the first is published in *Journal of Geophysical research – Solid Earth*, the second is accepted in the same journal, and the third is under revision in *Nature*. Revisions of the third paper sparked further research based on work presented in paper three. Results of the additional work are presented in form of a fourth paper, but will be in parts integrated into paper three in the future. Hence, paper three and four can be seen as one logical unit. The main findings of the research presented in this dissertation are summarized in the third part, where I also present ideas for future follow-up research. The articles constituting the main body of the thesis have been submitted or are published in different

journals. Therefore, the layout and referencing style varies between them.

This thesis is to a large degree built on numerical models with very dynamic behaviour that is best understood with the help of animations. Animations of all numerical models presented in this thesis can be found at:

```
https://www.dropbox.com/sh/1zrdip8btxrvqle/AABSVj3jwczGBsqVD4-irhLWa?
dl=0
```

In case this link is not active any more, model videos can be sent on request. Model animations for the published/accepted articles are furthermore permanently uploaded to figshare and can be found at: `https://doi.org/10.6084/m9.figshare.8152835.v3` for article 1; `https://doi.org/10.6084/m9.figshare.13347260` for article 2

Acknowledgements

It started in 2013 when I did an exchange semester at the University of Bergen and took a course in geodynamics with Ritske Huismans and Patience Cowie. With a great excitement about seeing plates move in geodynamic models, I did my Masters degree in Bergen with Ritske and before even finishing was told that there was an exciting project that I should apply to and do a PhD. Fast forward, it's now November 2020, and the time has come to finish this PhD and reflect on the fun and exciting years. The by far biggest thank you goes to Ritske Huismans. It is a real pleasure to learn from you and work together. You introduced me to geodynamic modelling, and your continuous support, involvement, open-mindedness, open-door policy, and try-it-out mentality has been extremely helpful, motivational and encouraging. We shared some great scientific discussions, had many memorable field-days together, discussed coding problems, and you always made sure that I stayed on track. I am especially grateful for the many opportunities, freedom and support you gave me to explore the research questions of this thesis. Thanks a lot to Jean Braun, you not only helped me develop the coupling between tectonics, surface processes and stratigraphy, but were also extremely motivational, inspirational and helpful in exploring the interplay between surface processes and tectonics during mountain building. It was and is a pleasure and privilege to learn from you on-site in Potsdam and during many meetings. A big thank you also to Josep-Anton Muñoz, especially for several field trips to the Andes and Pyrenees. Without you I wouldn't know what orogens actually look like. I would also like to acknowledge the feedback and inspiration from Patience Cowie, who sadly is not with us any more. Unfortunately, you could not be involved as much as I had hoped, but I am very thankful for your comments and inspirational personality. Thank you, Xiaoping Yuan for help with coupling FastScape, great feedback and co-operation. Maggie Curry, thanks for always being up for a laugh, it is fun to work with you. Thanks a lot also to Peter van der Beek for direct and very helpful feedback and discussion.

I am grateful for the lively and great research environment I was fortunate enough to be part of in Bergen. Thanks to all members of our research group for poly-directional and open discussions: Thomas Theunissen, thank you for being an ex-

tremely motivated and open-minded colleague and mental sparring-partner. I really enjoy your motto that there are no good and bad models, but only some that are useful and some that are not so useful. Guillaume Duclaux, thanks a lot for fun during conferences, great discussions, and help with pTatin3D. Zoltan Erdős, thanks for many meetings and discussions about subduction zones and recreational breaks at conferences. Romain Beucher, thanks for giving me the kick-off to use python. Annelen, Gang, Lorenz, Leonardo, thanks for great discussions about modelling and tectonics, during the occasional morning coffee. Thanks a lot also to young-at-heart Leo Zijerveld, for help with FANTOM, great chats and funny moments.

Outside my direct research group, but part of the University, I was lucky to have some great people around who became dear friends. Thank you, Johannes, for uncountable hours of science discussions, coffee breaks, walks in the park, climbing and being there in every situation. Edos, for being the best office mate there is. Felix, for nerdy discussions, brewing beer and doing sports together. Thilo, for making music together. Finally, thanks to the university climbing group and many others for fun in the evenings.

A special thank you also to my international colleagues, who made this PhD exciting and from whom I learned a lot. Thanks to Dave May for help in coupling FastScape and pTatin3D. It's inspirational how quick and efficient code development can be if one works with you. To the whole COLORS team, specifically Delphine Rouby, Jean Claude Ringenbach, Brendan Simon, Claude Gout, Matthieu Branellec, Núria Carrera, Anthony Joudon, Jean-Paul Callot, and the Brazilian group from Rio: Thanks a lot for great field trips, entertainment, and co-operation. A special thanks also to the members of the Norwegian DEEP research school. It was great to have the opportunity to get to know all of you and be part of the organising team for some time.

This thesis would not have been the same without the support from my parents and siblings. It was and is always great to come home to Munich and reload my batteries. I am lucky that the same accounts for my partner's parents and sister, who have become a second family to me. Last but not least, I would like to thank my partner Birte. Thank you for your endless support and love in easy but also difficult times during the PhD. It is a pleasure to be on your side, and I hope for many more adventures with you and our yet unborn baby. May this thesis be an inspiration for her to follow her dreams.

Abstract

The objective of this project is to advance our understanding of mountain building processes in different plate tectonic settings and with specific focus on the interaction between surface processes and tectonics. Three topics are investigated:

1. The factors controlling overriding plate extension or shortening in ocean-continent subduction systems.

2. The evolution of continent-continent collision orogens from small to large, their typical distribution of shortening, variable structural style, and associated controlling factors.

3. The relation between surface processes and tectonics during orogenic growth and decay and the factors controlling height, width, and longevity of collisional mountain belts.

The three research aspects are investigated with the help of numerical models and comparison to natural examples. The newly developed models allow for the first time to efficiently model the coupling between tectonic deformation, erosion and deposition. Results are synthesized in published or submitted articles, provide new geodynamic relationships, ideas, and theory, and simplify understanding of mountain building on Earth.

For topic 1, we use two-dimensional thermo-mechanical models, and show that back-arc extension or shortening of the overriding plate in ocean-continent subduction systems is determined by absolute plate velocities on Earth: Overriding plate movement towards the trench inhibits backarc extension and promotes overriding plate shortening, and a stable overriding plate or absolute plate movement away from the trench promote backarc extension. Additionally, a weak backarc lithospheric mantle, removed through Rayleigh-Taylor instabilities induced by the subduction process, is required for backarc extension and facilitates overriding plate shortening. Computation of driving and resisting forces during orogenesis shows near-balance of forces and explains why a weak and thinned backarc lithospheric mantle is pivotal for backarc extension and shortening. Comparison of model results with the Andes and Hellenic subduction zones corroborates that a weak and thinned backarc lithospheric mantle and absolute plate velocities determine overriding plate deformation.

In topic 2, we use two-dimensional thermo-mechanical continent-continent colli-
sion models tightly coupled to a 2D surface process model and show that distribution
of shortening during orogen growth follows a typical evolutionary pattern from a pro-
side-dominated cold wedge to an orogenic plateau. Internal crustal loading is the main
factor controlling the large scale deformation, while lithospheric pull only modulates
the plate driving forces to sustain orogenesis. To first order surface processes delay
orogenic growth, and modulate the structural style during growth. Utilizing a force-
balance analysis, we show how inherited structures, surface processes, and decoupling
between thick-and thin-skinned deformation influence the structures during orogenic
growth. Comparison of generic model results with the Pyrenees, Alps, and Himalaya-
Tibet shows applicability and limitations of model inferences.

For topic 3, we use two-dimensional thermo-mechanical continent-continent col-
lision models tightly coupled to a 2D surface process model and show that orogenic
growth and decay depend on crustal rheology and surface process efficiency, and can
be subdivided into two phases each. In growth-phase one, orogens grow primarily in
height, followed by lateral growth in phase 2. Depending on surface process efficiency,
phase-2-orogens can be classified into three types (Type 1, 2a, 2b): Type 1 orogens
are not in flux-steady state, and are characterised by longitudinal valleys in the oro-
gen core and low uplift and erosion rates. Flux-steady state, pre-dominantly transverse
river flow in the orogen core and high uplift and erosion rates are characteristic for
type 2 orogens. These orogens can furthermore be subdivided into types 2a and 2b, de-
pending on whether the pro-side of the mountain belt produces significant thrust sheets.
Based on model results, we derive an analytical scaling relationship of mountain belt
growth and present a new non-dimensional number, Be, that describes the interaction
between surface processes and tectonics during orogenic growth, and allows approxi-
mation of crustal strength and average fluvial erodibility of orogens on Earth. Finally,
we use our scaling relationship and model inferences to compare to several orogens
on Earth, specifically the Southern Alps of New Zealand, Taiwan, and Himalaya-Tibet.
Our model inferences imply that the height of most growing orogens on Earth is con-
trolled by the crustal strength of the foreland, and not by surface processes efficiency.
In contrast, orogenic decay is primarily dependent on surface process efficiency. In
decay-phase one, short-wavelength "tectonic" topography is quickly removed within
few Myrs, before an effectively local-isostatic rebound creates slow decay of topogra-
phy, with a timescale depending on surface process efficiency. We conclude that sur-
vival of orogenic topography for several tens to hundreds of Myrs is likely the default
behaviour on Earth.

List of publications

Paper I

Sebastian G. Wolf, Ritske S. Huismans. **Mountain Building or Backarc Extension in Ocean-Continent Subduction Systems: A Function of Backarc Lithospheric Strength and Absolute Plate Velocities**, *Journal of Geophysical Research: Solid Earth* **124**, 7461–7482. doi: `https://doi.org/10.1029/2018JB017171`.

Paper II

Sebastian G. Wolf, Ritske S. Huismans, Josep-Anton Muñoz, Magdalena Ellis Curry, Peter van der Beek. **Mountain belt growth from small and cold to large and hot - inferences from geodynamic models**, *accepted in Journal of Geophysical Research: Solid Earth*.

Paper III

Sebastian G. Wolf, Ritske S. Huismans, Jean Braun, Xiaoping Yuan. **Topographic evolution of mountain belts controlled by Rheology and surface process efficiency**, *submitted to Nature*, under review.

Paper IV

Sebastian G. Wolf, Ritske S. Huismans, Jean Braun, Xiaoping Yuan. **Deriving scaling laws of orogenic growth from thermo-mechanical-surface-process models**, *manuscript draft related to paper III*.

Contents

1 Introduction

With the emergence of plate tectonics in the 1960s, scholars started to develop under-
standing of plate movement and deformation on Earth (Dietz 1961; Hess 1962; Vine
and Matthews 1963; Wilson 1966; Le Pichon 1968; Morgan 1968). Thereby models
based on the basic physical principles of mass, momentum, and energy conservation
were a main source to find and quantify the main factors controlling plate tectonics.
From the beginning, modelling followed the still valid rules of simplicity and physi-
cal intuition, idealizing Earth-like behaviour and testing the possible parameter space
(e.g. McKenzie et al. 1974). Although early models utilized highly idealized analytical
or numerical solutions, they gave already first order insight into geodynamic processes
(e.g. McKenzie 1969; Minear and Toksöz 1970; McKenzie et al. 1974; Forsyth and
Uyeda 1975). As a result of the still ongoing evolution of computing systems, the ba-
sic, coupled, non-linear physical equations could be solved numerically, which created
the possibility to gain insight into the dynamic time- and space- dependent interac-
tion of different processes on Earth. Combined with a feedback-loop of observations,
numerical modelling has now become one of the main tools to test geoscientific hy-
potheses and provide a theoretical framework for processes on Earth. Following the
aphorism:

"All models are wrong, some are useful." (Box 1976),

I will in this thesis present and utilize hopefully useful numerical geodynamic models
to investigate mountain building processes on Earth.

   The thesis is split into three different parts: An introduction chapter about the state
of the art of mountain building with special focus on recent modelling advances leads to
the main research questions investigated here. In the chapter following the introduction,
I present the methods used in this thesis, with a focus on new implementations related
to the coupling between surface processes and tectonics, that I developed. The second
part, the main part of the thesis, consists of four articles investigating the presented
research questions, whereof articles 3 and 4 form one logical unit and inferences from
paper 4 will be used in revisions for paper 3. The last part contains a synthesis of the

conclusions which can be drawn from this thesis, and an outlook section in which I propose future research avenues based on the results presented in this thesis.

1.1 Mountain building at different scales

In a very basic sense, mountain belts on Earth are topographically elevated regions that formed through any form of tectonic process. The most characteristic process creating mountainous topography is crustal thickening, although dynamic mantle support or rift-flank uplift might also (temporarily) provide topography. Classically, mountain belts were divided into "Cordilleran"-type orogens, growing through magmatic addition of crustal material, and "Collision"-type orogens, growing through crustal shortening (Dewey and Bird 1970). However, it has been shown that also classical "Cordilleran"-type mountain belts like the Andes are built to a large degree through significant crustal shortening (Oncken et al. 2006; Arriagada et al. 2008). The most striking difference between both orogenic types is their plate tectonic configuration. In Cordilleran-type orogens, the overriding plate of an ocean-continent subduction system shortens internally, like for instance the South American plate forming the Andes, while in Collision-type orogens two continental plates collide, like for instance the collision between India and Eurasia forming the Himalaya-Tibetan orogen (e.g. Yin and Harrison 2000). It is furthermore common that a stage of pre-collisional subduction precedes continent-continent collision. A Cordilleran-type orogen can therefore transition into a Collision-type orogen.

Independent of the mechanical process, orogenesis creates surface uplift and thus topography. Orogenic topography in turn modifies the global wind circulation system and is the main locus for (orographic) precipitation in form of rain or snow. Ice flow in glaciers and water flow in rivers shape the mountainous topography, lower its elevation through erosion, and redistribute mass by transport and deposition of eroded material in form of sediments, creating a feedback loop between tectonics and surface processes. Therefore, surface processes, and in the non-glaciated case, fluvial erosion provide the link between climate, erosion and tectonics (Whipple and Tucker 1999; Willett 1999; Whipple 2009). Erosion and exhumation rates can be very high, in the same order as plate velocities on Earth. Very high rates have for instance been reported in Taiwan (Dadson et al. 2003), the southern Alps of New Zealand (see review in Jiao et al. 2017), and the Himalayas (e.g. Beaumont et al. 2001; Herman et al. 2010). These high rates highlight that surface processes are not merely a decoration on top of the mountain
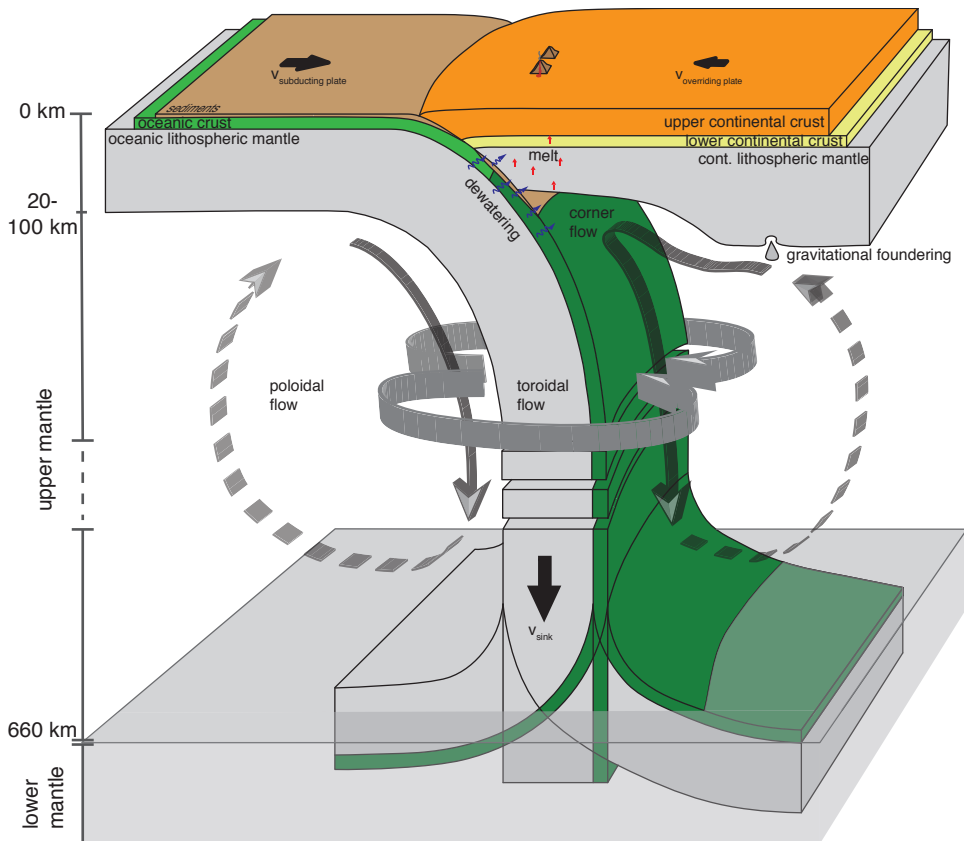
Figure 1.1: Sketch of an ocean-continent subduction zone with key processes influencing deformation of the overriding plate. Modified from Wolf (2016).

belt, but have the potential to strongly modulate mountain belt formation and even fully counteract orogenic growth (e.g. Willett and Brandon 2002).

1.1.1 Cordilleran-type mountain belts – ocean-continent subduction

Ocean-continent subduction on Earth can lead to variable tectonic styles in the overriding plate. Classical end-members are back-arc extension, like for instance in the Hellenic subduction zone (Jolivet et al. 2013; Faccenna et al. 2014), and mountain belt formation with several hundreds of kilometres of shortening as in the central Andes (Oncken et al. 2006; Arriagada et al. 2008; Armijo et al. 2015). The Andes even record both end-member styles, because Cenozoic mountain building is in wide areas preceded by Mesozoic extension (e.g. Carrera et al. 2006; Iaffa et al. 2011). To under-

stand the forces leading to either back-arc extension or overriding plate shortening, it is illustrative to follow the journey of an oceanic lithosphere subducting below a continent and through the mantle. To initiate subduction, the slab bending resistance and strength of the plate interface need to be overcome (Conrad and Hager 1999). With increasing subduction, the temperature difference between slab and mantle, and the eclogite phase change of oceanic crust develop into a growing slab pull, which turns into the main force driving subduction (Forsyth and Uyeda 1975). Slab pull is considered to be the main driving force of plate tectonics, which explains why plates attached to a subducting oceanic plate move generally in the subduction direction, and are faster (3 to 10 cm/yr) than plates without an attached slab (0 to 3 cm/yr, Kreemer et al. 2003; O'Neill et al. 2005; Schellart et al. 2007; Schellart 2008). Besides plate bending and interface shearing, slab pull is also counteracted by viscous shear resistance on the sides of the slab, slab suction, and P-T-dependent phase changes in the sub-lithospheric mantle (Funiciello et al. 2003; Billen 2008; Rodriguez-Gonzalez and Negredo 2012; Agrusta et al. 2017). Most notable of these are a) the shear resistance of the slab in the lower mantle, which is assumed to have a higher viscosity than the sub-lithospheric upper mantle (Mitrovica and Forte 2004), and b) the phase transition between upper and lower mantle, which provides positive buoyancy due to a negative Clapeyron slope (Billen 2010; Agrusta et al. 2017). The different forces driving and counteracting subduction lead to a natural sinking velocity v_{sink} of the slab in the mantle. In an isolated system consisting of one subduction zone, v_{sink} would be split into the velocity of the subducting plate and the overriding plate, with deformation occurring mainly at the plate interface and not inside the plates (Capitanio et al. 2010). However, subduction systems on Earth are not isolated features, and for instance lateral density and viscosity differences, several subducting edges, or sub-lithospheric mantle flow provide additional force to modulate the plate velocities and deform the overriding plate in ocean-continent subduction systems.

Indeed, early conceptual models proposed that absolute plate motions, and here mostly the overriding plate, determine whether the overriding plate extends or shortens (Hyndman 1972; Uyeda and Kanamori 1979). The control of absolute plate motions on the strain regime in the overriding plate implies that subducting slabs interact with the absolute frame of reference. A possible candidate for the absolute reference frame might be a relatively stable lower mantle. Seismological studies show that the interaction between slab and lower mantle in the transition zone is very variable and possibly important, with slabs that pierce straight into the lower mantle like in the Marianas, and slabs that flatten out in the transition zone, like under Japan (Li et al. 2008; Goes et al.

2017). Variable interaction of slabs with the lower mantle indicates that absolute velocity of plates indeed may play a role in determining the overriding plate strain regime. Global statistical analyses also suggest that movement of the overriding plate toward or away from the trench controls overriding plate extension or shortening (Jarrard 1986; Heuret and Lallemand 2005; Schellart 2008).

Different aspects of subduction dynamics have been investigated by a large set of analogue and numerical geodynamic models. Only focussing on modelling studies investigating factors influencing the overriding plate strain regime, we can synthesize the following observations: a) subducting slabs generally have a tendency to develop trench retreat (Funiciello et al. 2003; Stegman et al. 2006). b) Toroidal mantle return flow around slab edges constrains the propensity for slabs to retreat or advance (Funiciello et al. 2004; Schellart et al. 2007; Stegman et al. 2010; Schellart and Moresi 2013). Therefore, centres of wide, continuous slabs are generally more stationary than slab edges or small slabs. c) Overriding plate movement towards the trench is essential for overriding plate shortening (Sobolev and Babeyko 2005). d) A weak and stationary overriding plate promotes backarc extension (Capitanio et al. 2010).

Independent of the strain regime, many overriding plates in subduction zones on Earth are characterized by a removed lithospheric mantle, as for instance observed in Western North America (Hyndman et al. 2005), below the Central Andes (Schurr et al. 2006; DeCelles et al. 2009), and in the Hellenic subduction zone (Jolivet et al. 2013). Currie et al. (2008) showed that removal of the backarc lithospheric mantle might be connected to Rayleigh-Taylor instabilities developing through subduction induced shear flow at the base of a weak lithospheric mantle. The required weakening of the lithospheric mantle could be related to fluids raising from the subducting slab, subduction associated melting, or weaknesses inherited from previous deformation periods (Arcay et al. 2005, 2006; Faccenda et al. 2012). Weakening and removal of the lithospheric mantle reduces the integrated strength of the overriding plate from around $9 \times 10^{12}\,\text{N/m}$ to roughly $4 \times 10^{12}\,\text{N/m}$. This is mechanically very effective, because it drastically reduces the force required to induce either shortening or extension of the overriding plate. We note that in convergent settings the lithospheric mantle could also be removed en bloc through for instance ablative subduction (Pope and Willett 1998; Krystopowicz and Currie 2013).

Although large amounts of research has been done to investigate subduction dynamics, no modelling studies have yet investigated the combined effects of absolute plate motions and backarc lithospheric strength on the deformation of overriding plates

in subduction systems. This topic will be the main part of the first article of this thesis. I already worked with subduction models and the question of overriding plate deformation in ocean-continent subduction systems during my M.Sc-thesis. However, back then we did not succeed in developing a consistent set of models that describes the key-factors of overriding plate deformation, partly because our models did not include a lower mantle, and our subducting slabs were to "strong". Hence, although the subduction-modelling part of this thesis builds on my experience during my M.Sc-thesis, it can be considered a completely independent and new work.

In this section, we had a closer look at subduction dynamics, and the reasons for mountain building or backarc extension in ocean-continent subduction systems. Many of the inferences about subduction dynamics are based on the interplay between modelling studies, both numerical and analogue, and observations. Realistic numerical subduction models are a relatively new tool (e.g. van Hunen et al. 2000), as they require advanced thermo-mechanical techniques that resolve high viscosity contrasts and very localized deformation (see review in OzBench et al. 2008; Schmeling et al. 2008; Gerya 2011). In contrast, the earliest dynamic continent-continent collision models already came up during the 1980's (e.g. England and McKenzie 1982). In the following section we look at how the understanding of mountain building during continent-continent collision has changed during the last decades, based on the interplay of observations and numerical modelling.

1.1.2 Collision-type mountain belts – continent-continent collision

In the previous chapter we had a closer look at the large scale dynamics of an ocean-continent subduction setting. If, in this type of setting, a continent trails an oceanic plate, the subduction zone develops into a continent-continent collision orogen. The evolutionary sequence from subduction to collision is relatively common in collisional mountain belts, and can for instance be inferred in the Himalayas and Alps (Yin and Harrison 2000; Handy et al. 2010). The initial stage of continent-continent collision is often characterised by inversion of extensional basins or even a whole passive margin. The Pyrenees are a striking example for inversion of a passive margin with many of the shortening structures being reactivated extensional structures or influenced by the previous rifting phase (Muñoz 1992; Beaumont et al. 2000; Roca et al. 2011; Muñoz 2019). In some orogens, as for instance in the Western Alps, the initial stage of collision is furthermore characterised by creation and eduction of ultra-high pressure rocks

(e.g. Warren et al. 2008; Butler et al. 2013). If oceanic subduction preceded continental collision, still attached oceanic slabs typically detach from the down-going plate, owing to the buoyancy difference between subducting continental lithosphere and the subducting oceanic slab (Duretz et al. 2012). Slab detachment is for instance inferred during the formation of the Himalayas (e.g. Replumaz et al. 2010b). Dependent on its density decrease as function of chemical depletion, subduction of the continental lithospheric mantle during continent-continent collision can potentially provide a pull force which sustains mountain building. Depletion-related density decrease for Phanerozoic mantle is typically in the order of 20 to $30\,\mathrm{kg\,m^{-3}}$; Proterozoic continental lithosphere is in the order of 40 to $60\,\mathrm{kg\,m^{-3}}$ less dense than primitive mantle (Griffin et al. 1998; Djomani et al. 2001).

Using the thin-sheet approximation and assuming whole-lithosphere pure-shear thickening, England and McKenzie (1982, 1983) developed one of the first models of continent-continent collision. Non-dimensionalising the conservation of mass and momentum equations, they argued that orogen formation critically depends on the Argand number $Ar = \frac{P_{ex}}{\bar{\tau}}$, where P_{ex} is the excess pressure resulting from crustal thickening, and $\bar{\tau}$ is the average deviatoric stress necessary to deform the colliding medium. High Ar leads to low and wide orogens, while low Ar is characteristic for high and small orogens. However, and contradicting the assumption of whole-lithosphere pure-shear thickening, several seismic reflection and tomography studies showed in the following years, e.g. in the Pyrenees, Alps, Himalayas (Muñoz 1992; Schmid et al. 1996; Owens and Zandt 1997; Schmid and Kissling 2000), that collision of two continents most commonly creates one-sided subduction of one lithospheric mantle, and vertical thickening of crustal material that detaches in the viscous middle/lower crust. Separation between the downgoing "pro"-plate and the overriding "retro"-plate at a mantle singularity, called S-point, sparked a multitude of crustal-scale "S-point models" (e.g. Willett et al. 1993; Beaumont et al. 1994; Willett and Beaumont 1994; Braun and Beaumont 1995; Beaumont et al. 1996; Ellis et al. 1998; Batt and Braun 1999; Beaumont et al. 1999; Ellis and Beaumont 1999; Willett 1999; Beaumont et al. 2000, 2001; Vanderhaeghe et al. 2003). Ellis et al. (1995) provide a theoretical framework to these modelling studies, and show that crustal thickening can be described by a combination of the (crustal) Argand $Ar = \frac{Gravitational\ force}{Compressive\ force}$ and Ampferer numbers $Am = \frac{Basal\ traction\ force}{Compressive\ force}$. Here Ar describes the ratio between buoyancy forces arising from crustal thickening and strength of the crust, similar to England and McKenzie (1982, 1983), and Am describes the ratio between basal traction forces and the strength of the crust. Low and high Ar have the same effects as described above; low Am means little coupling be-

tween crust and mantle, and high *Am* means strong coupling between crust and mantle. Summarizing, it is the competition between basal drag, crustal strength, and buoyancy forces arising from crustal thickening that possibly determines crustal thickening during orogenesis.

To first order, mountain belt size increases with increasing accumulation of crustal material, and decreases during post-orogenic decay and extensional collapse. The amount of crustal material directly relates to orogenic temperature, as the crust is rich in heat-producing elements (e.g. Hacker et al. 2015). Based on the relationship between temperature and size, and in analogy to the Hertzsprung-Russel diagram, Beaumont et al. (2006) proposed a temperature-magnitude (T-M) diagram of orogenic growth, in which mountain belts grow from small and cold to large and hot along a "main orogenic sequence" (Fig. 1.2). Type examples in the T-M-diagram might be the Pyrenees, Alps and Himalaya-Tibet for a respectively small and cold, transitional, or large and hot mountain belt. The Pyrenees grew by inversion of a passive margin and additional crustal shortening of at most 165 km (Beaumont et al. 2000). Shortening is mainly localised in the inverted extensional structures and in the pro-plate of the orogen (Muñoz 1992; Beaumont et al. 2000). The evolution of the Alps is more complex, with precollisional subduction, terrane accretion, UHP-rock exhumation and passive margin inversion. Because of its complexity and size, crustal deformation has not been fully restored. However, simplified shortening estimates far exceed 150 km of shortening in the West-Central Alps (Schmid et al. 1996; Schmid and Kissling 2000; Schmid et al. 2017). Interestingly, shortening in the West-Central Alps involves thrust sheet formation in the Apulian retro-side of the orogen as well as the Eurasian pro-side (Fig. 1.2), while shortening in the Pyrenees involves primarily inversion of extensional structures and deformation of the Iberian pro-plate. The only actively growing large and hot collisional orogen with a plateau is the Himalayan-Tibetan orogen, which formed in its recent state through collision between India and Eurasia with post-collision convergence in the order of several 1000 km (Negredo et al. 2007). Interestingly, the retro-side of the Himalaya-Tibet orogen is larger than the pro-side, and consists of shortened, previously accreted terranes which now sit on the retro-side of the orogen (Owens and Zandt 1997; Chung et al. 2005; Kapp and DeCelles 2019).

Already the earliest S-point models investigated, amongst others, how much the pro- and retro-side of an orogen contribute to crustal thickening (Willett et al. 1993; Beaumont et al. 1994; Willett and Beaumont 1994; Ellis et al. 1995; Beaumont et al. 1999; Vanderhaeghe et al. 2003), which can be nicely described in terms of the PURCE
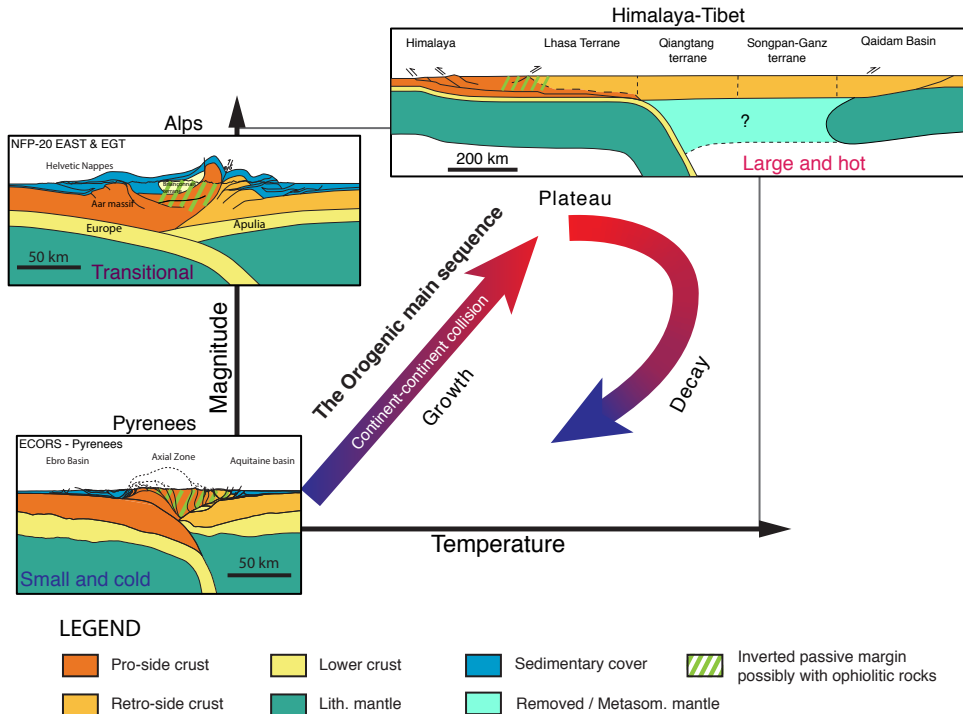
Figure 1.2: Conceptual Temperature-Magnitude diagram of orogenic growth as proposed by (Beaumont et al. 2006; Jamieson and Beaumont 2013), with cross sections through the Pyrenees (Muñoz 1992), Central Alps (Schmid et al. 1996), and Himalaya (Owens and Zandt 1997). Continent-continent collisional orogens grow from small and cold to large and hot during accumulation of crustal material. The orogen decays back to normal crustal thickness, once erosion and extensional collapse dominate over crustal shortening.

framework (Beaumont et al. 1999). Many S-point models showed a typical deformation pattern involving retro-and pro-side crust, and translation of the orogen onto the retro-side with growing size (Beaumont et al. 1994; Willett and Beaumont 1994; Willett 1999; Vanderhaeghe et al. 2003). In contrast, the next generation of upper-mantle scale thermo-mechanical models with self-consistent lithospheric subduction and strain localisation through strain-dependent softening showed that a weak overriding plate might be needed for retro-plate deformation (Butler et al. 2011), or that inversion of extensional structures during incipient collision is pre-requisite for retro-plate deformation (Erdős et al. 2014). Other upper-mantle-scale modelling studies showed that retro-side deformation occurs without any special additional process (Beaumont et al. 2006). Furthermore, Huangfu et al. (2018), Liao et al. (2018), and Vogt et al. (2018) show that variable distribution of orogenic shortening could also be related to lateral crustal strength contrasts between the two colliding plates, which is another possibility of variable pro- vs retro-side deformation. Interestingly, many orogens, including Taiwan, the Southern Alps of New Zealand, Pyrenees, Alps and Himalaya-Tibet, here at least the Indian plate, have a relatively similar rheological setup, with a viscous crustal detachment in the middle crust at 20 to 25 km depth and subduction of the lower crust and lithospheric mantle (Muñoz 1992; Schmid et al. 1996; Little 2004; Schmid et al. 2004; Herman et al. 2009; Replumaz et al. 2010a; Brown et al. 2012; Van Avendonk et al. 2014; Gao et al. 2016). Although this does not prove that there are no lateral differences in crustal strength, it indicates that the shortening distribution in many mountain belts on Earth might simply be related to different stages of growth along the "main orogenic sequence". The discrepancy between model results obtained with different modelling methods and setups highlights that the factors controlling pro-and retro-wedge deformation are not fully understood and require explanation and comparison with real orogens on Earth.

So far, we described and discussed the very large scale characteristics of continent-continent collision, like distribution of shortening and one-sided subduction, but did not consider the structures forming. Going back to an old discussion about the origin of mountain belts on Earth (Chamberlin 1919; Rodgers 1949), thrusting style can be divided into thin- or thick-skinned. Thin-skinned fold-thrust belts detach in a frictionally or viscously weak upper crustal layer at few kilometres depth, and are typically but not exclusively seen in forelands of mountain belts, as for instance the salt detached fold-thrust belts in the Southern Pyrenees, the Jura of the Western Alps, or the foreland fold-thrust belt in the Himalayas (Fig. 1.2, Sommaruga 1999; DeCelles et al. 2001; Robinson 2008; Muñoz 2019). Thick-skinned thrust sheets are commonly associated

with thrusts that cut the upper crust, and possibly root in the crustal brittle-ductile transition. They are consequently wider than thin-skinned thrust sheets, and often in the core of a mountain belt. Examples for thick-skinned thrust sheets are the different structural units of the Axial zone in the Pyrenees, and the Aar massif (see Fig. 1.2). Mechanically, the existence of thin-skinned thrust belts is therefore related to the presence and extent of a shallow weak décollement horizon, for instance the Triassic salt deposits in the Southern foreland of the Pyrenees (Muñoz 1992). Location and style of thrusting are furthermore strongly influenced by inherited weaknesses. Pre-collisional extensional structures or lithological contrasts are commonly exploited, the locus of thrusting, and strongly influence the thrusting style, as shown in many field studies (Gillcrist et al. 1987; Carrera et al. 2006; Iaffa et al. 2011; Roca et al. 2011; Carrera and Muñoz 2013; Kapp and DeCelles 2019). Summarizing, the structural style of crustal deformation typically depends on the depth to and superposition of different décollement levels, and inherited weaknesses in the crust.

Models of thin-skinned tectonics commonly investigate deformation on a fold-and thrust-belt scale, without modelling the feedback with the core of the orogenic belt, and to first order following the dynamics of a critical wedge (e.g. Simpson 2006; Selzer et al. 2007; Stockmal et al. 2007; Ings and Beaumont 2010; Ruh et al. 2012; Fillon et al. 2013; Ruh et al. 2017). These modelling studies showed that the thickness of the deforming layer, the strength of the décollement horizon, and the amounts of syn-tectonic deformation heavily influence structural style. Especially syn-tectonic sedimentation has a strong effect, as it locally changes the layer thickness and creates generally longer thrust sheets (Stockmal et al. 2007; Fillon et al. 2013). Very high resolution thermo-mechanical models allow now for the first time to model and investigate the feedbacks between thick- and thin-skinned tectonics (Erdős et al. 2014, 2015; Grool et al. 2019). Erdős et al. (2014, 2015) show that syn-tectonic sedimentation also creates wider thick-skinned thrust sheets, and Grool et al. (2019) show that a weak décollement horizon creates a feedback with the thick-skinned thrusts in the orogen core. However, the interaction between thick- and thin-skinned deformation has not yet been investigated with a full coupling between mass-conserving surface processes and tectonics. New, implicit formulations to solve the equations governing erosion and sedimentation now allow for the first time to investigate surface processes and tectonics and the interaction between thick- and thin-skinned deformation, which is part of this thesis.
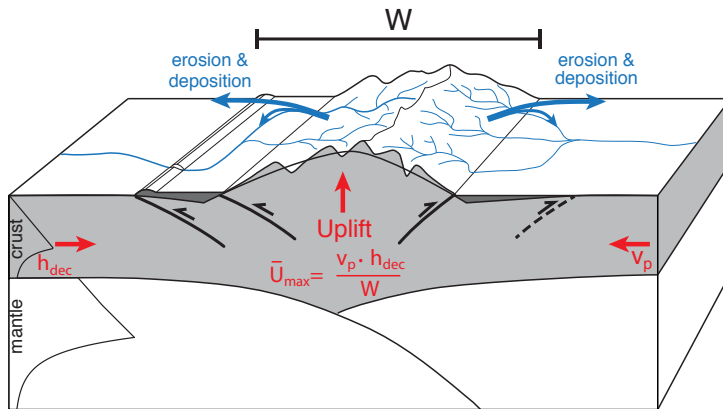
Figure 1.3: Block diagram of a growing mountain belt showing the interaction between fluvial erosion and tectonics. The maximum average uplift $\bar{U}_{max}$ is a function of the depth to the crustal decoupling level h_{dec}, the width of the orogen W, and plate velocities v_p. Erosion in the orogen core leads to deposition in the foreland basins and counteracts orogenic growth. At flux steady state, uplift is fully compensated by erosion, and the orogen does not widen.

1.1.3 The coupling between surface processes and tectonics

So far we looked at different causes for mountain building mainly from a tectonic, endogenous perspective. Exogenous processes, i.e. surface processes, determine the morphology of a mountain belt in terms of relief and plan-view texture, and relocate mass, thereby influencing orogenic growth and inducing decay (Fig. 1.3). In a very general sense, surface processes can be divided into long-range and short-range processes. Typical short-range processes act on a hillslope scale, as for instance landsliding and soil creep, while long-range processes typically act on a valley- to mountain-belt scale, like rivers and glaciers. In the non-glaciated case, river incision sets the boundary condition for hillslope processes, thus determining regional denudation rates and sediment yield. Since river erosion depends on rainfall and rainfall variability, it links climate to erosion and tectonics (Koons 1989; Molnar and England 1990; Beaumont et al. 1992; Whipple et al. 1999).

The physics of bedrock erosion is most commonly cast into a variation of the stream power law, which in its simplest form is formulated as (Howard and Kerby

1983; Whipple and Tucker 1999):

$$E = K_f A^m S^n$$
$$\frac{\partial h}{\partial t} = U - K_f A^m S^n,$$

(1.1)

where h is elevation, t is time, U is uplift rate, E is erosion rate, K_f is fluvial erodibility, A is drainage area, S is local slope, and m, n are the stream power law coefficients. m, n are relatively well known, with $1 \leq n \leq 3$ (Harel et al. 2016), and $\frac{m}{n}$ ranging from $0.3 - 0.5$ (Stock and Montgomery 1999). The fluvial erodibility, however, is largely unknown, as it integrates climatic variability, rock type, abrasive agents in streams, vegetation, channel geometry, and additional threshold terms (e.g. Tucker and Bras 2000; Sklar and Dietrich 2001; Hartshorn et al. 2002; Whipple 2004; Lague et al. 2005; Molnar et al. 2007; Whittaker et al. 2007; Cowie et al. 2008; DiBiase and Whipple 2011; Egholm et al. 2013; Starke et al. 2020). Typical values for K_f are in the order of $1 \times 10^{-6}\,\mathrm{m}^{0.2}/\mathrm{yr}$ to $1 \times 10^{-3}\,\mathrm{m}^{0.2}/\mathrm{yr}$, assuming $m = 0.4$ and $n = 1$ (Stock and Montgomery 1999). Non-dimensionalising the stream power law one can show that the dynamics of bedrock erosion is governed by the non-dimensional erosion-uplift number $N_E = \frac{K_f k^m L^{bm-n} H^n}{U}$ (Whipple and Tucker 1999; Willett 1999), where L, H, U are typical length, height, and uplift-scales, and $k \approx 0.5$, $b \approx 2$ are Hack's law coefficients. Assuming $m = 0.4$ and $n = 1$, as typically done, shows that N_E is linearly dependent on K_f, H and U, and only weakly dependent on L. Applying N_E to mountain building shows that the ability of erosion to counteract orogenic growth is mainly dependent on the fluvial erodibility, tectonic uplift, and height of the orogen. Understanding the controlling parameters of uplift, height, and fluvial erodibility in orogens is therefore paramount to understand the interplay between surface processes, tectonics and ultimately climate.

Motivated by high exhumation and erosion rates in the relatively small Southern Alps of New Zealand and the Olympic mountains, early and simple numerical models coupling tectonics and (river) erosion demonstrated the dynamic feedback between climate and erosion (Koons 1989; Beaumont et al. 1992; Brandon et al. 1998; Willett 1999). More specifically, the models showed that climate-induced spatially variable erosion can lead to focussed surface uplift and exhumation, strongly influencing mountain belt evolution. Beaumont et al. (2001) showed that the feedback between surface processes and tectonics is also important in large and hot orogens. Very high erosion rates in active mountain belts stand furthermore in stark contrast to long-term survival of topography as observed for instance in the Uralides and Appalachians. Topographic

decay of mountain belts has been investigated separately from tectonic growth and shown to be a function of the erosive power of rivers (Baldwin et al. 2003; Egholm et al. 2013). Hence, variable fluvial erodibility has a strong impact both during growth and decay of an orogen.

Rooted in critical wedge theory, the impact of erosion on tectonics led to the idea that active orogens can reach flux steady state, keeping a relatively constant width and height, if tectonic material influx and erosional outflux are balanced (Davis et al. 1983; Dahlen 1984; Willett and Brandon 2002; Hilley et al. 2004; Whipple and Meade 2004; Stolar et al. 2007). Potential type-examples of steady state orogens are the Southern Alps of New Zealand, the Taiwanese mountain belt, and the Olympic mountains in Washington state, USA, all of which are characterised by high uplift and erosion rates, and relatively small width (Koons 1989; Beaumont et al. 1992; Brandon et al. 1998; Dadson et al. 2003; Michel et al. 2019). Furthermore, based on the assumption of orogens behaving like a critical wedge, it was shown that changes in climate can possibly be detected by a concurrent decrease or increase of mountain belt width, relief and height (Whipple et al. 1999; Whipple and Meade 2004; Whipple 2009). This means that surface process efficiency potentially determines orogen height and width, which could fit with the observed limit of channel steepness on Earth (Hilley et al. 2019). However, it has long been known that the strength of the lithosphere also poses a limit to orogen height, certainly in large and hot orogens (Molnar and Lyon-Caen 1988; Sandiford and Powell 1990; Bird 1991; Zhou and Sandiford 1992). Furthermore, critical wedge theory is limited by its assumption of frictional deformation throughout the orogen. While this assumption is potentially true for thin-skinned foreland fold-thrust belt, it might not be adequate when considering deformation of the whole crustal column, including viscous flow in the middle and/or lower crust.

The latter demonstrates that in order to gain more insight into the interactions between surface processes, climate and orogenesis, one needs to account for a proper representation of tectonic deformation, i.e. one that inherently includes isostasy, discrete faulting, mantle lithosphere subduction, and earth-like rheologies. Coupling proper tectonic deformation to surface processes will give more information about the controlling factors for height, width, relief and longevity of mountain belts on Earth.

1.2 Research questions and objectives

Building on the previous three subsections, the main part of this thesis consists of three thematic units that are subdivided into four articles for which I will present the main research questions and objectives in this chapter. The main body of each article consists of geodynamic numerical models inspired by the overarching question:

> What controls the evolution of mountain belts on Earth?

Thereby my motivation is not to produce models which resemble a specific geological cross section, but to understand the underlying controlling factors and forces that drive model evolution and apply the resulting insights to nature.

In the introductory chapter I highlighted that mountain belts form primarily either above a subduction zone, or through continent-continent collision. While it is relatively straight forward that continent-continent collision leads to crustal thickening and mountain building, the underlying controls for mountain building in ocean-continent subduction systems are not fully understood. More precisely, no modelling study has yet provided a set of models that explains how ocean-continent subduction can either lead to overriding plate extension in form of backarc spreading, or overriding plate shortening. This leads to the first research question:

1. What controls overriding plate extension or shortening in ocean-continent subduction systems?

As introduced in chapter 1.1.1, research in the last decades has shown that ocean-continent subduction dynamics involves the interaction of processes on a deep, lower mantle scale, depends on variable absolute plate velocities, and possibly requires a relatively weak and removed backarc lithospheric mantle. We integrate these ideas into a model setup and investigate the influence of variable absolute plate velocities and overriding plate lithospheric strength on the overriding plate strain regime. Furthermore, we quantify the different forces guiding model evolution and compare modelling results to the central Andes and the Hellenic subduction zone. Summarizing, the objectives of the first part are:

1.1 to find the factors controlling overriding plate extension or shortening in ocean-continent subduction systems,

1.2 to quantify the different forces guiding model evolution,

1.3 to compare model results to the deformation history of the Andes and Hellenic

subduction zone, two prominent examples of ocean-continent subduction systems.

Inspired by the review article by Jamieson and Beaumont (2013), and building on the previous experience with subduction zones and tectonic forces, I started investigating orogenesis during continent-continent collision. I found that there are different, in part conflicting ideas, about retro-vs pro-side deformation in growing orogens, as described above. In contrast, I found that many active orogens on Earth seem to have a relatively similar rheological setup, with detachment of upper crust on top of a subducting lower crust and lithospheric mantle, and sometimes weak shallow décollement levels forming thin-skinned fold-thrust belts. Furthermore, all mountain belts are affected by surface processes, but the efficiency of surface processes varies. These conflicting differences and similarities led me to the research question:

2. What are the first order factors controlling distribution of shortening and different structural styles during orogenic growth from small to large in a continent-continent collision setting?

Coming from the experience that slab pull is the main driver of subduction, and possibly also plate tectonics, I hypothesized that the pull of the subducting lithospheric mantle could control deformation distribution and drive mountain building on Earth. Furthermore, motivated by fieldwork in the Pyrenees and Andes and previous modelling studies (Erdős et al. 2014), I explored how extensional inheritance, weak décollement horizons, and surface processes influence mountain growth. The objectives I pursue in this second part can be split into three parts:

2.1 to use high resolution 2D thermo-mechanical models coupled to a 2D surface-process model to find a typical distribution of shortening and structural style as a function of orogen size, and quantify their underlying controls,

2.2 to investigate the influence of lithospheric pull, extensional inheritance, weak shallow detachments and surface process efficiency on mountain growth,

2.3 to compare model results to natural examples of well studied orogens, more specifically the Pyrenees, Alps and Himalaya-Tibet.

One of the interesting outcomes of my coupled tectonic-surface process models in the previous study was: a) we needed to use very high fluvial erodibility to create flux steady state mountain belts, b) relatively independent on mountain belt size and fluvial erodibility the modelled orogens reached a similar height and c) the landscape evolving

on top of the model was highly dynamic and variable. Additionally, the dichotomy between very high erosion rates in active orogens and long term survival of topography in other mountain belts drove us too look further into the evolution of orogenic topography during growth and decay. This naturally led to the idea to investigate the interaction between surface processes and tectonics from a more geomorphological perspective and pursue the following research question:

3. What are the factors controlling the evolution of topography in terms of width, height, relief and longevity during mountain belt growth and decay?

To answer the research question of the third part, I propose to sequentially address the following objectives:

3.1 to investigate the key parameters controlling topographic growth and decay during continent-continent collision,

3.2 to compare geomorphic characteristics derived from the models to nature,

3.3 to propose a typical evolution of orogenic growth and decay in natural orogenic systems.

One of the main outcomes of paper 3 was that mountain height in growing orogens seems to be controlled by lithospheric strength, relatively independent of surface process efficiency, and that landscape topology gives information about surface process efficiency. However, there might be situations on Earth where the fluvial erodibility is higher than in the models presented in paper 3, so that orogens are not able to reach the height supported by the strength of the lithosphere. Also, as the lithosphere is composed of crust and mantle, what are the isolated influences of mantle and crustal strength on orogenic height, respectively? Furthermore, our models for paper 3 had a deliberately simple structural style, without any thin-skinned deformation. Does more complex structural styles, e.g. with additional thin-skinned deformation notably influence landscape topology? Finally, reviewer comments on the third paper remarked that we did not reach the ultimate goal of a universal analytical scaling relationship linking tectonics and surface processes. Reaching a scaling relationship would inherently answer most of the posed questions above, and link numerical models back to the physics of mountain building and surface processes. These ideas and additional questions naturally led to an additional research question:

4. Can we derive an analytical scaling relationship of orogenic growth and relate it to well studied orogens, and how does structural complexity influence landscape

topology?

To answer the research question of the fourth part, I propose to sequentially address the following objectives:

4.1 to investigate the influence of crustal and mantle strength on orogen height,

4.2 to investigate the influence of additional thin-skinned deformation on geomorphic characteristics of modelled orogens,

4.3 to propose three orogen types based on model results,

4.4 to derive an analytical scaling relationship linking tectonics and surface processes,

4.5 to compare analytical relationships with well studied mountain belts, namely Taiwan, the Southern Alps of New Zealand, and Himalaya-Tibet.

I note that although paper 4 is a stand-alone article, my co-authors and I intend to use most of the content of article 4 for revisions of article 3. Because paper 4 builds on, and is an extension of, paper 3, both articles can be seen as one logical unit in which I try to understand the interplay between tectonics and surface processes during orogenic growth and decay.

In the following section I give an overview of the methods I will use to answer the research questions and objectives introduced here. Findings of this thesis were presented at several international scientific meetings, and contributions are listed in a subsequent section. Furthermore, research in this thesis is the product of a collaborative effort, and I also contributed to several additional scientific studies which are not part of this thesis. These are listed in the last section of chapter one. The second chapter contains the four scientific articles which focus on the introduced research questions, and the thesis concludes with a synthesis and outlook in the third chapter.

1.3 Methods

To answer the research questions in this thesis, I use 2D thermo-mechanical geodynamic models coupled to a 2D surface processes model. Coupling between a geodynamic and surface processes model was first attempted by Beaumont et al. (1992), but limited in resolution and computational power. A second generation of coupled models looked at the interplay between crustal tectonics and erosion, excluding deposition and also limited by resolution (Willett 1999; Stolar et al. 2007; Thieulot et al. 2014). New,

implicit, $O(n)$ surface processes algorithms computing hillslope creep, stream power law erosion, sediment transport and marine deposition (Braun and Willett 2013; Yuan et al. 2019a,b), and high resolution 2D thermo-mechanical models (e.g. Erdős et al. 2014) allow for the first time to efficiently couple mantle scale geodynamic models to surface process models which include erosion and deposition. In the course of my PhD, I implemented this coupling, and developed a module connecting stratigraphy, surface processes and tectonics.

In the next two subsections (1.3.1,1.3.2), the basics of thermo-mechanical modelling and surface process modelling are presented with a special focus on new, added implementations. Details are omitted, as both methods are described in detail in the respective publications of this thesis and in published articles (e.g. Thieulot 2011; Braun and Willett 2013). The final subsection (1.3.3) of the methods section describes the newly developed coupling between surface processes and tectonics in more detail.

1.3.1 Thermo-mechanical modelling

We use a modified version of the 2D, finite element (FEM), Arbitrary Eulerian-Lagrangian (ALE), thermo-mechanically coupled code FANTOM (Thieulot 2011). To model mountain building subduction, or extension, we solve for plane strain deformation of incompressible creeping flows (Eq. 1.2, 1.3) and heat transfer (Eq. 1.4) in the model domain:

$$\frac{\partial v_i}{\partial x_i} = 0 \quad i = 1, 2, \tag{1.2}$$

$$\frac{\partial \sigma_{ij}}{\partial x_i} + \rho g = 0 \quad i, j = 1, 2, \tag{1.3}$$

$$c_p \rho \left(\frac{\partial T}{\partial t} + v_i \frac{\partial T}{\partial x_i} \right) = k \frac{\partial}{\partial x_i} \frac{\partial T}{\partial x_i} + H + v_j \alpha \rho T g, \tag{1.4}$$

where v_i are velocity components, x_i are spatial coordinates, σ_{ij} is the stress tensor, ρ is density, g is gravitational acceleration, c_p is specific heat, T is temperature, t is time, k is thermal conductivity, H is radioactive heat production per unit volume, and α is the volumetric thermal expansion coefficient. The first two equations describe mass and momentum conservation, and the third equation describes the temperature evolution through time as a function of heat conduction, advection, production and

adiabatic heating/cooling.

The model domain is typically filled with material that deforms through either frictional-plastic, or viscous flow. Frictional-plastic deformation is modelled by a pressure dependent Drucker-Prager yield criterion:

$$\sigma'_{plast} = P \cdot \sin(\phi_{eff}) + C \cdot \cos(\phi_{eff}), \qquad (1.5)$$

where σ'_{plast} is the square root of the second invariant of the deviatoric stress, P is dynamic pressure, ϕ_{eff} is the effective angle of internal friction, C is cohesion. Frictional-plastic softening is accounted for by reducing ϕ_{eff} and C as a function of strain.

In case of viscous deformation, we use a non-linear, thermally-activated power law creep formulation, which relates temperature, pressure and strain rate to the effective viscous flow stress, σ'_{visc}

$$\sigma'_{visc} = f \cdot A^{-\frac{1}{n}} \cdot (\dot{\varepsilon}_{eff})^{\frac{1}{n}} \cdot exp\left(\frac{Q+VP}{nRT}\right), \qquad (1.6)$$

where $\dot{\varepsilon}_{eff}$ is the square root of the second invariant of the deviatoric strain rate, f is a scaling factor, A the pre-exponential factor converted to plane strain, n the power-law exponent, Q activation energy, V activation volume, P the dynamic pressure, and R the universal gas constant. Model materials are generally based on a small set of well established laboratory flow laws, which are scaled by a factor f, to account for different geological settings and interpolation uncertainties between laboratory and nature.

In some models we apply an upper limit for the viscous flow stress (e.g. Andrews and Billen 2009; Magni et al. 2014; Butler et al. 2015), which approximates a temperature insensitive creep mechanism in olivine, active at high pressures, high differential stresses, and low temperatures (Tsenn and Carter 1987; Katayama and Karato 2008). This creep mechanism weakens the strong core of subducting lithosphere, which affects the bending and unbending of subducting slabs.

The density of model materials changes as a function of temperature and is given by $\rho(T) = \rho_0 \cdot (1 - \alpha(T - T_0))$. The thermal expansion coefficient α is P-T-dependent in Olivine and its polymorphs (Tosi et al. 2013). This is important for slab pull during subduction and therefore used in article 1.

Modelling subduction or continent-continent collision with a free surface is restricted to small time steps, to prevent so called "bathtub" or "drunken sailor" oscillations. To be able to use larger time steps, I implemented and carefully tested the

free-surface stabilisation algorithm from Kaus et al. (2010). For simplicity, the stabilisation is only applied at the free surface.

For visualisation of model output, I developed a python package based on an earlier post-processing software developed by Romain Beucher for use with the code SOPALE. The post-processing routines rely heavily on the matplotlib and numpy packages, and are now widely used in our research group. Some model videos and snapshots are created with Paraview. Visualisation codes and paraview-state files are therefore based solely on open source software, and can be obtained upon request.

1.3.2 Surface processes modelling

Surface processes are modelled using an extended version of the Landscape evolution model (LEM) FastScape (Braun and Willett 2013; Yuan et al. 2019a,b). Above sealevel, the LEM solves for the change of elevation h with time t, as a function of uplift U, stream power law erosion (K_f-term), hillslope diffusion (K_c-term), and deposition in the stream (G-term):

$$\frac{\partial h}{\partial t} = U - K_f A^m S^n + K_c \nabla^2 h + \frac{G}{A} \int_A (U - \frac{\partial h}{\partial t}) dA, \qquad (1.7)$$

where K_f is the fluvial erodibility, A is catchment area upstream, S is local slope, m,n are the stream power law exponents, K_c is the hillslope diffusion coefficient, and G is a deposition coefficient.

Below sealevel, the LEM solves for marine deposition as a result of sand and silt transport, approximated by diffusion:

$$\frac{\partial h}{\partial t} = K_{silt} \nabla \cdot (F \nabla h) + K_{sand} \nabla \cdot ((1 - F) \nabla h) + Q_{silt} + Q_{sand}, \qquad (1.8)$$

where h is elevation, t is time, K_i are the marine transport coefficients of respectively sand and silt, F is the silt fraction, and Q_i are the sand and silt fluxes provided by rivers to the shoreline.

We additionally account for mass-conserving filling of local minima by filling from the bottom of local minima according to available sediments. This is crucial to get proper deposition of sediments for instance in a mountainous foreland basin above sealevel. Local minima are furthermore bridged, and spill incoming water into the neighbouring catchment with the lowest sill. This ensures river connection to the
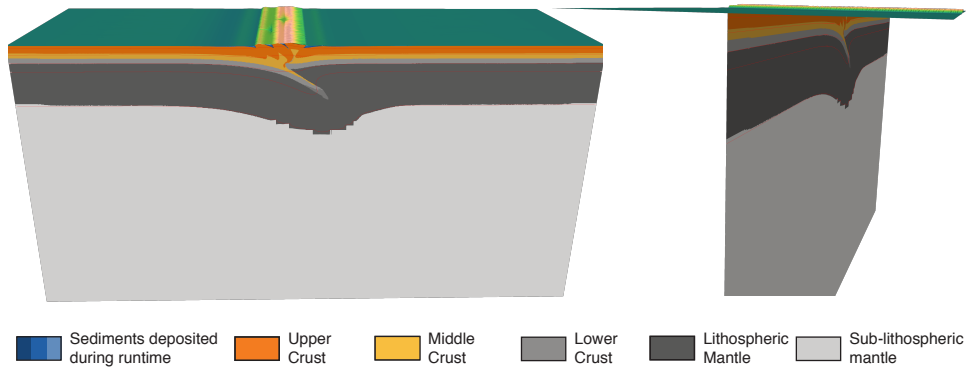
Figure 1.4: Two different views of a coupled thermo-mechanical-surface-process model of continent-continent collision. Left panel shows front view, right panel highlights the T-coupling between both numerical codes. The whole model domain is 1200 wide and 600 km deep.

lateral side boundaries. Boundary conditions are typically cylindrical on the N and S boundary and open on the W and E boundary (Fig. 1.4). This means water flowing out on the N-side flows back in on the S-side, and vice versa.

1.3.3 Coupled tectonic-surface process model

The surface process code FastScape and the thermo-mechanical code FANTOM are tightly coupled in a T-coupling manner (Beaumont et al. 1992, Fig. 1.4). After each thermo-mechanical time step, the computed velocity field is given to FastScape as a cylindrical signal. At first, the landscape is advected horizontally by solving the advection equation for the horizontal velocity component. Next, the vertical velocity field is used as an input to solve for erosion and deposition with equations 1.7, 1.8. Subsequently, the new average surface elevation is used directly as the new free-surface in the thermo-mechanical code and time-stepping continues. Erosion and deposition in FANTOM is accounted for by adding or removing Lagrangian marker particles. FastScape and FANTOM have the same horizontal resolution so that no interpolation between both grids is needed. Hence, FastScape literally "sits" on top of the thermo-mechanical model (Fig. 1.4, 1.5).

Additionally, I developed and implemented a 3D particle in cell method (Fig. 1.5) which tracks the sediments deposited by FastScape and gives information about stratigraphy during model evolution. After each time step in FastScape, a sediment particle
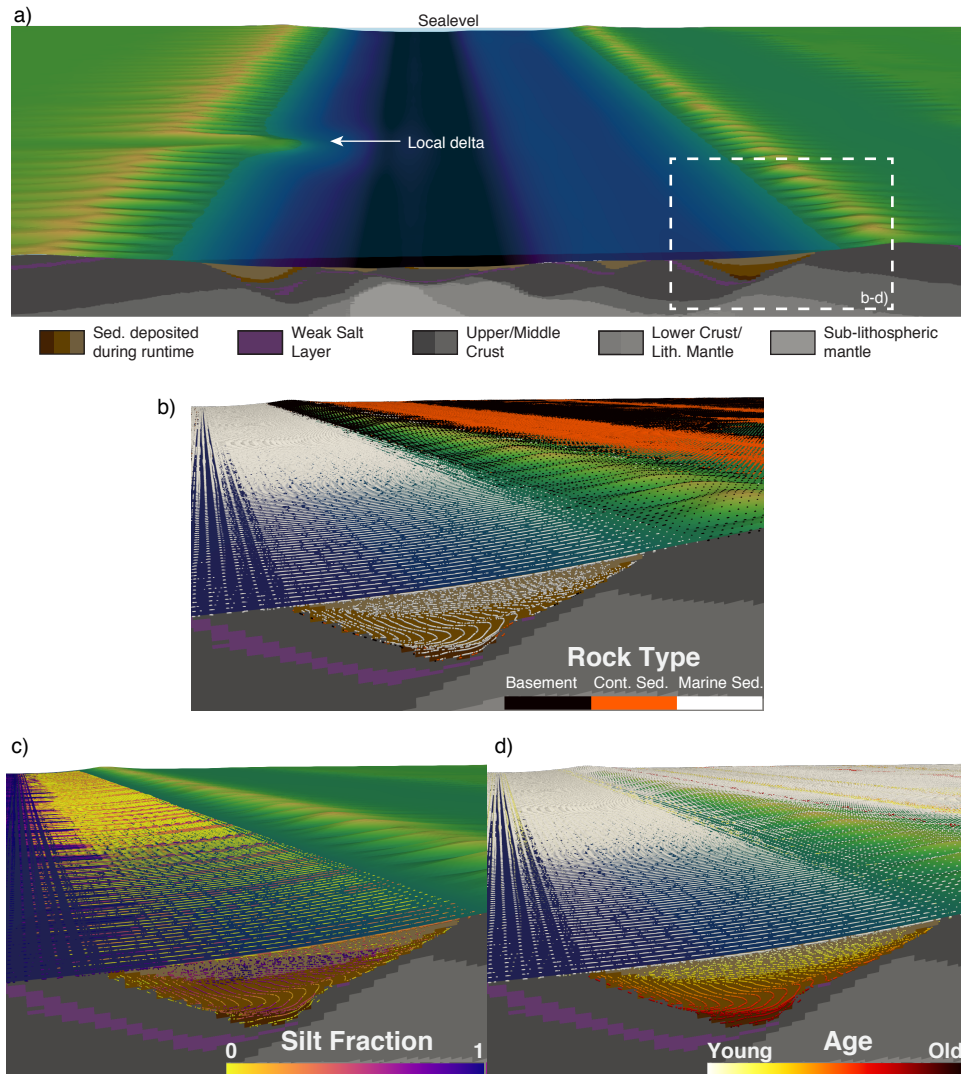
Figure 1.5: Overview (a) and zooms (b, c, d) of coupled 2D thermo-mechanical-landscape evolution model applied to continental rifting. a) Top Panel shows thermo-mechanical model and Landscape evolution model right before continental break-up. Rift flank uplift creates topography, which gets eroded and leads to sediment transport and deposition in the basin. Larger deltas form where rivers breach the rift flanks. b-d) Zoom snapshots which additionally show the stratigraphic marker particles with rock type (b), silt fraction (c), and sediment age (d). Note orange continental deposits behind the rift flank in sub-figure b).

is deposited at each node of FastScape. This particle contains information about a) the rock type at the surface, i.e. basement, continental sediment, or marine sediment, b) the age of the sediment, and c) the silt-fraction if the particle was deposited offshore (Fig. 1.5). During time-stepping, the particles are advected according to the computed, 3D, cylindrical velocity field, and particles above the FastScape surface are removed. This leads to basins that contain a thick pile of sediment particles that track stratigraphy and deformation (Fig. 1.5). Random removal of particles where particle density is high prevents memory overflow.

Although coupling between a thermo-mechanical code and a 2D surface process code has been done before (Beaumont et al. 1992; Stolar et al. 2006; Thieulot et al. 2014; Ueda et al. 2015), this coupling developed here is the first that includes horizontal advection, erosion, deposition, stratigraphy, and the resolution to resolve deformation of deposited sediments and stratigraphy in the thermo-mechanical model. Therefore, we call this type of coupling a "tight-coupling". We also note that we did not use marine sedimentation in the articles presented in this thesis, as this would have added unnecessary complexity. For the same reason, we did not exploit the full capabilities of the stratigraphy routines.

1.4 Contributions at scientific meetings

Wolf, Sebastian G.; Huismans, Ritske S.: From back-arc extension to orogenic plateau formation – a numerical modeling study of ocean-continent subduction systems. (Poster) *European Geosciences Union General Assembly*; 2017-04-24 – 2017-04-28, Wien, Austria.

Wolf, Sebastian G.; Huismans, Ritske S.: From back-arc extension to orogenic plateau formation – a numerical modeling study of ocean-continent subduction systems. (Poster) *XV International Workshop on Modelling of Mantle and Lithosphere Dynamics*; 2017-08-27 – 2017-08-31, Putten, Netherlands

Wolf, Sebastian G.; Huismans, Ritske S.: Factors controlling back-arc extension or overriding plate shortening – a numerical modeling study of ocean-continent subduction systems. (Poster) *European Geosciences Union General Assembly*; 2018-04-08 – 2018-04-13, Wien, Austria.

Wolf, Sebastian G.; Huismans, Ritske S.; van der Beek, Peter: From small and cold
to large and hot orogens: Investigating the influence of extensional inheritance
and surface processes. (Oral) *European Geosciences Union General Assembly*;
2018-04-08 – 2018-04-13, Wien, Austria.

Wolf, Sebastian G.; Huismans, Ritske S.: Factors controlling back-arc extension or
overriding plate shortening – a numerical modeling study of ocean-continent sub-
duction systems. (Oral) *GeoMod 2018*; 2018-10-01 – 2018-10-04, Barcelona,
Spain.

Wolf, Sebastian G.; Huismans, Ritske S.; van der Beek, Peter: From small and cold to
large and hot orogens: How do they grow and what are the influences of exten-
sional inheritance and surface processes? (Poster) *GeoMod 2018*; 2018-10-01 –
2018-10-04, Barcelona, Spain.

Wolf, Sebastian G.; Huismans, Ritske S.; Muñoz, Josep-Anton; v. d. Beek, Peter;
Curry, Magdalena E.: From small and cold to large and hot: What controls moun-
tain belt growth? (Oral) *European Geosciences Union General Assembly*; 2019-
04-07 – 2019-04-12, Wien, Austria.

Wolf, Sebastian G.; Huismans, Ritske S.; Braun, Jean; Yuan, Xiaoping: Topographic
evolution of mountain belts controlled by rheology and surface process efficiency
(Oral) *European Geosciences Union General Assembly*; 2020-05-03 – 2020-05-
08, Wien, Austria.

1.5 Scientific co-contributions

1.5.1 Articles

Magdalene E. Curry, Peter van der Beek, Ritske S. Huismans, Sebastian G. Wolf,
Josep-Anton Muñoz. **Evolving paleotopography and lithospheric flexure of
the Pyrenean Orogen from 3D flexural modeling and basin analysis**, *Earth*

and Planetary Science Letters **515**. doi: `https://doi.org/10.1016/j.epsl.`
`2019.03.009`.

Magdalene E. Curry, Peter van der Beek, Ritske S. Huismans, Sebastian G. Wolf,
Charlotte Fillon, Josep-Anton Muñoz. **Spatio-temporal patterns of Pyrenean
exhumation revealed by inverse thermo-kinematic modeling of a large ther-
mochronologic dataset**, *Under revision in Geology.*

Zoltan Erdős, Ritske S. Huismans, Claudio Faccenna, Sebastian G. Wolf. **The role of
subduction interface strength on back-arc extension**, *In preparation for Geo-
chemistry, Geophysics, Geosystems.*

Anna H. Geurts, Ritske S. Huismans, Patience A. Cowie, Sebastian G. Wolf. **Dy-
namic normal fault behaviour and surface uplift in response to mantle litho-
sphere removal: A numerical modelling study motivated by the central Ital-
ian Apennines**, *In preparation for Earth and Planetary Science Letters.*

Thilo Wrona, Ritske S. Huismans, Sebastian G. Wolf. **Effective viscous strain weak-
ening in mid-to-lower continental crust**, *In preparation for Geophysical Re-
search Letters.*

1.5.2 Meetings

Curry et al.: Evolving lithospheric flexure and paleotopography of the Pyrenean Oro-
gen from 3D flexural modeling and basin analysis. *European Geosciences Union
General Assembly*; 2018-04-08 – 2018-04-13, Wien, Austria.

Curry et al.: Spatio-temporal evolution of exhumation and topography of the Pyrenees
Mountains. *American Geophysical Union Fall Meeting*; 2018-12-10 – 2018-12-
14, Washington D.C., USA.

Huismans et al.: The role of extensional inheritance and amount of shortening on moun-
tain belt evolution. *European Geosciences Union General Assembly*; 2019-04-07
– 2019-04-12, Wien, Austria.

Wrona et al.: A limit to effective viscous weakening in the mid-to-lower crust. *American Geophysical Union Fall Meeting*; 2019-12-09 – 2019-12-13, San Francisco, USA.

Curry et al.: Peak- to post-orogenic landscape evolution of the Pyrenees Mountains from numerical modeling and thermochronology. *American Geophysical Union Fall Meeting*; 2019-12-09 – 2019-12-13, San Francisco, USA.

Michel et al.: Evolution of topography, sediment yield and efficiency of erosion in intra-continental rift settings: A perspective from numerical modeling using coupled surface processes and tectonic models. *European Geosciences Union General Assembly*; 2020-05-03 – 2020-05-08, Wien, Austria.

References cited in the introduction

Agrusta, R., Goes, S., and van Hunen, J. (2017). "Subducting-slab transition-zone interaction: Stagnation, penetration and mode switches". In: *Earth and Planetary Science Letters* 464, pp. 10–23. DOI: 10.1016/j.epsl.2017.02.005.

Andrews, E. R. and Billen, M. I. (2009). "Rheologic controls on the dynamics of slab detachment". In: *Tectonophysics* 464.1-4, pp. 60–69. DOI: 10.1016/j.tecto.2007.09.004.

Arcay, D., Doin, M. P., Tric, E., Bousquet, R., and de Capitani, C. (2006). "Overriding plate thinning in subduction zones: Localized convection induced by slab dehydration". In: *Geochemistry Geophysics Geosystems* 7. DOI: 10.1029/2005gc001061.

Arcay, D., Tric, E., and Doin, M. P. (2005). "Numerical simulations of subduction zones - Effect of slab dehydration on the mantle wedge dynamics". In: *Physics of the Earth and Planetary Interiors* 149.1-2, pp. 133–153. DOI: 10.1016/j.pepi.2004.08.020.

Armijo, R., Lacassin, R., Coudurier-Curveur, A., and Carrizo, D. (2015). "Coupled tectonic evolution of Andean orogeny and global climate". In: *Earth-Science Reviews* 143, pp. 1–35. DOI: 10.1016/j.earscirev.2015.01.005.

Arriagada, C., Roperch, P., Mpodozis, C., and Cobbold, P. R. (2008). "Paleogene building of the Bolivian Orocline: Tectonic restoration of the central Andes in 2-D map view". In: *Tectonics* 27.6. DOI: 10.1029/2008TC002269.

Baldwin, J. A., Whipple, K. X., and Tucker, G. E. (2003). "Implications of the shear stress river incision model for the timescale of postorogenic decay of topography". In: *Journal of Geophysical Research-Solid Earth* 108.B3. DOI: Artn215810.1029/2001jb000550.

Batt, G. E. and Braun, J. (1999). "The tectonic evolution of the Southern Alps, New Zealand: insights from fully thermally coupled dynamical modelling". In: *Geophysical Journal International* 136.2, pp. 403–420. DOI: DOI10.1046/j.1365-246X.1999.00730.x.

Beaumont, C., Ellis, S., and Pfiffner, A. (1999). "Dynamics of sediment subduction-accretion at convergent margins: Short-term modes, long-term deformation, and tectonic implications". In: *Journal of Geophysical Research-Solid Earth* 104.B8, pp. 17573–17601. DOI: Doi10.1029/1999jb900136.

Beaumont, C., Fullsack, P., and Hamilton, J. (1992). "Erosional control of active compressional orogens". In: *Thrust tectonics*. Springer, pp. 1–18.

— (1994). "Styles of Crustal Deformation in Compressional Orogens Caused by Subduction of the Underlying Lithosphere". In: *Tectonophysics* 232.1-4, pp. 119–132. DOI: Doi10.1016/0040-1951(94)90079-5.

Beaumont, C., Jamieson, R. A., Nguyen, M. H., and Lee, B. (2001). "Himalayan tectonics explained by extrusion of a low-viscosity crustal channel coupled to focused surface denudation". In: *Nature* 414.6865, pp. 738–742. DOI: DOI10.1038/414738a.

Beaumont, C., Kamp, P. J. J., Hamilton, J., and Fullsack, P. (1996). "The continental collision zone, South Island, New Zealand: Comparison of geodynamical models and observations". In: *Journal of Geophysical Research-Solid Earth* 101.B2, pp. 3333–3359. DOI: Doi10.1029/95jb02401.

Beaumont, C., Muñoz, J. A., Hamilton, J., and Fullsack, P. (2000). "Factors controlling the Alpine evolution of the central Pyrenees inferred from a comparison of observations and geodynamical models". In: *Journal of Geophysical Research-Solid Earth* 105.B4, pp. 8121–8145. DOI: Doi10.1029/1999jb900390.

Beaumont, C., Nguyen, M. H., Jamieson, R. A., and Ellis, S. (2006). "Crustal flow modes in large hot orogens". In: *Geological Society, London, Special Publications* 268.1, pp. 91–145.

Billen, M. I. (2008). "Modeling the dynamics of subducting slabs". In: *Annual Review of Earth and Planetary Sciences* 36, pp. 325–356. DOI: 10.1146/annurev.earth.36.031207.124129.

— (2010). "Slab dynamics in the transition zone". In: *Physics of the Earth and Planetary Interiors* 183.1-2, pp. 296–308. DOI: 10.1016/j.pepi.2010.05.005.

Bird, P. (1991). "Lateral Extrusion of Lower Crust from under High Topography, in the Isostatic Limit". In: *Journal of Geophysical Research-Solid Earth and Planets* 96.B6, pp. 10275–10286. DOI: Doi10.1029/91jb00370.

Box, G. E. P. (1976). "Science and Statistics". In: *Journal of the American Statistical Association* 71.356, pp. 791–799. DOI: 10.1080/01621459.1976.10480949.

Brandon, M. T., Roden-Tice, M. K., and Garver, J. I. (1998). "Late Cenozoic exhumation of the Cascadia accretionary wedge in the Olympic Mountains, northwest Washington State". In: *Geological Society of America Bulletin* 110.8, pp. 985–1009. DOI: Doi10.1130/0016-7606(1998)110<0985:Lceotc>2.3.Co;2.

Braun, J. and Beaumont, C. (1995). "3-Dimensional Numerical Experiments of Strain Partitioning at Oblique Plate Boundaries - Implications for Contrasting Tectonic Styles in the Southern Coast Ranges, California, and Central South Island, New-Zealand". In: *Journal of Geophysical Research-Solid Earth* 100.B9, pp. 18059–18074. DOI: Doi10.1029/95jb01683.

Braun, J. and Willett, S. D. (2013). "A very efficient O(n), implicit and parallel method to solve the stream power equation governing fluvial incision and landscape evolution". In: *Geomorphology* 180, pp. 170–179. DOI: 10.1016/j.geomorph.2012.10.008.

Brown, D., Alvarez-Marron, J., Schimmel, M., Wu, Y. M., and Camanni, G. (2012). "The structure and kinematics of the central Taiwan mountain belt derived from geological and seismicity data". In: *Tectonics* 31. DOI: ArtnTc501310.1029/2012tc003156.

Butler, J. P., Beaumont, C., and Jamieson, R. A. (2011). "Crustal emplacement of exhuming (ultra)high-pressure rocks: Will that be pro- or retro-side?" In: *Geology* 39.7, pp. 635–638. DOI: 10.1130/G32166.1.

— (2013). "The Alps 1: A working geodynamic model for burial and exhumation of (ultra)high-pressure rocks in Alpine-type orogens". In: *Earth and Planetary Science Letters* 377, pp. 114–131. DOI: 10.1016/j.epsl.2013.06.039.

— (2015). "Paradigm lost: Buoyancy thwarted by the strength of the Western Gneiss Region (ultra)high-pressure terrane, Norway". In: *Lithosphere* 7.4, pp. 379–407. DOI: 10.1130/L426.1.

Capitanio, F. A., Stegman, D. R., Moresi, L. N., and Sharples, W. (2010). "Upper plate controls on deep subduction, trench migrations and deformations at convergent margins". In: *Tectonophysics* 483.1-2, pp. 80–92. DOI: 10.1016/j.tecto.2009.08.020.

Carrera, N. and Muñoz, J. A. (2013). "Thick-skinned tectonic style resulting from the inversion of previous structures in the southern Cordillera Oriental (NW Argentine Andes)". In: *Geological Society, London, Special Publications* 377.1, pp. 77–100. DOI: 10.1144/sp377.2.

Carrera, N., Muñoz, J. A., Sabat, F., Mon, R., and Roca, E. (2006). "The role of inversion tectonics in the structure of the Cordillera Oriental (NW Argentinean Andes)". In: *Journal of Structural Geology* 28.11, pp. 1921–1932. DOI: 10.1016/j.jsg.2006.07.006.

Chamberlin, R. T. (1919). "The Building of the Colorado Rockies". In: *The Journal of Geology* 27.3, pp. 145–164.

Chung, S. L. et al. (2005). "Tibetan tectonic evolution inferred from spatial and temporal variations in post-collisional magmatism". In: *Earth-Science Reviews* 68.3-4, pp. 173–196. DOI: 10.1016/j.earscirev.2004.05.001.

Conrad, C. P. and Hager, B. H. (1999). "Effects of plate bending and fault strength at subduction zones on plate dynamics". In: *Journal of Geophysical Research-Solid Earth* 104.B8, pp. 17551–17571. DOI: 10.1029/1999jb900149.

Cowie, P. A., Whittaker, A. C., Attal, M., Roberts, G., Tucker, G. E., and Ganas, A. (2008). "New constraints on sediment-flux-dependent river incision: Implications for extracting tectonic signals from river profiles". In: *Geology* 36.7, pp. 535–538. DOI: 10.1130/G24681a.1.

Currie, C. A., Huismans, R. S., and Beaumont, C. (2008). "Thinning of continental backarc lithosphere by flow-induced gravitational instability". In: *Earth and Planetary Science Letters* 269.3-4, pp. 435–446. DOI: 10.1016/j.epsl.2008.02.037.

Dadson, S. J. et al. (2003). "Links between erosion, runoff variability and seismicity in the Taiwan orogen". In: *Nature* 426.6967, pp. 648–651. DOI: 10.1038/nature02150.

Dahlen, F. A. (1984). "Noncohesive Critical Coulomb Wedges - an Exact Solution". In: *Journal of Geophysical Research* 89.Nb12, pp. 125–133. DOI: DOI10.1029/JB089iB12p10125.

Davis, D., Suppe, J., and Dahlen, F. A. (1983). "Mechanics of Fold-and-Thrust Belts and Accretionary Wedges". In: *Journal of Geophysical Research* 88.Nb2, pp. 1153–1172. DOI: DOI10.1029/JB088iB02p01153.

DeCelles, P. G., Ducea, M. N., Kapp, P., and Zandt, G. (2009). "Cyclicity in Cordilleran orogenic systems". In: *Nature Geoscience* 2.4, pp. 251–257. DOI: 10.1038/Ngeo469.

DeCelles, P. G., Robinson, D. M., Quade, J., Ojha, T. P., Garzione, C. N., Copeland, P., and Upreti, B. N. (2001). "Stratigraphy, structure, and tectonic evolution of the Himalayan fold-thrust belt in western Nepal". In: *Tectonics* 20.4, pp. 487–509. DOI: Doi10.1029/2000tc001226.

Dewey, J. F. and Bird, J. M. (1970). "Mountain Belts and New Global Tectonics". In: *Journal of Geophysical Research* 75.14, pp. 2625–&. DOI: DOI10.1029/JB075i014p02625.

DiBiase, R. A. and Whipple, K. X. (2011). "The influence of erosion thresholds and runoff variability on the relationships among topography, climate, and erosion rate". In: *Journal of Geophysical Research-Earth Surface* 116. DOI: ArtnF0403610.1029/2011jf002095.

Dietz, R. S. (1961). "Continent and Ocean Basin Evolution by Spreading of Sea Floor". In: *Nature* 190.477, pp. 854–&. DOI: DOI10.1038/190854a0.

Djomani, Y. H. P., O'Reilly, S. Y., Griffin, W. L., and Morgan, P. (2001). "The density structure of subcontinental lithosphere through time". In: *Earth and Planetary Science Letters* 184.3-4, pp. 605–621.

Duretz, T., Schmalholz, S. M., and Gerya, T. V. (2012). "Dynamics of slab detachment". In: *Geochemistry Geophysics Geosystems* 13. DOI: 10.1029/2011gc004024.

Egholm, D. L., Knudsen, M. F., and Sandiford, M. (2013). "Lifespan of mountain ranges scaled by feedbacks between landsliding and erosion by rivers". In: *Nature* 498.7455, pp. 475–+. DOI: 10.1038/nature12218.

Ellis, S. and Beaumont, C. (1999). "Models of convergent boundary tectonics: implications for the interpretation of Lithoprobe data". In: *Canadian Journal of Earth Sciences* 36.10, pp. 1711–1741. DOI: 10.1139/e99-075.

Ellis, S., Beaumont, C., Jamieson, R. A., and Quinlan, G. (1998). "Continental collision including a weak zone: the vise model and its application to the Newfoundland Appalachians". In: *Canadian Journal of Earth Sciences* 35.11, pp. 1323–1346. DOI: 10.1139/e97-100.

Ellis, S., Fullsack, P., and Beaumont, C. (1995). "Oblique Convergence of the Crust Driven by Basal Forcing - Implications for Length-Scales of Deformation and Strain Partitioning in Orogens". In: *Geophysical Journal International* 120.1, pp. 24–44. DOI: DOI10.1111/j.1365-246X.1995.tb05909.x.

England, P. and McKenzie, D. (1982). "A Thin Viscous Sheet Model for Continental Deformation". In: *Geophysical Journal of the Royal Astronomical Society* 70.2, pp. 295–321. DOI: DOI10.1111/j.1365-246X.1982.tb04969.x.

— (1983). "Correction to - a Thin Viscous Sheet Model for Continental Deformation". In: *Geophysical Journal of the Royal Astronomical Society* 73.2, pp. 523–532. DOI: DOI10.1111/j.1365-246X.1983.tb03328.x.

Erdős, Z., Huismans, R. S., and van der Beek, P. (2015). "First-order control of syntectonic sedimentation on crustal-scale structure of mountain belts". In: *Journal of Geophysical Research-Solid Earth* 120.7, pp. 5362–5377. DOI: 10.1002/2014jb011785.

Erdős, Z., Huismans, R. S., van der Beek, P., and Thieulot, C. (2014). "Extensional inheritance and surface processes as controlling factors of mountain belt struc-

ture". In: *Journal of Geophysical Research-Solid Earth* 119.12, pp. 9042–9061. DOI: 10.1002/2014jb011408.

Faccenda, M., Gerya, T. V., Mancktelow, N. S., and Moresi, L. (2012). "Fluid flow during slab unbending and dehydration: Implications for intermediate-depth seismicity, slab weakening and deep water recycling". In: *Geochemistry Geophysics Geosystems* 13.1. DOI: 10.1029/2011gc003860.

Faccenna, C. et al. (2014). "Mantle dynamics in the Mediterranean". In: *Reviews of Geophysics* 52.3, pp. 283–332. DOI: 10.1002/2013rg000444.

Fillon, C., Huismans, R. S., van der Beek, P., and Muñoz, J. A. (2013). "Syntectonic sedimentation controls on the evolution of the southern Pyrenean fold-and-thrust belt: Inferences from coupled tectonic-surface processes models". In: *Journal of Geophysical Research-Solid Earth* 118.10, pp. 5665–5680. DOI: 10.1002/jgrb.50368.

Forsyth, D. and Uyeda, S. (1975). "Relative Importance of Driving Forces of Plate Motion". In: *Geophysical Journal of the Royal Astronomical Society* 43.1, pp. 163–200. DOI: 10.1111/j.1365-246X.1975.tb00631.x.

Funiciello, F., Faccenna, C., and Giardini, D. (2004). "Role of lateral mantle flow in the evolution of subduction systems: insights from laboratory experiments". In: *Geophysical Journal International* 157.3, pp. 1393–1406. DOI: 10.1111/j.1365-246X.2004.02313.x.

Funiciello, F., Faccenna, C., Giardini, D., and Regenauer-Lieb, K. (2003). "Dynamics of retreating slabs: 2. Insights from three-dimensional laboratory experiments". In: *Journal of Geophysical Research-Solid Earth* 108.B4. DOI: 10.1029/2001jb000896.

Gao, R., Lu, Z. W., Klemperer, S. L., Wang, H. Y., Dong, S. W., Li, W. H., and Li, H. Q. (2016). "Crustal-scale duplexing beneath the Yarlung Zangbo suture in the western Himalaya (vol 9, pg 555, 2016)". In: *Nature Geoscience* 9.7. DOI: 10.1038/ngeo2730.

Gerya, T. (2011). "Future directions in subduction modeling". In: *Journal of Geodynamics* 52.5, pp. 344–378. DOI: 10.1016/j.jog.2011.06.005.

Gillcrist, R., Coward, M., and Mugnier, J.-L. (1987). "Structural inversion and its controls : examples from the Alpine foreland and the French Alps". In: *Geodinamica Acta* 1.1, pp. 5–34. DOI: 10.1080/09853111.1987.11105122.

Goes, S., Agrusta, R., van Hunen, J., and Garel, F. (2017). "Subduction-transition zone interaction: A review". In: *Geosphere* 13.3, pp. 644–664. DOI: 10.1130/Ges01476.1.

Griffin, W., O'Reilly, S. Y., Ryan, C., Gaul, O., and Ionov, D. (1998). "Secular variation in the composition of subcontinental lithospheric mantle: geophysical and geodynamic implications". In: *Structure and evolution of the Australian continent* 26, pp. 1–26.

Grool, A. R., Huismans, R. S., and Ford, M. (2019). "Salt decollement and rift inheritance controls on crustal deformation in orogens". In: *Terra Nova* 31.6, pp. 562–568. DOI: 10.1111/ter.12428.

Hacker, B. R., Kelemen, P. B., and Behn, M. D. (2015). "Continental Lower Crust". In: *Annual Review of Earth and Planetary Sciences* 43.1h, pp. 167–205. DOI: 10. 1146/annurev-earth-050212-124117.

Handy, M. R., Schmid, S. M., Bousquet, R., Kissling, E., and Bernoulli, D. (2010). "Reconciling plate-tectonic reconstructions of Alpine Tethys with the geological-geophysical record of spreading and subduction in the Alps". In: *Earth-Science Reviews* 102.3-4, pp. 121–158. DOI: 10.1016/j.earscirev.2010.06.002.

Harel, M.-A., Mudd, S., and Attal, M. (2016). "Global analysis of the stream power law parameters based on worldwide 10Be denudation rates". In: *Geomorphology* 268, pp. 184–196.

Hartshorn, K., Hovius, N., Dade, W. B., and Slingerland, R. L. (2002). "Climate-driven bedrock incision in an active mountain belt". In: *Science* 297.5589, pp. 2036–2038. DOI: DOI10.1126/science.1075078.

Herman, F., Cox, S. C., and Kamp, P. J. J. (2009). "Low-temperature thermochronology and thermokinematic modeling of deformation, exhumation, and development of topography in the central Southern Alps, New Zealand". In: *Tectonics* 28. DOI: ArtnTc501110.1029/2008tc002367.

Herman, F. et al. (2010). "Exhumation, crustal deformation, and thermal structure of the Nepal Himalaya derived from the inversion of thermochronological and thermobarometric data and modeling of the topography". In: *Journal of Geophysical Research-Solid Earth* 115. DOI: ArtnB0640710.1029/2008jb006126.

Hess, H. H. (1962). "History of Ocean Basins". In: *Petrologic Studies*. Geological Society of America, DOI: 10.1130/Petrologic.1962.599.

Heuret, A. and Lallemand, S. (2005). "Plate motions, slab dynamics and back-arc deformation". In: *Physics of the Earth and Planetary Interiors* 149.1-2, pp. 31–51. DOI: 10.1016/j.pepi.2004.08.022.

Hilley, G. E., Porder, S., Aron, F., Baden, C. W., Johnstone, S. A., Liu, F., Sare, R., Steelquist, A., and Young, H. H. (2019). "Earth's topographic relief potentially limited by an upper bound on channel steepness". In: *Nature Geoscience* 12.10, pp. 828–+. DOI: 10.1038/s41561-019-0442-3.

Hilley, G. E., Strecker, M. R., and Ramos, V. A. (2004). "Growth and erosion of fold-and-thrust belts with an application to the Aconcagua fold-and-thrust belt, Argentina". In: *Journal of Geophysical Research-Solid Earth* 109.B1. DOI: ArtnB0141010.1029/2002jb002282.

Howard, A. D. and Kerby, G. (1983). "Channel Changes in Badlands". In: *Geological Society of America Bulletin* 94.6, pp. 739–752. DOI: Doi10.1130/0016-7606(1983)94<739:Ccib>2.0.Co;2.

Huangfu, P. P., Li, Z. H., Gerya, T., Fan, W. M., Zhang, K. J., Zhang, H., and Shi, Y. L. (2018). "Multi-terrane structure controls the contrasting lithospheric evolution beneath the western and central-eastern Tibetan plateau". In: *Nature Communications* 9. DOI: ARTN378010.1038/s41467-018-06233-x.

Hyndman, R. D. (1972). "Plate Motions Relative to Deep Mantle and Development of Subduction Zones". In: *Nature* 238.5362, pp. 263–&. DOI: DOI10.1038/238263b0.

Hyndman, R. D., Currie, C. A., and Mazzotti, S. P. (2005). "Subduction zone backarcs, mobile belts, and orogenic heat". In: *GSA Today* 15.2, pp. 4–10. DOI: 10.1130/1052-5173(2005)015<4:SZBMBA>2.0.CO;2.

Iaffa, D. N., Sabat, F., Muñoz, J. A., Mon, R., and Gutierrez, A. A. (2011). "The role of inherited structures in a foreland basin evolution. The Metan Basin in NW Argentina". In: *Journal of Structural Geology* 33.12, pp. 1816–1828. DOI: 10.1016/j.jsg.2011.09.005.

Ings, S. J. and Beaumont, C. (2010). "Continental margin shale tectonics: preliminary results from coupled fluid-mechanical models of large-scale delta instability". In: *Journal of the Geological Society* 167.3, pp. 571–582. DOI: 10.1144/0016-76492009-052.

Jamieson, R. A. and Beaumont, C. (2013). "On the origin of orogens". In: *Geological Society of America Bulletin* 125.11-12, pp. 1671–1702. DOI: Doi10.1130/B30855.1.

Jarrard, R. D. (1986). "Relations among Subduction Parameters". In: *Reviews of Geophysics* 24.2, pp. 217–284. DOI: 10.1029/RG024i002p00217.

Jiao, R., Herman, F., and Seward, D. (2017). "Late Cenozoic exhumation model of New Zealand: Impacts from tectonics and climate". In: *Earth-Science Reviews* 166, pp. 286–298. DOI: 10.1016/j.earscirev.2017.01.003.

Jolivet, L. et al. (2013). "Aegean tectonics: Strain localisation, slab tearing and trench retreat". In: *Tectonophysics* 597, pp. 1–33. DOI: 10.1016/j.tecto.2012.06.011.

Kapp, P. and DeCelles, P. G. (2019). "Mesozoic-Cenozoic Geological Evolution of the Himalayan-Tibetan Orogen and Working Tectonic Hypotheses". In: *American Journal of Science* 319.3, pp. 159–254. DOI: 10.2475/03.2019.01.

Katayama, I. and Karato, S. I. (2008). "Low-temperature, high-stress deformation of olivine under water-saturated conditions". In: *Physics of the Earth and Planetary Interiors* 168.3-4, pp. 125–133. DOI: 10.1016/j.pepi.2008.05.019.

Kaus, B. J. P., Muhlhaus, H., and May, D. A. (2010). "A stabilization algorithm for geodynamic numerical simulations with a free surface". In: *Physics of the Earth and Planetary Interiors* 181.1-2, pp. 12–20. DOI: 10.1016/j.pepi.2010.04.007.

Koons, P. O. (1989). "The Topographic Evolution of Collisional Mountain Belts - a Numerical Look at the Southern Alps, New-Zealand". In: *American Journal of Science* 289.9, pp. 1041–1069. DOI: DOI10.2475/ajs.289.9.1041.

Kreemer, C., Holt, W. E., and Haines, A. J. (2003). "An integrated global model of present-day plate motions and plate boundary deformation". In: *Geophysical Journal International* 154.1, pp. 8–34. DOI: 10.1046/j.1365-246X.2003.01917.x.

Krystopowicz, N. J. and Currie, C. A. (2013). "Crustal eclogitization and lithosphere delamination in orogens". In: *Earth and Planetary Science Letters* 361, pp. 195–207. DOI: 10.1016/j.epsl.2012.09.056.

Lague, D., Hovius, N., and Davy, P. (2005). "Discharge, discharge variability, and the bedrock channel profile". In: *Journal of Geophysical Research-Earth Surface* 110.F4. DOI: ArtnF0400610.1029/2004jf000259.

Le Pichon, X. (1968). "Sea-Floor Spreading and Continental Drift". In: *Journal of Geophysical Research* 73.12, pp. 3661–+. DOI: DOI10.1029/JB073i012p03661.

Li, C., van der Hilst, R. D., Engdahl, E. R., and Burdick, S. (2008). "A new global model for P wave speed variations in Earth's mantle". In: *Geochemistry Geophysics Geosystems* 9.5. DOI: 10.1029/2007gc001806.

Liao, J., Gerya, T., and Malosa, M. G. (2018). "3D modeling of crustal shortening influenced by along-strike lithological changes: Implications for continental collision in the Western and Central Alps". In: *Tectonophysics* 746, pp. 425–438. DOI: 10.1016/j.tecto.2018.01.031.

Little, T. A. (2004). "Transpressive ductile flow and oblique ramping of lower crust in a two-sided orogen: Insight from quartz grain-shape fabrics near the Alpine fault, New Zealand". In: *Tectonics* 23.2. DOI: ArtnTc201310.1029/2002tc001456.

Magni, V., Faccenna, C., van Hunen, J., and Funiciello, F. (2014). "How collision triggers backarc extension: Insight into Mediterranean style of extension from 3-D numerical models". In: *Geology* 42.6, pp. 511–514. DOI: 10.1130/G35446.1.

McKenzie, D. P. (1969). "Speculations on Consequences and Causes of Plate Motions". In: *Geophysical Journal of the Royal Astronomical Society* 18.1, pp. 1–&. DOI: DOI10.1111/j.1365-246X.1969.tb00259.x.

McKenzie, D. P., Roberts, J. M., and Weiss, N. O. (1974). "Convection in the earth's mantle: towards a numerical simulation". In: *Journal of Fluid Mechanics* 62.3, pp. 465–538. DOI: 10.1017/S0022112074000784.

Michel, L., Glotzbach, C., Falkowski, S., Adams, B. A., and Ehlers, T. A. (2019). "How steady are steady-state mountain belts? A reexamination of the Olympic Mountains (Washington state, USA)". In: *Earth Surf. Dynam.* 7.1, pp. 275–299. DOI: 10.5194/esurf-7-275-2019.

Minear, J. W. and Toksöz, M. N. (1970). "Thermal Regime of a Downgoing Slab and New Global Tectonics". In: *Journal of Geophysical Research* 75.8, pp. 1397–1419. DOI: DOI10.1029/JB075i008p01397.

Mitrovica, J. X. and Forte, A. M. (2004). "A new inference of mantle viscosity based upon joint inversion of convection and glacial isostatic adjustment data". In: *Earth and Planetary Science Letters* 225.1-2, pp. 177–189. DOI: 10.1016/j.epsl.2004.06.005.

Molnar, P., Anderson, R. S., and Anderson, S. P. (2007). "Tectonics, fracturing of rock, and erosion". In: *Journal of Geophysical Research-Earth Surface* 112.F3. DOI: ArtnF0301410.1029/2005jf000433.

Molnar, P. and England, P. (1990). "Late Cenozoic Uplift of Mountain-Ranges and Global Climate Change - Chicken or Egg". In: *Nature* 346.6279, pp. 29–34. DOI: DOI10.1038/346029a0.

Molnar, P. and Lyon-Caen, H. (1988). "Some simple physical aspects of the support, structure, and evolution of mountain belts". In: *Geol. Soc. Am. Spec. Pap.* 218, pp. 179–207.

Morgan, W. J. (1968). "Rises Trenches Great Faults and Crustal Blocks". In: *Journal of Geophysical Research* 73.6, pp. 1959–&. DOI: DOI10.1029/JB073i006p01959.

Muñoz, J. A. (1992). "Evolution of a continental collision belt: ECORS-Pyrenees crustal balanced cross-section". In: *Thrust tectonics*. Springer, pp. 235–246.

— (2019). "Deformation and structure in the Northern Iberian margin (Pyrenees S.L.)" In: *The Geology of Iberia: A Geodynamic Approach*. Ed. by C. Quesada and J. Oliveira. Springer.

Negredo, A. M., Replumaz, A., Villasenor, A., and Guillot, S. (2007). "Modeling the evolution of continental subduction processes in the Pamir-Hindu Kush region". In: *Earth and Planetary Science Letters* 259.1-2, pp. 212–225. DOI: 10.1016/j.epsl.2007.04.043.

Oncken, O., Hindle, D., Kley, J., Elger, K., Victor, P., and Schemmann, K. (2006). "Deformation of the central Andean upper plate system - Facts, fiction, and constraints for plateau models". In: *The Andes. Frontiers in Earth Sciences*. Ed. by O. Oncken, G. Chong, G. Franz, P. Giese, H. J. Götze, V. A. Ramos, M. R. Strecker, and P. Wigger. Springer, Berlin, Heidelberg, pp. 3–27. DOI: 10.1007/978-3-540-48684-8_1.

O'Neill, C., Müller, D., and Steinberger, B. (2005). "On the uncertainties in hot spot reconstructions and the significance of moving hot spot reference frames". In: *Geochemistry Geophysics Geosystems* 6.4. DOI: 10.1029/2004gc000784.

Owens, T. J. and Zandt, G. (1997). "Implications of crustal property variations for models of Tibetan plateau evolution". In: *Nature* 387.6628, pp. 37–43. DOI: DOI10.1038/387037a0.

OzBench, M. et al. (2008). "A model comparison study of large-scale mantle-lithosphere dynamics driven by subduction". In: *Physics of the Earth and Planetary Interiors* 171.1-4, pp. 224–234. DOI: 10.1016/j.pepi.2008.08.011.

Pope, D. C. and Willett, S. D. (1998). "Thermal-mechanical model for crustal thickening in the central Andes driven by ablative subduction". In: *Geology* 26.6, pp. 511–514. DOI: 10.1130/0091-7613(1998)026<0511:Tmmfct>2.3.Co;2.

Replumaz, A., Negredo, A. M., Guillot, S., van der Beek, P., and Villasenor, A. (2010a). "Crustal mass budget and recycling during the India/Asia collision". In: *Tectonophysics* 492.1-4, pp. 99–107. DOI: 10.1016/j.tecto.2010.05.023.

Replumaz, A., Negredo, A. M., Guillot, S., and Villasenor, A. (2010b). "Multiple episodes of continental subduction during India/Asia convergence: Insight from seismic tomography and tectonic reconstruction". In: *Tectonophysics* 483.1-2, pp. 125–134. DOI: 10.1016/j.tecto.2009.10.007.

Robinson, D. M. (2008). "Forward modeling the kinematic sequence of the central Himalayan thrust belt, western Nepal". In: *Geosphere* 4.5, pp. 785–801. DOI: 10.1130/Ges00163.1.

Roca, E., Muñoz, J. A., Ferrer, O., and Ellouz, N. (2011). "The role of the Bay of Biscay Mesozoic extensional structure in the configuration of the Pyrenean orogen: Constraints from the MARCONI deep seismic reflection survey". In: *Tectonics* 30. DOI: ArtnTc200110.1029/2010tc002735.

Rodgers, J. (1949). "Evolution of Thought on Structure of Middle and Southern Appalachians". In: *Aapg Bulletin-American Association of Petroleum Geologists* 33.10, pp. 1643–1654.

Rodriguez-Gonzalez, J. and Negredo, A. M. (2012). "The role of the overriding plate thermal state on slab dip variability and on the occurrence of flat subduction". In: *Geochemistry Geophysics Geosystems* 13.1. DOI: 10.1029/2011gc003859.

Ruh, J. B., Gerya, T., and Burg, J.-P. (2017). "Toward 4D modeling of orogenic belts: Example from the transpressive Zagros Fold Belt". In: *Tectonophysics* 702.Supplement C, pp. 82–89. DOI: https://doi.org/10.1016/j.tecto.2015.09.035.

Ruh, J. B., Kaus, B. J. P., and Burg, J. P. (2012). "Numerical investigation of deformation mechanics in fold-and-thrust belts: Influence of rheology of single and multiple decollements". In: *Tectonics* 31. DOI: ArtnTc300510.1029/2011tc003047.

Sandiford, M. and Powell, R. (1990). "Some Isostatic and Thermal Consequences of the Vertical Strain Geometry in Convergent Orogens". In: *Earth and Planetary Science Letters* 98.2, pp. 154–165. DOI: Doi10.1016/0012-821x(90)90056-4.

Schellart, W. P. (2008). "Overriding plate shortening and extension above subduction zones: A parametric study to explain formation of the Andes Mountains". In: *Geological Society of America Bulletin* 120.11-12, pp. 1441–1454. DOI: 10.1130/B26360.1.

Schellart, W. P., Freeman, J., Stegman, D. R., Moresi, L., and May, D. (2007). "Evolution and diversity of subduction zones controlled by slab width". In: *Nature* 446.7133, pp. 308–311. DOI: 10.1038/nature05615.

Schellart, W. P. and Moresi, L. (2013). "A new driving mechanism for backarc extension and backarc shortening through slab sinking induced toroidal and poloidal mantle flow: Results from dynamic subduction models with an overriding plate". In: *Journal of Geophysical Research-Solid Earth* 118.6, pp. 3221–3248. DOI: 10.1002/jgrb.50173.

Schmeling, H. et al. (2008). "A benchmark comparison of spontaneous subduction models-Towards a free surface". In: *Physics of the Earth and Planetary Interiors* 171.1-4, pp. 198–223. DOI: 10.1016/j.pepi.2008.06.028.

Schmid, S. M., Fugenschuh, B., Kissling, E., and Schuster, R. (2004). "Tectonic map and overall architecture of the Alpine orogen". In: *Eclogae Geologicae Helvetiae* 97.1, pp. 93–117. DOI: 10.1007/s00015-004-1113-x.

Schmid, S. M. and Kissling, E. (2000). "The arc of the western Alps in the light of geophysical data on deep crustal structure". In: *Tectonics* 19.1, pp. 62–85. DOI: Doi10.1029/1999tc900057.

Schmid, S. M., Kissling, E., Diehl, T., van Hinsbergen, D. J. J., and Molli, G. (2017). "Ivrea mantle wedge, arc of the Western Alps, and kinematic evolution of the Alps-Apennines orogenic system". In: *Swiss Journal of Geosciences* 110.2, pp. 581–612. DOI: 10.1007/s00015-016-0237-0.

Schmid, S. M., Pfiffner, O. A., Froitzheim, N., Schonborn, G., and Kissling, E. (1996). "Geophysical-geological transect and tectonic evolution of the Swiss-Italian Alps". In: *Tectonics* 15.5, pp. 1036–1064. DOI: Doi10.1029/96tc00433.

Schurr, B., Rietbrock, A., Asch, G., Kind, R., and Oncken, O. (2006). "Evidence for lithospheric detachment in the central Andes from local earthquake tomography". In: *Tectonophysics* 415.1-4, pp. 203–223. DOI: 10.1016/j.tecto.2005.12.007.

Selzer, C., Buiter, S. J. H., and Pfiffner, O. A. (2007). "Sensitivity of shear zones in orogenic wedges to surface processes and strain softening". In: *Tectonophysics* 437.1-4, pp. 51–70. DOI: 10.1016/j.tecto.2007.02.020.

Simpson, G. D. H. (2006). "Modelling interactions between fold-thrust belt deformation, foreland flexure and surface mass transport". In: *Basin Research* 18.2, pp. 125–143. DOI: 10.1111/j.1365-2117.2006.00287.x.

Sklar, L. S. and Dietrich, W. E. (2001). "Sediment and rock strength controls on river incision into bedrock". In: *Geology* 29.12, pp. 1087–1090. DOI: Doi10.1130/0091-7613(2001)029<1087:Sarsco>2.0.Co;2.

Sobolev, S. V. and Babeyko, A. Y. (2005). "What drives orogeny in the Andes?" In: *Geology* 33.8, pp. 617–620. DOI: 10.1130/G21557.

Sommaruga, A. (1999). "Decollement tectonics in the Jura foreland fold-and-thrust belt". In: *Marine and Petroleum Geology* 16.2, pp. 111–134. DOI: Doi10.1016/S0264-8172(98)00068-3.

Starke, J., Ehlers, T. A., and Schaller, M. (2020). "Latitudinal effect of vegetation on erosion rates identified along western South America". In: *Science* 367.6484, pp. 1358–1361. DOI: 10.1126/science.aaz0840.

Stegman, D. R., Farrington, R., Capitanio, F. A., and Schellart, W. P. (2010). "A regime diagram for subduction styles from 3-D numerical models of free subduction". In: *Tectonophysics* 483.1-2, pp. 29–45. DOI: 10.1016/j.tecto.2009.08.041.

Stegman, D. R., Freeman, J., Schellart, W. P., Moresi, L., and May, D. (2006). "Influence of trench width on subduction hinge retreat rates in 3-D models of slab rollback". In: *Geochemistry Geophysics Geosystems* 7. DOI: ArtnQ0301210.1029/2005gc001056.

Stock, J. D. and Montgomery, D. R. (1999). "Geologic constraints on bedrock river incision using the stream power law". In: *Journal of Geophysical Research: Solid Earth* 104.B3, pp. 4983–4993.

Stockmal, G. S., Beaumont, C., Nguyen, M., and Lee, B. (2007). "Mechanics of thin-skinned fold-and-thrust belts: Insights from numerical models Whence the Mountains? Inquiries into the Evolution of Orogenic Systems: A Volume in Honor of Raymond A. Price". In: ed. by J. W. Sears, T. A. Harms, and C. A. Evenchick. Vol. 433. Geological Society of America, DOI: 10.1130/2007.2433(04).

Stolar, D. B., Roe, G. H., and Willett, S. D. (2007). "Controls on the patterns of topography and erosion rate in a critical orogen". In: *Journal of Geophysical Research-Earth Surface* 112.F4. DOI: ArtnF0400210.1029/2006jf000713.

Stolar, D. B., Willett, S. D., and Roe, G. H. (2006). "Climatic and tectonic forcing of a critical orogen". In: *SPECIAL PAPERS-GEOLOGICAL SOCIETY OF AMERICA* 398, p. 241.

Thieulot, C. (2011). "FANTOM: Two- and three-dimensional numerical modelling of creeping flows for the solution of geological problems". In: *Physics of the Earth and Planetary Interiors* 188.1-2, pp. 47–68. DOI: 10.1016/j.pepi.2011.06.011.

Thieulot, C., Steer, P., and Huismans, R. S. (2014). "Three-dimensional numerical simulations of crustal systems undergoing orogeny and subjected to surface processes". In: *Geochemistry Geophysics Geosystems* 15.12, pp. 4936–4957. DOI: 10.1002/2014gc005490.

Tosi, N., Yuen, D. A., de Koker, N., and Wentzcovitch, R. M. (2013). "Mantle dynamics with pressure- and temperature-dependent thermal expansivity and conductivity".

In: *Physics of the Earth and Planetary Interiors* 217, pp. 48–58. DOI: 10.1016/j. pepi.2013.02.004.

Tsenn, M. C. and Carter, N. L. (1987). "Upper Limits of Power Law Creep of Rocks". In: *Tectonophysics* 136.1-2, pp. 1–26. DOI: 10.1016/0040-1951(87)90332-5.

Tucker, G. E. and Bras, R. L. (2000). "A stochastic approach to modeling the role of rainfall variability in drainage basin evolution". In: *Water Resources Research* 36.7, pp. 1953–1964. DOI: Doi10.1029/2000wr900065.

Ueda, K., Willett, S. D., Gerya, T., and Ruh, J. (2015). "Geomorphological-thermo-mechanical modeling: Application to orogenic wedge dynamics". In: *Tectonophysics* 659, pp. 12–30. DOI: 10.1016/j.tecto.2015.08.001.

Uyeda, S. and Kanamori, H. (1979). "Back-Arc Opening and the Mode of Subduction". In: *Journal of Geophysical Research* 84.Nb3, pp. 1049–1061. DOI: 10.1029/JB084iB03p01049.

Van Avendonk, H. J. A., Kuo-Chen, H., McIntosh, K. D., Lavier, L. L., Okaya, D. A., Wu, F. T., Wang, C. Y., Lee, C. S., and Liu, C. S. (2014). "Deep crustal structure of an arc-continent collision: Constraints from seismic traveltimes in central Taiwan and the Philippine Sea". In: *Journal of Geophysical Research-Solid Earth* 119.11, pp. 8397–8416. DOI: 10.1002/2014jb011327.

Van Hunen, J., van den Berg, A. P., and Vlaar, N. J. (2000). "A thermo-mechanical model of horizontal subduction below an overriding plate". In: *Earth and Planetary Science Letters* 182.2, pp. 157–169. DOI: Doi10.1016/S0012-821x(00)00240-5.

Vanderhaeghe, O., Medvedev, S., Fullsack, P., Beaumont, C., and Jamieson, R. A. (2003). "Evolution of orogenic wedges and continental plateaux: insights from crustal thermal-mechanical models overlying subducting mantle lithosphere". In: *Geophysical Journal International* 153.1, pp. 27–51. DOI: DOI10.1046/j.1365-246X.2003.01861.x.

Vine, F. J. and Matthews, D. H. (1963). "Magnetic Anomalies over Oceanic Ridges". In: *Nature* 199.489, pp. 947–&. DOI: DOI10.1038/199947a0.

Vogt, K., Willingshofer, E., Matenco, L., Sokoutis, D., Gerya, T., and Cloetingh, U. S. (2018). "The role of lateral strength contrasts in orogenesis: A 2D numerical study". In: *Tectonophysics* 746, pp. 549–561. DOI: 10.1016/j.tecto.2017.08.010.

Warren, C. J., Beaumont, C., and Jamieson, R. A. (2008). "Modelling tectonic styles and ultra-high pressure (UHP) rock exhumation during the transition from oceanic subduction to continental collision". In: *Earth and Planetary Science Letters* 267.1-2, pp. 129–145. DOI: 10.1016/j.epsl.2007.11.025.

Whipple, K. X. (2004). "Bedrock rivers and the geomorphology of active orogens". In: *Annual Review of Earth and Planetary Sciences* 32, pp. 151–185. DOI: 10.1146/annurev.earth.32.101802.120356.

— (2009). "The influence of climate on the tectonic evolution of mountain belts". In: *Nature Geoscience* 2.2, pp. 97–104. DOI: 10.1038/ngeo413.

Whipple, K. X., Kirby, E., and Brocklehurst, S. H. (1999). "Geomorphic limits to climate-induced increases in topographic relief". In: *Nature* 401.6748, pp. 39–43. DOI: Doi10.1038/43375.

Whipple, K. X. and Meade, B. J. (2004). "Controls on the strength of coupling among climate, erosion, and deformation in two-sided, frictional orogenic wedges at steady state". In: *Journal of Geophysical Research-Earth Surface* 109.F1. DOI: `ArtnF0101110.1029/2003jf000019`.

Whipple, K. X. and Tucker, G. E. (1999). "Dynamics of the stream-power river incision model: Implications for height limits of mountain ranges, landscape response timescales, and research needs". In: *Journal of Geophysical Research-Solid Earth* 104.B8, pp. 17661–17674. DOI: `Doi10.1029/1999jb900120`.

Whittaker, A. C., Cowie, P. A., Attal, M., Tucker, G. E., and Roberts, G. P. (2007). "Bedrock channel adjustment to tectonic forcing: Implications for predicting river incision rates". In: *Geology* 35.2, pp. 103–106. DOI: `10.1130/G23106a.1`.

Willett, S. D. (1999). "Orogeny and orography: The effects of erosion on the structure of mountain belts". In: *Journal of Geophysical Research-Solid Earth* 104.B12, pp. 28957–28981. DOI: `Doi10.1029/1999jb900248`.

Willett, S. D. and Beaumont, C. (1994). "Subduction of Asian Lithospheric Mantle beneath Tibet Inferred from Models of Continental Collision". In: *Nature* 369.6482, pp. 642–645. DOI: `DOI10.1038/369642a0`.

Willett, S. D. and Brandon, M. T. (2002). "On steady states in mountain belts". In: *Geology* 30.2, pp. 175–178. DOI: `Doi10.1130/0091-7613(2002)030<0175:Ossimb> 2.0.Co;2`.

Willett, S., Beaumont, C., and Fullsack, P. (1993). "Mechanical Model for the Tectonics of Doubly Vergent Compressional Orogens". In: *Geology* 21.4, pp. 371–374. DOI: `Doi10.1130/0091-7613(1993)021<0371:Mmftto>2.3.Co;2`.

Wilson, J. T. (1966). "Did Atlantic Close and Then Re-Open". In: *Nature* 211.5050, pp. 676–&. DOI: `DOI10.1038/211676a0`.

Wolf, S. G. (2016). "From slab rollback to orogenic plateau formation: a numerical modelling study of ocean-continent subduction systems". MA thesis. University of Bergen, Norway.

Yin, A. and Harrison, T. M. (2000). "Geologic Evolution of the Himalayan-Tibetan Orogen". In: *Annual Review of Earth and Planetary Sciences* 28.1, pp. 211–280. DOI: `10.1146/annurev.earth.28.1.211`.

Yuan, X. P., Braun, J., Guerit, L., Rouby, D., and Cordonnier, G. (2019a). "A New Efficient Method to Solve the Stream Power Law Model Taking Into Account Sediment Deposition". In: *Journal of Geophysical Research-Earth Surface* 124.6, pp. 1346–1365. DOI: `10.1029/2018jf004867`.

Yuan, X. P., Braun, J., Guerit, L., Simon, B., Bovy, B., Rouby, D., Robin, C., and Jiao, R. (2019b). "Linking continental erosion to marine sediment transport and deposition: A new implicit and O(N) method for inverse analysis". In: *Earth and Planetary Science Letters* 524. DOI: `UNSP11572810.1016/j.epsl.2019.115728`.

Zhou, S. H. and Sandiford, M. (1992). "On the Stability of Isostatically Compensated Mountain Belts". In: *Journal of Geophysical Research-Solid Earth* 97.B10, pp. 14207–14221. DOI: `Doi10.1029/92jb01091`.

2 Scientific results

Paper I

Mountain Building or Backarc Extension in Ocean-Continent Subduction Systems: A Function of Backarc Lithospheric Strength and Absolute Plate Velocities

Sebastian G. Wolf, Ritske S. Huismans

Department of Earth Science, University of Bergen, Bergen, Norway.

JGR Solid Earth

Key Points:
- Weak and removed backarc lithospheric mantle facilitates overriding plate deformation
- Trench-ward overriding plate movement inhibits backarc extension and is necessary for backarc shortening
- Comparison with the central Andean and Hellenic subduction zones corroborates model inferences

Correspondence to:
S. G. Wolf,
sebastian.wolf@uib.no

Mountain Building or Backarc Extension in Ocean-Continent Subduction Systems: A Function of Backarc Lithospheric Strength and Absolute Plate Velocities

Sebastian G. Wolf[1] and Ritske S. Huismans[1]

[1]Department of Earth Science, University of Bergen, Bergen, Norway

Abstract The crustal structure of overriding plates in subduction settings around the world varies between a wide range of deformation styles, ranging from extensional structures and backarc opening as in the Tonga or Hellenic subduction zone to large, plateau-like orogens such as the central Andes. Both end-member types have been intensively studied over the last decades, and several hypotheses have been proposed to explain their characteristics. Here we model ocean-continent collision using high-resolution, upper mantle scale plane-strain thermo-mechanical models, accounting for phase changes of rocks that enter the eclogite stability field and the phase transition at the 660 km mantle discontinuity. We test model sensitivity to varying plate velocities and backarc lithospheric strength as the main variables affecting the strain regime of the overriding plate in subduction zones. With our small set of variables, we reproduce both overriding plate extension and shortening and provide insight into the dynamics behind those processes. We find that absolute plate velocities determine the possible strain regimes in the overriding plate, where overriding plate movement toward the trench inhibits backarc extension and promotes overriding plate shortening. Additionally, a weak and removed backarc lithospheric mantle is required for backarc extension and facilitates overriding plate shortening. Comparison of the models with natural subduction systems, specifically the Andes and Hellenic subduction zones, corroborates that lithospheric removal and absolute plate velocities guide overriding plate deformation.

1. Introduction

The overriding plate in ocean-continent subduction systems on Earth has variable tectonic styles. Typical end-members (Uyeda & Kanamori, 1979) are backarc extension as in the Marianas or Hellenic subduction zone (Faccenna et al., 2014; Jolivet et al., 2013) and large orogenic plateau formation as in the central Andes with up to several hundreds of kilometers of overriding plate shortening (Arriagada et al., 2008; Oncken et al., 2006). During recent years, a multitude of geodynamic models (e.g., Agrusta et al., 2017; Arcay et al., 2006; Becker et al., 1999; Billen, 2008, 2010; Butler & Beaumont, 2017; Capitanio et al., 2007, 2010; Cizkova et al., 2002; Currie et al., 2008; Duretz et al., 2012; Faccenda et al., 2012, Faccenna et al., 2017; Funiciello et al., 2003, 2004; Gerya, 2011, Gerya et al., 2015; Holt et al., 2015; Morra et al., 2006; Schellart et al., 2007; Schmeling et al., 2008; Sobolev & Babeyko, 2005; Quinquis et al., 2011) highlights different aspects of subduction dynamics, but no set of working geodynamical models provides and summarizes the main factors which induce either overriding plate extension or shortening in ocean-continent subduction systems.

The tectonic plates on Earth move with absolute velocities of 0 to 10 cm/yr. Those that have a subducting oceanic slab attached to one of their boundaries move in the subduction direction and are significantly faster (3–10 cm/yr) than plates without an attached slab (0–3 cm/yr; Kreemer et al., 2003; O'Neill et al., 2005; Schellart et al., 2007, 2008). This indicates that slab pull, the negative buoyancy of the downgoing slab, provides a first-order control on plate movement (Forsyth & Uyeda, 1975). Slab pull is counteracted by shearing at the subduction interface, rheology-dependent slab deformation, slab suction, and P-T-dependent phase changes in the transition zone (Agrusta et al., 2017; Billen, 2008; Funiciello et al., 2003; Rodriguez-Gonzalez & Negredo, 2012; Sobolev & Babeyko, 2005). The combination of these factors leads to a "natural" sinking velocity (v_{sink}) of slabs in the mantle (Faccenna et al., 2014). In an isolated system, v_{sink} is accommodated by

the combined convergence rates of the subducting plate (v_{oc}) and the overriding plate (v_{cont}), and deformation occurs mostly at the subduction interface and not inside the plates (Capitanio et al., 2010). However, tectonic plates are no isolated features, have lateral density and viscosity variations, possibly several subducting edges (e.g., Pacific plate), and are dragged or pushed by topographic differences (e.g., ridge push) or sublithospheric mantle flow. These factors modify plate velocities and generate tensional or compressional tectonic stresses which can induce extension or shortening in the overriding plate.

The question why the overriding plate in subduction systems deforms has been addressed by several global statistical analyses (Heuret & Lallemand, 2005; Jarrard, 1986; Schellart, 2008), suggesting that overriding plate movement toward or away from the subduction zone provides a main control for variable overriding plate deformation, as already proposed by Uyeda and Kanamori (1979). Numerical modeling confirms that overriding plate movement toward the trench is crucial for mountain building (Sobolev & Babeyko, 2005), while a stationary plate with weak lithosphere promotes backarc spreading (Capitanio et al., 2010). Additionally, the efficiency of toroidal return flow around slab edges is shown to provide an important constraint on the propensity for slab retreat or advance (Funiciello et al., 2004; Schellart & Moresi, 2013; Schellart et al., 2007). Furthermore, large-scale poloidal mantle flow and local subduction-related upwellings have been suggested as a driving force for overriding plate deformation (Faccenna et al., 2010, 2017; Holt et al., 2015; Husson et al., 2012).

Seismological studies show that subduction zones exhibit not only contrasting overriding plate strain regimes but also variable structure at depth (Goes et al., 2017; Li et al., 2008). The two end-member styles are slabs that flatten out in the lower mantle transition zone (e.g., Japan-Izu-Bonin) and those that pierce directly into the lower mantle (e.g., Marianas). Slab stagnation for subduction zones with significant trench retreat has been attributed to the combined effects of the viscosity increase and positive buoyancy associated with the negative Clapeyron slope of the ringwoodite to bridgemanite and magnesiowüstite transition (Agrusta et al., 2017; Billen, 2010; Goes et al., 2017).

Although differing in overriding plate strain regime and deep structural style, many subduction zone backarcs are characterized by elevated heat flow values (Hyndman et al., 2005). While this is expected for regions with active backarc spreading, it requires an explanation for areas with an intact overriding plate. Currie et al. (2008) show with thermo-mechanical modeling that the high heat flow values may result from convective removal of the backarc lithospheric mantle. This requires a weakened backarc lithospheric mantle, for instances, related to fluids expelled from the subducting slab, inherited from earlier deformation periods or subduction-associated melting (Arcay et al., 2005, 2006; Faccenda et al., 2012). Removal of the backarc lithospheric mantle may be enhanced by foundering of dense melt residues (Currie et al., 2015; DeCelles et al., 2009).

We integrate these observations in a geodynamic model and investigate the influence of variable plate velocities and backarc lithospheric strength on the overriding plate strain regime. To advance our understanding of the controlling factors, we use whole mantle scale 2-D thermo-mechanically coupled numerical models that account for the phase transition at the 660 km mantle discontinuity. Our goal is to identify the main factors that control overriding plate extension or shortening and to extract characteristic tectonic and evolutionary features from our models.

Next we present the governing equations and setup of our modeling approach, followed by the model results and an analysis of driving and resisting forces. We then discuss the main parameters leading to overriding plate extension or shortening and compare our model inferences with the central Andes and the Hellenic subduction zone.

2. Methodology

2.1. Basic Principles

We use a modified version of the two-dimensional Arbitrary Lagrangian-Eulerian, thermo-mechanically coupled finite element code FANTOM (Erdos et al., 2014; Thieulot, 2011) to model ocean-continent subduction. We solve for plane-strain incompressible creeping (Stokes) flows ((1) and (2)) and heat transfer (3) in the model domain:

$$\frac{\partial v_i}{\partial x_i} = 0 \quad i = 1, 2, \tag{1}$$
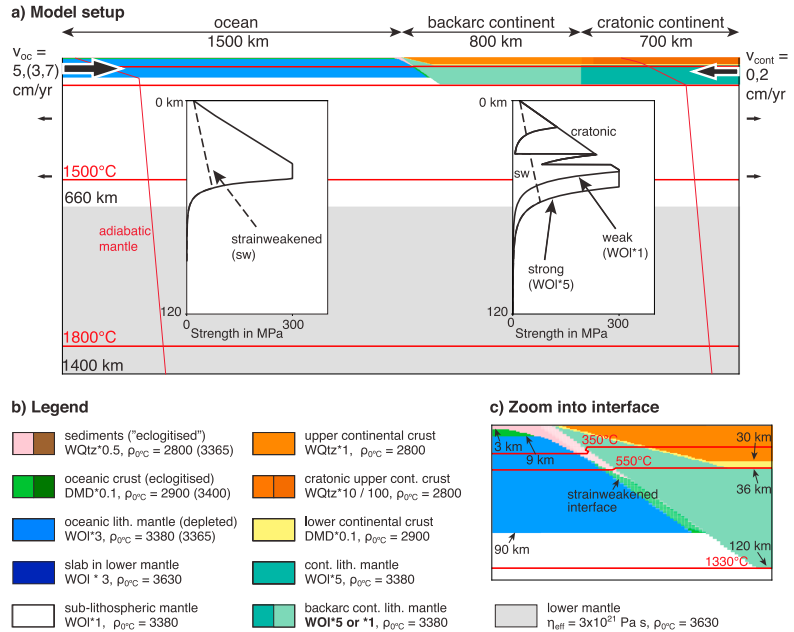
Figure 1. Initial model setup and boundary conditions. (a) The model consists of an oceanic and a continental domain overlying a sublithospheric upper and lower mantle. During model run, we apply a constant velocity boundary condition v_{oc} = 3, 5, and 7 cm/yr and v_{cont} = 0 and 2 cm/yr in, respectively, the oceanic and continental lithospheres. Inflow of oceanic material is balanced by outflow of the same amount of material on both sides of the sublithospheric upper mantle, and inflow of continental material is compensated by outflow of sublithospheric upper mantle on the continental side. The upper surface is free, and the side and bottom boundaries have free slip boundary conditions. The initial temperature profile of the continent corresponds to 1-D thermal steady state, and the underlying mantle has an adiabatic gradient of 0.4 °C/km. The side boundaries are insulated, and the bottom boundary has a fixed temperature boundary condition of 1,850 °C. The temperature in the oceanic lithosphere is linearly increasing from 0 to 1,314 °C resulting in a uniform temperature distribution. The inserts show initial yield strength envelopes of the oceanic and continental model domains. (b) Legend with scaled flow law and density in kilograms per cubic meter. WQtz is the wet quartz flow law as described in Gleason and Tullis (1995), DMD is the dry Maryland flow law from Mackwell et al. (1998), and WOl is the wet olivine flow law from Karato and Wu (1993). (c) Zoom into the interface between the two plates. The white overlay at the interface masks the initially strain-weakened region.

$$\frac{\partial \sigma_{ij}}{\partial x_i} + \rho g = 0 \quad i, j = 1, 2, \tag{2}$$

$$c_p \rho \left(\frac{\partial T}{\partial t} + v_i \frac{\partial T}{\partial x_i} \right) = k \frac{\partial}{\partial x_i} \frac{\partial T}{\partial x_i} + H + v_j \alpha \rho T g, \tag{3}$$

where v_i are velocity components, x_i are spatial coordinates, σ_{ij} is the stress tensor, ρ is density, g is gravitational acceleration, c_p is specific heat, T is temperature, t is time, k is thermal conductivity, H is radioactive heat production per unit volume, and α is the volumetric thermal expansion coefficient. The last term in (3) is the correction for adiabatic heating when material moves vertically.

For viscous deformation, a nonlinear, thermally activated power law creep formulation is used which relates pressure, temperature, and strain rate to the effective viscous flow stress, σ'_{visc}:

$$\sigma'_{visc} = f \cdot A^{-\frac{1}{n}} \cdot (\dot{\epsilon}_{eff})^{\frac{1}{n}} \cdot exp \left(\frac{Q + VP}{nRT} \right), \tag{4}$$

where σ'_{visc} is the square root of the second invariant of the deviatoric stress, $\dot{\epsilon}_{\text{eff}}$ is the square root of the second invariant of the deviatoric strain rate, f is a scaling factor, A the preexponential factor converted to plane strain, n the power law exponent, Q activation energy, V activation volume, P the dynamic pressure, and R the universal gas constant. We base our model materials on well-established flow laws and use the scaling factor f to account for uncertainties resulting from extrapolation from laboratory to natural conditions and different geological settings: wet quartz (Gleason & Tullis, 1995), dry Maryland diabase (Mackwell et al., 1998), and wet olivine (Karato & Wu, 1993).

Frictional-plastic deformation of the materials is approximated using a pressure-dependent Drucker-Prager yield criterion:

$$\sigma'_{\text{plast}} = P \cdot \sin(\phi_{\text{eff}}) + C \cdot \cos(\phi_{\text{eff}}), \tag{5}$$

where σ'_{plast} is the square root of the second invariant of the deviatoric stress, P is the dynamic pressure, ϕ_{eff} is the effective angle of internal friction, and C is cohesion. Strain weakening is accounted for by linearly reducing ϕ_{eff} from 15° to 2° through a predefined strain (ϵ) interval $0.4 < \epsilon < 1.4$ (Huismans & Beaumont, 2003).

The main deformation mechanism for olivine at high pressures, high differential stresses, and low temperatures is a temperature-insensitive exponential creep (Katayama & Karato, 2008; Tsenn & Carter, 1987). We approximate this deformation mechanism by limiting the plastic yield stress of all model materials based on the wet olivine flaw to $\sigma'_{\text{plast}} \leq 300$ MPa (e.g., Andrews & Billen, 2009; Butler et al., 2015).

The density of the model materials is temperature dependent and given by $\rho(T) = \rho_0 \cdot (1 - \alpha(T - T_0))$. The T-P dependence of α in olivine and its polymorphs (Tosi et al., 2013) is approximated by linearly increasing α from 3×10^{-5} to 4×10^{-5} K^{-1} in the temperature range of 500–2,000 K (e.g., Butler et al., 2015) and linearly decreasing α by a factor 1 to 0.5 between 0 to 45 GPa (Agrusta et al., 2017; Tosi et al., 2013).

2.2. Model Setup

Oceanic subduction under continental lithosphere is modeled using an idealized mantle scale model domain with 3,000 km horizontal and 1,400 km vertical extent (Figure 1 and Table 1). The oceanic lithosphere is composed of 3 km sediments, 6 km oceanic crust, and a 81 km thick lithospheric mantle which is depleted by 15 kg/m^3 down to a depth of 70 km. The continental domain, subdivided into backarc and cratonic continent, is composed of 30 km upper and middle crust and 6 km lower crust (Hacker et al., 2011; Huang et al., 2013; see also supporting information S1), underlain by lithospheric mantle up to a depth of 120 km. The width of the backarc domain in the overriding plate follows Currie et al. (2008). Tests with smaller or wider backarc domains gave similar results. The sublithosperic upper mantle ranges to 660 km depth with lower mantle between 660 km depth and the lower model boundary at 1,400 km. All materials have the same plastic parameters apart from oceanic sediments, which are additionally affected by strain weakening of the cohesion to focus deformation into the sediments that enter the subduction channel. The choice of modeling parameters follows earlier similar studies (Butler et al., 2015; Currie et al., 2008; Huismans & Beaumont, 2011; Pysklywec & Beaumont, 2004).

Viscous flow of the continental upper and middle crust follows a wet Quartz flow law (Gleason & Tullis, 1995). Cratonic crust is scaled by a factor of 10 and 100, accounting for stronger upper crust coupled to the mantle lithosphere. The oceanic and lower continental crust follow a dry Maryland diabase flow law (Mackwell et al., 1998) scaled by a factor $f = 0.1$, representing partially hydrated strong mafic crust. Oceanic and continental lithospheric mantle rheologies are based on wet olivine (Karato & Wu, 1993), respectively, scaled by $f = 3$ and $f = 5$, representing dry, depleted lithospheric mantle. Models with a "weak" backarc have a backarc lithospheric mantle with the same rheology and compositional density as the underlying mantle. The sublithospheric mantle follows a wet olivine flow law with $f = 1$, resulting in a viscosity profile consistent with Mitrovica and Forte (2004). Lower mantle rheology is subject to a large range of uncertainties with viscosity estimated between 1×10^{21} and 5×10^{22} Pa s (Billen, 2010; Mitrovica & Forte, 2004). We adopt a uniform viscosity of 3×10^{21} Pa s for the lower mantle, leading to a viscosity increase at the 660 km discontinuity of approximately a factor of 30. All material that sinks below 1,200 km depth is converted to lower mantle to prevent interaction of the slab with the lower model boundary.

The initial temperature distribution reflects average values in the continental domain (Hacker et al., 2015), with a Moho temperature of ~550 °C and a 120 km thick lithosphere with 1,330 °C at its base, resulting in

Table 1
Mechanical and Thermal Properties of the Materials

Parameters	Oceanic plate			Continental plate			Sublithospheric mantle	Lower mantle
	Sediments	Crust	Mantle lithosphere	Upper/middle crust (cratonic)	Lower crust	Mantle lithosphere (**weak**)		
Plastic rheology								
C - C_{sw} (MPa)	20–4	20–20	20–20	20–20	20–20	20–20	20–20	—
$\phi - \phi_{sw}$ (°)	15–2	15–2	15–2	15–2	15–2	15–2	15–2	—
Viscous rheology								
Flow law	WQtz	DMD	WOl	WQtz	DMD	WOl	WOl	constant
f	0.5	0.1	3	1 (10;100)	0.1	5 (**1**)	1	viscosity of
A (Pa $s^{1/n}$)[a]	8.57×10^{-28}	5.78×10^{-27}	1.76×10^{-14}	8.57×10^{-28}	5.78×10^{-27}	1.76×10^{-14}	1.76×10^{-14}	3×10^{21} Pa s
n	4.0	4.7	3.0	4.0	4.7	3.0	3.0	—
Q (kJ/mol)	223	485	430	223	485	430	430	—
V (cm^3/mol)	0	0	1.1×10^{-5}	0	0	1.1×10^{-5}	1.1×10^{-5}	—
Density parameters								
ρ_0 (kg/m^3)	2,800 (3,365)[b]	2,900 (3,400)[b]	3,380/3,365 (depleted)	2,800	3,000	3,380	3,380	3,630
α (K^{-1})[c]	3×10^{-5}	3×10^{-5}	2×10^{-5}–4×10^{-5}	3×10^{-5}	3×10^{-5}	2×10^{-5}–4×10^{-5}	2×10^{-5}–4×10^{-5}	2×10^{-5}–4×10^{-5}
Thermal parameters								
k ($Wm^{-1}K^{-1}$)	2.25	2.25	2.25	2.25	2.25	2.25	2.25[d]	2.25[d]
H ($\mu W/m^3$)	1.1 (0)[b]	0	0	1.1	0.5	0	0	0
c_p (J kg^{-1} K)	750	750	1,250	750	750	1,250	1,250	1,250

Note. WQtz is the wet quartz flow law as described in Gleason and Tullis (1995); DMD is the dry Maryland flow law from Mackwell et al. (1998); and WOl is the wet olivine flow law from Karato and Wu (1993). [a]The laboratory-derived preexponential flow law exponent has been converted to conform with the second invariants of the stress and strain rates used in the model approach. [b]Metamorphic high pressure equivalent. The P-T field for the metamorphic reaction coincides with the eclogite stability field from Hacker (1996). [c]For mantle materials, thermal expansion coefficient is P-T dependent with a linear increase from 3×10^{-5} to 4×10^{-5} K^{-1} in the temperature range of 500–2,000 K and a linear decrease by a factor 1 to 0.5 from 0 to 45 GPa. [d]Thermal conductivity for low temperatures. Between 1,335 and 1,345 °C, the conductivity linearly increases from 2.25 to 52.0 W m^{-1} K^{-1}; to mimic active mantle convection at high Nusselt number, keep the adiabatic gradient and prevent the system from cooling.
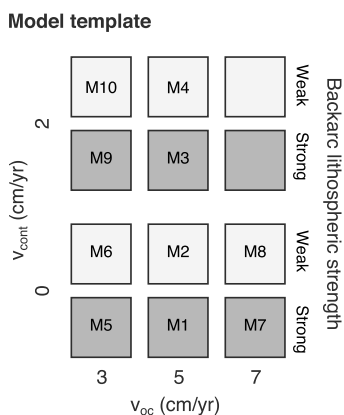
Model template

Figure 2. Template of models presented. Tested are the absolute subduction velocity (v_{oc}) and the overriding plate velocity (v_{cont}) with both a strong and weak backarc lithospheric mantle. M1 to M10 are the model numbers as used in the text.

a surface heat flow of 53 mW/m² and heat flux in the sublithospheric mantle of ∼20 mW/m². We assume a 90 km thick oceanic lithosphere with a geotherm that increases linearly from 0 to 1,314 °C. This results in a uniform temperature distribution in the sublithospheric and lower mantle with an adiabatic gradient of 0.4 °C/km. The side boundaries are insulated, and the bottom boundary has a constant temperature of 1,850 °C.

To maintain the heat flux at the lithosphere-asthenosphere boundary and an adiabatic gradient of 0.4 °C/km in the sublithospheric upper and lower mantle, k linearly increases from 2.25 to 52.0 W m⁻¹ K⁻¹ between 1,335 and 1,345 °C in the sublithospheric upper and lower mantle (Pysklywec & Beaumont, 2004). All other materials have a thermal conductivity $k = 2.25$ W m⁻¹ K⁻¹.

The models include an irreversible metamorphic phase change of oceanic crust to eclogite when entering the stability field of eclogite (Hacker, 1996). Eclogite has the same viscous flow law as the oceanic crust but a different density. In order to keep the models simple, we assume that sediments obtain a higher, metamorphic density when entering the eclogite stability field. We acknowledge, however, that subduction of buoyant sediments can have strong implications for subduction dynamics (Currie et al., 2007; Hacker et al., 2015). All slab and mantle materials are subject to a reversible phase change with a Clapeyron slope of −2 MPa/K at the 660 km discontinuity, corresponding to the break down of ringwoodite to bridgemanite and magnesiowüstite (see discussion in Billen, 2010; Goes et al., 2017). For simplicity, slab materials are converted to one lower mantle material, which has the viscous flow law of the oceanic lithosphere. The phase changes do not account for latent heat and are not mass conserving. However, they illustrate the first-order effects of important metamorphic phase changes affecting subduction systems and are thus assumed to be sufficient.

Subduction is modeled using velocity boundary conditions on the sides of the model. Inflow of oceanic material is balanced by a small distributed outflow at both sides of the model in the sublithospheric upper mantle. Inflow of continental material is balanced by outflow only on the right, continental side (see Figure 1). Further boundary conditions are free slip at the model walls and base and a stress-free upper surface.

The Eulerian grid consists of 1,000 cells in the horizontal direction and 280 cells in the vertical direction. The distribution of cells is vertically nonuniform, with 150 cells in the upper 150 km, 10 cells in the following 50 km, and 120 cells in the remaining 1,200 km. Consequently, the horizontal resolution is 3 km, and the vertical resolution is 1 km in the lithosphere and 10 km in the sublithospheric domain, respectively. Tests with higher and lower spatial resolution gave consistently similar results.

We do not attempt to resolve subduction initiation processes, and subduction is initialized by introducing a 10 km wide strain-weakened zone composed of a sediment wedge in the oceanic lithosphere at the ocean-continent boundary. To establish a similar subduction interface for all models, each model has the same 3 Myr long subduction initiation phase. During this phase, the oceanic lithosphere is pushed with 5 cm/yr, the continent is not moving, and the continental lithospheric mantle is "strong" over the whole continental domain.

2.3. Parameter Variations in the Models Presented

With a set of 10 models (Figure 2), we test the effect of backarc lithospheric strength and absolute plate velocities on overriding plate strain regime in ocean-continent subduction systems. Models M1 to M4 are described in detail with several time steps, while models M5 to M10 are summarized with their final configuration (Figure 7). Key viscosity plots of models M1–M4 are shown in Figures S1 and S2. The free-surface evolution of all models is presented in Figure 8, and an animation of every model is uploaded to a data repository (see Acknowledgements). Four additional models related to M3 and M4 (M4b, M4c, M3_1000, and M4_1000) are in supplementary Figures S4 and S5.
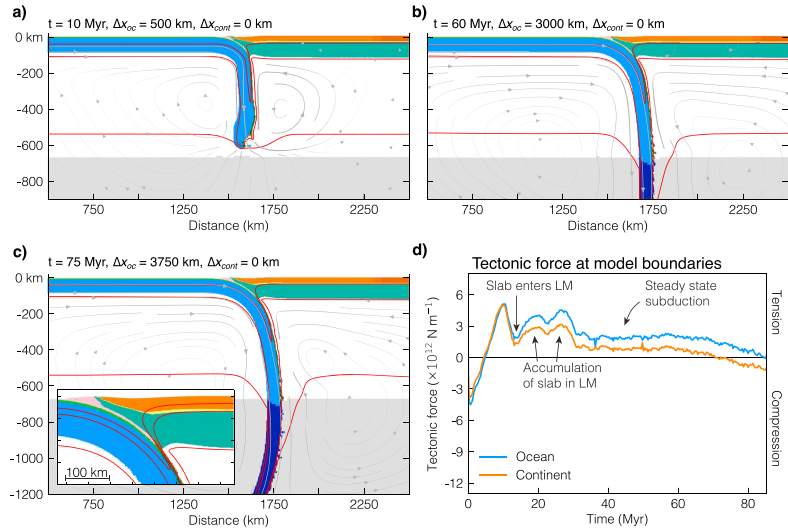
M1: v_{oc}= 5 cm/yr, v_{cont} = 0 cm/yr, Strong backarc lithosphere

Figure 3. Reference model (M1) with a neutral overriding plate strain regime. (a–c) Material colors (see Figure 1) with isotherms (550, 1,330, and 1,500 °C) and streamlines scaled in thickness to velocity. t is model time, and Δx_{oc} and Δx_{cont} are the amounts of oceanic and continental convergence. (c) Inset contains zoom with additional isotherm at 350 °C. (d) Tectonic forces (integrated horizontal deviatoric stresses). LM is abbreviation for lower mantle. See Movie S1 for a model animation.

The models are driven by velocity boundary conditions and do not account for mid-oceanic ridge(s), lateral temperature and viscosity variations, neighboring plates, or large-scale convective drag. To better understand model behavior and to see whether model evolution is Earth-like, we track the tectonic boundary force (see supporting information S1 for more information about its computation) in the lithosphere at the model domain boundaries (Butler & Beaumont, 2017). An in-depth assessment of the forces acting during model evolution is given in section 4.

3. Results

3.1. M1: Reference Model

The reference model M1 has a subducting plate velocity of 5 cm/yr, a fixed upper plate, and a strong backarc lithospheric mantle with the same viscosity throughout the whole model domain (Figures 3 and 8a).

The first phase of subduction is characterized by initial localization of deformation along the weak interface. After 5 Myr, the slab steepens and subducts vertically through the upper mantle until ~12 Myr, when it enters the lower mantle. After a phase of slab accumulation and bending in the lower mantle (15 to 35 Myr, see also Movie S1), the subduction zone enters steady-state subduction, characterized by a steep slab that shows no interaction with the transition zone. Two whole model scale poloidal flow cells form on both sides of the slab (Figure 3c). The position of the trench is not changing during the model run, and the free surface is steady (Figure 8a).

The model evolution is reflected in the development of the boundary forces (Figure 3d). Initial convergence is associated with compressive tectonic forces in both plates. From 5 Myr, the boundary forces in both plates are tensional and reach their maximum at ~10 Myr, right before the slab reaches the lower mantle. Tectonic stresses drop once the slab enters the lower mantle followed by relatively constant and small ($< 3 \times 10^{12}$ N/m) tectonic boundary forces during steady-state subduction.
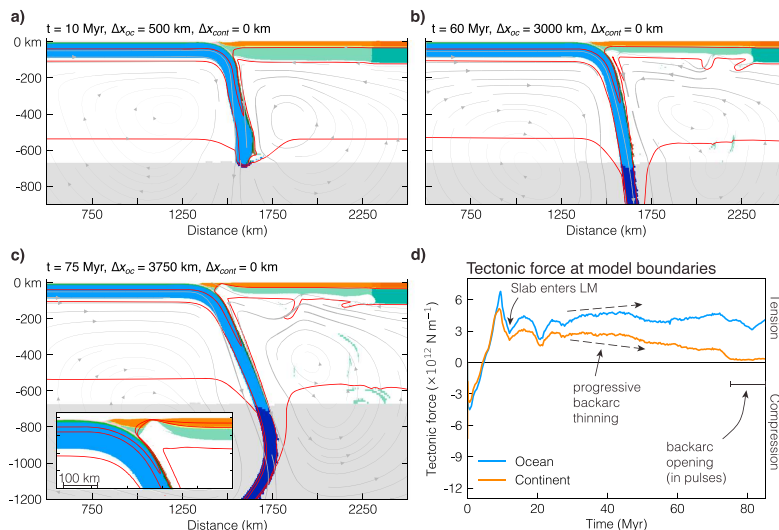
Figure 4. M2 showing backarc spreading. (a–c) Material colors (see Figure 1) with isotherms (550, 1,330, and 1,500 °C) and streamlines scaled in thickness to velocity. t is model time, and Δx_{oc} and Δx_{cont} are the amounts of oceanic and continental convergence. (c) Inset contains zoom with additional isotherm at 350 °C. (d) Tectonic forces (integrated horizontal deviatoric stress). LM is abbreviation for lower mantle. See Movie S2 for a model animation.

3.2. M2: Weak Backarc Lithospheric Mantle

Model M2 has the same velocity boundary conditions as M1 but a weak backarc lithospheric mantle with identical compositional density and rheology as the underlying sublithospheric mantle (Figures 4 and 8b).

After subduction initiation and before the slab enters the lower mantle (between 7 and 10 Myr), a short phase of trench retreat results in pure shear thinning of the weak continental lithosphere (see Movie S2), accompanied by moderate slab shallowing (Figures 4a and 8b). During ongoing subduction, two model scale poloidal flow cells form on both sides of the slab. The resulting subhorizontal shear flow of the sublithospheric mantle at the base of the backarc lithosphere evokes small thermal and mechanical perturbations which develop into Rayleigh-Taylor instabilities leading to convective thinning of the backarc mantle lithosphere in the weak domain (10 to 60 Myr). With ongoing subduction, corner flow induces increased thinning of the mantle lithosphere about 150 km landward from the trench (Figure 4b) ultimately resulting in backarc rupture at around 75 Myr with a 150 km wide block that is rifted off the overriding plate (Figure 4c). Backarc opening and associated trench retreat are faster than slab retreat in the lower mantle, and the slab dip decreases until the slab bends inward at around 400 km depth, inducing a back and forward movement of the slab. Repeated folding of the slab is associated with pulse-like backarc opening with a recurrence time of ~10 Myr (Figure 8b and Movies S1–S6). Convective thinning of the backarc lithospheric mantle leads to conductive heating and an increase of surface heat flow > 60 mW/m².

3.3. M3: Overriding Plate Movement Toward the Trench, Strong Backarc Lithospheric Mantle

Model M3 has a subduction velocity of 5 cm/yr, a trenchward overriding plate velocity of 2 cm/yr, and a strong backarc continental lithospheric mantle (Figures 5 and 8c). Note that the backarc crust is weaker than the strong "cratonic" crust (e.g., Figure 1).

During the first 10 Myr, the slab sinks relatively vertical through the upper mantle and reaches the lower mantle transition zone with an almost vertical angle. Further overriding plate movement leads to slab flattening, as the trench retreats faster than the slab sinks into the lower mantle. Slab bending at 20 and 40 Myr

M3: v_{oc} = 5 cm/yr, v_{cont} = 2 cm/yr, Strong backarc lithosphere
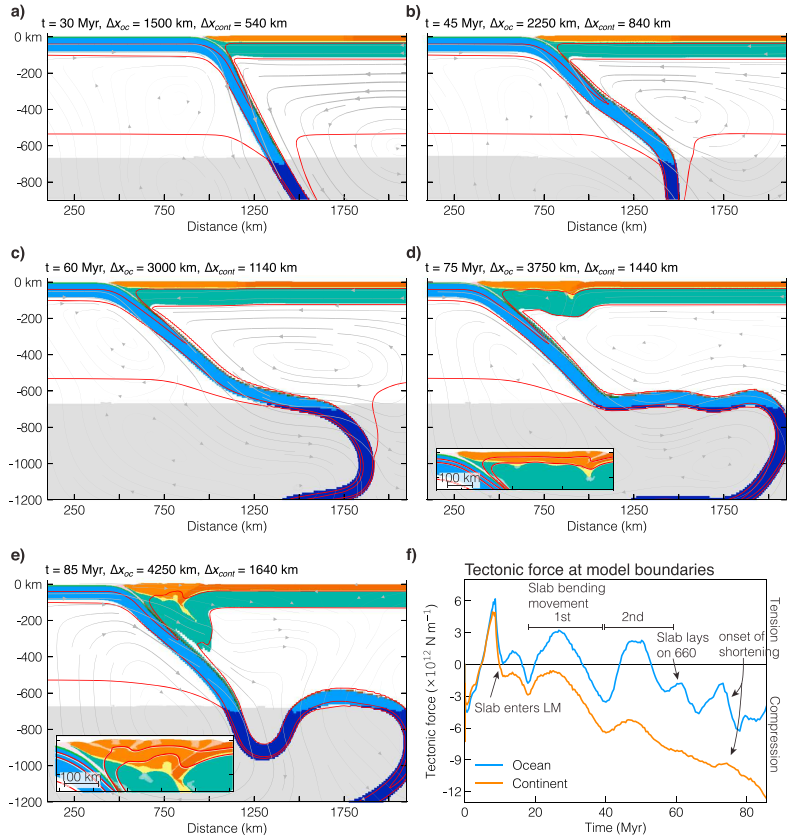
Figure 5. M3 showing underthrusting of the cratonic region and overriding plate shortening. (a–e) Material colors (see Figure 1) with isotherms (550, 1,330, and 1,500 °C) and streamlines scaled in thickness to velocity. t is model time, and Δx_{oc} and Δx_{cont} are the amounts of oceanic and continental convergence. (d,e) Inset contains zoom with additional isotherm at 350 °C. The white overlay highlights strain-weakened shear zones. (f) Tectonic forces (integrated horizontal deviatoric stress). LM is abbreviation for lower mantle. See Movie S3 for a model animation.

induces minor back and forward slab movements, as in M2, linked with slab advance in the lower mantle and slab stagnation in the transition zone (Figure 5c). After 70 Myr, the backarc continental lithosphere fails through large-scale folding followed shortly after (at 75 Myr) by underthrusting of the strong cratonic crust (Figure 5e). Subsequently, significant trench advance is associated with ablative subduction and backarc lithospheric mantle shearing off from the overriding crust (Figure 8c).

The boundary forces show the different stages of model evolution (Figure 5f). The two slab bending events are reflected in periodic increase and decrease of boundary forces between 20 and 60 Myr. Further trench retreat leads to an increase in boundary forces until shortening, and subsequent mountain building of the backarc continent results in a very high continental boundary force exceeding 9×10^{12} to 12×10^{12} N/m. Supplementary model M3_1000 (Figure S5) with an extended ocean has a very similar model development, showing that overriding plate shortening is not induced by approaching the left model boundary.

M4: v_{oc}= 5 cm/yr, v_{cont} = 2 cm/yr, Weak backarc lithosphere
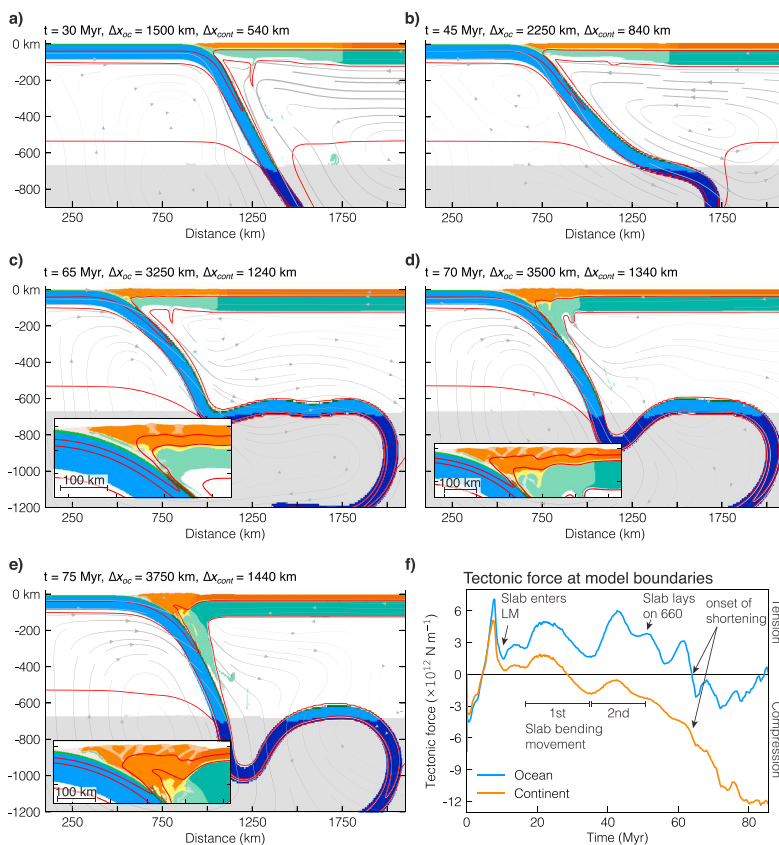
Figure 6. M4 showing overriding plate shortening through failure of the weak backarc lithosphere. (a–e) Material colors (see Figure 1) with isotherms (550, 1,330, and 1,500 °C) and streamlines scaled in thickness to velocity. t is model time, and Δx_{oc} and Δx_{cont} are the amounts of oceanic and continental convergence. (c–e) Inset contains zoom with additional isotherm at 350 °C. The white overlay highlights strain-weakened shear zones. (f) Tectonic forces (integrated horizontal deviatoric stress). LM is abbreviation for lower mantle. See Movie S4 for a model animation.

3.4. M4: Overriding Plate Movement Toward the Trench, Weak Backarc Lithospheric Mantle

Model M4 has the same velocity boundary conditions as M3 but a weak backarc lithospheric mantle (Figures 6 and 8d).

During the first 10 Myr, before the slab interacts with the lower mantle, trench retreat exceeds the overriding plate velocity resulting in pure shear thinning of the backarc lithosphere and a slight shallowing of the slab similar to M2. Subsequent model evolution is governed by the interplay between backarc weakening through convective thinning and slab anchoring in the lower mantle. Corner flow enhances convective removal and weakening of the lithospheric mantle 150 km landward of the trench. Similar to M3, the interaction between slab folding and differential velocities of the trench and the slab in the lower mantle result in two back and forth movements of the slab, after which the slab lays down on the mantle transition zone (Figure 6b). Further overriding plate movement toward to trench leads to shortening of the continent after 65
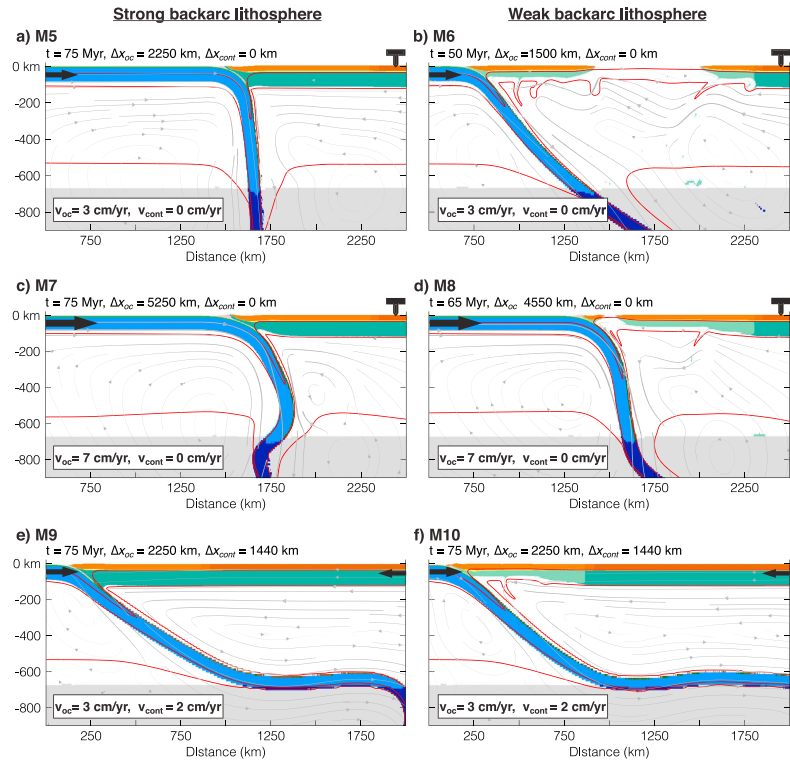
Figure 7. M5–M10 sensitivity to different plate velocities. M5, M7, M9, and M10 have a neutral overriding plate strain regime, while M6 and M8 show backarc spreading. (a–f) Material colors (see Figure 1) with isotherms (550, 1,330, and 1,500 °C) and streamlines scaled in thickness to velocity. t is model time, and Δx_{oc} and Δx_{cont} are the amounts of oceanic and continental convergence.

Myr (Figure 6c). Crustal thickening and mountain building starts near the plate interface and migrates from there inland (Figure 6d), as the continental lithospheric mantle is initially the thinnest at the trench. The first fault zone nearest to the trench separates a marginal block from the rest of the mountain belt, related to deflection of the temperature field. During subsequent shortening, the remaining lithospheric mantle is ablatively subducted. The trench advances until the cratonic lithosphere thrusts under the evolving mountain belt blocking further shortening, followed by trench retreat with approximately the same velocity as the overriding plate (Figure 8d). Mountain building is completed within 20 Myr.

Similar to M3, the tectonic boundary forces record two slab bending movements between 20 and 50 Myr. Further overriding plate movement induces increasing compressional stresses in the continental plate resulting in shortening once the compressive forces are $>5 \times 10^{12}$ N/m. Supplementary model M4_1000 (Figure S5) with an extended ocean has a very similar model development as M4, showing that overriding plate shortening is not induced by approaching the left model boundary.

3.5. Sensitivity to Different Plate Velocities
Models M5 to M10 (Figure 7) comprise three model pairs where we test the effect of different plate velocities on the overriding plate strain regime. Each set of models consists of one model with a strong and one model with a weak backarc lithospheric mantle.
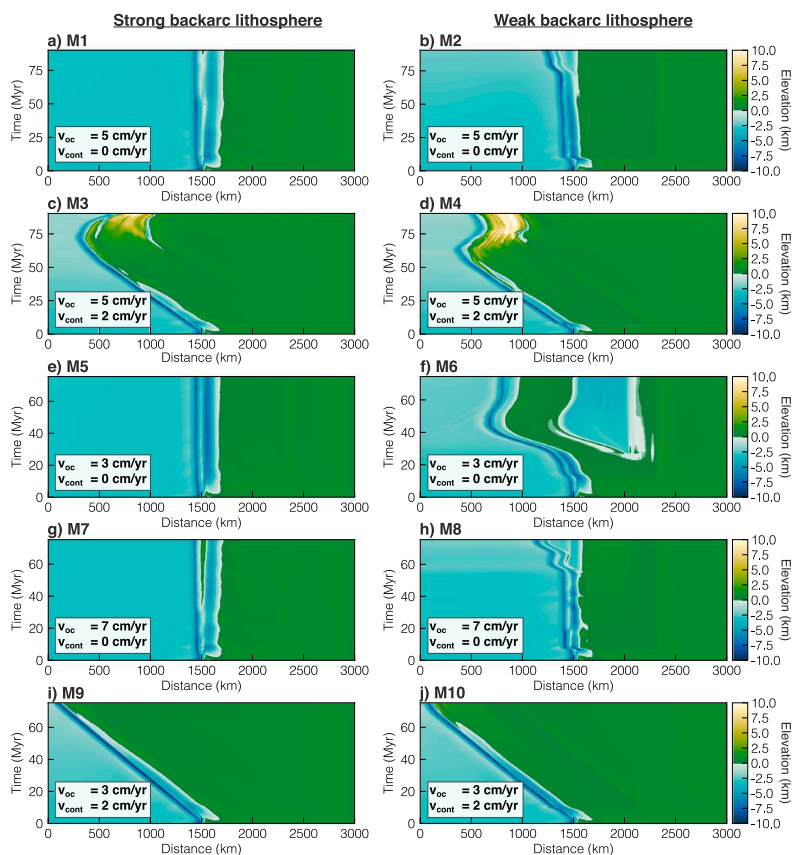
Figure 8. Evolution of free-surface elevation of models M1–M10. The colorbar is the same for all models, and the continental side boundary is assumed to be stable at 800 m above sea level. Note the pulse-like backarc opening in models 2, 6, and especially 8. Note also that onset of shortening in M3 starts in the continent, while shortening in M4 begins near the trench and migrates inland.

Models M5 and M6 have a low subduction velocity of 3 cm/yr and zero overriding plate velocity. In case of the strong continental mantle (M5), subduction is stable, and the overriding plate does not deform (Figures 7a and 8e). In model M6, the weak backarc lithosphere develops convective thinning in a similar fashion to M2. However, backarc extension occurs earlier than in M2 after 28 Myr of model evolution. Additionally, convective thinning further inland leads to necking significantly offset from the trench by >500 km. The post-opening retreat of the trench and continental block is very rapid (5 cm/yr) until the slab has reached a shallow dip angle and large amount of slab material has accumulated in the lower mantle (45 Myr). Subsequent slab steeping is accompanied by a short phase of trench advance followed by stationary subduction (Figure 8f and Movies M5 and M6).

Models M7 and M8 have a high subduction velocity of 7 cm/yr and zero overriding plate velocity. M7 and M8 have the same relative convergence velocity as models M3 and M4. They do, however, not exhibit overriding plate shortening but result in a very similar behavior as M1 and M2, with overriding plate extension if the overriding lithospheric mantle is weak (M7). The subduction velocity of 7 cm/yr induces more slab bending

movement in the upper mantle compared to models with a subduction velocity of 5 cm/yr. The tectonic forces at both plate boundaries vary between -2×10^{12} and 4×10^{12} N/m during model evolution (Figure S3).

Models M9 and M10 have a low subducting plate velocity of 3 cm/yr and an overriding plate velocity of 2 cm/yr. Hence, M9 and M10 have the same relative convergence velocity as models M1 and M2. Nevertheless, they do not show overriding plate extension but a neutral strain regime throughout the whole model evolution. In both models, trench retreat occurs at the same velocity as overriding plate movement, with the slab laying down in the transition zone after 50 to 60 Myr of model evolution.

4. Analysis of Forces Driving Model Evolution

Subduction and model evolution are guided by the balance of slab pull and a number of counteracting forces. Because of the dynamic nature of the models, it is not possible to develop an analytical force balance solution for model development. However, to better understand model evolution, it is useful to consider the magnitude of different forces acting during subduction.

4.1. Driving Force: Slab pull, F_{sp}

The only internally developing force driving subduction in the models is slab pull (F_{sp}), which is a result of the thermal anomaly and density difference of the subducting slab. In the models presented here, the negative density of the slab is on average 60 kg/m³. The resulting slab pull is increasing with slab length to 2.5×10^{13} N/m before the slab enters the lower mantle and reaches a maxium of 4.5×10^{13} N/m during whole model subduction.

4.2. Resisting Forces

Several resisting forces dissipate the gravitational potential energy of the slab pull: shear resistance at the interface (F_{int}), viscous drag in the upper and lower mantle ($F_{vd} = F_{um} + F_{lm}$), buoyancy related to the negative Clapeyron slope of the upper- to lower-mantle phase change (F_{660}), slab suction (F_{suc}), and internal deformation of the slab (F_{def}).

4.2.1. F_{int}

The dominantly frictional subduction interface reaches down to the backarc lithosphere-asthenosphere boundary (z_{lab}) and can be approximated by its integrated frictional strength:

$$F_{int} = \int_0^{z_{lab}} \sigma'_{plast}(z)dz = \frac{1}{2}\rho g z_{lab}^2 \sin(\phi_{eff}) + C z_{lab} \cos(\phi_{eff}). \tag{6}$$

For models with a strong backarc, z_{lab} is not changing considerably during model evolution and reaches down to 120 km, with $F_{int}(120\,km) \approx 8 \times 10^{12}$ N/m. In case of a weak backarc, thinning of the mantle lithosphere results in an elevated lithosphere-asthenosphere boundary with values of $F_{int}(80\,km) \approx 4 \times 10^{12}$ N/m and $F_{int}(40\,km) \approx 1 \times 10^{12}$ N/m.

4.2.2. F_{vd}

The viscous shear resistance of the mantle on the sides of the slab is difficult to assess, since there is no fixed length scale for the boundary layer accommodating the shear. Inferring an average length scale (w) from the forward models, we can express the viscous shear force as (Billen, 2008)

$$F_{vd} = \frac{2v}{w}\mu L = \frac{2v}{w}(\mu_{um}L_{um} + \mu_{lm}L_{lm}), \tag{7}$$

where v is subduction velocity, L is slab length, μ is effective viscosity in the upper mantle (um) and lower mantle (lm), and v is velocity. An effective viscosity of $\mu_{um} = 1 \times 10^{19} - 1 \times 10^{20}$ Pa s, and average $w = 100$ km, in the vicinity of the slab leads to an upper mantle viscous drag two orders of magnitude less than slab pull and therefore negligible. Viscous drag at base of plates is similarly not significant in our models, because potentially high strain rates lead to very low viscosities of $\mu_{um} = \sim 1 \times 10^{19}$ Pa s within a similar length scale $w = \sim 100$ km. Viscous shearing in the lower mantle, however, requires a considerable force in the order of slab pull. For instance, a 400 km long slab with a sinking velocity of 5 cm/yr, $w = 100$ km, and $\mu_{lm} = 3 \times 10^{21}$ Pa s induces a shear resistance of $F_{lm} = 2 \times 10^{13}$ N/m, almost half of the maximum slab pull.

4.2.3. F_{660}

The positive buoyancy force added by the negative Clapeyron slope of the lower mantle phase transition is in the order of $2–4 \times 10^{12}$ N/m in case of straight slab penetration through the transition zone. Models 3, 4, 9, and 10 show that a shallower subduction angle can lead to foundering in the transition zone, which leads to

a much larger positive buoyancy force. F_{660} is therefore highly variable and can have a significant influence on slab evolution in the transition zone. Agrusta et al. (2017) show that the Clapeyron slope of the phase transition has a large impact on slab foundering, where a steeper negative slope enhances slab stagnation.

4.2.4. F_{suc}

Slab suction is an upward-directed force for shallow dipping slabs ($\lesssim 30°$, Stevenson & Turner, 1977) and can be the cause of flat slab subduction during the subduction initiation phase (Rodriguez-Gonzalez & Negredo, 2012; Huangfu et al., 2016). The models presented here do not develop flat slab subduction, as the average upper mantle slab dip during model evolution is never less than 45°, resulting in a negligible suction force $F_{suc} < 3 \times 10^{11}$ N/m.

4.2.5. F_{def}

Following Conrad and Hager (1999) and Funiciello et al. (2003), the internal deformation of a plate in terms of viscous bending can be approximated by

$$F_{bending} \approx \nu \mu_{eff} \frac{h^3}{r^3}, \tag{8}$$

where μ_{eff} is effective viscosity, h is plate thickness, and r is the bending radius. Assuming that slab bending induced deformation occurs at several locations $F_{def} = n \times F_{bending}$. This will typically lead to values of $F_{def} = 5 \times 10^{11}$–$5 \times 10^{12}$ N/m, in the order but lower than the shear resistance at the interface (F_{int}). F_{def} increases when the overriding plate also deforms.

4.3. Summary of Forces

The main forces resisting slab pull (F_{sp}) are viscous drag in the lower mantle, shearing of the subduction interface, internal lithospheric deformation, and the dynamically changing buoyancy force of the phase transition in the transition zone. Another force visible in the tectonic boundary forces of M3 and M4 is the gravitational stress exerted by rising topography (F_{topo}). A 3 km high mountain belt exerts a force of 3×10^{12} to 4×10^{12} N/m onto its foreland (Stüwe, 2007), while a 6 km high mountain range with a 70 km thick crust exerts a force of 8×10^{12} to 9×10^{12} N/m.

Summarizing, the tectonic boundary force (F_{TBF}) can be approximated as a combination of

$$F_{TBF} \approx F_{sp} - \left(F_{lm} + F_{int} + F_{def} + F_{660} + F_{topo} \right). \tag{9}$$

In all our models, except during later stages of mountain building models M3 and M4, the absolute resulting tectonic boundary forces have the same magnitude as ridge push (see Figure S3), which is in the order of 3×10^{12} (to 7×10^{12}) N/m (Parsons & Richter, 1980; Turcotte & Schubert, 1982). This shows that model evolution is Earth-like. In nature, subduction zone mountain belts are expected to be self-limiting in their behavior and will either not reach the later stages of our models (M3, M4, M4c, and M4b) or exhibit slow down of the overlying plate. Basal drag associated with large-scale poloidal flow in addition to buoyant upwellings could provide additional forces driving mountain building as proposed for the Andes (Husson et al., 2012; Faccenna et al., 2017). The evolution of boundary forces can also be interpreted as a measure of how much the plates need to be pushed or pulled in order to obtain the given velocity boundary conditions. For instance, the tensional stress peak in all models around 10 Myr and also the slab bending movements in M3 and M4 coincide with plate acceleration and deceleration phases in free subduction models (Agrusta et al., 2017; Capitanio et al., 2010; Funiciello et al., 2004; Garel et al., 2014).

Our force balance analysis shows that the forces driving and resisting subduction are in the same order of magnitude and result only in a small absolute surplus to deform the overriding plate. Therefore, a weak backarc is crucial for extension or shortening of the overriding plate, as discussed in the next section.

5. Mode Selection of Overriding Plate Deformation

With our small set of models, we can reproduce overriding plate extension or shortening in ocean-continent settings and show that deformation is primarily controlled by the strength of the backarc lithospheric mantle and the absolute plate velocities of the subducting and overriding plate (Figure 9). In the following three subsections, we will discuss in depth the role of these primary controlling factors.
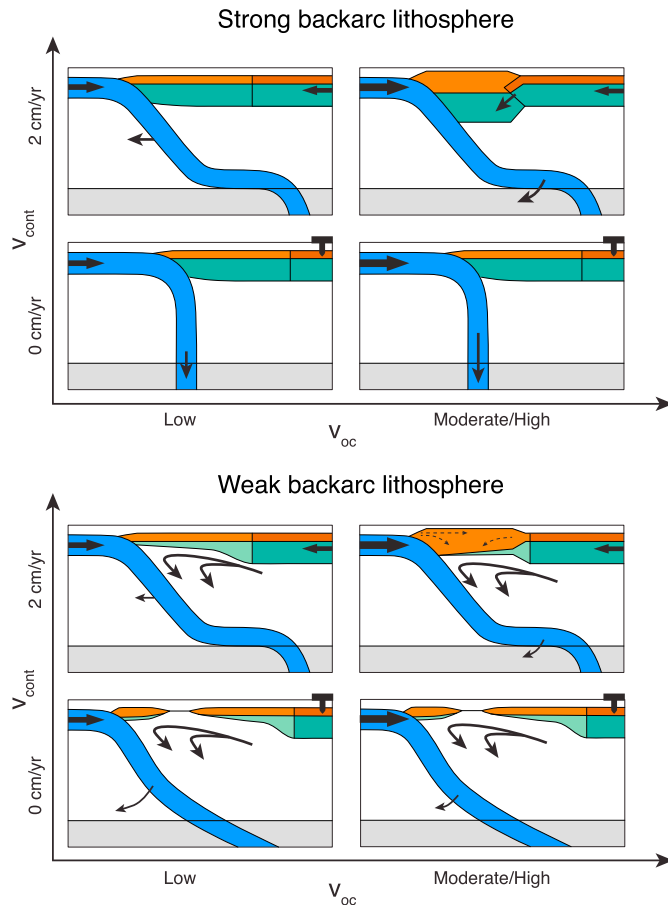
Figure 9. Summary of model behavior as a function of lithospheric strength (upper and lower panels), the subduction velocity (v_{oc}), and the overriding plate velocity (v_{cont}). The models with a strong backarc lithospheric mantle have a neutral overriding plate strain regime, unless the subduction velocity is high and the overriding plate moves toward the trench (M3). This situation leads to overriding plate shortening through underthrusting of the strong cratonic hinterland. A weak backarc lithosphere will be removed through gravitational instabilities, which can induce backarc spreading independent of the subduction velocity, but only if the overriding plate does not move toward the trench. When slab sinking is balanced by a low subduction velocity and an overriding plate which moves toward the trench, then the strain regime is neutral. If the subduction velocity is increased, the overriding plate shortens.

5.1. The Influence of Backarc Lithospheric Strength

To first order, the backarc will deform if the net tectonic driving force is larger than the plate's integrated strength. The strength of the backarc lithospheric mantle is therefore pivotal in determining whether the overriding plate can extend and how it shortens (Figure 9). Continental lithosphere with a strong mantle has an integrated strength of $\sim 9 \times 10^{12}$ N/m, while the strength of lithosphere with a weak mantle not yet affected by thinning is $\sim 5 \times 10^{12}$ N/m. Convective thinning and removal of weak backarc mantle lithosphere results in additional weakening to a minimum strength of 3×10^{12} N/m. Removal of the backarc lithosphere

also reduces the length of the subduction interface, lowering the interface resistance and increasing the net pull exerted by the slab. The combination of lithospheric thinning, thermal weakening, and subduction interface shortening enables backarc extension. In case of even weaker backarc mantle, extension and backarc opening is likely to occur shortly before the slab interacts with the lower mantle, shown by tensional stress peaks around 10 Myr in all models.

Overriding plate shortening is possible with and without a weak backarc lithospheric mantle. In case of strong backarc lithosphere (as in model M3), the tectonic driving forces in the overriding plate need to exceed the high integrated strength of 9×10^{12} N/m, while for a weak backarc lithospheric mantle (as in model M4), onset of shortening occurs when the driving force is in the order of $\sim 5 \times 10^{12}$ N/m. Supplementary models M4b and M4c test the sensitivity to overriding plate velocity (M4b) and enhanced backarc mantle lithosphere weakening (M4c; Figure S4). M4b with a lower overriding plate velocity results in shortening at $\sim 4 \times 10^{12}$ N/m, similar to M4, while model M4c with an even weaker lithospheric mantle (wet Olivine*0.5, Figure S4) exhibits enhanced lithospheric removal, inducing earlier shortening at a lower initial tectonic boundary force of $\sim 3 \times 10^{12}$ N/m. These models show that onset of shortening in subduction zones with a weak and partially removed backarc lithospheric mantle does not require a significant tectonic force in addition to ridge push. Kelly et al. (2016), Krystopowicz and Currie (2013), and Z. H. Li et al. (2016) show in continent-continent collision models that large amounts of backarc lithospheric mantle can be removed, similar to M3. Models presented here indicate that this requires a large tectonic force and may provide a viable mechanism for systems that are shortening but is unlikely to induce backarc opening.

5.2. Influence of the Subduction Velocity v_{oc}

The results presented here indicate that the velocity of the subducting plate may provide a secondary control on overriding plate extension. However, the model results suggest that it must be larger than 3 cm/yr for overriding plate shortening to occur (Figure 9). The impact of the subduction velocity can be best understood in the context of the slab's natural sinking velocity (v_{sink}), considering that the slab will exert a tensional force onto the overriding plate if v_{oc} is smaller than v_{sink}. Accordingly, overriding plate extension occurs earliest in M6, where v_{oc} is the smallest (v_{oc} = 3 cm/yr). Interestingly, overriding plate extension occurs earlier in M8 (v_{oc} = 7 cm/yr) than in M2 (v_{oc} = 5 cm/yr). This is most likely related to faster removal of the backarc lithosphere through faster corner flow in front of the slab.

5.3. Influence of the Overriding Plate Velocity v_{cont}

The overriding plate velocity plays a critical role in determining overriding plate deformation (Figure 9) and is linked to slab anchoring in the lower mantle. If trench retreat resulting from overriding plate motion toward the trench is faster than slab retreat in the lower mantle, the slab dip decreases, and the subduction system favors overriding plate shortening and suppresses extension. This is illustrated by model M10, which does not exhibit overriding plate extension although the cumulative convergence velocity is 5 cm/yr and, hence, the same as in M2. All models with backarc extension show that backarc opening is not a continuous process but occurs episodically without changing the boundary conditions (Figure 8). This is also caused by periodic slab dip flattening during fast trench retreat.

Overriding plate shortening occurs when it is moving toward the trench and when the net convergence velocity is larger than the average slab sinking and retreat velocity in the lower mantle. Both M3 and M4 exhibit slab foundering in the lower mantle transition zone before overriding plate shortening. Supplementary model M4b with a lower v_{cont} of 1 cm/yr (Figures S4a and S4b) shows that slab foundering is not required for overriding plate shortening.

Conversely, slab anchoring in the lower mantle enhances overriding plate extension, if the overriding plate moves away from the trench. However, extension would in this case require a weak and thin lithospheric mantle, as a strong backarc has a greater strength than the subduction interface.

The analysis of driving and resisting forces shows that slab anchoring is largely related to the large viscous drag in the lower mantle. However, also volumetric considerations which are not captured by the force analysis may play an important role. The slab is separating two poloidal flow cells with only limited exchange of material at the bottom of the model domain. Mass conservation of the two flow cells leads to slab flattening in response to trench retreat, and vice versa, and enhances a stable position of the slab in the lower mantle.

5.4. Model Limitations

Our models are a simplified representation of nature, and there are several processes we do not account for including most notably 3-D aspects of subduction systems, the role of water and fluid flow, variable oceanic plate age, stronger or weaker continental rheology, and more comprehensive mantle phase changes.

Toroidal (i.e., horizontal) return flow around the slab edge may have a significant influence on subduction dynamics. A short slab edge distance facilitates return flow and may enhance slab retreat, while zones far away from subduction edges cannot so easily retreat and favor a stable position (Funiciello et al., 2004; Schellart et al., 2007; Schellart, 2008). The models presented here are 2-D and do not include toroidal flow and may be taken to represent the center of large subduction zones. Toroidal return flow is expected to lead to reduced slab anchoring and promote overriding plate extension. Accordingly, higher subduction and or overriding plate velocity is required in order to obtain overriding plate shortening. Similarly, subducting lithosphere with a larger or smaller negative buoyancy will shift the set of models toward more extension in case of a heavier plate or more shortening in case of a lighter subducting plate.

Another 3-D effect which we do not capture is how adjacent collision of two continental blocks may influence the stress regime and facilitate backarc opening (Magni et al., 2014; Moresi et al., 2014).

Mountain building models M3 and M4 show ablative subduction of the backarc lithospheric mantle during the later stages of mountain building, resulting from viscous coupling at the plate interface. Fluids derived from the subducting slab may weaken the subduction interface at depth for natural systems and may inhibit ablative subduction (Arcay et al., 2005; Faccenda et al., 2012; Gorczyk, Gerya, et al., 2007, Gorczyk, Willner, et al., 2007). We note, however, that ablative subduction has been proposed to explain the formation of a mountain belt on top of a subduction zone (Pope & Willett, 1998).

We tested the influence of a weaker or stronger rheology of the overriding plate crust, and although showing some differences in timing of deformation and mountain belt structure, the overall behavior is similar. Fluids and (fluid induced) melting may have a strong weakening effect on the continental lithosphere and possibly also on the subduction interface. A melt-weakened lithospheric mantle would possibly be even weaker than in our models, enhancing lithospheric removal leading to earlier backarc extension and shortening (Figure S4).

Our models do not account for latent heat of phase changes, viscous dissipation, and more complex and variable phase changes in the upper and lower mantle. Further studies could include those and investigate their effect on the overriding plate strain regime.

5.5. Comparison With Natural Systems

We next proceed with comparing the inferred controls on the mode of overriding plate deformation with observations from natural systems. The Tonga, Scotian, and the Mediterranean subduction zones with extensive backarc spreading activity have a very low (<1 cm/yr) absolute overriding plate velocity perpendicular to the trench in common (O'Neill et al., 2005; Schellart et al., 2008). This is consistent with model inference which indicates that backarc spreading requires that the overriding plate does not move toward the trench. The (central) Andes in contrast are the only area with major recent overriding plate shortening in an ocean-continent subduction setting (Schellart et al., 2007). Here the overriding South American plate moves toward the trench with 1–2 cm/yr, and the oceanic Nazca plate subducts with 6–7 cm/yr (O'Neill et al., 2005; Schellart et al., 2008). This velocity configuration is also consistent with the model predictions presented here. Below we investigate in detail the role of subduction dynamics at depth and the influence of backarc lithospheric strength for the central Andean and the Hellenic subduction zones (Figure 10).

Oceanic subduction below the central Andes started in the Jurassic and induced backarc extension within the stable overriding plate during most of the Mesozoic (Armijo et al., 2015; Charrier et al., 2007; Coira et al., 1982; Horton, 2018). The main shortening phase started around 50 Ma (Armijo et al., 2015; Barnes & Ehlers, 2009; Oncken et al., 2006), following some earlier local shortening around 100 Ma (Arriagada et al., 2006; Coira et al., 1982; Horton, 2018). Phases of extension and shortening have been attributed to absolute velocity changes of the overriding plate (Horton, 2018; Maloney et al., 2013), with inception of the main shortening phase coinciding with plate reorganization in the Pacific around 50 Ma (e.g., Seton et al., 2012; Torsvik et al., 2010; Wessel et al., 2006). Shortening started in the west and progressed landward (Horton, 2018; Oncken et al., 2006), leading to underthrusting of the Brazilian shield and bivergent orogenic growth during the last 10 Myr (Armijo et al., 2015; Oncken et al., 2006). A rigid "marginal" block offsets deforma-
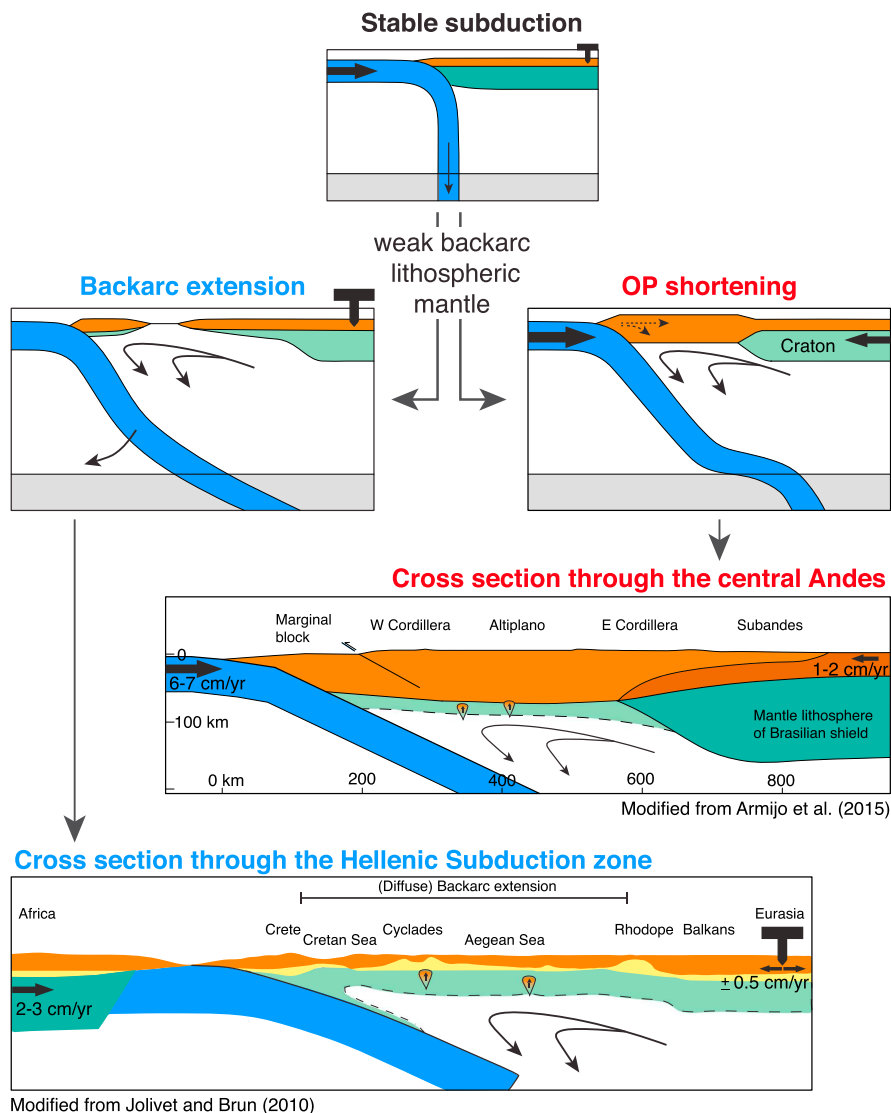
Figure 10. Cartoon and two natural examples showing the parameters which are needed to go from stable subduction to backarc extension or overriding plate shortening. Backarc extension requires an overriding plate which is not moving toward the trench and a weak backarc lithospheric mantle which is removed through gravitational instabilities. This situation matches with the plate tectonic configuration in the Hellenic subduction zone, where oceanic lithosphere associated with the African plate slowly subducts under the more or less stable Eurasian continent. A removed lithospheric mantle and thickened continental crust led to diffuse backarc extension with lower crustal flow (yellow material) during the last 35 Ma (Faccenna et al., 2014; Jolivet et al., 2013). Overriding plate shortening requires the overriding plate to move toward the trench and is facilitated by a removed lithospheric mantle. This is the case for the central Andes, where the South American plate is moving toward the trench against the subducting Nazca plate. The strong marginal block as well as progression of shortening landward (Armijo et al., 2015; Horton, 2018; Lamb, 2011; Oncken et al., 2006) can be explained by our models with a removed lithospheric mantle.

tion approximately 200 km from the trench into the hinterland throughout the shortening phase (Armijo et al., 2015; Lamb, 2011). Orogenic growth and magmatism in the Andes is often interpreted to be associated with delamination of dense backarc lithospheric material (DeCelles et al., 2009; Pelletier et al., 2010; Rapp & Watson, 1995; Wolf & Wyllie, 1993). Seismic tomography indicates very thin backarc lithospheric mantle below the central Andes (Schurr et al., 2006) and landward anchoring of the slab in the lower mantle (Li et al., 2008). Models M4, M4b, and M4c (Supporting Information S1) with overriding plate movement toward the trench and high subducting plate velocity are consistent with the plate velocity framework in the central Andes and show overriding plate strain regimes that compare well with the natural system. Weak backarc lithospheric mantle models with convective thinning (e.g., models M4, M4b, and M4c) exhibit shortening of the overriding plate lithosphere with deformation starting near the trench, landward progression of shortening ending with cratonic underthrusting, matching the evolution of mountain building in the central Andes. Rapid shortening in M4 produces a thicker lithospheric mantle than observed below the central Andes today. Self-limiting growth and slow down of the overriding plate (see section 4.3; M4b, Figure S4), an even weaker backarc lithospheric mantle (M4c, Figure S4), and a thinner lithospheric mantle inherited from preceding backarc extension possibly retained a thin Andean lithospheric mantle during mountain building. Based on the inferred controls on the mode of overriding plate deformation, we suggest that plate reorganizations and the corresponding velocity changes of the South American plate are the main causes of shortening in the Andes. At a crustal scale, the rigid marginal forearc block in the west central Andes may be explained resulting from the low temperatures owing to subduction leading to formation of the first shear zone approximately 200 km landward of the trench (Figures 6 and S4).

The active Hellenic subduction zone is another example that shows the influence of differential velocities on the overriding plate strain regime (Figure 10). Here the northern, oceanic continuation of the African plate subducts under a widely extended backarc region. The current absolute velocity of the African slab is 2–3 cm/yr, and the overriding plate is stable with a velocity of ± 0.5 cm/yr (O'Neill et al., 2005; Schellart et al., 2008). Onset of backarc extension is estimated at 35–30 Ma and accelerates at 15 Ma after accretion of a continental block (Faccenna et al., 2014; Jolivet & Brun, 2010). Backarc extension affected thickened crust stacked with continental terranes and a thin, possibly actively delaminating, lithospheric mantle (Altunkaynak & Dilek, 2006; Jolivet & Brun, 2010; Jolivet et al., 2013; Pe-Piper & Piper, 2006). The thick, likely hot, weak crust facilitated middle to lower crustal flow and widespread thinning during rifting in the Aegean (Figure 10). Tomographic models show a moderately dipping slab (45–60°), anchored in the lower mantle (Li et al., 2008; Piromallo & Morelli, 2003; Zhu et al., 2012). Model M6 with a weak and thin backarc mantle and zero overriding plate velocity is consistent with the tectonic context of the Hellenic subduction zone. The subducting slab connected with the large and slowly moving African plate leads to a configuration where the slab's natural sinking velocity is larger than the subduction velocity. Slab pull in the Hellenic case is probably even higher than in our models, as the subducting plate is very old and cold (Müller et al., 2008). These factors in combination with a stable Eurasian plate and a removed lithospheric mantle create a system that strongly promotes backarc extension. The amount of cumulative trench retreat in the Hellenic subduction zone is ~400 km (Faccenna et al., 2014), comparable with model M6, where the slab retreats 500 km within 20 Ma.

6. Conclusion

We use thermo-mechanical models to investigate the principal parameters that determine the overriding plate strain regime in an ocean-continent subduction setting and draw the following conclusions.

1. Weak backarc lithospheric mantle, removed through gravitational instability, is required for nature-like deformation of the overriding plate.
2. Strong backarc lithospheric mantle inhibits backarc extension.
3. Owing to slab anchoring in the lower mantle, the absolute and not the relative plate velocities determine whether and how the overriding plate deforms: (a) Overriding plate extension is promoted if the overriding plate is not moving toward the trench. (b) Overriding plate shortening is promoted when the overriding plate moves toward the trench and the subduction velocity is high.
4. The force balance analysis provides an estimate and shows near equilibrium of the driving and resisting forces during subduction. The near equilibrium supports the necessity of a weak overriding plate to deform it.

5. Comparison with the central Andean and Hellenic subduction zones supports the idea that removal of the overriding plate lithospheric mantle and absolute plate velocities determine the overriding plate strain regime.

References

Agrusta, R., Goes, S., & van Hunen, J. (2017). Subducting-slab transition-zone interaction: Stagnation, penetration and mode switches. *Earth and Planetary Science Letters*, *464*, 10–23. https://doi.org/10.1016/j.epsl.2017.02.005

Altunkaynak, S., & Dilek, Y. (2006). Timing and nature of postcollisional volcanism in western Anatolia and geodynamic implications. In Y. Dilek, & S. Pavlides (Eds.), *Postcollisional tectonics and magmatism in the Mediterranean region and Asia* (Vol. 409). Boulder, Colorado: Geological Society of America. https://doi.org/10.1130/2006.2409(17)

Andrews, E. R., & Billen, M. I. (2009). Rheologic controls on the dynamics of slab detachment. *Tectonophysics*, *464*(1-4), 60–69. https://doi.org/10.1016/j.tecto.2007.09.004

Arcay, D., Doin, M. P., Tric, E., Bousquet, R., & de Capitani, C. (2006). Overriding plate thinning in subduction zones: Localized convection induced by slab dehydration. *Geochemistry, Geophysics, Geosystems*, *7*, Q02007. https://doi.org/10.1029/2005gc001061

Arcay, D., Tric, E., & Doin, M. P. (2005). Numerical simulations of subduction zones—Effect of slab dehydration on the mantle wedge dynamics. *Physics of the Earth and Planetary Interiors*, *149*(1-2), 133–153. https://doi.org/10.1016/j.pepi.2004.08.020

Armijo, R., Lacassin, R., Coudurier-Curveur, A., & Carrizo, D. (2015). Coupled tectonic evolution of Andean orogeny and global climate. *Earth-Science Reviews*, *143*, 1–35. https://doi.org/10.1016/j.earscirev.2015.01.005

Arriagada, C., Cobbold, P. R., & Roperch, P. (2006). Salar de Atacama basin: A record of compressional tectonics in the central Andes since the mid-Cretaceous. *Tectonics*, *25*, TC1008. https://doi.org/10.1029/2004tc001770

Arriagada, C., Roperch, P., Mpodozis, C., & Cobbold, P. R. (2008). Paleogene building of the Bolivian orocline: Tectonic restoration of the central Andes in 2-D map view. *Tectonics*, *27*, TC6014. https://doi.org/10.1029/2008TC002269

Barnes, J. B., & Ehlers, T. A. (2009). End member models for Andean plateau uplift. *Earth-Science Reviews*, *97*(1-4), 105–132. https://doi.org/10.1016/j.earscirev.2009.08.003

Becker, T. W., Faccenna, C., O'Connell, R. J., & Giardini, D. (1999). The development of slabs in the upper mantle: Insights from numerical and laboratory experiments. *Journal of Geophysical Research*, *104*(B7), 15,207–15,226. https://doi.org/10.1029/1999jb900140

Billen, M. I. (2008). Modeling the dynamics of subducting slabs. *Annual Review of Earth and Planetary Sciences*, *36*, 325–356. https://doi.org/10.1146/annurev.earth.36.031207.124129

Billen, M. I. (2010). Slab dynamics in the transition zone. *Physics of the Earth and Planetary Interiors*, *183*(1-2), 296–308. https://doi.org/10.1016/j.pepi.2010.05.005

Butler, J. P., & Beaumont, C. (2017). Subduction zone decoupling/retreat modeling explains south Tibet (Xigaze) and other supra-subduction zone ophiolites and their UHP mineral phases. *Earth and Planetary Science Letters*, *463*, 101–117. https://doi.org/10.1016/j.epsl.2017.01.025

Butler, J. P., Beaumont, C., & Jamieson, R. A. (2015). Paradigm lost: Buoyancy thwarted by the strength of the Western Gneiss Region (ultra)high-pressure terrane, Norway. *Lithosphere*, *7*(4), 379–407. https://doi.org/10.1130/L426.1

Capitanio, F. A., Morra, G., & Goes, S. (2007). Dynamic models of downgoing plate-buoyancy driven subduction: Subduction motions and energy dissipation. *Earth and Planetary Science Letters*, *262*(1-2), 284–297. https://doi.org/10.1016/j.epsl.2007.07.039

Capitanio, F. A., Stegman, D. R., Moresi, L. N., & Sharples, W. (2010). Upper plate controls on deep subduction, trench migrations and deformations at convergent margins. *Tectonophysics*, *483*(1-2), 80–92. https://doi.org/10.1016/j.tecto.2009.08.020

Charrier, R., Pinto, L., & Rodríguez, M. P. (2007). Tectonostratigraphic evolution of the Andean orogen in Chile. In T. Moreno & W. Gibbons (Eds.), *The geology of Chile* pp. 21–114). London: Geological Society of London. https://doi.org/10.1144/GOCH.3

Cizkova, H., van Hunen, J., van den Berg, A. P., & Vlaar, N. J. (2002). The influence of rheological weakening and yield stress on the interaction of slabs with the 670 km discontinuity. *Earth and Planetary Science Letters*, *199*(3-4), 447–457. https://doi.org/10.1016/S0012-821X(02)00586-1

Coira, B., Davidson, J., Mpodozis, C., & Ramos, V. (1982). Tectonic and magmatic evolution of the Andes of northern Argentina and Chile. *Earth-Science Reviews*, *18*(3-4), 303–332. https://doi.org/10.1016/0012-8252(82)90042-3

Conrad, C. P., & Hager, B. H. (1999). Effects of plate bending and fault strength at subduction zones on plate dynamics. *Journal of Geophysical Research*, *104*(B8), 17,551–17,571. https://doi.org/10.1029/1999jb900181

Currie, C. A., Beaumont, C., & Huismans, R. S. (2007). The fate of subducted sediments: A case for backarc intrusion and underplating. *Geology*, *35*(12), 1111–1114. https://doi.org/10.1130/G24098a.1

Currie, C. A., Ducea, M. N., DeCelles, P. G., & Beaumont, C. (2015). Geodynamic models of Cordilleran orogens: Gravitational instability of magmatic arc roots. *Geological Society of America Memoirs*, *212*, 1–22. https://doi.org/10.1130/2015.1212(01)

Currie, C. A., Huismans, R. S., & Beaumont, C. (2008). Thinning of continental backarc lithosphere by flow-induced gravitational instability. *Earth and Planetary Science Letters*, *269*(3-4), 435–446. https://doi.org/10.1016/j.epsl.2008.02.037

DeCelles, P. G., Ducea, M. N., Kapp, P., & Zandt, G. (2009). Cyclicity in Cordilleran orogenic systems. *Nature Geoscience*, *2*(4), 251–257. https://doi.org/10.1038/Ngeo469

Duretz, T., Schmalholz, S. M., & Gerya, T. V. (2012). Dynamics of slab detachment. *Geochemistry, Geophysics, Geosystems*, *13*, Q03020. https://doi.org/10.1029/2011gc004024

Erdos, Z., Huismans, R. S., van der Beek, P., & Thieulot, C. (2014). Extensional inheritance and surface processes as controlling factors of mountain belt structure. *Journal of Geophysical Research: Solid Earth*, *119*, 9042–9061. https://doi.org/10.1002/2014jb011408

Faccenda, M., Gerya, T. V., Mancktelow, N. S., & Moresi, L. (2012). Fluid flow during slab unbending and dehydration: Implications for intermediate-depth seismicity, slab weakening and deep water recycling. *Geochemistry, Geophysics, Geosystems*, *13*, Q01010. https://doi.org/10.1029/2011gc003860

Faccenna, C., Becker, T. W., Auer, L., Billi, A., Boschi, L., Brun, J. P., et al. (2014). Mantle dynamics in the Mediterranean. *Reviews of Geophysics*, *52*, 283–332. https://doi.org/10.1002/2013rg000444

Faccenna, C., Becker, T. W., Lallemand, S., Lagabrielle, Y., Funiciello, F., & Piromallo, C. (2010). Subduction-triggered magmatic pulses: A new class of plumes? *Earth and Planetary Science Letters*, *299*(1-2), 54–68. https://doi.org/10.1016/j.epsl.2010.08.012

Faccenna, C., Oncken, O., Holt, A. F., & Becker, T. W. (2017). Initiation of the Andean orogeny by lower mantle subduction. *Earth and Planetary Science Letters*, *463*, 189–201. https://doi.org/10.1016/j.epsl.2017.01.041

Forsyth, D., & Uyeda, S. (1975). Relative importance of driving forces of plate motion. *Geophysical Journal of the Royal Astronomical Society*, *43*(1), 163–200. https://doi.org/10.1111/j.1365-246X.1975.tb00631.x

Funiciello, F., Faccenna, C., & Giardini, D. (2004). Role of lateral mantle flow in the evolution of subduction systems: Insights from laboratory experiments. *Geophysical Journal International*, *157*(3), 1393–1406. https://doi.org/10.1111/j.1365-246X.2004.02313.x

Funiciello, F., Faccenna, C., Giardini, D., & Regenauer-Lieb, K. (2003). Dynamics of retreating slabs: 2. Insights from three-dimensional laboratory experiments. *Journal of Geophysical Research*, *108*(B4), 2207. https://doi.org/10.1029/2001jb000896

Garel, F., Goes, S., Davies, D. R., Davies, J. H., Kramer, S. C., & Wilson, C. R. (2014). Interaction of subducted slabs with the mantle transition-zone: A regime diagram from 2-D thermo-mechanical models with a mobile trench and an overriding plate. *Geochemistry, Geophysics, Geosystems*, *15*, 1739–1765. https://doi.org/10.1002/2014gc005257

Gerya, T. (2011). Future directions in subduction modeling. *Journal of Geodynamics*, *52*(5), 344–378. https://doi.org/10.1016/j.jog.2011.06.005

Gerya, T. V., Stern, R. J., Baes, M., Sobolev, S. V., & Whattam, S. A. (2015). Plate tectonics on the Earth triggered by plume-induced subduction initiation. *Nature*, *527*(7577), 221–225. https://doi.org/10.1038/nature15752

Gleason, G. C., & Tullis, J. (1995). A flow law for dislocation creep of quartz aggregates determined with the molten-salt cell. *Tectonophysics*, *247*(1-4), 1–23. https://doi.org/10.1016/0040-1951(95)00011-B

Goes, S., Agrusta, R., van Hunen, J., & Garel, F. (2017). Subduction-transition zone interaction: A review. *Geosphere*, *13*(3), 644–664. https://doi.org/10.1130/Ges01476.1

Gorczyk, W., Gerya, T. V., Connolly, J. A. D., & Yuen, D. A. (2007). Growth and mixing dynamics of mantle wedge plumes. *Geology*, *35*(7), 587–590. https://doi.org/10.1130/G23485a.1

Gorczyk, W., Willner, A. P., Gerya, T. V., Connolly, J. A. D., & Burg, J. P. (2007). Physical controls of magmatic productivity at Pacific-type convergent margins: Numerical modelling. *Physics of the Earth and Planetary Interiors*, *163*(1-4), 209–232. https://doi.org/10.1016/j.pepi.2007.05.010

Hacker, B. R. (1996). Eclogite formation and the rheology, buoyancy, seismicity, and H_2O content of oceanic crust. In G. E Bebout, D. W. Scholl, S. H. Kirby, & J. P. Platt (Eds.), *Subduction: Top to bottom* (pp. 337–346). Washington, DC: American Geophysical Union. https://doi.org/10.1029/GM096p0337

Hacker, B. R., Kelemen, P. B., & Behn, M. D. (2011). Differentiation of the continental crust by relamination. *Earth and Planetary Science Letters*, *307*(3-4), 501–516. https://doi.org/10.1016/j.epsl.2011.05.024

Hacker, B. R., Kelemen, P. B., & Behn, M. D. (2015). Continental lower crust. *Annual Review of Earth and Planetary Sciences*, *43*(1h), 167–205. https://doi.org/10.1146/annurev-earth-050212-124117

Heuret, A., & Lallemand, S. (2005). Plate motions, slab dynamics and back-arc deformation. *Physics of the Earth and Planetary Interiors*, *149*(1-2), 31–51. https://doi.org/10.1016/j.pepi.2004.08.022

Holt, A. F., Becker, T. W., & Buffett, B. A. (2015). Trench migration and overriding plate stress in dynamic subduction models. *Geophysical Journal International*, *201*(1), 172–192. https://doi.org/10.1093/gji/ggv011

Horton, B. K. (2018). Tectonic regimes of the central and southern Andes: Responses to variations in plate coupling during subduction. *Tectonics*, *37*, 402–429. https://doi.org/10.1002/2017tc004624

Huang, Y., Chubakov, V., Mantovani, F., Rudnick, R. L., & McDonough, W. F. (2013). A reference Earth model for the heat-producing elements and associated geoneutrino flux. *Geochemistry, Geophysics, Geosystems*, *14*, 2003–2029. https://doi.org/10.1002/ggge.20129

Huangfu, P. P., Wang, Y. J., Cawood, P. A., Li, Z. H., Fan, W. M., & Gerya, T. V. (2016). Thermo-mechanical controls of flat subduction: Insights from numerical modeling. *Gondwana Research*, *40*, 170–183. https://doi.org/10.1016/j.gr.2016.08.012

Huismans, R. S., & Beaumont, C. (2003). Symmetric and asymmetric lithospheric extension: Relative effects of frictional-plastic and viscous strain softening. *Journal of Geophysical Research*, *108*(B10), 2496. https://doi.org/10.1029/2002jb002026

Huismans, R. S., & Beaumont, C. (2011). Depth-dependent extension, two-stage breakup and cratonic underplating at rifted margins. *Nature*, *473*(7345), 74–78. Retrieved from http://www.ncbi.nlm.nih.gov/pubmed/21544144 https://doi.org/10.1038/nature09988

Husson, L., Conrad, C. P., & Faccenna, C. (2012). Plate motions, Andean orogeny, and volcanism above the South Atlantic convection cell. *Earth and Planetary Science Letters*, *317*, 126–135. https://doi.org/10.1016/j.epsl.2011.11.040

Hyndman, R. D., Currie, C. A., & Mazzotti, S. P. (2005). Subduction zone backarcs, mobile belts, and orogenic heat. *GSA Today*, *15*(2), 4–10. https://doi.org/10.1130/1052-5173(2005)015<4:SZBMBA>2.0.CO;2

Jarrard, R. D. (1986). Relations among subduction parameters. *Reviews of Geophysics*, *24*(2), 217–284. https://doi.org/10.1029/RG024i002p00217

Jolivet, L., & Brun, J. P. (2010). Cenozoic geodynamic evolution of the Aegean. *International Journal of Earth Sciences*, *99*(1), 109–138. https://doi.org/10.1007/s00531-008-0366-4

Jolivet, L., Faccenna, C., Huet, B., Labrousse, L., Le Pourhiet, L., Lacombe, O., et al. (2013). Aegean tectonics: Strain localisation, slab tearing and trench retreat. *Tectonophysics*, *597*, 1–33. https://doi.org/10.1016/j.tecto.2012.06.011

Karato, S., & Wu, P. (1993). Rheology of the upper mantle—A synthesis. *Science*, *260*(5109), 771–778. https://doi.org/10.1126/science.260.5109.771

Katayama, I., & Karato, S. I. (2008). Low-temperature, high-stress deformation of olivine under water-saturated conditions. *Physics of the Earth and Planetary Interiors*, *168*(3-4), 125–133. https://doi.org/10.1016/j.pepi.2008.05.019

Kelly, S., Butler, J. P., & Beaumont, C. (2016). Continental collision with a sandwiched accreted terrane: Insights into Himalayan-Tibetan lithospheric mantle tectonics? *Earth and Planetary Science Letters*, *455*, 176–195. https://doi.org/10.1016/j.epsl.2016.08.039

Kreemer, C., Holt, W. E., & Haines, A. J. (2003). An integrated global model of present-day plate motions and plate boundary deformation. *Geophysical Journal International*, *154*(1), 8–34. https://doi.org/10.1046/j.1365-246X.2003.01917.x

Krystopowicz, N. J., & Currie, C. A (2013). Crustal eclogitization and lithosphere delamination in orogens. *Earth and Planetary Science Letters*, *361*, 195–207. https://doi.org/10.1016/j.epsl.2012.09.056

Lamb, S. (2011). Did shortening in thick crust cause rapid late Cenozoic uplift in the northern Bolivian Andes? *Journal of the Geological Society*, *168*(5), 1079–1092. https://doi.org/10.1144/0016-76492011-008

Li, Z. H., Liu, M. A., & Gerya, T. (2016). Lithosphere delamination in continental collisional orogens: A systematic numerical study. *Journal of Geophysical Research: Solid Earth*, *121*, 5186–5211. https://doi.org/10.1002/2016jb013106

Li, C., van der Hilst, R. D., Engdahl, E. R., & Burdick, S. (2008). A new global model for P wave speed variations in Earth's mantle. *Geochemistry, Geophysics, Geosystems*, *9*, Q05018. https://doi.org/10.1029/2007gc001806

Mackwell, S. J., Zimmerman, M. E., & Kohlstedt, D. L. (1998). High-temperature deformation of dry diabase with application to tectonics on Venus. *Journal of Geophysical Research*, *103*(B1), 975–984. https://doi.org/10.1029/97JB02671

Magni, V., Faccenna, C., van Hunen, J., & Funiciello, F. (2014). How collision triggers backarc extension: Insight into Mediterranean style of extension from 3-D numerical models. *Geology*, *42*(6), 511–514. https://doi.org/10.1130/G35446.1

Maloney, K. T., Clarke, G. L., Klepeis, K. A., & Quevedo, L. (2013). The late Jurassic to present evolution of the Andean margin: Drivers and the geological record. *Tectonics*, *32*, 1049–1065. https://doi.org/10.1002/tect.20067

Mitrovica, J. X., & Forte, A. M. (2004). A new inference of mantle viscosity based upon joint inversion of convection and glacial isostatic adjustment data. *Earth and Planetary Science Letters*, *225*(1-2), 177–189. https://doi.org/10.1016/j.epsl.2004.06.005

Moresi, L., Betts, P. G., Miller, M. S., & Cayley, R. A. (2014). Dynamics of continental accretion. *Nature*, *508*(7495), 245–248. https://doi.org/10.1038/nature13033

Morra, G., Regenauer-Lieb, K., & Giardini, D. (2006). Curvature of oceanic arcs. *Geology*, *34*(10), 877–880. https://doi.org/10.1130/G22462.1

Müller, R. D., Sdrolias, M., Gaina, C., & Roest, W. R. (2008). Age, spreading rates, and spreading asymmetry of the world's ocean crust. *Geochemistry, Geophysics, Geosystems*, *9*, Q04006. https://doi.org/10.1029/2007gc001743

O'Neill, C., Müller, D., & Steinberger, B. (2005). On the uncertainties in hot spot reconstructions and the significance of moving hot spot reference frames. *Geochemistry, Geophysics, Geosystems*, *6*, Q04003. https://doi.org/10.1029/2004gc000784

Oncken, O., Hindle, D., Kley, J., Elger, K., Victor, P., & Schemmann, K. (2006). Deformation of the central Andean upper plate system—Facts, fiction, and constraints for plateau models. In O. Oncken, et al. (Eds.), *The Andes Frontiers in Earth sciences* (pp. 3–27). Berlin, Heidelberg: Springer. https://doi.org/10.1007/978-3-540-48684-8n_1

Parsons, B., & Richter, F. M. (1980). A relation between the driving force and geoid anomaly associated with mid-ocean ridges. *Earth and Planetary Science Letters*, *51*(2), 445–450. https://doi.org/10.1016/0012-821x(80)90223-X

Pe-Piper, G., & Piper, D. J. W. (2006). Unique features of the cenozoic igneous rocks of Greece. In Y. Dilek, & S. Pavlides (Eds.), *Postcollisional tectonics and magmatism in the Mediterranean region and Asia* (vol. 409). Boulder, Colorado: Geological Society of America. https://doi.org/10.1130/2006.2409(14)

Pelletier, J. D., DeCelles, P. G., & Zandt, G. (2010). Relationships among climate, erosion, topography, and delamination in the Andes: A numerical modeling investigation. *Geology*, *38*(3), 259–262. https://doi.org/10.1130/g30755.1

Piromallo, C., & Morelli, A. (2003). P wave tomography of the mantle under the Alpine-Mediterranean area. *Journal of Geophysical Research*, *108*(B2), 2065. https://doi.org/10.1029/2002jb001757

Pope, D. C., & Willett, S. D. (1998). Thermal-mechanical model for crustal thickening in the central Andes driven by ablative subduction. *Geology*, *26*(6), 511–514. https://doi.org/10.1130/0091-7613(1998)026<0511:Tmmfct>2.3.Co;2

Pysklywec, R. N., & Beaumont, C. (2004). Intraplate tectonics: Feedback between radioactive thermal weakening and crustal deformation driven by mantle lithosphere instabilities. *Earth and Planetary Science Letters*, *221*(1-4), 275–292. https://doi.org/10.1016/S0012-821x(04)00098-6

Quinquis, M. E. T., Buiter, S. J. H., & Ellis, S. (2011). The role of boundary conditions in numerical models of subduction zone dynamics. *Tectonophysics*, *497*(1-4), 57–70. https://doi.org/10.1016/j.tecto.2010.11.001

Rapp, R. P., & Watson, E. B. (1995). Dehydration melting of metabasalt at 8–32 kbar—Implications for continental growth and crust-mantle recycling. *Journal of Petrology*, *36*(4), 891–931. https://doi.org/10.1093/petrology/36.4.891

Rodriguez-Gonzalez, J., & Negredo, A. M. (2012). The role of the overriding plate thermal state on slab dip variability and on the occurrence of flat subduction. *Geochemistry, Geophysics, Geosystems*, *13*, Q01002. https://doi.org/10.1029/2011gc003859

Schellart, W. P. (2008). Overriding plate shortening and extension above subduction zones: A parametric study to explain formation of the Andes mountains. *Geological Society of America Bulletin*, *120*(11-12), 1441–1454. https://doi.org/10.1130/B26360.1

Schellart, W. P., Freeman, J., Stegman, D. R., Moresi, L., & May, D. (2007). Evolution and diversity of subduction zones controlled by slab width. *Nature*, *446*(7133), 308–311. https://doi.org/10.1038/nature05615

Schellart, W. P., & Moresi, L. (2013). A new driving mechanism for backarc extension and backarc shortening through slab sinking induced toroidal and poloidal mantle flow: Results from dynamic subduction models with an overriding plate. *Journal of Geophysical Research: Solid Earth*, *118*, 3221–3248. https://doi.org/10.1002/jgrb.50173

Schellart, W. P., Stegman, D. R., & Freeman, J. (2008). Global trench migration velocities and slab migration induced upper mantle volume fluxes: Constraints to find an Earth reference frame based on minimizing viscous dissipation. *Earth-Science Reviews*, *88*(1-2), 118–144. https://doi.org/10.1016/j.earscirev.2008.01.005

Schmeling, H., Babeyko, A. Y., Enns, A., Faccenna, C., Funiciello, F., Gerya, T., et al. (2008). A benchmark comparison of spontaneous subduction models—Towards a free surface. *Physics of the Earth and Planetary Interiors*, *171*(1-4), 198–223. https://doi.org/10.1016/j.pepi.2008.06.028

Schurr, B., Rietbrock, A., Asch, G., Kind, R., & Oncken, O. (2006). Evidence for lithospheric detachment in the central Andes from local earthquake tomography. *Tectonophysics*, *415*(1-4), 203–223. https://doi.org/10.1016/j.tecto.2005.12.007

Seton, M., Müller, R. D., Zahirovic, S., Gaina, C., Torsvik, T. H., Shephard, G., et al. (2012). Global continental and ocean basin reconstructions since 200 Ma. *Earth-Science Reviews*, *113*(3-4), 212–270. https://doi.org/10.1016/j.earscirev.2012.03.002

Sobolev, S. V., & Babeyko, A. Y. (2005). What drives orogeny in the Andes? *Geology*, *33*(8), 617–620. https://doi.org/10.1130/G21557

Stevenson, D. J., & Turner, J. S. (1977). Angle of subduction. *Nature*, *270*(5635), 334–336. https://doi.org/10.1038/270334a0

Stüwe, K. (2007). *Geodynamics of the lithosphere* (2nd ed.). Berlin Heidelberg: Springer Verlag. https://doi.org/10.1007/978-3-540-71237-4

Thieulot, C. (2011). Fantom: Two- and three-dimensional numerical modelling of creeping flows for the solution of geological problems. *Physics of the Earth and Planetary Interiors*, *188*(1-2), 47–68. https://doi.org/10.1016/j.pepi.2011.06.011

Torsvik, T. H., Steinberger, B., Gurnis, M., & Gaina, C. (2010). Plate tectonics and net lithosphere rotation over the past 150 My. *Earth and Planetary Science Letters*, *291*(1-4), 106–112. https://doi.org/10.1016/j.epsl.2009.12.055

Tosi, N., Yuen, D. A., de Koker, N., & Wentzcovitch, R. M. (2013). Mantle dynamics with pressure- and temperature-dependent thermal expansivity and conductivity. *Physics of the Earth and Planetary Interiors*, *217*, 48–58. https://doi.org/10.1016/j.pepi.2013.02.004

Tsenn, M. C., & Carter, N. L. (1987). Upper limits of power law creep of rocks. *Tectonophysics*, *136*(1–2), 1–26.

Turcotte, D. L., & Schubert, G. (1982). *Geodynamics*. New York: John Wiley.

Uyeda, S., & Kanamori, H. (1979). Back-arc opening and the mode of subduction. *Journal of Geophysical Research*, *84*(Nb3), 1049–1061. https://doi.org/10.1029/JB084iB03p01049

Wessel, P., Harada, Y., & Kroenke, L. W. (2006). Toward a self-consistent, high-resolution absolute plate motion model for the Pacific. *Geochemistry, Geophysics, Geosystems*, *7*, Q03L12. https://doi.org/10.1029/2005GC001000

Wolf, M. B., & Wyllie, P. J. (1993). Garnet growth during amphibolite anatexis—Implications of a garnetiferous restite. *Journal of Geology*, *101*(3), 357–373. https://doi.org/10.1086/648229

Zhu, H. J., Bozdag, E., Peter, D., & Tromp, J. (2012). Structure of the european upper mantle revealed by adjoint tomography. *Nature Geoscience*, *5*(7), 493–498. https://doi.org/10.1038/ngeo1501

Supporting Information for "Mountain building or backarc extension in ocean-continent subduction systems - a function of backarc lithospheric strength and absolute plate velocities"

Sebastian G. Wolf[1], Ritske S. Huismans[1]

Contents of this file

Additional Supporting Information (Files uploaded separately)

[1]Department of Earth Science, Bergen University, Bergen N-5007, Norway

Introduction

The supplementary material contains, in order of appearance, a derivation of the tectonic boundary force, a discussion of our choice of backarc continental lower crustal thickness and composition, key snapshots of the viscosity field of models M1-M4 (Figs. S1, S2), and the evolution of tectonic boundary forces of the models presented in the article (Fig. S3).

We also show four additional models which highlight and clarify certain aspects of mountain building models M3 and M4. The first two models (M4b, M4c, Fig. S4) are a variation of M4. M4b (Fig. S4a,b) has a lower overriding plate velocity (1 cm/yr) than M4. This model shows that slab foundering in the transition zone is not necessary for overriding plate shortening. In this model onset of shortening requires a continental compressional boundary force of 4×10^{12} N/m. M4c (Fig. S4c,d) has the same velocity boundary conditions as M4, but an even weaker backarc lithospheric mantle (wet Olivine*0.5). The weak mantle is removed faster than in M4 and shortening starts earlier at compressional boundary forces of 3×10^{12} N/m. The other two additional models M3_1000 and M4_1000 are variations of M3 and M4 with a respectively 1000 km wider oceanic domain. They show a very similar tectonic evolution as models M3, M4 and clarify that overriding plate shortening in M3 and M4 is not influenced by approaching the left model boundary.

Animations of all models are uploaded to a data repository. See acknowledgements for DOI.

Tectonic boundary force:

The tectonic boundary force F_{TBF} is defined as

$$F_{TBF} = \int_0^{z_{lab}} \sigma'_{xx} dz = \int_0^{z_{lab}} 2\dot{\epsilon}_{xx} \mu_{eff} dz, \qquad (1)$$

where z_{lab} is lithosphere thickness, σ'_{xx} is horizontal deviatoric stress, $\dot{\epsilon}_{xx}$ is horizontal strain rate, and μ_{eff} is effective viscosity. We calculate F_{TBF} at the sides of the model with $z_{lab} = 90$ km in the oceanic and $z_{lab} = 120$ km in the continental domain. We define net pull, i.e. tensional stresses, as positive. The tectonic force is the net force resulting from the given boundary conditions, slab pull, and resisting forces, as described in section 4.3.

Discussion of backarc continental lower crustal thickness and composition:

Generally, the composition and rheology of continental lower crust is poorly known and understood, and therefore subject to large uncertainties (Hacker et al., 2015). Following Huang et al. (2013), the average Earth's crust is 34.4 km $\pm$ 4.1 km thick, where the upper/mid 24 km are felsic and the lower 10 km are mafic. Hacker et al. (2011)

proposed that crust near active (subduction) margins might be completely felsic because of relamination of felsic material into the crust. To account for a weaker crust as a consequence of relamination, we chose a 30 km thick felsic upper/mid crust and a 6 km thick mafic lower crust in the backarc area. The models presented here are part of a very large set of models and we also tested a 24 km felsic with a 12 km thick mafic crust, following Currie et al. (2008), and a fully felsic crust. Model evolution does not change significantly between the different model sets and we believe that our crustal setup gives a good representation of the strength of continental overriding crust in ocean-continent subduction systems.

Labelling of animations in data repository (see acknowledgements for DOI):

v_{oc} is the subduction velocity and v_{cont} is the overriding plate velocity. $v_{cont} > 0$ means movement towards the trench. All animations show the whole modelled domain in the lower panel and a zoom inset in the upper panel. Both plots show the Material colors (see legend in Fig. 1) and the velocity field as quivers. The length of the quiver is scaled relatively to the local magnitude of the velocity. Additionally, the temperature field is displayed with isotherms: 550 °C, 1330 °C, 1500 °C in lower panel and 350 °C, 550 °C, 1330 °C, 1500 °C in upper panel. The white overlay in the upper panel highlights strain-weakened shear zones.

Animation MS01: M1, $v_{oc} = 5$ cm/yr; $v_{cont} = 0$ cm/yr, strong backarc lithospheric mantle

Animation MS02: M2, $v_{oc} = 5$ cm/yr; $v_{cont} = 0$ cm/yr, weak backarc lithospheric mantle

Animation MS03: M3, $v_{oc} = 5$ cm/yr; $v_{cont} = 2$ cm/yr, strong backarc lithospheric mantle

Animation MS04: M4, $v_{oc} = 5$ cm/yr; $v_{cont} = 2$ cm/yr, weak backarc lithospheric mantle

Animation MS05: M5, $v_{oc} = 3$ cm/yr; $v_{cont} = 0$ cm/yr, strong backarc lithospheric mantle

Animation MS06: M6, $v_{oc} = 3$ cm/yr; $v_{cont} = 0$ cm/yr, weak backarc lithospheric mantle

Animation MS07: M7, $v_{oc} = 7$ cm/yr; $v_{cont} = 0$ cm/yr, strong backarc lithospheric mantle

Animation MS08: M8, $v_{oc} = 7$ cm/yr; $v_{cont} = 0$ cm/yr, weak backarc lithospheric mantle

Animation MS09: M9, $v_{oc} = 3$ cm/yr; $v_{cont} = 2$ cm/yr, strong backarc lithospheric mantle

Animation MS10: M10, $v_{oc} = 3$ cm/yr; $v_{cont} = 2$ cm/yr, weak backarc lithospheric mantle

Animation MS11: M4b, $v_{oc} = 5$ cm/yr; $v_{cont} = 1$ cm/yr, weak backarc lithospheric mantle

Animation MS12: M4c, $v_{oc} = 5$ cm/yr; $v_{cont} = 2$ cm/yr, very weak backarc lithospheric mantle
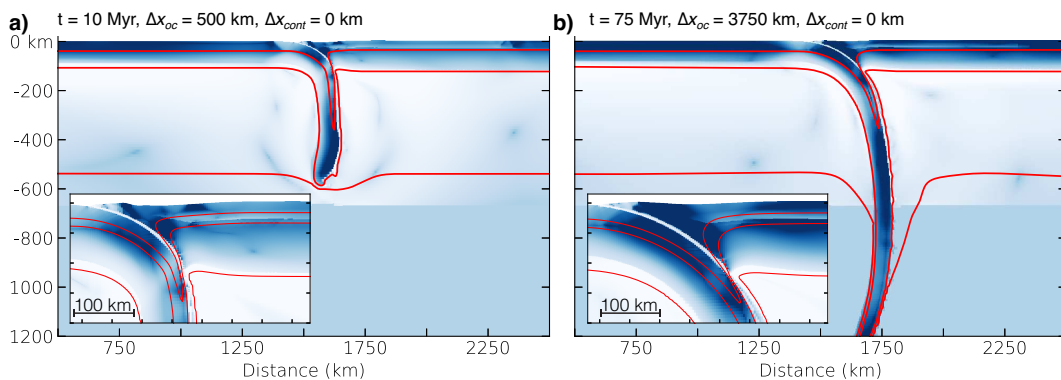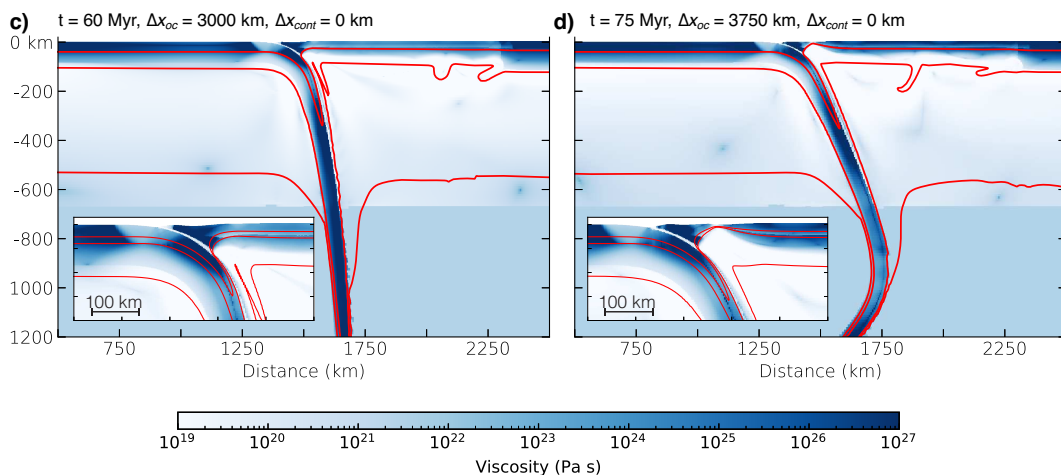
M1: v$_{oc}$= 5 cm/yr, v$_{cont}$ = 0 cm/yr, Strong backarc lithosphere

Figure S1. Viscosity plots of models M1 (a,b) and M2 (c,d) with logarithmic colorscale and isotherms (550 °C, 1330 °C, 1500 °C). Insets include an additional isotherm at 350 °C. t is model time, Δx_{oc} and Δx_{cont} are the amounts of oceanic and continental convergence.
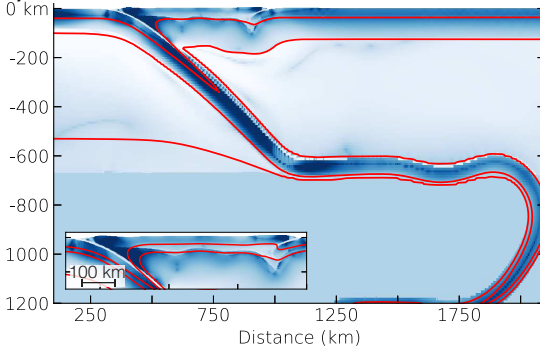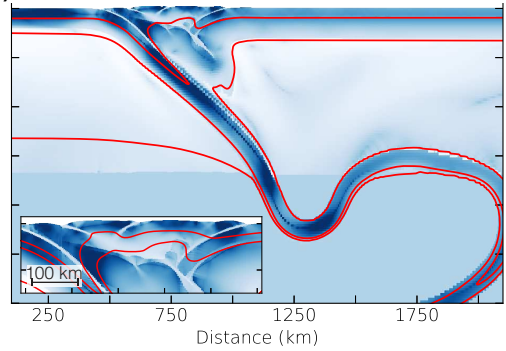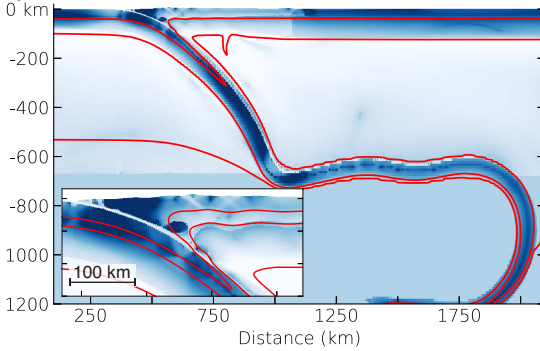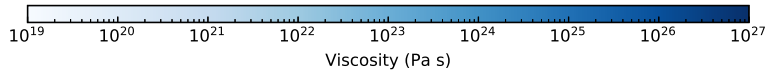
M3: v_{oc} = 5 cm/yr, v_{cont} = 2 cm/yr, Strong backarc lithosphere

a) t = 75 Myr, Δx_{oc} = 3750 km, Δx_{cont} = 1440 km

b) t = 85 Myr, Δx_{oc} = 4250 km, Δx_{cont} = 1640 km

M4: v_{oc} = 5 cm/yr, v_{cont} = 2 cm/yr, weak backarc lithosphere

c) t = 65 Myr, Δx_{oc} = 3250 km, Δx_{cont} = 1240 km

d) t = 70 Myr, Δx_{oc} = 3500 km, Δx_{cont} = 1360 km
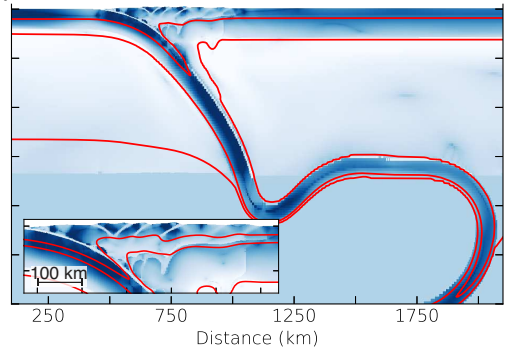
Viscosity (Pa s)

Figure S2. Viscosity plots of models M3 (a,b) and M4 (c,d) with logarithmic colorscale and isotherms (550 °C, 1330 °C, 1500 °C). Insets include an additional isotherm at 350 °C. t is model time, Δx_{oc} and Δx_{cont} are the amounts of oceanic and continental convergence.

Strong backarc lithosphere

Weak backarc lithosphere
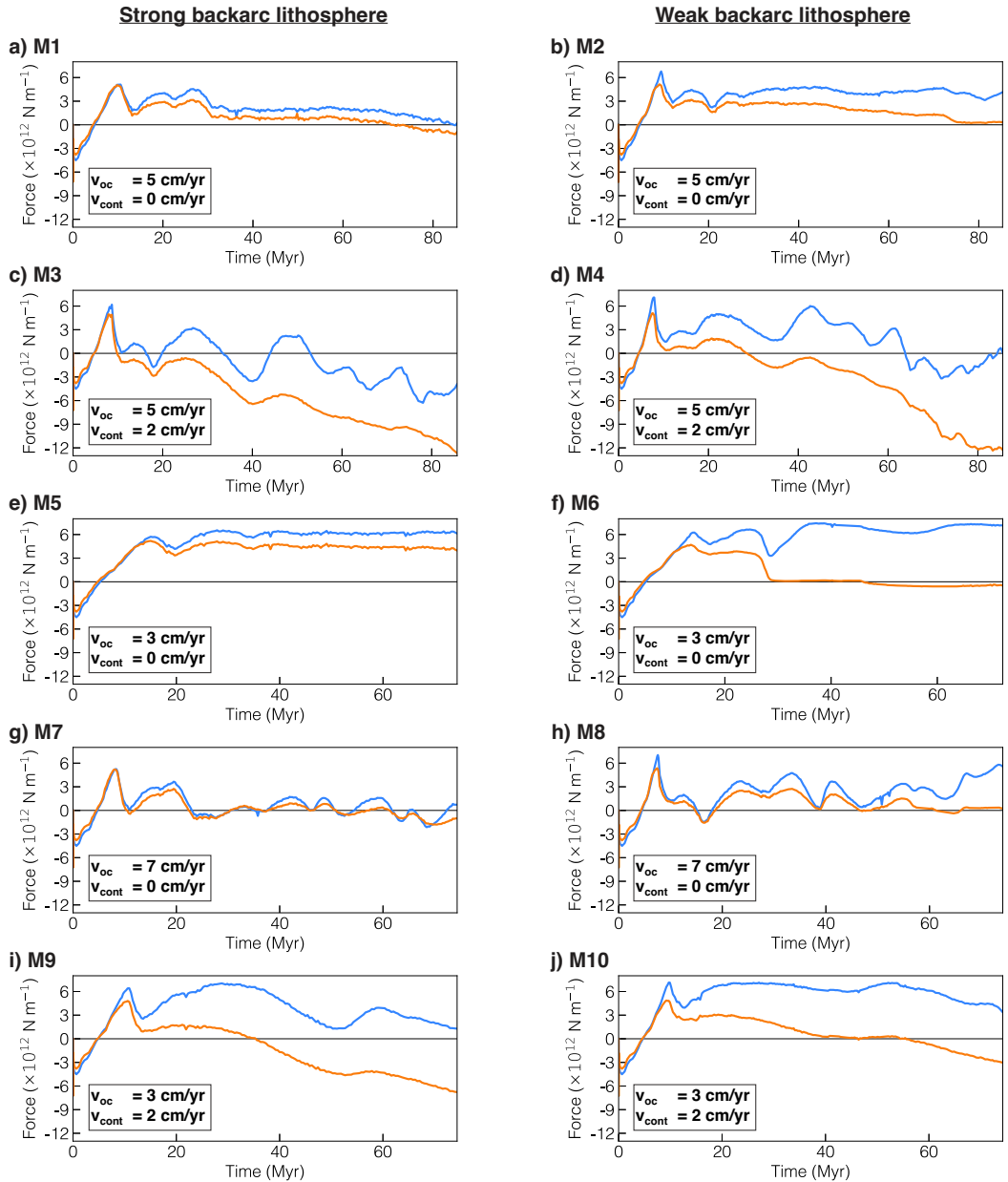
Figure S3. Tectonic boundary forces, i.e. the integrated horizontal deviatoric stresses in the lithosphere at the model boundary, for all models presented in this article. The blue line represents the teconic force at the oceanic, left side and the orange line corresponds to the right, continental side. Tensional forces are positive and compressional forces are negative.
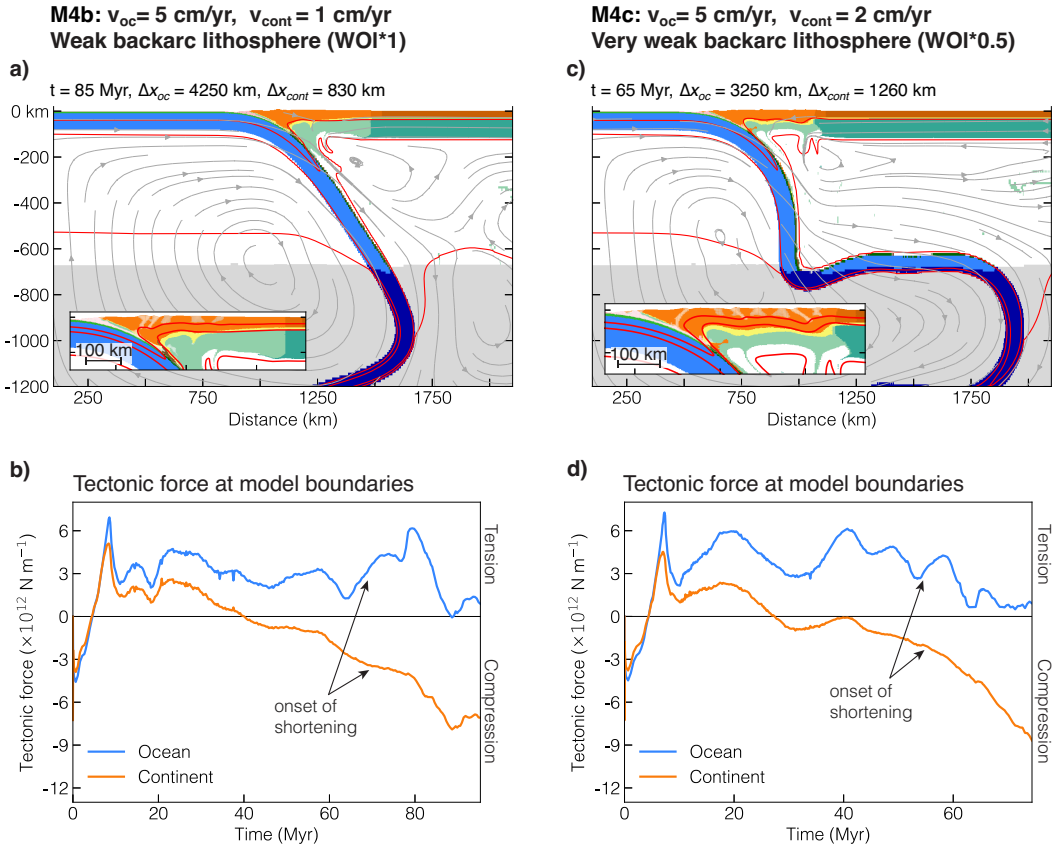
Figure S4. Supplementary models M4b (a,b) and M4c (c,d). Model M4b is the same as M4, but with a lower overriding plate velocity. This model shows that overriding plate shortening does not require foundering of the slab in the lower mantle. Additionally, a smaller force is needed for the onset of deformation when the overriding plate moves slower. Model M4c is the same as M4, but with a weaker backarc lithospheric mantle. This model shows that an even weaker backarc lithospheric mantle leads to earlier backarc shortening which requires less tectonic force. (a,c) Material colors (see Fig. 1) with isotherms (550 °C, 1330 °C, 1500 °C) and streamlines scaled in thickness to velocity. t is model time, Δx_{oc} and Δx_{cont} are the amounts of oceanic and continental convergence. Insets contain zoom with additional isotherm at 350 °C. (b,d) Tectonic forces (integrated horizontal deviatoric stress).

M3_1000 = M3 + 1000 km ocean: v_{oc} = 5 cm/yr, v_{cont} = 2 cm/yr, Strong backarc lithosphere

a)   t = 75 Myr, Δx_{oc} = 3750 km, Δx_{cont} = 1440 km
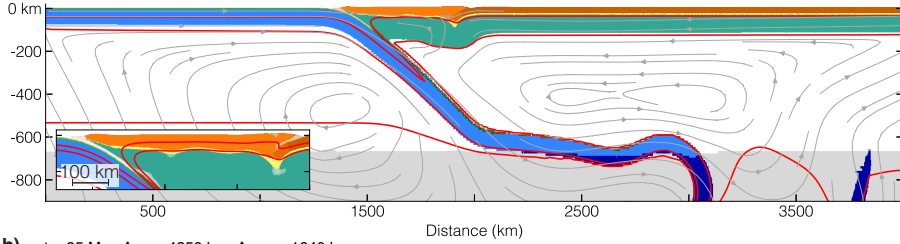
b)   t = 85 Myr, Δx_{oc} = 4250 km, Δx_{cont} = 1640 km
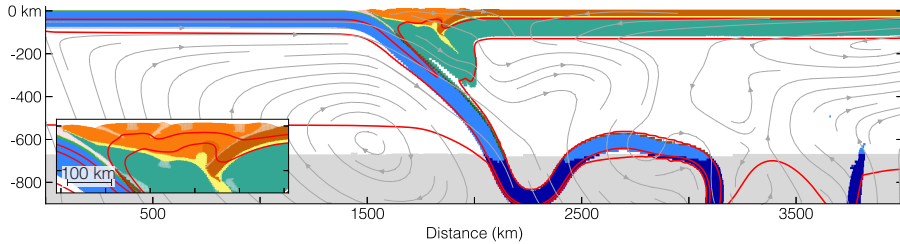
M4_1000 = M4 + 1000 km ocean: v_{oc} = 5 cm/yr, v_{cont} = 2 cm/yr, Weak backarc lithosphere

c)   t = 65 Myr, Δx_{oc} = 3250 km, Δx_{cont} = 1240 km
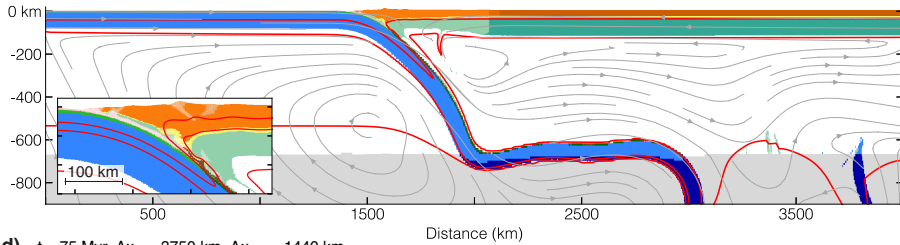
d)   t = 75 Myr, Δx_{oc} = 3750 km, Δx_{cont} = 1440 km
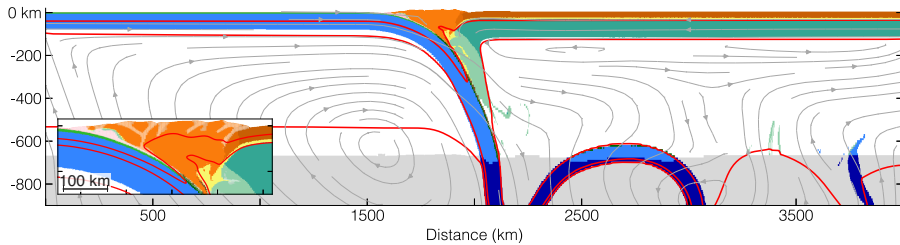
Figure S5. Mountain building models with the same setup as M3, M4 but with a 1000 km wider oceanic domain, increasing the model width to 4000 km. The number of finite elements was increased accordingly to keep the same mesh resolution. (a-d) Material colors (see Fig. 1 with isotherms (550 °C, 1330 °C, 1500 °C) and streamlines scaled in thickness to velocity. t is model time, Δx_{oc} and Δx_{cont} are the amounts of oceanic and continental convergence. Insets contain zoom with additional isotherm at 350 °C. The white overlay highlights strain-weakened shear zones. Model evolution, onset and progression of deformation and final lithospheric structure are very similar to M3 and M4. This shows that overriding plate shortening in M3 and M4 is not induced by approaching the left model boundary.

Paper II

Growth of collisional orogens from small and cold to large and hot - inferences from geodynamic models

Sebastian G. Wolf[1], Ritske S. Huismans[1], Josep-Anton Muñoz[2], Magdalena Ellis Curry[3,4], Peter van der Beek[3,5]

[1] Department of Earth Science, University of Bergen, Bergen, Norway.
[2] Geomodels Research Institute, University of Barcelona, Barcelona, Spain.
[3] Université Grenoble Alps, CNRS, ISTerre, CS40700, 38058 Grenoble Cedex.
[4] Department of Earth and Atmospheric Sciences, University of Houston, 77004 Texas, United States of America
[5] Insitut für Geowissenschaften, Universität Potsdam, 14476 Potsdam, Germany

Growth of collisional orogens from small and cold to large and hot - inferences from geodynamic models

Sebastian G. Wolf[1], Ritske S. Huismans[1], Josep-Anton Muñoz[2], Magdalena Ellis Curry[3,4], Peter van der Beek[3,5]

[1]Department of Earth Science, Bergen University, Bergen N-5007, Norway
[2]Geomodels Research Institute, University of Barcelona, Barcelona, Spain
[3]Université Grenoble Alps, CNRS, ISTerre, CS40700, 38058 Grenoble, France
[4]Department of Earth and Atmospheric Sciences, University of Houston, 77004 Texas, United States of America
[5]Insitut für Geowissenschaften, Universität Potsdam, 14476 Potsdam, Germany

Key Points:

- Coupled thermo-mechanical-surface-process models are used to investigate orogenic growth from small and cold to large and hot
- Models give insight into typical shortening distribution and structural style of growing mountain belts
- Comparison to Pyrenees, Alps and Himalaya-Tibet, highlights key similarities and differences between models and natural examples

Corresponding author: Sebastian G. Wolf, `sebastian.wolf@uib.no`

Abstract

It is well documented that the interplay between crustal thickening and surface processes determines growth of continent-continent collision orogens from small and cold to large and hot. Additionally, studies have demonstrated that the structural style of a mountain belt is strongly influenced by inherited (extensional) structures, the pattern of erosion and deposition, as well as the distribution of shallow detachment horizons. However, the factors controlling distribution of shortening and variable structural style as a function of convergence and surface process efficiency remain less explored. We use a 2D upper-mantle scale plane-strain thermo-mechanical model (Fantom) coupled to a planform, mass conserving surface-process model (Fastscape), to investigate the long-term evolution of mountain belts and the influence of lithospheric pull, extensional inheritance, surface processes efficiency, and decoupling between thin-and thick-skinned tectonics. We establish an evolutionary shortening distribution for orogenic growth from a mono-vergent wedge to an orogenic plateau, and find that internal crustal loading is the main factor controlling the large scale evolution, while lithospheric pull modulates the plate driving force for orogenesis. Limited foreland-basin filling and minor exhumation of the orogen core are characteristic for low surface-process efficiency, while thick foreland-basin fill, and profound exhumation of the orogen core are characteristic for high surface-process efficiency. Utilizing a force balance analysis, we show how inherited structures, surface processes, and decoupling between thin-and thick-skinned deformation influence structural style during orogenic growth. Finally, we present a comparison of our generic modeling results with natural systems, with a particular focus on the Pyrenees, Alps and Himalaya.

1 Introduction

Continent-continent collision creates mountain belts that grow in size with increasing amounts of plate convergence. Orogenic temperature is directly related to the amount of crustal thickening by horizontal shortening, as heat producing elements are concentrated in upper and middle crustal rocks (e.g. Hacker et al., 2015). Crustal heating, in turn, has a weakening effect on crustal rheology and controls regional metamorphism; influencing mountain-belt structure and deformation. During orogenic growth, surface processes shape mountain-belt topography, fill the evolving foreland basins and exhume metamorphic rocks. In the end-member case, erosion may even fully balance orogenic growth, creating a flux steady state between tectonics and erosion (Willett & Brandon, 2002; Stolar et al., 2007). Beaumont et al. (2006) propose a temperature-magnitude relationship for orogenic growth from small and cold to large and hot, in analogy to the Hertzsprung-Russel diagram of stellar classification. The temperature-magnitude diagram, however, does not explain whether there is a characteristic distribution of shortening and structural style (e.g. thin- and thick-skinned deformation, thrusting style) as a function of orogen size, and its controlling factors. In this study, we use thermo-mechanical models that are fully coupled to a landscape-evolution model, to investigate the first-order factors controlling the distribution of shortening and the different structural styles related to orogenic growth from small and cold to large and hot during continent-continent collision.

A typical example of a small and cold orogen is the Pyrenean mountain belt, which grew by inversion of a rift system with additional crustal shortening and plate convergence of at most 165 km (Muñoz, 1992; Beaumont et al., 2000). The Alps, an intermediate size orogen, have a more complex history, that includes subduction, Ultra-High-Pressure (UHP)-rock exhumation, passive margin inversion and terrane accretion preceding continent-continent collision. Crustal shortening is difficult to estimate and variable along strike but certainly exceeds 150 km in the west-central part (Schmid et al., 1996; Schmid & Kissling, 2000; Schmid et al., 2017). The only modern large and hot, continent-continent collision system with an orogenic plateau

is the Himalayan-Tibetan orogen. This mountain belt is characterised by a hot, and viscously weak middle crust on top of a flat Moho, and formed in its recent state by collision between India and Eurasia with post-collision convergence estimated to be larger than 2000 km (Negredo et al., 2007). Continent-continent collision was preceded by oceanic subduction and accretion of small continental masses at the Asian margin, which today are partly underlain by metasomatised or highly thinned lithospheric mantle (Owens & Zandt, 1997; Chung et al., 2005).

These three examples show that continent-continent collision is often preceded by passive margin inversion, subduction of oceanic lithosphere, and/or terrane accretion. Hence, continent-continent collision of plates with normal crustal thickness is typically preceded by a heterogeneous shortening phase, which includes inversion of inherited structures. Despite their differences, the three type-examples presented above have important first order similarities: The Pyrenees, Alps, and Himalayas have thin-skinned foreland fold-thrust belts, fed partly by syn-contractional sediments, which are detaching in weak décollement horizons (Muñoz, 1992; Sommaruga, 1999; DeCelles et al., 2001; Robinson, 2008). Furthermore, crustal material detaches on top of the lower crust to form thick-skinned thrust sheets, and the lithospheric mantle and lower crust of one plate subduct into the underlying upper mantle. This separates the down-going pro-plate from the overriding retro-plate at a mantle singularity, also termed "S-point" (Willett et al., 1993). During continent-continent collision, the pull exerted by the subducting pro-lithosphere is dependent on its degree of chemical depletion (Griffin et al., 1998; Poudjom Djomani et al., 2001), and can be augmented by the pull of an oceanic slab, in cases in which it remains attached to the downgoing continental lithospheric mantle. Slab pull, developing from subducting oceanic lithosphere, provides a first-order control on plate movement on Earth (Forsyth & Uyeda, 1975). Similarly, the pull of the subducting lithospheric mantle during continent-continent collision has the potential to strongly influence the tectonic forces required to drive plate convergence and thus orogeny (Cloos, 1993; Becker & Faccenna, 2011; Capitanio et al., 2010). However, no studies have yet specifically investigated the influence of lithospheric pull on structure, deformation, and the resulting tectonic forces in growing mountain belts.

Subduction of the lithospheric mantle motivated early crustal-scale numerical models with a kinematically controlled velocity discontinuity (S-point) (Willett et al., 1993; Willett & Beaumont, 1994; Beaumont et al., 1994; Braun & Beaumont, 1995; Beaumont et al., 1999, 2001; Vanderhaeghe et al., 2003; Beaumont et al., 2006). These models investigated, amongst others, how much the subducting pro-plate respectively the overlying retro-plate contribute to crustal thickening (Willett et al., 1993; Willett & Beaumont, 1994; Willett, 1999; Ellis & Beaumont, 1999; Beaumont et al., 1999; Vanderhaeghe et al., 2003). They showed that there can be different modes of pro-and retro-wedge deformation, elegantly described in terms of the PURCE framework (P,R = Pro-,Retro-side, U=uplifted plug, C= subduction channel, E = elevated plateau, Beaumont et al., 1999; Jamieson & Beaumont, 2013). More specifically, already the earliest S-point models showed a characteristic deformation pattern involving pro-and retro-side crust and movement of the orogen onto the retro-side as function of orogen size (Willett & Beaumont, 1994; Beaumont et al., 1994; Willett, 1999). In contrast, the next generation of upper-mantle scale numerical models with self-consistent lithospheric subduction showed that a weak overriding plate might be prerequisite for retro-plate deformation (J. P. Butler et al., 2011), or that extensional inheritance might be the main factor controlling retro-plate deformation during continent-continent collision (Erdős et al., 2014). The discrepancy between results obtained with different modelling methods and setups indicates that the factors controlling pro-and retro-wedge deformation in growing continent-continent collision orogens are not fully understood and require explanation.

It has long been shown that there is a strong feedback between surface processes and tectonics, where high erosional efficiency can lead to a steady state between tectonic material influx and erosional outflux of material (Beaumont et al., 1992; Willett, 1999; Beaumont et al., 2001; Willett & Brandon, 2002; Stolar et al., 2007; Hilley et al., 2004; Whipple & Meade, 2004, 2006). Understanding the interplay between surface processes and tectonics has historically been approached from either a surface-process perspective (e.g. Whipple & Tucker, 1999; Hilley et al., 2004; Whipple & Meade, 2004; Stolar et al., 2007), assuming simplified deformation and omitting deposition, or from a tectonic perspective, using simplified surface processes (e.g. Beaumont et al., 2001; Erdős et al., 2014, 2015; Grool et al., 2019). New surface-process algorithms (Braun & Willett, 2013; Yuan et al., 2019) and high resolution thermo-mechanical tectonic models (Thieulot, 2011; Erdős et al., 2014; Andrews & Billen, 2009; Ueda et al., 2015; Ruh et al., 2017) facilitate the first investigations into the full coupling between landscape evolution, erosion, sedimentation and tectonics. This advancement not only bridges the gap between surface processes and tectonics, but also permits investigation into the interaction between thin- and thick-skinned deformation during orogenic growth, which previously has been investigated separately (e.g. Stockmal et al., 2007; Fillon et al., 2013).

Here, we investigate whether there is a common relationship between mountain-belt size, distribution of deformation, and structural style in terms of thin- vs thick-skinned deformation, thrust spacing, influence of inherited weaknesses, and consequences of surface processes, and are particularly driven to understand the underlying physical controls. To that end we use high-resolution 2D thermo-mechanical forward models coupled to a 2D, mass-conserving surface process model and investigate the influences of slab pull, extensional inheritance, surface-process efficiency, and decoupling of the foreland-fold-thrust belts on the growth of continent-continent collision orogens from small and cold to large and hot. To find key similarities and differences between our modelling results and mountain belts on Earth, we compare model inferences with the three orogens introduced above: the Pyrenees, Alps, and Himalayan-Tibetan orogen.

2 Methodology

2.1 Model design

We use the thermo-mechanically coupled 2D finite element code FANTOM to model mountain building (Thieulot, 2011; Wolf & Huismans, 2019, see Appendix A1, A2). The initial model geometry represents a 1200 km wide and 600 km deep, idealised, crustal and upper mantle cross-section (Fig. 1, Table 1). It consists of a laterally uniform continental lithosphere with 35 km thick crust, 85 km thick lithospheric mantle, and sub-lithospheric upper mantle down to the lower model boundary. Crustal material is subdivided into pre-deformation sedimentary rocks on top of a mechanically weak horizon acting as a future décollement for thin-skinned thrusts (from here on referred to as décollement horizon), followed by upper- and mid-crust to 25 km depth, and lower crust to 35 km depth. All materials have the same frictional-plastic parameters affected by strain weakening, apart from the décollement below the pre-deformation sedimentary rocks. The latter is represented by an effective angle of internal friction $\phi_{eff} = 2°$ and cohesion $C = 4$ MPa, which corresponds to fully strain weakened material. This layer allows for the evolution of a thin-skinned fold-thrust belt. In model M7 (see table 2) we test the influence of a very weak décollement horizon with fixed viscosity of 1×10^{19} Pa s, mimicking a salt layer at shallow depth. The terms thin-skinned and thick-skinned deformation are used throughout the manuscript to describe whether thrusts originate in the weak décollement horizon or in the viscous middle crust.
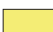
a) Model Setup

b) Materials

Figure 1. Model setup with boundary conditions (a) and material properties (b). (a) The model is 1200 km wide, 600 km deep, and has a uniform distribution of materials. Mountain building is modelled by applying an inward velocity of 0.5 cm/yr in the lithosphere on both model sides. Inflow is balanced by a small distributed outflow in the sub-lithospheric domain. Extension is modelled by reversing the velocity boundary conditions. The upper surface is free and the side and bottom boundaries have free-slip boundary conditions. The initial temperature profile of the continent corresponds to 1D-thermal steady state and the underlying mantle has an adiabatic gradient of $0.4\,°C\,km^{-1}$. The side boundaries are insulated and the bottom boundary has a fixed temperature boundary condition of $1522\,°C$. The inserts show a zoom of the continental lithosphere with the corresponding initial yield-strength envelope computed with $\dot{\epsilon} = 1 \times 10^{-15}\,s^{-1}$. Our model materials also account for strain weakening by linearly reducing the effective angle of internal friction and cohesion as a function of strain. (b) Material description shows colour, scaled flow law, and density of model materials. WQtz is the wet quartz flow law as described in Gleason and Tullis (1995), DMD is the dry Maryland flow law from Mackwell et al. (1998), and wet Ol is the wet olivine flow law from Karato and Wu (1993). The density of the lithospheric mantle is varied in Models M1 to M3.

Table 1.   Mechanical and thermal properties of the materials.

Parameters	Sedimentary rocks	Décollement horizon	Upper & middle crust	Lower crust	Mantle lithosphere	Sub-lithospheric mantle
Plastic rheology						
C - C_{sw}[a] (MPa)	20-4	4-4	20-4	20-4	20-4	20-4
ϕ_{eff} - $\phi_{eff,sw}$[a] (°)	15-2	2-2	15-2	15-2	15-2	15-2
Viscous rheology						
Flow law[b]	WQtz	WQtz	WQtz	DMD	WOl	WOl
f	1	1	1	1	5	1
A $(\mathrm{Pa\,s}^{1/n})$[c]	8.57×10^{-28}	8.57×10^{-28}	8.57×10^{-28}	5.78×10^{-27}	1.76×10^{-14}	1.76×10^{-14}
n	4.0	4.0	4.0	4.7	3.0	3.0
Q $(\mathrm{kJ\ mol}^{-1})$	223	223	223	485	430	430
V $(\mathrm{cm}^3\,\mathrm{mol}^{-1})$	0	0	0	0	0	10×10^{-6}
Density						
ρ_0 $(\mathrm{kg\,m}^{-3})$[d]	2800	2300	2800	2990	3380/ 3360/ 3340 (depleted)	3380
α (K^{-1})	3×10^{-5}	3×10^{-5}	3×10^{-5}	3×10^{-5}	3×10^{-5}	3×10^{-5}
Thermal						
k $(\mathrm{W\,m}^{-1}\,\mathrm{K}^{-1})$[e]	2.25	2.25	2.25	2.25	2.25	2.25
H $(\mathrm{\mu W\ m}^{-3})$	1.15	1.15	1.15	0.5	0	0
c_p $(\mathrm{J\,kg}^{-1}\,\mathrm{K})$[f]	804	987	804	762	682	1250

[a] C and ϕ_{eff} are linearly affected by strain weakening within the plastic strain interval [0.1, 1.1]
[b] WQtz is the wet quartz flow law as described in Gleason and Tullis (1995); DMD is the dry Maryland flow law from Mackwell et al. (1998); WOl is the wet olivine flow law from Karato and Wu (1993).
[c] The laboratory derived pre-exponential flow law constant has been converted to conform with the second invariants of the stress and strain rates used in the model approach.
[d] Metamorphic high pressure equivalent. The P-T-field for the metamorphic reaction coincides with the eclogite stability field from Hacker (1996).
[e] Thermal conductivity for low temperatures. Between 1335 °C and 1345 °C the conductivity linearly increases from 2.25 to 52.0 $\mathrm{W\,m}^{-1}\,\mathrm{K}^{-1}$, to mimic active mantle convection at high Nusselt number, keep the adiabatic gradient and prevent the system from cooling.
[f] c_p is scaled to give initial uniform diffusivity of $1 \times 10^{-6}\,\mathrm{m}^2/\mathrm{s}$.

Viscous flow of upper and mid crustal materials follows a wet quartz flow law (Gleason & Tullis, 1995), and the lower crust is represented by a dry Maryland diabase flow law (Mackwell et al., 1998). Lithospheric mantle is based on a wet Olivine flow law (Karato & Wu, 1993), scaled by a factor $f = 5$ to represent dry- and melt-depleted conditions, and the sub-lithospheric mantle follows the wet Olivine flow law scaled by $f = 1$. Lithospheric mantle density depends on its degree of chemical depletion. Typical Phanerozoic mantle is 20 to $30\,\mathrm{kg\,m^{-3}}$ less dense, and Proterozoic mantle is typically $50\,\mathrm{kg\,m^{-3}}$ less dense than primitive mantle (Griffin et al., 1998; Poudjom Djomani et al., 2001). Depletion related density decrease of the lithospheric mantle has a strong effect on lithospheric pull and is explored in Models 1 to 3 (see table 2).

The thermal setup reflects average values (see Table 1), with a Moho temperature of $550\,^\circ\mathrm{C}$ and $1330\,^\circ\mathrm{C}$ at the base of the lithosphere, resulting in a surface heat flow of $53\,\mathrm{mW\,m^{-2}}$ and heat flux in the sublithospheric mantle of $20.8\,\mathrm{mW\,m^{-2}}$ (Hacker et al., 2015).

The resulting rheological setup generates a viscous decoupling horizon on top of the lower crust, and coupling of the lower crust with the lithospheric mantle. This is motivated by the Pyrenees, Alps and Himalayas which are all characterized by a viscous decoupling horizon in the middle crust and subduction of the lower crust along with the lithospheric mantle (Muñoz, 1992; Schmid et al., 1996; Replumaz et al., 2010; Gao et al., 2016).

The models include an irreversible metamorphic phase change of the strong, mafic lower continental crust at UHP-conditions, when entering the eclogite field specified in the phase diagram of Hacker (1996). For simplicity, the metamorphic equivalent has the same rheology and density as lithospheric mantle. The metamorphosed lower crust is also affected by viscous strain weakening by reducing the scaling factor f by up to 0.01 in the predefined viscous strain ($\epsilon_{viscous}$) interval $0.1 < \epsilon_{viscous} < 1.1$. Viscous weakening is not active at temperatures higher than $1000\,^\circ\mathrm{C}$. Viscous weakening ensures proper decoupling between the downgoing and overriding plate during the initial convergence phase, and mimics a slightly weaker plate suture zone originating for instance from preceding subduction or passive margin inversion.

Orogenesis and pre-collisional rifting are modelled by applying velocity boundary conditions of $0.5\,\mathrm{cm/yr}$, at the model sides (see Fig. 1). To localise deformation, we place a strain weakened seed in the lower crust in the model centre.

The tectonic model is fully coupled to the surface process model Fastscape (Braun & Willett, 2013; Yuan et al., 2019), which computes stream-power law erosion, hill-slope diffusion and continental deposition (see section A.3). The effects of surface processes are investigated in models 5 to 7, and supplementary models SM5 and SM6. Denudation in fluvial landscapes is largely set by the efficiency of fluvial erosion, here modelled using a variation of the stream-power law. We chose typical values for the various coefficients of the extended stream-power law (Whipple & Tucker, 1999; Yuan et al., 2019), with $K_c = 1 \times 10^{-2}\,\mathrm{m^2/yr}$, $G = 1$, $m = 0.4$, $n = 1$. Fluvial erosion is strongly dependent on the fluvial erodibility K_f, which incorporates variations as a function of rock type, climate, vegetation, and erosive agents (Stock & Montgomery, 1999; Braun, 2006; Cowie et al., 2008). Given $m = 0.4$, $n = 1$, typical values of K_f lie between $1 \times 10^{-6}\,\mathrm{m^{0.2}/yr}$ to $1 \times 10^{-4}\,\mathrm{m^{0.2}/yr}$ (Stock & Montgomery, 1999). We test the effects of surface process efficiency on mountain growth with two end-member models with $K_f = 0.5 \times 10^{-5}\,\mathrm{m^{0.2}/yr}$ and $K_f = 5 \times 10^{-5}\,\mathrm{m^{0.2}/yr}$, respectively. For simplicity, deposited sediments have the same nominal density and rheological properties as upper crust. The relatively high sediment density slightly overestimates sedimentary loading, but is considered sufficient. Furthermore, we do not focus on the

Table 2. Parameter variations in the models presented. Models 2-6 are different from the reference model M1 in one parameter, model 7 is different from model 5 in one parameter. $\Delta\rho_{0,m}$ is the density difference between sub-lithospheric and lithospheric mantle at surface temperature.

Model nr.	Model name	Test Parameter	Parameter Value	Explanation
M1	MRef	-	$\Delta\rho_{0,m} = 0\,\mathrm{kg\,m^{-3}}$	Shows influence of pulling slab; Reference model
M2	M20kg	ρ_0 of lithospheric mantle	$\Delta\rho_{0,m} = 20\,\mathrm{kg\,m^{-3}}$	Shows influence of neutrally buoyant slab
M3	M40kg	ρ_0 of lithospheric mantle	$\Delta\rho_{0,m} = 40\,\mathrm{kg\,m^{-3}}$	Shows influence of positively buoyant slab
M4	MExt	Boundary condition	150km extension before convergence	Shows influence of pre-orogenic extension
M5	MSpLow	Low surface process efficiency	$K_f = 0.5 \times 10^{-5}\,\mathrm{m^{0.2}/yr}$	Shows influence of low surface process efficiency
M6	MSpHigh	high surface process efficiency	$K_f = 5 \times 10^{-5}\,\mathrm{m^{0.2}/yr}$	Shows influence of high surface process efficiency
M7	MSpDéc	Low surface process efficiency + weak décollement	$K_f = 0.5 \times 10^{-5}\,\mathrm{m^{0.2}/yr}$, $\eta_{décollement} = 1 \times 10^{19}\,\mathrm{Pa\,s}$	Shows influence of decoupling between thick and thin-skinned tectonics
Supplementary models				
SM1	SMleft	velocity b.c. only on left side	$v_{left} = 1\,\mathrm{cm/yr}$, $v_{right} = 0\,\mathrm{cm/yr}$	Shows that model evolution is independent of absolute plate movement
SM2	SMright	velocity b.c only on right side	$v_{left} = 0\,\mathrm{cm/yr}$, $v_{right} = 1\,\mathrm{cm/yr}$	Shows that model evolution is independent of absolute plate movement
SM3	SMvel3	convergence velocity	$v_{left} = v_{right} = 1.5\,\mathrm{cm/yr}$	Shows influence of high convergence velocity on plateau formation
SM4	SMhighH	Crustal radioactive heat production	$H_{UC,MC} = 1.63\,\mathrm{\mu W}$ $\mathrm{m^{-3}}$, $H_{LC} = 0$	Shows influence of high radioactive heat production in upper & middle crust
SM5	SMSpMed	Medium surface process efficiency	$K_f = 1 \times 10^{-5}\,\mathrm{m^{0.2}/yr}$	Shows influence of moderately high surface process efficiency
SM6	MSpVeryHigh	very high surface process efficiency	$K_f = 7.5 \times 10^{-5}\,\mathrm{m^{0.2}/yr}$	Shows influence of very high surface process efficiency

highly dynamic evolution of the landscape on top of the mountain belt, but rather investigate the large scale effects of surface processes on mountain belt formation.

2.2 Parameter Variations in the Models Presented

With a set of 7 models (table 2) we test the effects of depleted lithospheric mantle (M1, M2, M3), and thus slab pull, extensional inheritance (M4), surface process efficiency (M5, M6), and surface processes with a weak salt décollement (M7) on the evolution of an orogen from small and cold to large and hot. In models M1, M2, and M3 we monitor the pull exerted by the subducting lithospheric mantle and the tectonic boundary force in the lithosphere at the model boundaries (see section A4). The latter give insight into the force balance required to drive mountain belt growth. Animations of each model and the Fastscape-model plots of M5 to M7 can be found in the supplementary material. The supplement also contains six additional models testing boundary condition kinematics, convergence velocity, crustal heat production, and medium respectively very high surface process efficiency (table 2).
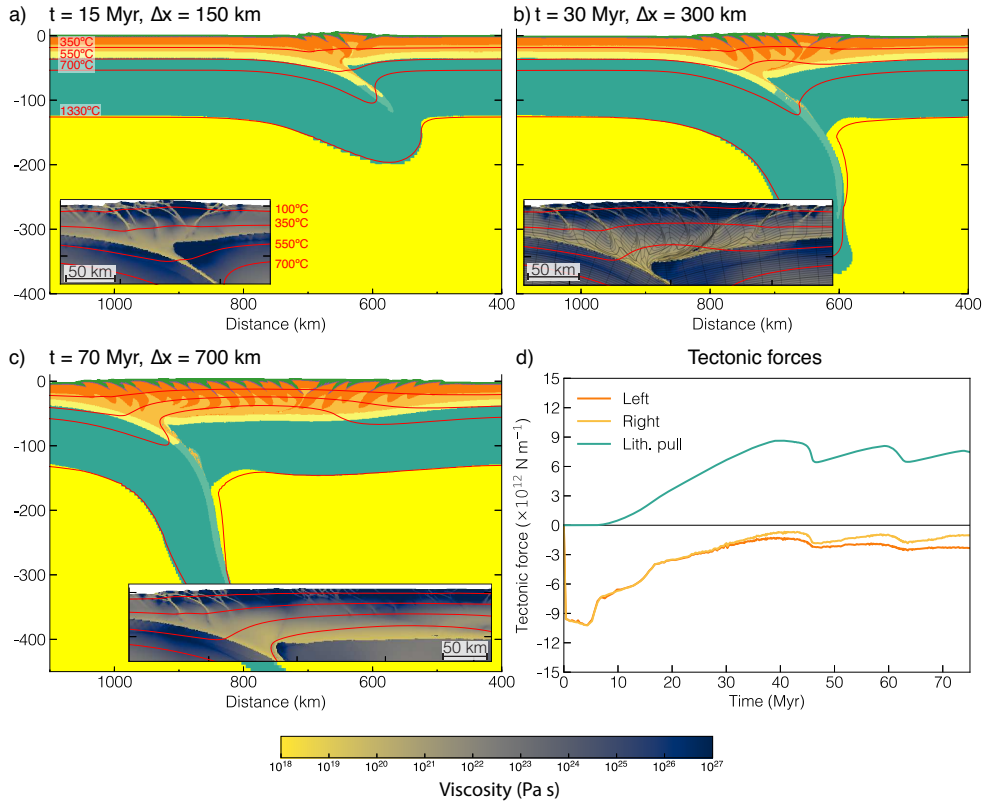
M1 (MRef): Reference model, No depletion of lithospheric mantle

Figure 2. Reference model M1 (MRef) without depletion of the lithospheric mantle. (a-c) Material colors (see Fig. 1) with isotherms. t is model time, Δx is the amount of convergence. The zoom insets show the viscosity field with logarithmic colormap and temperature isotherms. The viscosity inset in b) also shows a grey grid passively tracking deformation. (d) Tectonic forces (integrated horizontal deviatoric stresses) at the left and right boundaries. Negative values are compressional. Additionally, the integrated pull (positive value is pull) exerted by the subducting lithospheric slab is shown as green line. See supplementary material for a model animation (MS01).

3 Results

3.1 Reference model M1 (MRef): No depletion of lithospheric mantle

Convergence initiates deformation at the weak seed, forming a triangular uplifted plug. Subsequent shortening produces thick-skinned thrust sheets on the pro-side, and the pro-side lithospheric mantle and lower crust start to subduct (Fig. 2a). Subduction deflects the Moho isotherm downwards, leading to a cold and small orogen. Ongoing convergence results in more pro-side shortening, and formation of a first crustal retro-side thrust sheet. At the same time, the strong retro-lithosphere bends downwards and the orogen starts to 1) heat up and 2) migrate onto the retro-lithosphere (Fig. 2b). Further orogenic shortening forms thrust sheets on the pro-and retro-sides, and the orogen translates onto the indenting retro-lower crust and mantle. Translation of pro-side thrust sheets onto the retro-side creates inclined to recumbent folds facing to the retro-wedge and flat lying foliation on top of the lower crust (Fig. 2b, viscosity inset). Radioactive heating of thickened crustal material lowers the middle crustal viscosity and the retro-Moho starts to become horizontal after 500 km of convergence, when the viscously weak crust has reached a temperature of $\sim 700\,^\circ$C. Onset of retro-Moho flattening coincides to first order with formation of a plateau on the retro-side (Fig. 2c). Once deformation starts on the retro-wedge, i.e. after >150 km of convergence, shortening is distributed into 60 % pro-wedge and 40 % retro-wedge deformation; the pro-wedge grows in width by $\sim$5 km/Myr and the retro-wedge by $\sim$3.3 km/Myr.

The model evolution is reflected in the evolution of the tectonic boundary forces (see Methods section for computation of forces). The pull exerted by the subducting lithospheric mantle increases up to $9 \times 10^{12}\,\mathrm{N\,m^{-1}}$. Simultaneously, the compressional tectonic force at the left and right boundary decreases from $9 \times 10^{12}\,\mathrm{N\,m^{-1}}$ to $\sim 2 \times 10^{12}\,\mathrm{N\,m^{-1}}$. Two drops in lithospheric pull and tectonic forces after $\sim$45 Myr and $\sim$65 Myr are caused by two drips of the subducting lithospheric mantle (see supplementary video MS1). Supplementary models SM1 (MRef_Right) and SM2 (MRef_Left) with full velocity boundary conditions applied only on the right and left side, respectively, show that model evolution is independent of the direction of plate movement (supplementary Fig. S1). A supplementary model with higher upper- and middle-crustal heat production (SM4, SMhighH) shows retro-Moho-flattening and thus plateau formation after less convergence and with a lower crustal thickness, and a supplementary model with high convergence velocity (SM3, SMvel3) shows plateau formation after greater amounts of convergence and with a thicker crust (supplementary Fig. S2).
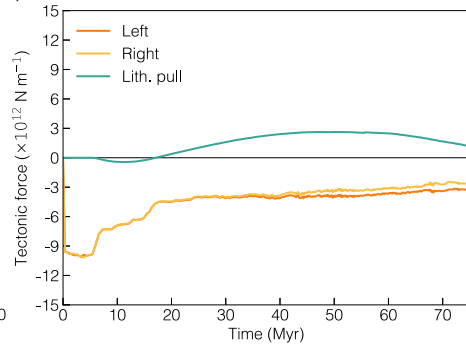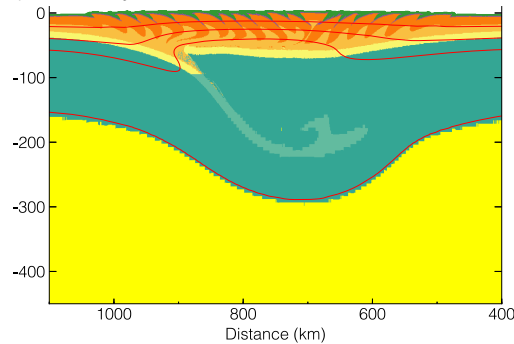
3.2 Models M2 and M3: Depleted lithospheric mantle

Models M2 (M20kg, Fig. 3a, b) and M3 (M40kg, Fig. 3c, d) with $20\,\mathrm{kg\,m^{-3}}$ and $40\,\mathrm{kg\,m^{-3}}$ nominal depletion, respectively, show a very similar crustal evolution as the reference model. Shortening initially creates thrust sheets only on the pro-side. After more than 150 km of convergence, retro-shortening starts, the orogen moves onto the retro-plate, and shortening is distributed into 60 % pro-wedge and 40 % retro-wedge deformation.

The influence of lithospheric depletion can be seen in the deep structure. In M2 the cold subducting lithosphere is initially negatively buoyant and subducts. Conductive heating leads to late upward bending of the subducting lithosphere (Fig. 3a). The subducting lithospheric mantle exerts a small pull of maximum $\sim 3 \times 10^{12}\,\mathrm{N\,m^{-1}}$ and the compressional tectonic forces at the side are on average at $\sim 4 \times 10^{12}\,\mathrm{N\,m^{-1}}$ (Fig. 3b). In M3 the downgoing lithospheric mantle and lower crust are always positively buoyant and thrust under the overlying mantle (Fig. 3c). The buoyancy force exerted by the resulting lithospheric slab increases steadily up to $\sim$10 $\times 10^{12}\,\mathrm{N\,m^{-1}}$ and the compressional tectonic boundary forces are in the order of $\sim 6 \times 10^{12}\,\mathrm{N\,m^{-1}}$.

M2 (M20kg): 20 kg/m³ depletion of lithospheric mantle
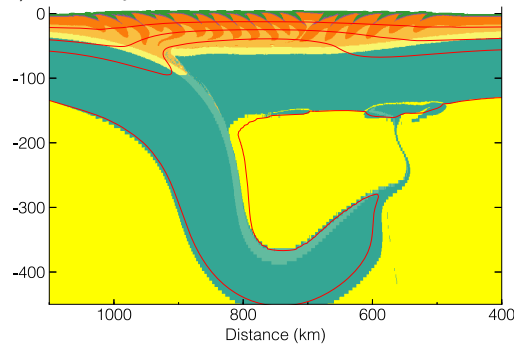
M3 (M40kg): 40 kg/m³ depletion of lithospheric mantle
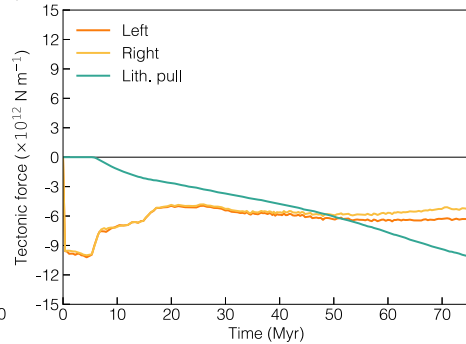
Figure 3. Models M2 (M20kg, a, b) and M3 (M40kg, c, d) with respectively $20 \, \mathrm{kg \, m^{-3}}$ and $40 \, \mathrm{kg \, m^{-3}}$ depletion of the lithospheric mantle. (a, c) Material colors (see Fig. 1) with isotherms ($350 \, °\mathrm{C}$, $550 \, °\mathrm{C}$, $700 \, °\mathrm{C}$, $1330 \, °\mathrm{C}$). t is model time, Δx is the amount of convergence. Snapshots are flipped left-right (see x-axis) to simplify comparison with the other models. (b, d) Tectonic forces (integrated horizontal deviatoric stresses) at the left and right boundaries. Negative values are compressional. The integrated pull exerted by the subducting lithospheric slab is shown as green line. Positive values represent overall pull and negative values overall push. See supplementary material for model animations (MS02, MS03).

3.3 Model 4 (MExt): No lithospheric depletion, with extensional inheritance

Model M4 has the same setup as model M1, but convergence is preceded by 150 km of extension. Extension creates an asymmetric margin that is almost fully broken up, with several extensional blocks on the right side and a narrow extensional domain on the left side (Fig. 4a). Inversion of the passive margin re-activates the weak extensional structures and creates a structurally complex central plug. Inversion also traps small fragments of exhumed lithospheric and upper mantle in the uplifted plug (Fig. 4b).

The subsequent model evolution is similar to the reference model, with creation of thrust sheets mainly on the pro-side, before onset of retro-side thrusting and migration of the mountain belt onto the retro side. The uplifted plug composed of weak extensional structures leads to earlier loading of the retro-side and simultaneously delays formation of thick-skinned thrust sheets on the retro-side (Fig. 4c, d).

3.4 Model 5 (MSpLow): No lithospheric depletion, with low surface process efficiency

Model M5 (MSpLow) has the same setup as model M1 (MRef), and additionally includes surface processes with spatially and temporally uniform values (Fig. 5, supplementary Fig. S3 for corresponding Fastscape snapshots). Fluvial erodibility $K_f = 0.5 \times 10^{-5} \, \mathrm{m}^{0.2}/\mathrm{yr}$, which leads to low surface process efficiency.

The crustal evolution is again similar to the reference model with initial thrusting on the pro-side, before retro-thrusting starts and the orogen migrates onto the overlying plate (Fig. 5). Growing topography leads to increased erosion and sedimentation, which fills the evolving foreland basin. New thick-skinned thrusts progressively capture the filled foreland basins and transport them into the mountain belt, where the sediments get re-eroded. During the first 30 Myrs both evolving foreland basins are underfilled, while between 35 - 50 Myrs, foreland basin filling and capture by new thrusts occur roughly on the same time-scale (Fig. 6a). The recycling of sediments deposited in the foreland into the orogen leads to no net-loss of material by erosion during the first ∼50 Myr. With ongoing orogenic growth, erosion outpaces deposition and orogenic crustal accretion is delayed by on average ∼15 %. Consequently, mountain width is similar to M1 during the first ∼50 Myr, and slightly but consistently lower during the consecutive 25 Myrs (Fig. 6c). The crustal thrust sheets become slightly wider with increasing sedimentation, most pronounced on the retro-side (Fig. 5b, c). Some thin-skinned thrust sheets form in the foreland basins, detaching in the frictional décollement layer (Fig. 5b, c). Erosion slowly exhumes the thrust sheets in the centre of the mountain belt.

A supplementary model with medium fluvial erodibility $K_f = 1 \times 10^{-5} \, \mathrm{m}^{0.2}/\mathrm{yr}$ (see supplementary Fig. S6 & S7) shows a similar evolution. However, already after ∼30 Myr erosion is more effective than deposition, and the subsequent orogenic growth is delayed on average by 30 % to 40 % (Fig. 6c).

3.5 Model 6 (MSpHigh): No lithospheric depletion, with high surface process efficiency

Model M6 (MSpHigh) has the same setup as M5 (MSpLow), but includes highly efficient surface processes with a fluvial erodibility $K_f = 5 \times 10^{-5} \, \mathrm{m}^{0.2}/\mathrm{yr}$.

Initial shortening creates an uplifted plug, and pro-side thrust sheets similar to the reference model. Erosion is very efficient already during the early stages of orogenic growth, leading to overfilled foreland basins, which are especially thick on the pro-side
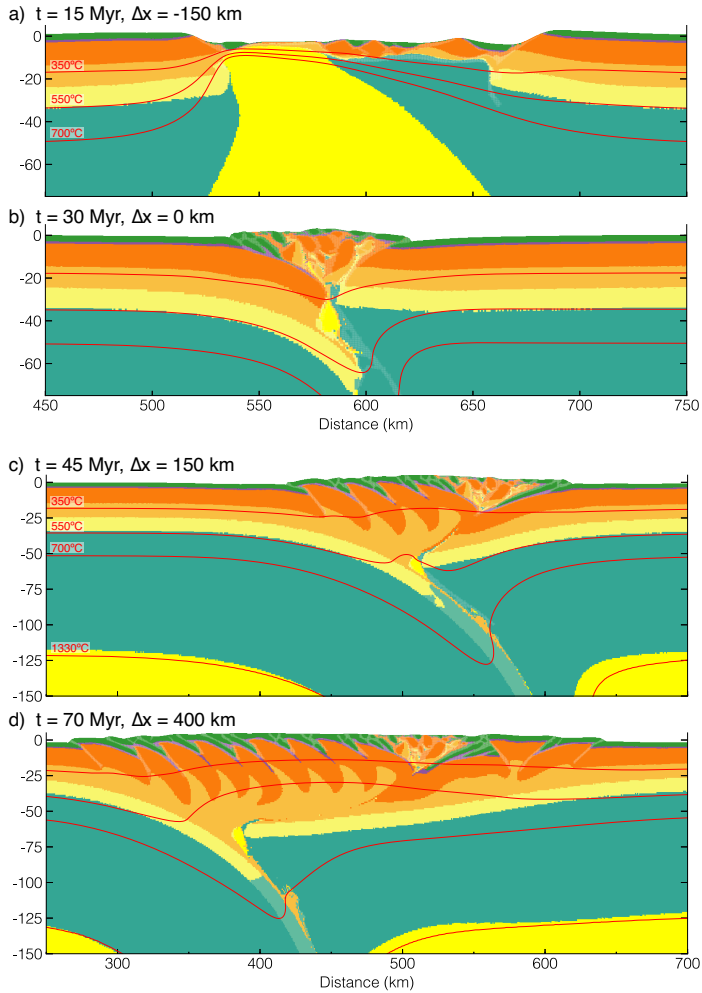
M4 (MExt): No depletion, extension before shortening

a) t = 15 Myr, Δx = -150 km

b) t = 30 Myr, Δx = 0 km

c) t = 45 Myr, Δx = 150 km

d) t = 70 Myr, Δx = 400 km

Figure 4. Model M4 (MExt) without depletion of the lithospheric mantle but with 150 km of extensional inheritance. (a-d) Material colors (see Fig. 1) with isotherms. t is model time, Δx is the amount of convergence. The white, transparent overlay highlights strain-weakened shear zones.
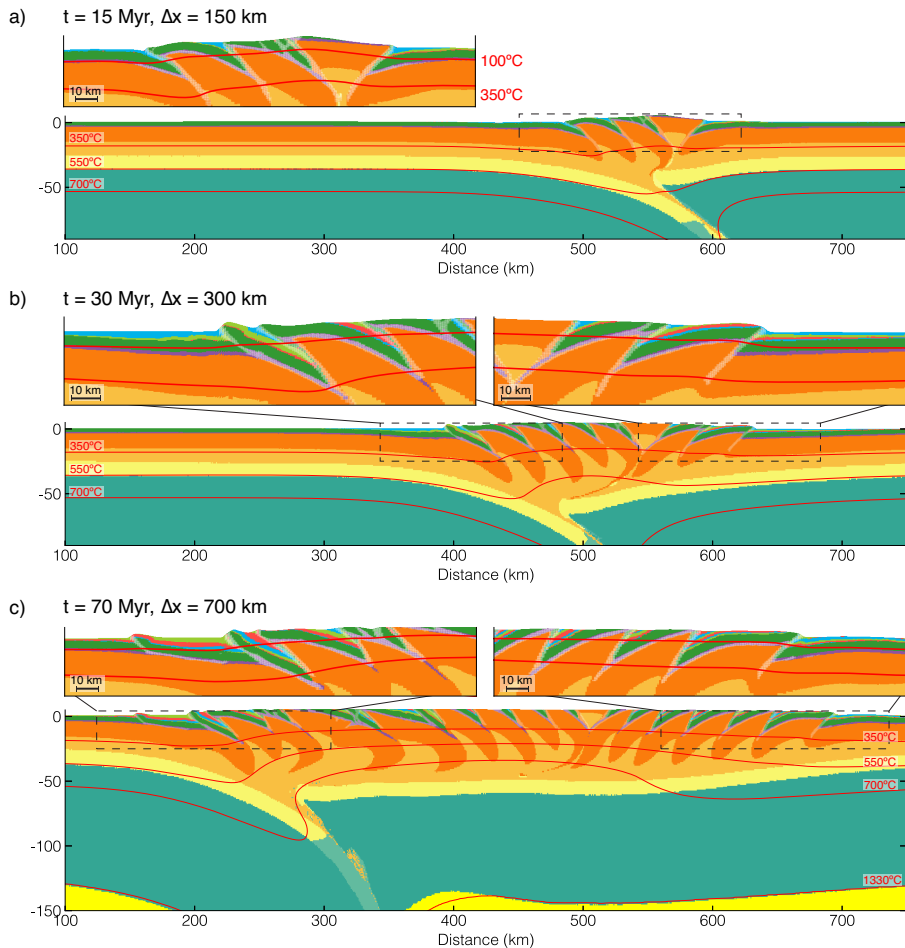
M5: No depletion, with surface processes, low surface process efficiency

a)   t = 15 Myr, Δx = 150 km

b)   t = 30 Myr, Δx = 300 km

c)   t = 70 Myr, Δx = 700 km

Figure 5.   Model M5 (MSpLow) without depletion of the lithospheric mantle, including a full coupling with surface processes. Surface process efficiency is medium, with K_f = $0.5 \times 10^{-5}\,\mathrm{m}^{0.2}/\mathrm{yr}$. (a-c) Material colors (see Fig. 1) with isotherms. t is model time, Δx is the amount of convergence. Zoom insets show close-up of crustal domains. The white, transparent overlay highlights strain-weakened shear zones. Note the small thin-skinned foreland fold-thrust belt on pro- (and retro-) side, detaching in the décollement horizon (purple). Corresponding Fastscape surfaces can be found in supplementary Fig. S3.
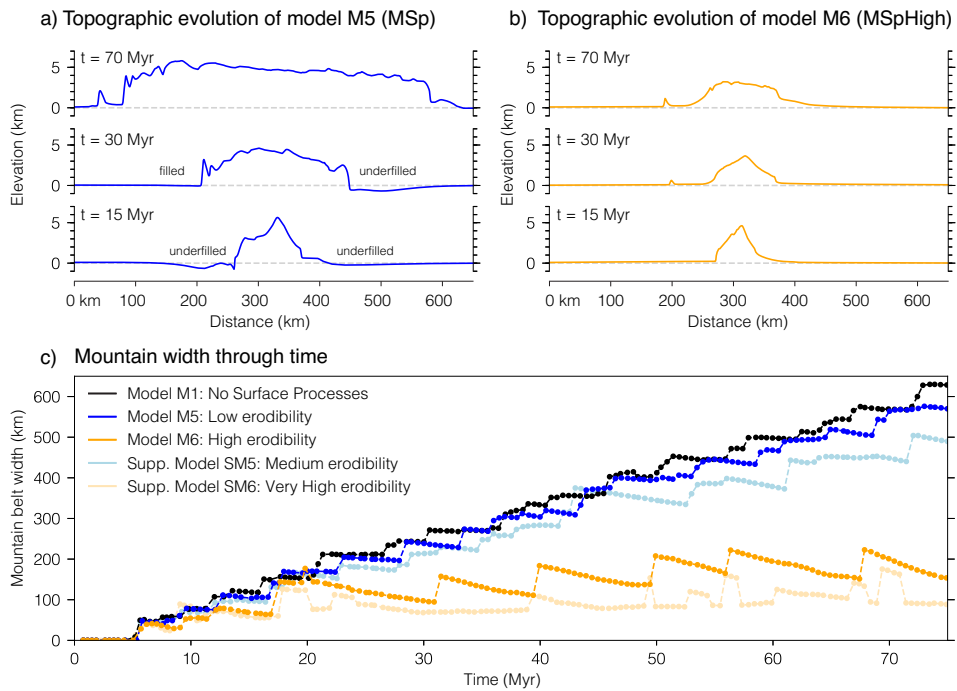
Figure 6. (a, b) Topographic evolution of models MSpLow and MSpHigh. c) Plot of mountain width through time. The mountain width is calculated every 0.5 Myrs between the two outermost points which are above 1000 m. Steps in width correspond to new outward-propagating thrusts.

M6: No depletion, with surface processes, high surface process efficiency

a)   t = 15 Myr, Δx = 150 km
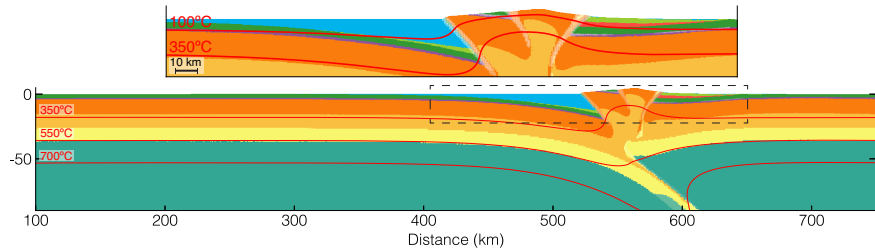
b)   t = 30 Myr, Δx = 300 km
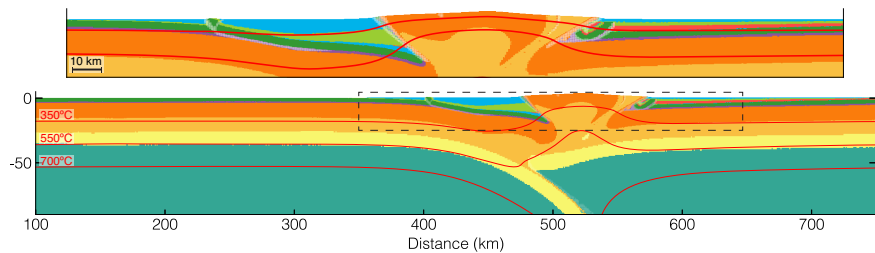
c)   t = 70 Myr, Δx = 700 km
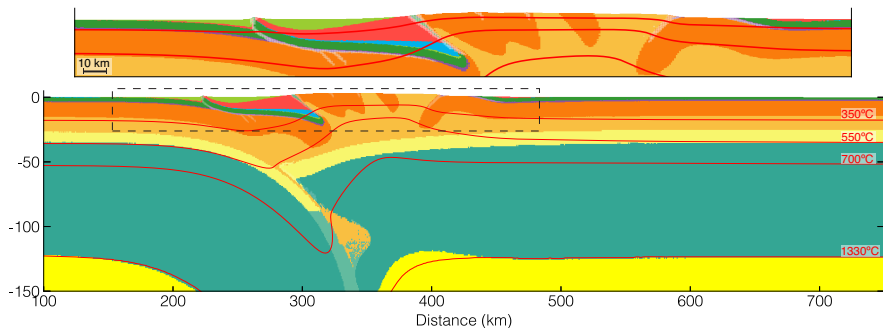
Figure 7. Model M6 (MSpHigh) without depletion of the lithospheric mantle, including a full coupling with surface processes. Surface process efficiency is high, with $K_f \;=\; 5 \times 10^{-5}\,\mathrm{m}^{0.2}/\mathrm{yr}$ (a-c) Material colors (see Fig. 1) with isotherms. t is model time, Δx is the amount of convergence. Zoom insets show close-up of crustal domains. The white, transparent overlay highlights strain-weakened shear zones. Note the thin-skinned foreland fold-thrust belt on pro- (and retro-) side, detaching in the décollement horizon (purple). Corresponding Fastscape surfaces can be found in supplementary Fig. S4.

(Fig. 7, Fig. 6b). During the whole model evolution, thick-skinned thrusts only form on the pro-side apart from one retro-thrust sheet forming after ~ 20 Myr. Thrusts capture the filled foreland basins and form thick-skinned thrust sheets. Thrust sheets have a similar size as in the reference model (M1) during the first 15 Myr of model evolution, and are wider once they capture the thick, filled foreland basins (Fig. 7a, b). Some decoupling between thin-and thick-skinned deformation can be observed, especially once the foreland basins are thick (Fig. 7b, c). Efficient erosion exhumes the thrust sheets in the core of the mountain belt, which advects the temperature field and creates a high geothermal gradient at the surface. The life-span of thick-skinned thrust sheets between formation, transport into the orogen core and erosion is typically 20 Myr. Erosion almost balances crustal accretion so that the orogen only grows several 10s of km in width during the last 50 Myr of model evolution (Fig. 6b, c). Throughout the model run, the retro-side lower crust and lithospheric mantle slowly thrust under the orogen and the mountain belt migrates onto the retro-side (Fig. 7c).

Supplementary model SM6, with very high fluvial erodibility $K_f = 7.5 \times 10^{-5}\,\mathrm{m}^{0.2}/\mathrm{yr}$ shows that an even higher surface process efficiency leads to a steady state between erosion and tectonic accretion (supplementary Fig. S8 & S9, Fig. 7c). Crustal evolution in the supplementary model is similar to M6 (MSpHigh), with thrust sheets forming primarily on the retro-side, thick foreland basins, and slow underthrusting of the lower retro-lithosphere.

3.6 Model 7 (MSpDéc): No lithospheric depletion, with surface processes, with weak salt décollement

Model M7 (MSpDéc) has the same setup as model M5 with low surface process efficiency, but a much weaker décollement horizon with constant viscosity of $1 \times 10^{19}\,\mathrm{Pa\,s}$ (Fig. 8, supplementary Fig. S5 for corresponding Fastscape snapshots). The model is 500 km wider than the others to prevent interaction of the evolving foreland fold-thrust belt with the side boundaries. The numerical resolution is kept constant by increasing the amount of finite elements.

The large-scale crustal evolution is again similar to the reference model with initial thrusting on the pro-side, before retro-thrusting starts and the orogen migrates onto the overlying plate. The weak décollement effectively decouples the thick-and thin-skinned deformation in the mountain belt and thin-skinned foreland fold-thrust belts develop in both foreland basins. During the first 150 km of convergence, the syn-deformation sediment supply is limited and many small thin-skinned thrust sheets form on the pro-side and in the centre of the orogen (Fig. 8a). With increased shortening, the topography grows and the sediment supply increases. Large and long thin-skinned thrust sheets form on the pro-side and also the retro-foreland basin deforms. The thick-skinned thrust sheets in the centre of the orogen have a shallower dip than those in Models 1 - 6 (Fig. 8b). With further shortening the pro-side foreland fold-thrust belt forms new thrust sheets, shortens internally, and becomes thicker. Newly forming thick-skinned thrusts do not break the foreland belt, but come up in the back of the foreland belt and form an antiformal duplex stack (Fig. 8c). The retro-side foreland fold-thrust belt records less shortening than the pro-side.

4 Discussion

We present a suite of geodynamic numerical models that investigate the influence of slab pull, extensional inheritance, surface processes, and a weak décollement horizon on mountain-belt growth from small and cold to large and hot. In the following sections we will first discuss the influence of each of these tested factors on the distribution of deformation and structural style during growth. Subsequently, we derive a simple force-balance analysis, which quantifies thrust formation and the interaction between
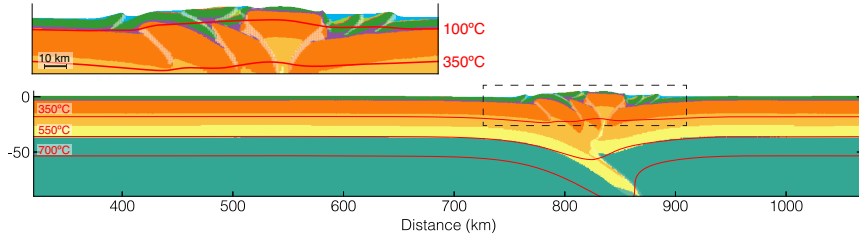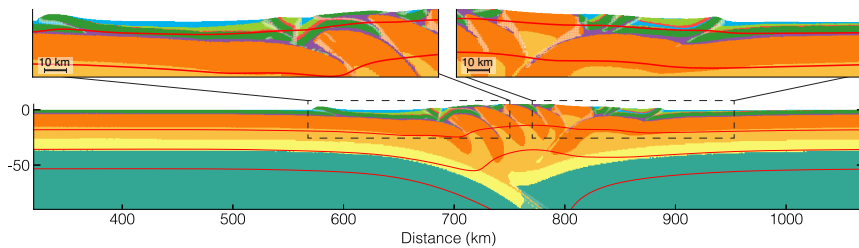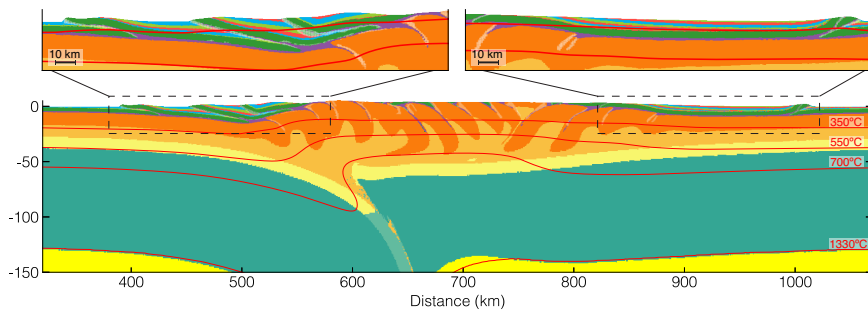
M7: No depletion, with surface processes, with weak décollement

a)   t = 15 Myr, Δx = 150 km

b)   t = 30 Myr, Δx = 300 km

c)   t = 60 Myr, Δx = 600 km

Figure 8. Model M7 (MSpDéc) without depletion of the lithospheric mantle, including a full coupling with surface processes and with a weak salt décollement with fixed viscosity of 1×10^{19} Pa s. (a-c) Material colors (see Fig. 1) with isotherms. t is model time, Δx is the amount of convergence. Zoom insets show close-up of crustal domains. The white, transparent overlay highlights strain-weakened shear zones. Note the thin-skinned foreland fold-thrust belts on pro- and retro-side, detaching in the very weak décollement horizon (purple). Corresponding Fastscape surfaces can be found in supplementary Fig. S5.

thin-and thick-skinned deformation, followed by a section addressing model limitations and a comparison to previous modelling studies.

4.1 Distribution of shortening as a function of orogen size

All models shown here exhibit a similar distribution of crustal shortening that develops as a function of orogen size (Fig 9). In models without surface processes, orogen size is a function of plate convergence. Since erosion counteracts orogenic growth, different stages of orogen evolution are most accurately described as a function of cross-sectional area (CA = plate convergence times crustal decoupling depth minus erosion):

If the orogen is small and cold, continent-continent collision creates a structurally mono-vergent wedge consisting of the uplifted plug (U) and several pro-side thrust sheets (P). The retro-lithosphere acts as an indenter and does not form thrust sheets (Fig. 9b). The cross-sectional area (CA) is lower than $3.75 \times 10^9 \, \text{m}^2$, corresponding to at most 150 km of convergence in M1. Increased shortening leads to loading of the retro-plate, heating of the orogen, and retro-wedge (R) deformation, forming a transitional orogen defined by a structurally bi-vergent wedge (Fig. 9c). With ongoing convergence, the strong retro-lithosphere thrusts under the pro-wedge, which results in tight, overturned folds with flat-lying foliation on top of the lower crust (Fig. 9d). A central, elevated plateau with a flat Moho, characteristic for a large, hot orogen, forms once $CA > 12.5 \times 10^9 \, \text{m}^2$, equivalent to $> 500 \, \text{km}$ of convergence in reference model M1. Under-thrusting of the retro-side lithosphere and steady evolution of crustal shortening and thickening highlights the decoupled evolution of crust and mantle in large and hot orogens. Convergence is partitioned to $60\,\%$ pro- and $40\,\%$ retro-side deformation after onset of retro-wedge shortening ($\Delta x > 150 \, \text{km}$ in M1). Supplementary figure S10 shows the distribution of shortening as a function of convergence in M1.

We identify several aspects that naturally develop in our models and are needed for the characteristic evolution presented above (Fig. 9a): A pro-and retro-step-up shear zone (Willett et al., 1993), a mantle singularity (S-point), and a viscous decoupling horizon in the crust. All of those aspects can be inferred in the Pyrenees, Alps and Himalayas, and we will compare the shortening distribution and other features with those orogens below. However, as will become apparent in the comparison to the Himalayan-Tibetan orogen, if any of the four primary controlling factors is altered in a mountain belt on Earth, the orogen will develop differently, which in turn gives important insight into the peculiarities of this mountain belt. The importance and existence of the retro-step-up shear zone is discussed below.

We define the onset of plateau formation with flattening of the retro-side Moho. A horizontal Moho implies that the radioactively heated, weak viscous base of the upper crust does not support and flows laterally under applied pressure gradients. The onset of plateau formation is dependent on viscous weakening resulting from crustal thickening and associated radioactive heating, and has a thermal equilibration timescale independent of convergence rate. The difference between convergence rate and the time scale of thermal equilibration explains delayed plateau formation in the supplementary model with high convergence velocity (SMvel3). This model furthermore highlights that the convergence and cross-sectional area values for onset of plateau formation given above are a rough guideline and not unique for plateau formation on Earth.

4.1.1 The influence of lithospheric depletion

Models M1 to M3 show the influence of depletion-related lithospheric density changes and thus pull of the subducting lower lithosphere on mountain-belt growth.
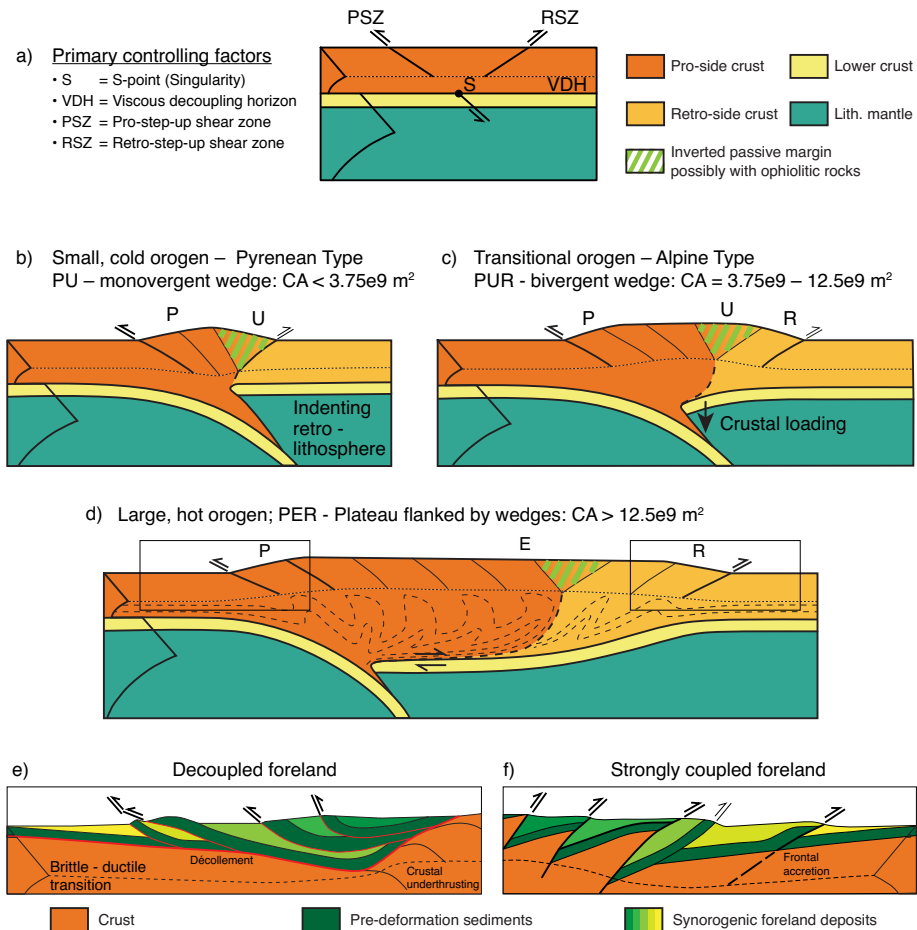
Figure 9. Distribution of shortening during mountain building from small and cold to large and hot. a) Given the existence of a viscous decoupling horizon in the mid or lower crust and a pro- and retro-side thrust and mantle singularity, a mountain belt is expected to develop in the following manner: b) Initial inversion of inherited structures forms an uplifted plug (U) and deformation on the pro-side (P). The retro-side is acting as indenter. c) Ongoing shortening loads the retro-plate and the retro-side shortens (R). The retro-side lithosphere starts to thrust under the central part of the orogen, which creates tight, inclined to recumbent folds with flat-lying foliation on top of the lower crust. It is worth noting that the vergence of these deep folds is the opposite with respect to the upper crustal ones (d). Further shortening is distributed into 60 % on the pro-side and 40 % on the retro-side. Ongoing horizontal shortening and crustal radioactive heating creates an orogenic plateau with a flat Moho (E). e,f) Show the differences in structural style related to (de-)coupling of thin-and thick-skinned deformation.

The three models have a similar crustal evolution in common despite a negatively (M1) or positively (M3) buoyant lithospheric mantle, which shows that orogenic growth and in particular the onset of retro-side shortening are largely independent of the negative or positive buoyancy of the subducting lower lithosphere, and solely a function of internal crustal loading. However, high lithospheric pull leads to low absolute tectonic boundary forces at the model sides, in the order of or less than ridge push ($\sim 3 \times 10^{12}\,\mathrm{N\,m^{-1}}$, Turcotte & Schubert, 1982). The low tectonic forces show that in nature orogeny can occur at relatively low plate-driving forces, in the order of ridge push, in case of an un-depleted lithospheric mantle or an oceanic slab that is still attached to the subducting continental lithosphere. In contrast, orogenesis involving a refractory depleted mantle lithosphere requires significantly higher plate driving forces exceeding ridge push.

4.1.2 The effects of extensional inheritance

Extension creates structural weaknesses that are reactivated during the inversion phase and form the central, uplifted plug. Inversion can incorporate mantle materials, exhumed to shallow depth during rifting, into the uplifted plug. Passive-margin inversion can be more complicated than shown in the models presented here, with large mantle blocks remaining in the upper crust as for instance seen in the Alpine Ivrea zone and possibly in the Pyrenean Labourd anomaly.

The idea that passive margins are the locus of deformation during continent-continent collision has long been proposed and is a fundamental part of the Wilson cycle (Wilson, 1966). Furthermore, it has been shown since the 1980s that the structural style and locus of deformation in many mountain belts, amongst others the Pyrenees, Alps, Andes, and Himalayan-Tibetan orogen, are controlled by inherited rifts that pre-date shortening but become inverted and part of the orogen, as modelled in M4 (MExt) (Gillcrist et al., 1987; Cooper & Williams, 1989; Muñoz, 1992; Beaumont et al., 2001; Amilibia et al., 2008; Kapp & DeCelles, 2019; Grier et al., 1991; Carrera et al., 2006; Iaffa et al., 2011). These observations corroborate model inferences that rifts will be the locus of deformation once boundary conditions change and show that the monotonous structural style of thick-skinned thrusts in our models is not expected to be equally observed in nature. Rather, pre-existing extensional structures or any form of inherited weaknesses (e.g. Carrera & Muñoz, 2013; R. W. H. Butler et al., 2006) may control the position of new outward propagating thrusts.

Above we showed a characteristic shortening distribution as a function of orogenic growth and explain that it requires a pro-and retro-step-up shear zone. Given that orogens on Earth typically have an initial phase of reactivation of inherited extensional faults or other types of weaknesses, it is also expected that orogens form both a pro- and a retro-step-up shear zone, thus potentially following the evolution of growth shown above. Removing the retro-shear zone has a profound effect on mountain-belt growth, as it does not allow retro-wedge loading and thus propagation of deformation onto the retro-wedge. This behaviour is commonly observed in thermo-mechanical models that start with an inclined weak seed (Liao & Gerya, 2017), or subduction before collision (J. P. Butler et al., 2011), when weak inherited structures are not included in the model setup.

4.1.3 The effects of surface processes

We tested the effects of surface processes on the evolution of orogen growth from small to large with two end-member models with respectively low and high surface-process efficiency. Erosion leads to exhumation of the central part of the orogen. Deposition of sediments in the foreland basin, subsequent recycling by thick-skinned thrusting and re-erosion in the core of the orogen buffers the effect of erosion. Once

foreland basin filling is faster than creation of accommodation space through tectonics, i.e. once sediments bypass the foreland basin, orogenic growth will be slowed down. With low surface process efficiency, this transition occurs once the orogen has accumulated a cross-sectional area equivalent to 300 to 500 km of horizontal convergence in our models. If surface-process efficiency is high, the transition is reached once the initial uplifted plug has created significant topography, within few Myrs after the onset of shortening. High surface-process efficiency can create a steady state between tectonic material influx and erosional outflow. At (near-)steady state, the orogen remains in its growth phase (e.g., Fig. 9), i.e. in case it is small, as in M6 (MSpHigh), it will keep producing thrust sheets mainly from the pro-side. Near-steady state during growth is characterized by strong metamorphic gradients of rocks exhumed to the surface and a high geothermal gradient at the surface. In contrast, orogenic growth far from steady state is characterized by little exhumation in the core of the mountain belt, with possible preservation of syn- or pre-orogenic sedimentary deposits.

High erosion rates in the core of the mountain belt are reflected in thick foreland basin fill, most pronounced on the pro-side, which induces longer upper-crustal thrust sheets. This behaviour can be best seen in the supplementary model with medium fluvial erodibility, leading to high sedimentation rates once the orogen is large and hot (supplementary Fig. S6 & S7). The impact of deposition and erosion on the structural style of a mountain belt is further discussed in the force-balance section below.

The efficiency of surface processes should be assessed relative to the rate of surface uplift U (eq. A6), which in turn depends on the plate convergence rate. Therefore, the K_f values that we classify as leading to "low" or "high" surface process efficiency only apply if the convergence rate is 1 cm/yr, as used in our models. Lower convergence rates will have a similar effect as higher K_f, and vice versa.

4.1.4 The influence of a weak, shallow décollement

A weak décollement creates efficient decoupling between thick-skinned and thin-skinned structures. Furthermore, the combination of décollement strength and amount of syn-tectonic sediment determines the length of thin-skinned thrust sheets (Stockmal et al., 2007; Erdős et al., 2015; Fillon et al., 2013). Work-minimisation favors long thrust sheets in case of abundant syn-tectonic sediments and a weak décollement, and vice versa (see section below). The evolving thin-skinned foreland fold-thrust belt also has a feedback on thick-skinned tectonics. A large thin-skinned belt detaching in a weak layer, as seen in M6 (Fig. 8c), is not incorporated by new thick-skinned thrust sheets. Rather, it slides forward during shortening and new thick-skinned thrusts come up in the hinterland, forming an antiformal duplex stack and leading to exhumation of basement rocks. Hence, a weak décollement horizon in combination with syn-tectonic sediments has a strong structural feedback on the mountain belt (Fig. 9e), but does not alter the general distribution of shortening.

4.2 Dynamic analysis of thick- and thin-skinned thrust formation

We next quantify thrust formation during orogenic widening and the resulting variable structural styles using simple force-balance considerations. Orogenic growth is often explained using critical-wedge theory (Davis et al., 1983; Dahlen, 1984). However, critical-wedge theory does not account for viscous deformation, localized shear and strain-weakening of thrusts, and is hence not well suited to understand the dynamic evolution of deformation observed in our models. The dynamic analysis of thrust formation requires quantifying three types of forces: a) the integrated strength, F_{int} required to deform parts of the lithospheric column, b) the integrated viscous resistance of horizontal shear in different domains of the crust, F_V, and c) the buoyancy force related to the topographic potential of the orogen, F_B. First, we will derive the
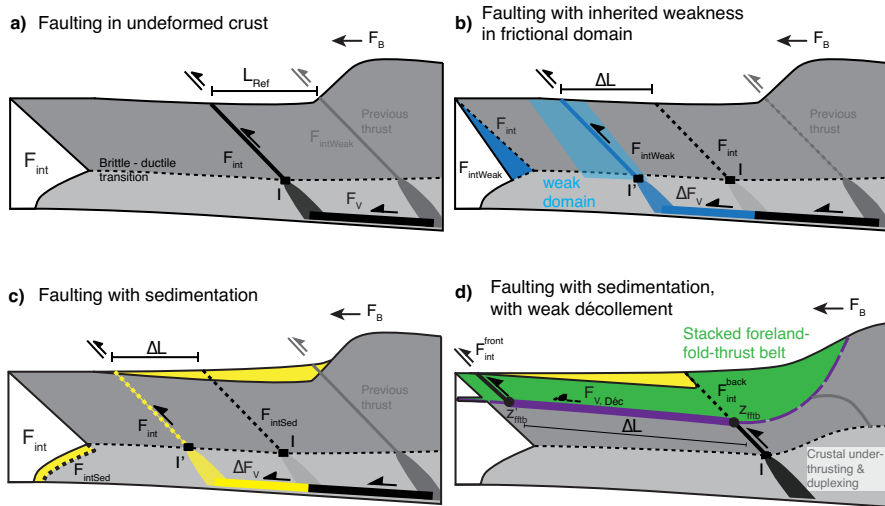
Figure 10.   Theoretical cross sections through a mountain front with force considerations for different scenarios of lateral orogenic growth. Once the buoyancy force related to crustal thickening (F_B) exceeds the integrated strength of the crust (F_{int}), i.e. once outward growth is energetically more favourable than an increase in elevation, a new outward propagating thrust forms. a) In the theoretical case of a homogeneous crust, new thrusts originate in I with constant thrust spacing of L_{Ref}. b) Weak inherited structures will be re-activated if favoured by the net force balance, increasing the potential thrust spacing by ΔL and possibly influencing the structural style of the mountain belt. c) Sedimentation fills the evolving foreland basin and leads to strengthening of the crust if sedimentation rates are high. This leads to longer thick-skinned thrust sheets, as work minimisation favours deformation of the crust further out in the basin. d) If the crust contains a décollement layer (purple), the foreland fold-thrust belt can become decoupled from the thick-skinned deformation of the crust. Decoupling is favoured if the décollement is weak and if the foreland-fold-thrust belt is thick through internal stacking or sediment loading.

typical reference thrust spacing (L_{Ref}) in our models, then investigate modifications to the reference thrust spacing and structural style as a function of inherited weaknesses, sedimentation and foreland decoupling (Fig. 10).

Surface uplift through crustal thickening raises the topographic potential energy, which results in a horizontal force per meter orogen (F_B) that the mountain belt exerts onto its foreland. If this force equals the integrated strength F_{int} and overpressure P_o of the foreland, where $F_{int} \approx P_o$, i.e. if outward growth is energetically more favourable than continued surface uplift, a new outward propagating thrust forms and the orogen grows in width (Fig. 10a, Molnar & Lyon-Caen, 1988; Sandiford & Powell, 1990; Zhou & Sandiford, 1992; Schmalholz et al., 2014). More specifically, and assuming efficient decoupling between crust and mantle lithosphere, outward propagating thrusting requires deformation of the un-weakened upper-and middle crust (F_{int}) and viscous shear in the middle crust (F_V), which is balanced with F_B and continued slip on a strain-weakened shear zone in the orogen with strength $F_{intWeak}$ (Fig. 10a):

$$F_{int} + F_V = F_{intWeak} + 0.5 * F_B. \tag{1}$$

F_{int} of pristine model-crust is approximately $1.7 \times 10^{12} \, \mathrm{N\,m^{-1}}$ and strain-weakened crust has an integrated strength $F_{intWeak}$ of $\sim 0.4 \times 10^{12} \, \mathrm{N\,m^{-1}}$, given a typical strain-rate $\dot{\epsilon} = 1 \times 10^{-14} \, \mathrm{s^{-1}}$. As discussed above, $0.5 * F_B$ is roughly equal to F_{int} (Molnar & Lyon-Caen, 1988; Schmalholz et al., 2014). $F_V = L_{Ref} 2\eta\dot{\epsilon}$, where L_{Ref} is the reference thrust spacing and η middle crustal viscosity. Taking typical model values of $\eta = 1 \times 10^{21} - 2 \times 10^{21} \, \mathrm{Pa\,s}$, $\dot{\epsilon} = 2 \times 10^{-15} - 1 \times 10^{-14} \, \mathrm{s^{-1}}$ gives $L_{Ref} = 10 \, \mathrm{km}$ to $100 \, \mathrm{km}$. Our models without surface processes develop a steady, homogeneous pattern of thick-skinned thrust sheets with a horizontal thrust spacing L_{Ref} of 30 to 50 km (Fig. 2 - 4), which fits well with our simple predictions (Fig. 10a). In the following three paragraphs we will investigate how inherited weaknesses, sedimentation, and a weak décollement horizon modify L_{Ref} and influence the structural style of orogenic growth.

Assuming force balance, localisation in a weak domain at location I' is favoured over localisation at the reference location I (Fig. 10b) if:

$$F_{intWeak} + \Delta F_V \leq F_{int}, \tag{2}$$

where F_{int} and $F_{intWeak}$ are the integrated strengths at I and I', respectively, and ΔF_V is the force required to shear the viscous domain between I and I'. Given that $\Delta F_V = \Delta L 2\eta\dot{\epsilon}$, using typical model values (Fig. 2), $\dot{\epsilon} = 1 \times 10^{-14} \, \mathrm{s^{-1}}$, $\eta = 2 \times 10^{21} \, \mathrm{Pa\,s}$, and assuming a frictionally weak domain (Fig. 10b) with strength equal to fully strain-weakened crust, results in a maximum thrust length increase $\Delta L = 32.5 \, \mathrm{km}$. ΔL and L_{Ref} are therefore approximately equally large.

A similar relationship holds for the effect of sedimentation, as derived by Erdős et al. (2015). Sedimentation increases the strength of the crustal column above I and it is favourable to increase thrust sheet length (Fig. 10c), if

$$F_{int} + \Delta F_V \leq F_{intSed}. \tag{3}$$

Using the same values for viscosity and strain rate as used above, $\Delta L = 20 \, \mathrm{km}$ for 5 km of syn-deformational sediments (Erdős et al., 2015), showing that the effect of sedimentation is potentially equally important as the effect of inherited weaknesses. However, the calculation does not account for conductive and radioactive heating during deposition, which explains why thrust sheet lengthening is less pronounced in model MSpLow than in SMSpMed. Thrust sheet lengthening as a function of foreland basin fill relies on the supply of sediment, which increases with surface process efficiency and mountain belt size.

We show in model MSpDéc that a weak décollement horizon together with syntectonic sedimentation has a strong structural feedback on orogen style (Fig. 9e,f). This

585   can be readily understood by looking at the force balance of thrust formation with
586   a weak décollement horizon (Fig. 10d). In this case, thick-skinned thrusts will origi-
587   nate at the reference location I, creating a shear zone between I and the décollement
588   horizon at z_{fftb}. Furthermore, if

$$F_{int}^{front} + F_{V,Déc} \leq F_{int}^{back}, \tag{4}$$

590   faulting will localise in the décollement horizon and the frontal thrust shown in (Fig. 10d).
591   Here, F_{int}^{front} and F_{int}^{back} are the integrated strengths of the frictional domain between
592   the surface and the décollement at depth z'_{fftb} and z_{fftb}, respectively, and $F_{V,Déc}$ is
593   the force required to shear the décollement, which can thus also be expressed as:

$$\int_{surface}^{z'_{fftb}} (P \cdot \sin(\phi_{eff}) + C \cdot \cos(\phi_{eff}))\, dz + \Delta L 2\eta\dot{\epsilon} \leq \int_{surface}^{z_{fftb}} (P \cdot \sin(\phi_{eff}) + C \cdot \cos(\phi_{eff}))\, dz. \tag{5}$$

595   Assuming lithostatic pressure, a negligible slope in the foreland fold-thrust belt, and
596   a linear viscous décollement we can compute maximum ΔL analytically from eq. 5,
597   with:

$$\Delta L \leq \frac{\left(0.5\rho g z^2 \sin(\phi_{eff}) + Cz\cos(\phi_{eff})\right)\Big|_{z'_{fftb}}^{z_{fftb}}}{2\eta\dot{\epsilon}}, \tag{6}$$

599   see Methods section and table 1 for parameter definitions and values. Assuming values
600   motivated from model MSpDéc, thin-skinned thrusting would capture a 1 km thick sed-
601   imentary wedge of up to $\Delta L = 223$ km length. If the wedge is smaller, the thin-skinned
602   fault will localise at the pinch-out of the sediments, as is the case in model MSpDéc
603   (Fig. 8). Equation 6 shows that ΔL linearly decreases with décollement viscosity
604   and strain rate, and super-linearly increases with overburden thickness ($z'_{fftb} - z_{fftb}$).
605   Therefore, decoupling between thin-and thick-skinned deformation is favoured if the
606   décollement is weak or the overburden thick, e.g. through stacking of multiple thin-
607   skinned thrust sheets or abundant syn-tectonic sedimentation. A frictionally weak
608   décollement with $\phi_{eff} = 2°$, as used in all models but MSpDéc, is commonly too
609   strong to create efficient decoupling between thin-and thick-skinned tectonics. We
610   only observe efficient decoupling in model MSpHigh and once foreland filling creates a
611   thick foreland basin fill (Fig. 7c, b), which is readily explained by the above relation-
612   ship.

613   Our models and force balance analysis predict a) a reference thrust sheet length
614   L_{Ref}, b) thrust sheet lengthening (ΔL) as a function of sedimentation and inherited
615   weaknesses, and c) decoupling of the foreland-fold-thrust belt and antiformal duplexing
616   of thick-skinned thrust sheets in the hinterland of the foreland belt. L_{Ref} and ΔL are
617   in the same order of magnitude and increase if the crust has a weaker rheology. Our
618   quantification explains why the structural style in many mountain belts on Earth
619   is strongly influenced by inherited weaknesses, sedimentation and weak decoupling
620   horizons. The force balance is a simplified approximation of complex and non-linear
621   model behaviour. In nature, we expect that a combination of the different presented
622   factors influences mountain belt style.

4.3 Model limitations

624   Our models are a simplified representation of nature and there are several pro-
625   cesses that are not accounted for, notably the effect of varying crustal rheology, pre-
626   collisional subduction, mantle delamination, and spatially variable surface processes
627   linked to, for instance, orographic effects.

628   We do not investigate the influence of varying crustal rheology. Jammes and
629   Huismans (2012) investigated the influence of crustal rheology in a similar setup to
630   ours. They show that a weaker upper and middle crust enhances crustal decoupling,

favours outward propagation of structures, promotes retro-wedge loading and accelerates orogenic plateau formation. A stronger upper and middle crust promotes opposing behaviour. Many modern orogens, including the Alps, Pyrenees, and Himalaya, are characterized by a rheologically strong lower crust and a detachment level in the middle crust, as used here (Muñoz, 1992; Schmid et al., 1996; Replumaz et al., 2010; Gao et al., 2016). Thus, our rheological model setup is probably to first order representative for these orogenic systems. Liao and Gerya (2017); Liao et al. (2018); Vogt et al. (2018); Huangfu et al. (2018) show that lateral crustal strength contrasts have a strong influence on the distribution of deformation. Lateral variability in crustal rheology can be invoked if the simple distribution of shortening shown here cannot explain the distribution of shortening in a natural mountain belt (see discussion in comparison to nature section).

Our models do not include full lithospheric break-up with ocean formation, followed by lithospheric cooling, and inversion starting with oceanic subduction. Subduction deflects the temperature field downwards in the vicinity of the subduction zone (J. P. Butler et al., 2013; Wolf & Huismans, 2019), which allows for a transitional phase of continental subduction, UHP rock formation, heating and exhumation. This early collision phase may create a bigger central, uplifted plug than in our models, as shown by J. P. Butler et al. (2013). Also, deflection of the temperature field by pre-collisional subduction might temporarily induce a stronger, indenting retro-side, which delays progression of deformation onto the retro-orogen (J. P. Butler et al., 2013). This early collision phase will therefore affect early orogenic structure, but is not expected to change the distribution of shortening during later orogenic growth significantly.

We also do not investigate the influence of a weak or removed upper plate lithospheric mantle. Hyndman et al. (2005) and Currie et al. (2008) show that subduction zones often have a weak and thinned back-arc lithospheric mantle, which seems to be required for back-arc deformation to occur (Wolf & Huismans, 2019). Weakening of the back-arc lithospheric mantle through removal or metasomatism (Chung et al., 2005) unpins the position of the mantle singularity (S-point) and may lead to thrusting of the pro-lithosphere under the retro-plate crust during orogenic growth (Kelly et al., 2016; Li et al., 2016; Huangfu et al., 2018; Kelly et al., 2020). Such a process could be operating in the Himalayan-Tibetan orogen, see below.

We only explore the effect of spatially and temporally uniform surface processes on model evolution. Typically, mountain belts create an orographic barrier that can induce differential erosion within a mountain belt, which is shown to have a strong effect on orogenic growth (e.g. Willett, 1999; Beaumont et al., 2001). As will become apparent in the comparison to the Himalaya, spatially non-uniform surface process with high efficiency exert a strong influence on mountain building and have the potential to modify the shortening distribution shown in figure 9.

4.4 Comparison with previous modelling studies

The large-scale evolution of shortening distribution (e.g., Figure 9) can already be observed in some early S-point models (Willett et al., 1993; Beaumont et al., 1994; Willett & Beaumont, 1994; Vanderhaeghe et al., 2003), as reviewed by Jamieson and Beaumont (2013). The migration of the uplifted plug onto the retro-side of the orogen led Willett and Beaumont (1994) to propose that subduction of Asian lithosphere below India formed the Himalayan-Tibetan orogen, opposite to the nowadays commonly recognised subduction direction (e.g. Owens & Zandt, 1997; Nabelek et al., 2009; Replumaz et al., 2010). Models of these early studies also developed step-up shear zones, a viscous decoupling horizon and a mantle singularity (S-point), which we infer to be the primary controlling factors of model evolution (Fig. 9a). This congruence

corroborates our model inferences for the controlling factors of model evolution, and shows how early S-point models and newer upper-mantle-scale models, as used here, relate. However, upper-mantle-scale models that include strain-dependent weakening do not necessarily produce a retro-step-up shear zone, which has a profound effect on shortening distribution during orogen growth, as discussed above. Erdős et al. (2014) inferred that extensional inheritance is key to produce retro-wedge deformation, while we can simplify this to the existence of a retro-step up-shear zone. We believe that the latter is likely to exist, given that most mountain belts on Earth include a phase of inversion of inherited weak structures during the initial collision phase. We can furthermore show that slab pull has no primary influence on mountain belt structure, but can provide a force to drive orogenesis, and that internal loading through crustal shortening is the cause for the evolution shown in Fig. 9.

Full coupling between fluvial surface processes and tectonics during mountain building was first investigated by Beaumont et al. (1992), followed by a series of modelling studies that looked at the interplay between tectonics and fluvial erosion (Willett, 1999; Willett et al., 2001; Stolar et al., 2006, 2007). These studies focused on mountain belts that reach steady state between tectonic material influx and erosional outflux; they did not have sufficient resolution to include deposition and the interaction between thin-skinned and thick-skinned deformation. Beaumont et al. (2000); Erdős et al. (2014, 2015); Grool et al. (2019) included a weak décollement horizon in the crust as used here and investigated its influence on relatively small orogenic wedges. Simplified sedimentation and erosion routines are relatively commonplace in geodynamic modelling (e.g. Erdős et al., 2014, 2015; Grool et al., 2019; J. P. Butler et al., 2013; Kelly et al., 2020). However, fully coupled landscape-evolution models and thermomechanical models, as we use here, are far less common (e.g. Thieulot et al., 2014; Ueda et al., 2015). This study is the first to show end-member models that investigate the interaction between tectonics and surface processes during mountain growth from small to large, with a 2D mass conserving landscape-evolution model, and including a weak shallow crustal décollement. Using these models, we show how fluvial erosion and deposition modify orogenic growth in terms of width, topography and structural style. The latter is supported by a force-balance analysis that quantifies thrusting during orogenic growth.

5 Comparison to Natural Examples

The comparison of the distribution of shortening and variable structural style during mountain growth predicted by the models (Fig. 9, Fig. 10) with natural examples requires well-studied mountain belts with deep reflection seismic surveys and preferably balanced crustal- or lithospheric-scale cross sections. There are only a few mountain belts on Earth that fulfill (some of) these criteria, preventing a statistical comparison of shortening distribution as a function of orogen size with natural examples. Instead, we compare our model inferences to the well-studied Pyrenean, Alpine, and Himalayan-Tibetan orogens, and provide a quantitative comparison of shortening estimates, deformation history, and structural style. Within those mountain belts we will look more specifically at the ECORS-profile in the Pyrenees (Muñoz, 1992), the NFP-20 EAST profile from the western European Alps (Schmid et al., 1996), and the cross section through the southern half of the the Himalayan-Tibetan orogen from Nabelek et al. (2009) (Fig. 11). For each orogen we first look at similarities to the shortening distribution and influences on structural style derived from our models, before discussing notable differences. We note that compared to the Pyrenees and Alps, the Himalayan-Tibetan orogen is far less comprehensively understood. However, it is the only modern continent-continent collisional orogen containing an elevated plateau, and is thus an important part of this comparison to natural examples.
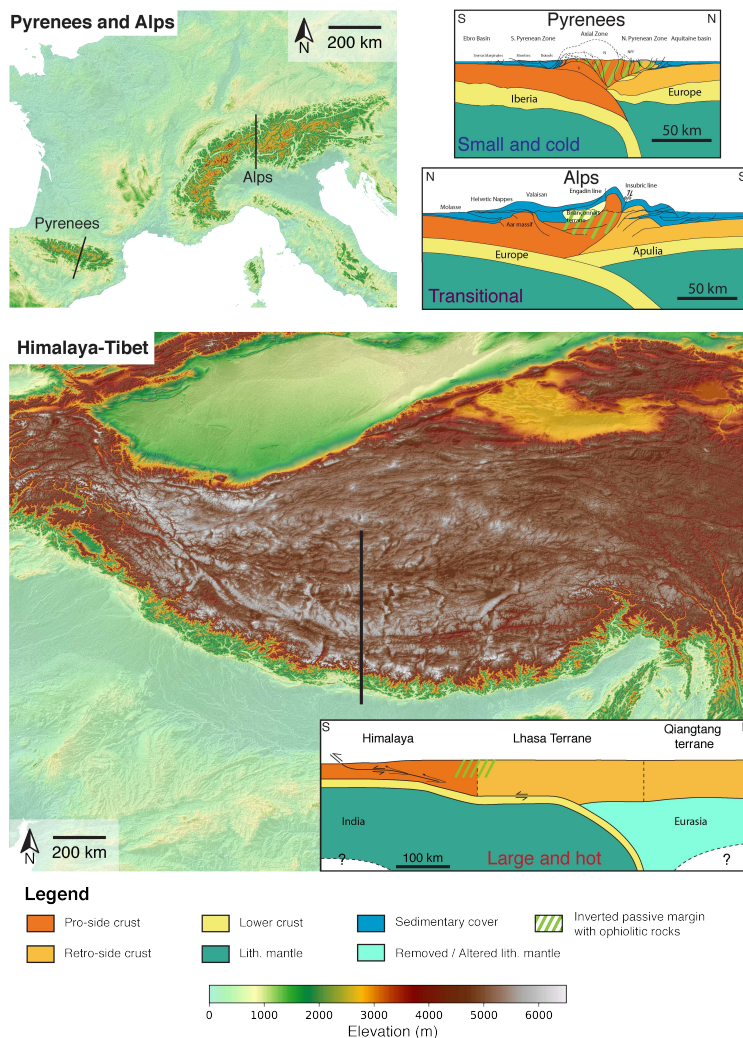
Figure 11. Digital elevation model (DEM) of the Pyrenees, European Alps and Himalaya-Tibet orogen and corresponding cross sections. The two DEMs have the same colorbar and scale. The Pyrenees is an example of a small and cold orogen (cross section modified from Muñoz (1992)), the Western Alps, although variable along strike, might be an example of a transitional orogen (cross section modified from Schmid et al. (1996)), and the Himalaya-Tibet orogen is the only recent example of a large and hot continent-continent collision orogen (cross section modified from Nabelek et al. (2009)). Crustal units and structures in the Himalaya-Tibet orogen are strongly simplified, also omitting a differentiation between crust and sedimentary cover. The lower bounds of the Indian and Eurasian lithospheric mantles are inferred from Owens and Zandt (1997). The Pyrenean and Alpine cross sections have the same scale but are flipped North-South.

5.1 Pyrenees

Mesozoic extension resulted in rift-basin formation and mantle exhumation along the Iberia-Europe plate boundary (Sibuet et al., 2004; Jammes et al., 2009; Tugend et al., 2014). Subsequent shortening started in the Late Cretaceous (∼80 Ma), peaked during Eocene-Oligocene times and continued into the Miocene (Muñoz, 1992, 2019; Beaumont et al., 2000). Shortening was accommodated by outward-propagating inversion of weak upper crustal extensional structures, and underthrusting of the Iberian lower crust and lithospheric mantle beneath Europe (Muñoz, 1992; Beaumont et al., 2000). The former Iberian margin and several additional crustal thrust sheets form the main body of the mountain belt, and build an antiformal stack known as the Axial Zone (Muñoz, 1992, 2019). Inversion of the former northern hyperextended rift domain forms the narrow North Pyrenean Zone, consisting primarily of inverted extensional blocks (Teixell et al., 2018; Grool et al., 2018). Lherzolite bodies are exposed along the former main extensional detachment between Iberia and Europe. The foreland basins preserve syn-deformational deposits and have a structural style controlled by the distribution of pre-rift Triassic salt deposits, which form a weak décollement horizon (Muñoz, 1992, 2019). Convergence estimates for the Eastern Pyrenees (ECORS) vary between 90 km and 165 km (Muñoz, 1992; Beaumont et al., 2000; Mouthereau et al., 2014; Grool et al., 2018). Shortening is accomodated by inversion of the rift margin extensional faults and newly formed thrust sheets from the Iberian crust (pro-side). On the contrary, no new thrust sheet developed in the undeformed European crust. As most shortening is accommodated in the pro-wedge and the inverted plug, this system can be considered an example of a small PU orogenic wedge (Fig. 9). The antiformal stack is related to a salt-detached foreland fold-thrust belt, as shown in model MSpDéc and quantified in (Fig. 10d). As the occurence of antiformal stacking depends on the thickness of the foreland fold-thrust belt (see model MSpDéc), supra-salt, syn-extensional deposits potentially enhanced antiformal stack formation already at the start of orogenesis. The exhumed Lherzolite bodies document crustal thinning and mantle exhumation before mountain building in the Pyrenees, as seen in MExt.

5.2 Alps

Orogenesis in the Central Alps results from a complex tectonic and paleogeographic evolution during collision of Europe and Adria. Subduction of the Piemont-Liguria ocean and northward movement of Adria led to early nappe stacking, terrane accretion, subduction of the European passive margin, UHP metamorphism, and subsequent exhumation of UHP-metamorphic rocks through the late Eocene (∼35 Ma). The ensuing continent-continent collision is characterised by subduction of the European lower crust and mantle lithosphere, bivergent orogenic thrusting, and underthrusting of the Adriatic lower crust and lithospheric mantle below the orogenic wedge (Stampfli et al., 1998; Schmid et al., 2004; Handy et al., 2010; Schmid et al., 2017; Rosenberg & Kissling, 2013, see Fig. 11). Reconstructing the amount of crustal shortening and plate convergence is difficult, especially for the early (pre 35 Ma) nappe stacking phase. Some convergence estimates are a) ∼160 km since 40 Ma for profile NFP-20 East (Fig. 11; Schmid et al., 1996), b) 98 km for post 35 Ma collision for the same profile (Rosenberg & Kissling, 2013), and c) 165 km for post 35 Ma collision a bit SW of the NFP-20 East profile (Schmid et al., 2017). As these estimates do not include the early nappe-stacking phase, cumulative convergence for the profile presented in Fig. 11 is certainly greater than 150 km. Our models with low to medium surface-process efficiency require 200 - 300 km of convergence of normal crustal thickness plates to produce an orogen with a size comparable to the Central Alps. The amount of crustal shortening and retro-wedge deformation in the Central and Western Alps decreases systematically towards the SW (Bellahsen et al., 2014; Schmid et al., 2017). These lateral variations potentially document the shift from a small PU wedge in the SW to a PUR wedge with significant retro-wedge shortening and under-thrusting of the

retro-wedge lower crust and lithospheric mantle in the Central Alps. The Central and Western Alps also show antiformal thrust-sheet stacking in the hinterland of the salt-detached Jura fold-thrust belt (Schmid & Kissling, 2000; Schmid et al., 2004), as seen in model M6, and explained in our force balance analysis (Fig. 10d). Our models do not include pre-collision subduction, UHP rock formation and exhumation. As shown by J. P. Butler et al. (2013), exhumed UHP rocks become part of the central uplifted plug (U). Liao and Gerya (2017); Liao et al. (2018); Vogt et al. (2018) attribute variable retro-wedge deformation in the Western Alps to the rheological contrast induced by the Ivrea mantle body, which was exhumed during pre-collisional extension and remained at upper crustal levels during collision. Our models suggest that the limited retro-wedge deformation in the Western Alps may also be a natural consequence of limited crustal shortening resulting in dominantly pro-wedge deformation.

5.3 Himalayan-Tibetan orogen

During the Mesozoic, the Tibetan plateau was assembled by the successive accretion of several terranes (Fig. 11; Yin & Harrison, 2000; Kapp & DeCelles, 2019). Subduction of the Indian oceanic slab during the Mesozoic and early Paleogene led to collision of thinned Indian lithosphere at $\sim$59 Ma (DeCelles et al., 2014; Hu et al., 2015). Collision of normal thickness lithosphere started at around 50 to 45 Ma (Guillot et al., 2003; Replumaz & Tapponnier, 2003; Negredo et al., 2007; Kapp & DeCelles, 2019). Total post $\sim$59 Ma convergence estimates vary greatly and are in the order of 2900 ± 750 km (Dupont-Nivet et al., 2010; Guillot & Replumaz, 2013). Guillot and Replumaz (2013) quantify convergence accommodated within the pro-plate to 1500 ± 300 km, versus >1100 km within the Tibetan retro-plate, giving a distribution of 58 % pro- and 42 % retro-wedge shortening since the onset of continent-continent collision. The southern, Himalayan, foreland fold-thrust belt records shortening, estimated from cross-section balancing, of 500 to 750 km (DeCelles et al., 2001; Robinson, 2008; Long et al., 2011). Antiformal crustal duplexing is inferred in the back of the foreland fold-thrust belt (Gao et al., 2016). Thrusting and crustal shortening in the Qiangtang and Lhasa terranes started already in Late-Cretaceous times, before onset of continent-continent collision (Kapp et al., 2003, 2005; DeCelles et al., 2002; Volkmer et al., 2007; Wang et al., 2014). Therefore, India collided with already thickened crust of an Andean-type orogen, which may have formed a plateau (Lhasaplano) during Late-Cretaceous - Eocene times (Kapp et al., 2007; Kapp & DeCelles, 2019). Thermochronological data indicate that a high plateau with low erosion rates was probably established in Tibet by Eocene times (van der Beek et al., 2009; Rohrmann et al., 2012), consistent with 26 - 27 Ma high-elevation paleoaltimetry dating in the centre of the Tibetan Plateau (DeCelles et al., 2007; Molnar et al., 2010). Low erosion rates in the dry Tibetan plateau stand in stark contrast to monsoon-driven high erosion and exhumation rates in the frontal part of the Himalaya (e.g. Burbank et al., 1996; Lavé & Avouac, 2001; Wobus et al., 2003; Herman et al., 2010). During continent-continent collision, thrust activity propagated to first order from the possibly pre-thickened Qiangtang terrane towards the Tibetan plateau margins (see review in Wang et al., 2014; Kapp & DeCelles, 2019). This explains significant northward translation of the India-Asia suture during early continent-continent collision (DeCelles et al., 2002; Yi et al., 2011). However, simultaneous shortening in spatially very different locations for instance at the India-Asia suture zone and in the Qiangtang terrane is documented (Kapp & DeCelles, 2019). Shortening included (consecutive) magmatic "sweeps" and "jumps", possibly connected to removal of mantle lithosphere pieces genetically related to the accreted terranes (Chung et al., 2005; Liu et al., 2014; Kapp & DeCelles, 2019; Kelly et al., 2020). Furthermore, facilitated by a weak or removed Tibetan lithospheric mantle, the present day Indian lithospheric mantle and lower crust have thrust far under the orogen, leading to a position of the S-point below the accreted

Tibetan terranes and not below thickened Indian crust (Fig. 11; Owens & Zandt, 1997; Nabelek et al., 2009).

Our models and the inferred shortening distribution as a function of convergence can explain the first-order characteristics of the Himalaya-Tibet orogen as a plateau flanked by wedges (Fig. 9), decoupling of over-thickened crust from the lithospheric mantle, and independent evolution of crust and mantle lithosphere. Crustal underthrusting and duplexing in the hinterland of the thick Himalayan foreland fold-thrust belt (Gao et al., 2016) fits well with the predictions of our force balance analysis (Fig. 10d). Furthermore, the distribution of shortening as compiled by Guillot and Replumaz (2013) is consistent with values inferred from our models. However, the sketch shown in Fig. 9d clearly does not match the present day structure of the Himalayan-Tibetan orogen. Especially the position of the India-Asia suture zone and the present day S-point position of the Indian plate are reversed in comparison to our model evolution and require explanation. Recent modelling studies (Li et al., 2016; Huangfu et al., 2018; Kelly et al., 2016, 2020) show that several key aspects of Himalayan mountain building can be explained by continent-continent collision, including delamination tectonics facilitated by strength and density contrasts in the lithospheric mantle genetically related to accreted terranes. Kelly et al. (2020) propose that indentation of India induces initiation of shortening in the North part of the Qiangtang terrane, facilitated by a weak Qiangtang-lithospheric mantle, followed by lateral North-South spreading of shortening similar to our models. Lateral growth is accompanied by peeling and removal of several lithospheric mantle pieces, creating space for late underthrusting of the buoyant Indian lithospheric mantle. High erosion and exhumation rates at the Himalayan mountain front (e.g. Burbank et al., 1996; Lavé & Avouac, 2001; Herman et al., 2010) counteract accumulation of Indian crustal material and reduce the contribution of pro-side material to the mountain belt. These modelling studies highlight that rheological decoupling between crust and lithospheric mantle can lead to a strongly independent evolution of the crust and mantle in large and hot orogens. However, the above modelling studies do not investigate the influence of a pre-thickened Cordilleran-type orogen on the retro-plate during continent-continent collision. Crustal thickening in Cordilleran-type orogens like the Andes is typically related to removal of the overriding plate lithospheric mantle in Rayleigh-Taylor instabilities (Schurr et al., 2006; DeCelles et al., 2009; Wolf & Huismans, 2019). Pre-collision removal of the Asian lithospheric mantle would facilitate underthrusting of the Indian lithosphere during continent-continent collision, translating the S-point beneath the upper plate. This could be a modified explanation for the large-scale lithospheric evolution of the Himalaya-Tibet orogen, which does not require peeling and removal of several pieces of lithospheric mantle. Hence, initiation of shortening in the Qiangtang terrane or collision with a pre-existing orogen, efficient erosion of Himalayan crustal material, removal of retro-lithospheric mantle and underthrusting of the Indian lower lithosphere can explain the first order differences between nature and our presented model evolution.

6 Conclusions

We have used thermo-mechanical models coupled to a surface process model to investigate the effects of mantle-lithosphere density, extensional inheritance, surface-process efficiency, and decoupling between thin-and thick-skinned tectonics, on orogen growth from small and cold to large and hot. We have also derived a force-balance analysis of thrust formation during orogenic growth and compared our model inferences to the Pyrenees, Alps and Himalayas, to draw the following conclusions:

We find a relationship between orogen size and distribution of shortening in terms of pro- versus retro-wedge deformation: 1) Small and cold orogens with cross-sectional area (CA) $< 3.75 \times 10^9\,\mathrm{m}^2$, corresponding to at most $150\,\mathrm{km}$ of convergence in our

reference model, are expected to form a mountain belt in which deformation is mainly localised on the pro-side and within (inverted) structures from the early collision stage, forming the uplifted plug. 2) Transitional orogens with $3.75 \times 10^9 \, \text{m}^2 < CA <\sim 12.5 \times 10^9 \, \text{m}^2$ (150 km to 500 km of collisional convergence in the reference model) are expected to additionally exhibit thick-skinned retro-wedge deformation. 3) If crustal shortening creates $CA >\sim 12.5 \times 10^9 \, \text{m}^2$, a large and hot plateau forms, located mostly on the retro-side as a consequence of underthrusting of the retro-mantle. The onset of plateau formation is additionally dependent on radioactive heat production and the timescale of thermal equilibration of the crust.

The shortening distribution in orogens as they evolve from small and cold to large and hot is controlled by internal crustal loading. Slab pull of the subducting lithosphere can provide a driving force of orogenesis but does not affect the distribution and structural style of deformation. Pre-collisional extensional inheritance results in emplacement of mantle material close to the surface and a structural domain dominated by inversion tectonics, but provides only a secondary control on large-scale mountain-belt development. Increased orogenic topography enhances erosion such that mountain-belt growth is delayed as a function of orogen size and surface-process efficiency. Strong erosion in the orogen core is linked to deep, overfilled foreland basins. Limited exhumation characterises low surface-process efficiency, while exhumation of deep crustal rocks characterises high surface-process efficiency. Only very high surface-process efficiency can induce flux steady state between crustal accretion and erosion.

The force-balance analysis explains variable structural styles of orogenic growth as a function of inherited weaknesses, sedimentation and (de-)coupling between thin- and thick-skinned deformation. A reference thrust spacing can be defined and depends on crustal strength and mid-crustal viscosity. Thrust spacing is amplified by syntectonic sedimentation or inherited weaknesses, which are also expected to modify the structural style of the mountain belt. A weak décollement horizon and thick foreland fold-thrust belt efficiently decouple thin- and thick-skinned deformation. Decoupled systems are characterized by a stacked foreland fold-thrust belt recording significant deformation, and crustal underthrusting leading to antiformal duplexing in the hinterland of the thin-skinned belt.

Comparison with the Pyrenees, Alps and Himalaya shows the applicability but also the limitations of the idealized evolutionary sequence developed here. The Pyrenees and Alps exhibit the first two characteristic phases identified here, and show further similarities with model evolution and derived structural style. We cannot reproduce the complex deformation history of the Himalaya, however, possibly because our model does not take lithospheric delamination of inherited accreted terranes or pre-collisional thickening into account. Yet, the large and hot Himalayan-Tibetan orogen shows some of the first-order characteristics and structural styles presented here for orogens with the largest amounts of shortening.

Appendix A Modelling Methods

A1 Thermo-mechanical model

We use the modified 2-dimensional Arbitrary Lagrangian-Eulerian (ALE), thermo-mechanically coupled finite element code FANTOM (Thieulot, 2011; Wolf & Huismans, 2019), coupled to the surface process model Fastscape (Braun & Willett, 2013; Yuan et al., 2019, see section A3), to investigate the dynamics of orogenic growth as a function of convergence. The thermo-mechanical model computes momentum and mass conservation (A1, A2) of plane-strain incompressible creeping fluids, and heat transport (A3) in the model domain:

$$\frac{\partial \sigma_{ij}}{\partial x_i} + \rho g = 0 \quad i,j = 1,2, \tag{A1}$$

$$\frac{\partial v_i}{\partial x_i} = 0 \quad i = 1, 2, \tag{A2}$$

$$c_p \rho \left(\frac{\partial T}{\partial t} + v_i \frac{\partial T}{\partial x_i} \right) = k \frac{\partial}{\partial x_i} \frac{\partial T}{\partial x_i} + H + v_j \alpha \rho T g, \tag{A3}$$

where v_i are velocity components, x_i are spatial coordinates, σ_{ij} is the stress tensor, ρ is density, g is gravitational acceleration, c_p is specific heat, T is temperature, t is time, k is thermal conductivity, H is radioactive heat production per unit volume, α is the volumetric thermal expansion coefficient. The last term in (A3) is the correction for adiabatic heating when material moves vertically. The density ρ changes as a function of the thermal expansion coefficient α.

Model materials deform either by frictional-plastic or by viscous flow. Frictional-plastic behaviour is modelled using a pressure dependent Drucker-Prager yield criterion

$$\sigma'_{plast} = P \cdot \sin(\phi_{eff}) + C \cdot \cos(\phi_{eff}), \tag{A4}$$

where σ'_{plast} is the square root of the second invariant of the deviatoric stress, P is the dynamic pressure, ϕ_{eff} is the effective angle of internal friction and C is cohesion. Strain-weakening is accounted for by linearly reducing ϕ_{eff} from $15° - 2°$ and C from $20 - 4\,\mathrm{MPa}$ through a predefined plastic strain ($\epsilon_{plastic}$) interval $0.1 < \epsilon_{plastic} < 1.1$ (Huismans & Beaumont, 2003).

Viscous deformation is described by a non-linear, thermally-activated power law creep formulation which relates pressure, temperature and strain rate to the viscous flow stress, σ'_{visc}:

$$\sigma'_{visc} = f \cdot A^{-\frac{1}{n}} \cdot (\dot{\epsilon}_{eff})^{\frac{1}{n}} \cdot exp \left(\frac{Q + VP}{nRT} \right), \tag{A5}$$

where σ'_{visc} is the square root of the second invariant of the deviatoric stress, $\dot{\epsilon}_{eff}$ is the square root of the second invariant of the deviatoric strain rate, f is a scaling factor, A the pre-exponential factor converted to plane strain, n the power-law exponent, Q activation energy, V activation volume, P the dynamic pressure, and R the universal gas constant.

At high pressures, high differential stresses, and low temperatures, olivine mainly deforms by a temperature-insensitive exponential (Peierl's) creep (Tsenn & Carter, 1987; Katayama & Karato, 2008). We approximate this deformation mechanism by limiting the flow stress of all model materials based on the wet olivine flaw to $\sigma'_{plast} \leq 300\,\mathrm{MPa}$ (e.g., Andrews & Billen, 2009; J. P. Butler et al., 2015).

A2 Model geometry and boundary conditions

Continent-continent collision is modelled using an idealised upper mantle domain with 1200 km horizontal and 600 km vertical extent (Fig. 1, Table 1). The model domain has a typical layered setup of 25 km of upper/mid crust, 10 km lower crust, and 85 km lithospheric mantle down to 120 km, overlying the sub-lithospheric upper mantle (see section 2.1 for detailed information).

The initial temperature distribution in the model domain represents typical Phanerozoic values and is at steady state, with a Moho temperature of $550\,°\mathrm{C}$ and $1330\,°\mathrm{C}$ at the base of the lithosphere, resulting in a surface heat flow of $53\,\mathrm{mW\,m^{-2}}$ and heat flux in the sublithospheric mantle of $20.8\,\mathrm{mW\,m^{-2}}$. To mimic mantle convection at high Nusselt number, and to maintain the heat flux at the lithosphere-asthenosphere boundary k linearly increases from $2.25\,\mathrm{W\,m^{-1}\,K^{-1}}$ to $52.0\,\mathrm{W\,m^{-1}\,K^{-1}}$ between 1330 and $1340\,°\mathrm{C}$ in the sublithospheric mantle (Pysklywec & Beaumont, 2004). The values are scaled to keep an adiabatic gradient of $0.4\,°\mathrm{C\,km^{-1}}$ in the sublithospheric domain. All other materials have a thermal conductivity $k = 2.25\,\mathrm{W\,m^{-1}\,K^{-1}}$.

The side boundaries are insulated and the top and bottom boundaries have a constant temperature boundary condition of respectively 0 °C and 1522 °C.

Continent-continent collision is modelled by applying velocity boundary conditions on the model sides. Inflow of lithospheric material is balanced by a small distributed outflow in the sub-lithospheric mantle. The upper surface is stress free, and the lower and side boundaries have free slip conditions.

The Eulerian grid consists of 1600 cells in the horizontal and 323 cells in the vertical direction. The distribution of cells is non-uniform in the vertical direction, with 100 cells in the uppermost 25 km, 135 cells in the following 135 km, and 88 cells in the lowermost 440 km. This leads to vertical resolutions of 200 m, 1 km and 5 km respectively, and a uniform horizontal resolution of 750 m. Eulerian cells are initially filled with 5 uniformly spaced lagrangian particles. During model evolution, particle numbers per cell are kept between minimum 5 and maximum 50.

A3 Surface process model

We use the 2-dimensional, finite difference, implicit, O(n) surface process code Fastscape (Braun & Willett, 2013) which has been extended by a continental sediment transport and deposition term (Yuan et al., 2019) to model erosion and mass conserving deposition:

$$\frac{\partial h}{\partial t} = U - K_f A^m S^n + K_c \nabla^2 h + \frac{G}{A} \int_A (U - \frac{\partial h}{\partial t}) dA, \tag{A6}$$

h is surface elevation, t is time, U is the uplift rate, K_f is the fluvial erosion coefficient, A is catchment area upstream, S is the local slope, m, n are the stream power law exponents, K_c is the hillslope diffusion coefficient, and G is a deposition coefficient. The model accounts for a change in topography as a function of uplift, Stream-power law erosion (K_f-term), hillslope creep (K_c-term), and continental deposition as a function of the average erosion upstream. We additionally account for mass conserving filling of local minima, i.e. lakes and the orogenic foreland basin, by filling up from the deepest point of the local minimum according to the available sediments. All rivers are connected to either the left or right side boundary by bridging local minima to their lowest neighbour catchment.

The two codes are fully coupled in a T-coupling manner (Beaumont et al., 1992). After each mechanical timestep of Fantom, the resulting 1D surface velocity is given to Fastscape as a cylindrical 2D signal. First the Fastscape surface is advected horizontally according to the given horizontal velocity field. Subsequently eq. A6 is solved with U being the vertical velocity signal. Finally, the average Fastscape elevation is given back as new free-surface to the mechanical code and time-stepping continues. In FANTOM areas above the old free surface are filled with sediment which has the same rheological and density properties as upper crust, but a different color (see Fig. 1)

A4 Calculation of tectonic force and lithospheric pull

The tectonic boundary force F_{TBF} is defined as

$$F_{TBF} = \int_0^{z_{lab}} \sigma'_{xx} dz = \int_0^{z_{lab}} 2\dot{\epsilon}_{xx} \mu_{eff} dz, \tag{A7}$$

where z_{lab} is lithosphere thickness, σ'_{xx} is horizontal deviatoric stress, $\dot{\epsilon}_{xx}$ is horizontal strain rate, and μ_{eff} is effective viscosity. We calculate F_{TBF} at the sides of the model with $z_{lab} = 120$ km. Net pull, i.e. tensional stresses, are defined as positive. The tectonic force is the net force resulting from the given boundary conditions, lithospheric pull or push, and resisting forces.

Lithospheric pull is calculated as the area-integrated density difference between slab material (i.e. metamorphosed lower crust and lithospheric mantle), and sub-lithospheric mantle. All lithospheric material below the lower bound of the lithospheric mantle is considered to contribute to slab pull and part of the computation.

Appendix B Supplementary Material

Supplementary material includes:

- Supplementary Models SM1 to SM6
- Fastscape surfaces of models M5, M6, and M7
- Diagram highlighting mountain belt development normalized to S-point.
- Animations of all models

References

Amilibia, A., Sabat, F., McClay, K. R., Munoz, J. A., Roca, E., & Chong, G. (2008). The role of inherited tectono-sedimentary architecture in the development of the central andean mountain belt: Insights from the cordillera de domeyko. *Journal of Structural Geology*, *30*(12), 1520-1539. doi: 10.1016/j.jsg.2008.08.005

Andrews, E. R., & Billen, M. I. (2009). Rheologic controls on the dynamics of slab detachment. *Tectonophysics*, *464*(1-4), 60-69. doi: 10.1016/j.tecto.2007.09.004

Beaumont, C., Ellis, S., & Pfiffner, A. (1999). Dynamics of sediment subduction-accretion at convergent margins: Short-term modes, long-term deformation, and tectonic implications. *Journal of Geophysical Research-Solid Earth*, *104*(B8), 17573-17601. doi: Doi10.1029/1999jb900136

Beaumont, C., Fullsack, P., & Hamilton, J. (1992). Erosional control of active compressional orogens. In *Thrust tectonics* (p. 1-18). Springer.

Beaumont, C., Fullsack, P., & Hamilton, J. (1994). Styles of crustal deformation in compressional orogens caused by subduction of the underlying lithosphere. *Tectonophysics*, *232*(1-4), 119-132. doi: Doi10.1016/0040-1951(94)90079-5

Beaumont, C., Jamieson, R. A., Nguyen, M. H., & Lee, B. (2001). Himalayan tectonics explained by extrusion of a low-viscosity crustal channel coupled to focused surface denudation. *Nature*, *414*(6865), 738-742. doi: DOI10.1038/414738a

Beaumont, C., Munoz, J. A., Hamilton, J., & Fullsack, P. (2000). Factors controlling the alpine evolution of the central pyrenees inferred from a comparison of observations and geodynamical models. *Journal of Geophysical Research-Solid Earth*, *105*(B4), 8121-8145. doi: Doi10.1029/1999jb900390

Beaumont, C., Nguyen, M. H., Jamieson, R. A., & Ellis, S. (2006). Crustal flow modes in large hot orogens. *Geological Society, London, Special Publications*,

268(1), 91-145.

Becker, T. W., & Faccenna, C. (2011). Mantle conveyor beneath the tethyan collisional belt. *Earth and Planetary Science Letters*, *310*(3-4), 453-461. doi: 10.1016/j.epsl.2011.08.021

Bellahsen, N., Mouthereau, F., Boutoux, A., Bellanger, M., Lacombe, O., Jolivet, L., & Rolland, Y. (2014). Collision kinematics in the western external alps. *Tectonics*, *33*(6), 1055-1088. doi: 10.1002/2013tc003453

Braun, J. (2006). Recent advances and current problems in modelling surface processes and their interaction with crustal deformation. *Geological Society, London, Special Publications*, *253*(1), 307-325. doi: 10.1144/gsl.Sp.2006.253.01.16

Braun, J., & Beaumont, C. (1995). 3-dimensional numerical experiments of strain partitioning at oblique plate boundaries - implications for contrasting tectonic styles in the southern coast ranges, california, and central south island, new-zealand. *Journal of Geophysical Research-Solid Earth*, *100*(B9), 18059-18074. doi: Doi10.1029/95jb01683

Braun, J., & Willett, S. D. (2013). A very efficient o(n), implicit and parallel method to solve the stream power equation governing fluvial incision and landscape evolution. *Geomorphology*, *180*, 170-179. doi: 10.1016/j.geomorph.2012.10.008

Burbank, D. W., Leland, J., Fielding, E., Anderson, R. S., Brozovic, N., Reid, M. R., & Duncan, C. (1996). Bedrock incision, rock uplift and threshold hillslopes in the northwestern himalayas. *Nature*, *379*(6565), 505-510. doi: DOI10.1038/379505a0

Butler, J. P., Beaumont, C., & Jamieson, R. A. (2011). Crustal emplacement of exhuming (ultra)high-pressure rocks: Will that be pro- or retro-side? *Geology*, *39*(7), 635-638. doi: 10.1130/G32166.1

Butler, J. P., Beaumont, C., & Jamieson, R. A. (2013). The alps 1: A working geodynamic model for burial and exhumation of (ultra)high-pressure rocks in alpine-type orogens. *Earth and Planetary Science Letters*, *377*, 114-131. doi: 10.1016/j.eps1.2013.06.039

Butler, J. P., Beaumont, C., & Jamieson, R. A. (2015). Paradigm lost: Buoyancy thwarted by the strength of the Western Gneiss Region (ultra)high-pressure terrane, Norway. *Lithosphere*, *7*(4), 379-407. doi: 10.1130/L426.1

Butler, R. W. H., Tavarnelli, E., & Grasso, M. (2006). Structural inheritance in mountain belts: An alpine-apennine perspective. *Journal of Structural Geology*, *28*(11), 1893-1908. doi: 10.1016/j.jsg.2006.09.006

Capitanio, F. A., Morra, G., Goes, S., Weinberg, R. F., & Moresi, L. (2010). India-asia convergence driven by the subduction of the greater indian continent. *Nature Geoscience*, *3*(2), 136-139. doi: 10.1038/Ngeo725

Carrera, N., & Muñoz, J. A. (2013). Thick-skinned tectonic style resulting from the inversion of previous structures in the southern cordillera oriental (nw argentine andes). *Geological Society, London, Special Publications*, *377*(1), 77-100. doi: 10.1144/sp377.2

Carrera, N., Muñoz, J. A., Sabat, F., Mon, R., & Roca, E. (2006). The role of inversion tectonics in the structure of the cordillera oriental (nw argentinean andes). *Journal of Structural Geology*, *28*(11), 1921-1932. doi: 10.1016/j.jsg.2006.07.006

Chung, S. L., Chu, M. F., Zhang, Y. Q., Xie, Y. W., Lo, C. H., Lee, T. Y., . . . Wang, Y. Z. (2005). Tibetan tectonic evolution inferred from spatial and temporal variations in post-collisional magmatism. *Earth-Science Reviews*, *68*(3-4), 173-196. doi: 10.1016/j.earscirev.2004.05.001

Cloos, M. (1993). Lithospheric buoyancy and collisional orogenesis - subduction of oceanic plateaus, continental margins, island arcs, spreading ridges, and seamounts. *Geological Society of America Bulletin*, *105*(6), 715-737. doi: Doi10.1130/0016-7606(1993)105⟨0715:Lbacos⟩2.3.Co;2

Cooper, M. A., & Williams, G. D. (Eds.). (1989). (Vol. 44) (No. 1). doi: 10.1144/gsl .Sp.1989.044.01.01

Cowie, P. A., Whittaker, A. C., Attal, M., Roberts, G., Tucker, G. E., & Ganas, A. (2008). New constraints on sediment-flux-dependent river incision: Implications for extracting tectonic signals from river profiles. *Geology*, *36*(7), 535-538. doi: 10.1130/G24681a.1

Currie, C. A., Huismans, R. S., & Beaumont, C. (2008). Thinning of continental backarc lithosphere by flow-induced gravitational instability. *Earth and Planetary Science Letters*, *269*(3-4), 435-446. doi: 10.1016/j.epsl.2008.02.037

Dahlen, F. A. (1984). Noncohesive critical coulomb wedges - an exact solution. *Journal of Geophysical Research*, *89*(Nb12), 125-133. doi: DOI10.1029/ JB089iB12p10125

Davis, D., Suppe, J., & Dahlen, F. A. (1983). Mechanics of fold-and-thrust belts and accretionary wedges. *Journal of Geophysical Research*, *88*(Nb2), 1153-1172. doi: DOI10.1029/JB088iB02p01153

DeCelles, P. G., Ducea, M. N., Kapp, P., & Zandt, G. (2009). Cyclicity in Cordilleran orogenic systems. *Nature Geoscience*, *2*(4), 251-257. doi: 10.1038/Ngeo469

DeCelles, P. G., Kapp, P., Gehrels, G. E., & Ding, L. (2014). Paleocene-eocene foreland basin evolution in the himalaya of southern tibet and nepal: Implications for the age of initial india-asia collision. *Tectonics*, *33*(5), 824-849. doi: 10.1002/2014tc003522

DeCelles, P. G., Quade, J., Kapp, P., Fan, M. J., Dettman, D. L., & Ding, L. (2007). High and dry in central tibet during the late oligocene. *Earth and Planetary Science Letters*, *253*(3-4), 389-401. doi: 10.1016/j.epsl.2006.11.001

DeCelles, P. G., Robinson, D. M., Quade, J., Ojha, T. P., Garzione, C. N., Copeland, P., & Upreti, B. N. (2001). Stratigraphy, structure, and tectonic evolution of the himalayan fold-thrust belt in western nepal. *Tectonics*, *20*(4), 487-509. doi: Doi10.1029/2000tc001226

DeCelles, P. G., Robinson, D. M., & Zandt, G. (2002). Implications of shortening in the himalayan fold-thrust belt for uplift of the tibetan plateau. *Tectonics*, *21*(6). doi: Artn106210.1029/2001tc001322

Dupont-Nivet, G., van Hinsbergen, D. J. J., & Torsvik, T. H. (2010). Persistently low asian paleolatitudes: Implications for the india-asia collision history. *Tectonics*, *29*. doi: ArtnTc501610.1029/2008tc002437

Ellis, S., & Beaumont, C. (1999). Models of convergent boundary tectonics: implications for the interpretation of lithoprobe data. *Canadian Journal of Earth Sciences*, *36*(10), 1711-1741. doi: 10.1139/e99-075

Erdős, Z., Huismans, R. S., & van der Beek, P. (2015). First-order control of syntectonic sedimentation on crustal-scale structure of mountain belts. *Journal of Geophysical Research-Solid Earth*, *120*(7), 5362-5377. doi: 10.1002/2014jb011785

Erdős, Z., Huismans, R. S., van der Beek, P., & Thieulot, C. (2014). Extensional inheritance and surface processes as controlling factors of mountain belt structure. *Journal of Geophysical Research-Solid Earth*, *119*(12), 9042-9061. doi: 10.1002/2014jb011408

Fillon, C., Huismans, R. S., & van der Beek, P. (2013). Syntectonic sedimentation effects on the growth of fold-and-thrust belts. *Geology*, *41*(1), 83-86. doi: 10 .1130/G33531.1

Forsyth, D., & Uyeda, S. (1975). Relative importance of driving forces of plate motion. *Geophysical Journal of the Royal Astronomical Society*, *43*(1), 163-200. doi: 10.1111/j.1365-246X.1975.tb00631.x

Gao, R., Lu, Z. W., Klemperer, S. L., Wang, H. Y., Dong, S. W., Li, W. H., & Li, H. Q. (2016). Crustal-scale duplexing beneath the yarlung zangbo suture in the western himalaya (vol 9, pg 555, 2016). *Nature Geoscience*, *9*(7). doi:

1189 10.1038/ngeo2730

Gillcrist, R., Coward, M., & Mugnier, J.-L. (1987). Structural inversion and its controls : examples from the alpine foreland and the french alps. *Geodinamica Acta*, *1*(1), 5-34. doi: 10.1080/09853111.1987.11105122

Gleason, G. C., & Tullis, J. (1995). A flow law for dislocation creep of quartz aggregates determined with the molten-salt cell. *Tectonophysics*, *247*(1-4), 1-23. doi: 10.1016/0040-1951(95)00011-B

Grier, M. E., Salfity, J. A., & Allmendinger, R. W. (1991). Andean reactivation of the cretaceous salta rift, northwestern argentina. *Journal of South American Earth Sciences*, *4*(4), 351-372. doi: Doi10.1016/0895-9811(91)90007-8

Griffin, W., O'Reilly, S. Y., Ryan, C., Gaul, O., & Ionov, D. (1998). Secular variation in the composition of subcontinental lithospheric mantle: geophysical and geodynamic implications. *Structure and evolution of the Australian continent*, *26*, 1-26.

Grool, A. R., Ford, M., Verges, J., Huismans, R. S., Christophoul, F., & Dielforder, A. (2018). Insights into the crustal-scale dynamics of a doubly vergent orogen from a quantitative analysis of its forelands: A case study of the eastern pyrenees. *Tectonics*, *37*(2), 450-476. doi: 10.1002/2017tc004731

Grool, A. R., Huismans, R. S., & Ford, M. (2019). Salt decollement and rift inheritance controls on crustal deformation in orogens. *Terra Nova*, *31*(6), 562-568. doi: 10.1111/ter.12428

Guillot, S., Garzanti, E., Baratoux, D., Marquer, D., Maheo, G., & de Sigoyer, J. (2003). Reconstructing the total shortening history of the nw himalaya. *Geochemistry Geophysics Geosystems*, *4*. doi: Artn106410.1029/2002gc000484

Guillot, S., & Replumaz, A. (2013). Importance of continental subductions for the growth of the tibetan plateau. *Bulletin De La Societe Geologique De France*, *184*(3), 199-223. doi: DOI10.2113/gssgfbull.184.3.199

Hacker, B. R. (1996). Eclogite formation and the rheology, buoyancy, seismicity, and H2O content of oceanic crust. In G. E. Bebout, D. W. Scholl, S. H. Kirby, & J. P. Platt (Eds.), *Subduction: Top to bottom* (p. 337-346). American Geophysical Union. doi: 10.1029/GM096p0337

Hacker, B. R., Kelemen, P. B., & Behn, M. D. (2015). Continental lower crust. *Annual Review of Earth and Planetary Sciences*, *43*(1h), 167-205. doi: 10.1146/annurev-earth-050212-124117

Handy, M. R., Schmid, S. M., Bousquet, R., Kissling, E., & Bernoulli, D. (2010). Reconciling plate-tectonic reconstructions of alpine tethys with the geological-geophysical record of spreading and subduction in the alps. *Earth-Science Reviews*, *102*(3-4), 121-158. doi: 10.1016/j.earscirev.2010.06.002

Herman, F., Copeland, P., Avouac, J. P., Bollinger, L., Maheo, G., Le Fort, P., . . . Henry, P. (2010). Exhumation, crustal deformation, and thermal structure of the nepal himalaya derived from the inversion of thermochronological and thermobarometric data and modeling of the topography. *Journal of Geophysical Research-Solid Earth*, *115*. doi: ArtnB0640710.1029/2008jb006126

Hilley, G. E., Strecker, M. R., & Ramos, V. A. (2004). Growth and erosion of fold-and-thrust belts with an application to the aconcagua fold-and-thrust belt, argentina. *Journal of Geophysical Research-Solid Earth*, *109*(B1). doi: ArtnB0141010.1029/2002jb002282

Hu, X. M., Garzanti, E., Moore, T., & Raffi, I. (2015). Direct stratigraphic dating of india-asia collision onset at the selandian (middle paleocene, 59 +/- 1 ma). *Geology*, *43*(10), 859-862. doi: 10.1130/G36872.1

Huangfu, P. P., Li, Z. H., Gerya, T., Fan, W. M., Zhang, K. J., Zhang, H., & Shi, Y. L. (2018). Multi-terrane structure controls the contrasting lithospheric evolution beneath the western and central-eastern tibetan plateau. *Nature Communications*, *9*. doi: ARTN378010.1038/s41467-018-06233-x

Huismans, R. S., & Beaumont, C. (2003). Symmetric and asymmetric litho-

1244   spheric extension: Relative effects of frictional-plastic and viscous strain
1245   softening.   *Journal of Geophysical Research-Solid Earth*, *108*(B10).   doi:
1246   10.1029/2002jb002026

1247   Hyndman, R. D., Currie, C. A., & Mazzotti, S. P. (2005). Subduction zone backarcs,
1248   mobile belts, and orogenic heat.   *GSA Today*, *15*(2), 4-10.   doi: 10.1130/1052
1249   -5173(2005)015⟨4:SZBMBA⟩2.0.CO;2

1250   Iaffa, D. N., Sabat, F., Muñoz, J. A., Mon, R., & Gutierrez, A. A.   (2011).   The
1251   role of inherited structures in a foreland basin evolution. the metan basin
1252   in nw argentina.   *Journal of Structural Geology*, *33*(12), 1816-1828.   doi:
1253   10.1016/j.jsg.2011.09.005

1254   Jamieson, R. A., & Beaumont, C. (2013). On the origin of orogens. *Geological Soci-*
1255   *ety of America Bulletin*, *125*(11-12), 1671-1702. doi: Doi10.1130/B30855.1

1256   Jammes, S., & Huismans, R. S.   (2012).   Structural styles of mountain building:
1257   Controls of lithospheric rheologic stratification and extensional inheritance.
1258   *Journal of Geophysical Research-Solid Earth*, *117*.   doi: ArtnB1040310.1029/
1259   2012jb009376

1260   Jammes, S., Manatschal, G., Lavier, L., & Masini, E.   (2009).   Tectonosedi-
1261   mentary evolution related to extreme crustal thinning ahead of a prop-
1262   agating ocean: Example of the western pyrenees.   *Tectonics*, *28*.   doi:
1263   ArtnTc401210.1029/2008tc002406

1264   Kapp, P., & DeCelles, P. G.   (2019).   Mesozoic-cenozoic geological evolution of the
1265   himalayan-tibetan orogen and working tectonic hypotheses.   *American Journal*
1266   *of Science*, *319*(3), 159-254. doi: 10.2475/03.2019.01

1267   Kapp, P., DeCelles, P. G., Gehrels, G. E., Heizier, M., & Ding, L. (2007). Geological
1268   records of the lhasa-qiangtang and indo-asian collisions in the nima area of
1269   central tibet.   *Geological Society of America Bulletin*, *119*(7-8), 917-932.   doi:
1270   10.1130/B26033.1

1271   Kapp, P., Murphy, M. A., Yin, A., Harrison, T. M., Ding, L., & Guo, J. H.   (2003).
1272   Mesozoic and cenozoic tectonic evolution of the shiquanhe area of western
1273   tibet. *Tectonics*, *22*(4). doi: Artn102910.1029/2001tc001332

1274   Kapp, P., Yin, A., Harrison, T. M., & Ding, L.   (2005).   Cretaceous-tertiary short-
1275   ening, basin development, and volcanism in central tibet.   *Geological Society of*
1276   *America Bulletin*, *117*(7-8), 865-878. doi: 10.1130/B25595.1

1277   Karato, S., & Wu, P.   (1993).   Rheology of the upper mantle - a synthesis.   *Science*,
1278   *260*(5109), 771-778. doi: 10.1126/science.260.5109.771

1279   Katayama, I., & Karato, S. I.   (2008).   Low-temperature, high-stress deformation of
1280   olivine under water-saturated conditions.   *Physics of the Earth and Planetary*
1281   *Interiors*, *168*(3-4), 125-133. doi: 10.1016/j.pepi.2008.05.019

1282   Kelly, S., Beaumont, C., & Butler, J. P. (2020).   Inherited terrane properties explain
1283   enigmatic post-collisional himalayan-tibetan evolution.   *Geology*. doi: 10.1130/
1284   g46701.1

1285   Kelly, S., Butler, J. P., & Beaumont, C.   (2016).   Continental collision with a
1286   sandwiched accreted terrane: Insights into himalayan-tibetan lithospheric
1287   mantle tectonics?   *Earth and Planetary Science Letters*, *455*, 176-195.   doi:
1288   10.1016/j.epsl.2016.08.039

1289   Lavé, J., & Avouac, J. P.   (2001).   Fluvial incision and tectonic uplift across the
1290   himalayas of central nepal.   *Journal of Geophysical Research-Solid Earth*,
1291   *106*(B11), 26561-26591. doi: Doi10.1029/2001jb000359

1292   Li, Z. H., Liu, M. A., & Gerya, T.   (2016).   Lithosphere delamination in continen-
1293   tal collisional orogens: A systematic numerical study.   *Journal of Geophysical*
1294   *Research-Solid Earth*, *121*(7), 5186-5211. doi: 10.1002/2016jb013106

1295   Liao, J., & Gerya, T.   (2017).   Partitioning of crustal shortening during continen-
1296   tal collision: 2-d thermomechanical modeling. *Journal of Geophysical Research-*
1297   *Solid Earth*, *122*(1), 592-606. doi: 10.1002/2016jb013398

1298   Liao, J., Gerya, T., & Malosa, M. G.   (2018).   3d modeling of crustal shortening

influenced by along-strike lithological changes: Implications for continental collision in the western and central alps. *Tectonophysics*, *746*, 425-438. doi: 10.1016/j.tecto.2018.01.031

Liu, D., Zhao, Z. D., Zhu, D. C., Niu, Y. L., DePaolo, D. J., Harrison, T. M., . . . Liu, J. L. (2014). Postcollisional potassic and ultrapotassic rocks in southern tibet: Mantle and crustal origins in response to india-asia collision and convergence. *Geochimica Et Cosmochimica Acta*, *143*, 207-231. doi: 10.1016/j.gca.2014.03.031

Long, S., McQuarrie, N., Tobgay, T., & Grujic, D. (2011). Geometry and crustal shortening of the himalayan fold-thrust belt, eastern and central bhutan. *Geological Society of America Bulletin*, *123*(7-8), 1427-U244. doi: 10.1130/B30203 .1

Mackwell, S. J., Zimmerman, M. E., & Kohlstedt, D. L. (1998). High-temperature deformation of dry diabase with application to tectonics on Venus. *Journal of Geophysical Research-Solid Earth*, *103*(B1), 975-984. doi: 10.1029/97JB02671

Molnar, P., Boos, W. R., & Battisti, D. S. (2010). Orographic controls on climate and paleoclimate of asia: Thermal and mechanical roles for the tibetan plateau. *Annual Review of Earth and Planetary Sciences, Vol 38*, *38*, 77-102. doi: 10.1146/annurev-earth-040809-152456

Molnar, P., & Lyon-Caen, H. (1988). Some simple physical aspects of the support, structure, and evolution of mountain belts. *Geol. Soc. Am. Spec. Pap.*, *218*, 179-207.

Mouthereau, F., Filleaudeau, P. Y., Vacherat, A., Pik, R., Lacombe, O., Fellin, M. G., . . . Masini, E. (2014). Placing limits to shortening evolution in the pyrenees: Role of margin architecture and implications for the iberia/europe convergence. *Tectonics*, *33*(12), 2283-2314. doi: 10.1002/2014tc003663

Muñoz, J. A. (1992). Evolution of a continental collision belt: Ecors-pyrenees crustal balanced cross-section. In *Thrust tectonics* (p. 235-246). Springer.

Muñoz, J. A. (2019). Deformation and structure in the Northern Iberian margin (Pyrenees s.l.). In C. Quesada & J. Oliveira (Eds.), *The geology of Iberia: A geodynamic approach.* Springer.

Nabelek, J., Hetenyi, G., Vergne, J., Sapkota, S., Kafle, B., Jiang, M., . . . Team, H.-C. (2009). Underplating in the himalaya-tibet collision zone revealed by the hi-climb experiment. *Science*, *325*(5946), 1371-1374. doi: 10.1126/science.1167719

Negredo, A. M., Replumaz, A., Villasenor, A., & Guillot, S. (2007). Modeling the evolution of continental subduction processes in the pamir-hindu kush region. *Earth and Planetary Science Letters*, *259*(1-2), 212-225. doi: 10.1016/j.epsl.2007.04.043

Owens, T. J., & Zandt, G. (1997). Implications of crustal property variations for models of tibetan plateau evolution. *Nature*, *387*(6628), 37-43. doi: DOI10 .1038/387037a0

Poudjom Djomani, Y. H., O'Reilly, S. Y., Griffin, W. L., & Morgan, P. (2001). The density structure of subcontinental lithosphere through time. *Earth and Planetary Science Letters*, *184*(3-4), 605-621.

Pysklywec, R. N., & Beaumont, C. (2004). Intraplate tectonics: feedback between radioactive thermal weakening and crustal deformation driven by mantle lithosphere instabilities. *Earth and Planetary Science Letters*, *221*(1-4), 275-292. doi: 10.1016/S0012-821x(04)00098-6

Replumaz, A., Negredo, A. M., Guillot, S., van der Beek, P., & Villasenor, A. (2010). Crustal mass budget and recycling during the india/asia collision. *Tectonophysics*, *492*(1-4), 99-107. doi: 10.1016/j.tecto.2010.05.023

Replumaz, A., & Tapponnier, P. (2003). Reconstruction of the deformed collision zone between india and asia by backward motion of lithospheric blocks. *Journal of Geophysical Research-Solid Earth*, *108*(B6). doi:

Artn228510.1029/2001jb000661

Robinson, D. M. (2008). Forward modeling the kinematic sequence of the central himalayan thrust belt, western nepal. *Geosphere*, *4*(5), 785-801. doi: 10.1130/Ges00163.1

Rohrmann, A., Kapp, P., Carrapa, B., Reiners, P. W., Guynn, J., Ding, L., & Heizler, M. (2012). Thermochronologic evidence for plateau formation in central tibet by 45 ma. *Geology*, *40*(2), 187-190. doi: 10.1130/G32530.1

Rosenberg, C. L., & Kissling, E. (2013). Three-dimensional insight into central-alpine collision: Lower-plate or upper-plate indentation? *Geology*, *41*(12), 1219-1222. doi: 10.1130/G34584.1

Ruh, J. B., Gerya, T., & Burg, J.-P. (2017). Toward 4d modeling of orogenic belts: Example from the transpressive zagros fold belt. *Tectonophysics*, *702*(Supplement C), 82-89. doi: https://doi.org/10.1016/j.tecto.2015.09.035

Sandiford, M., & Powell, R. (1990). Some isostatic and thermal consequences of the vertical strain geometry in convergent orogens. *Earth and Planetary Science Letters*, *98*(2), 154-165. doi: Doi10.1016/0012-821x(90)90056-4

Schmalholz, S. M., Medvedev, S., Lechmann, S. M., & Podladchikov, Y. (2014). Relationship between tectonic overpressure, deviatoric stress, driving force, isostasy and gravitational potential energy. *Geophysical Journal International*, *197*(2), 680-696. doi: 10.1093/gji/ggu040

Schmid, S. M., Fugenschuh, B., Kissling, E., & Schuster, R. (2004). Tectonic map and overall architecture of the alpine orogen. *Eclogae Geologicae Helvetiae*, *97*(1), 93-117. doi: 10.1007/s00015-004-1113-x

Schmid, S. M., & Kissling, E. (2000). The arc of the western alps in the light of geophysical data on deep crustal structure. *Tectonics*, *19*(1), 62-85. doi: Doi10.1029/1999tc900057

Schmid, S. M., Kissling, E., Diehl, T., van Hinsbergen, D. J. J., & Molli, G. (2017). Ivrea mantle wedge, arc of the western alps, and kinematic evolution of the alps-apennines orogenic system. *Swiss Journal of Geosciences*, *110*(2), 581-612. doi: 10.1007/s00015-016-0237-0

Schmid, S. M., Pfiffner, O. A., Froitzheim, N., Schonborn, G., & Kissling, E. (1996). Geophysical-geological transect and tectonic evolution of the swiss-italian alps. *Tectonics*, *15*(5), 1036-1064. doi: Doi10.1029/96tc00433

Schurr, B., Rietbrock, A., Asch, G., Kind, R., & Oncken, O. (2006). Evidence for lithospheric detachment in the central Andes from local earthquake tomography. *Tectonophysics*, *415*(1-4), 203-223. doi: 10.1016/j.tecto.2005.12.007

Sibuet, J. C., Srivastava, S. P., & Spakman, W. (2004). Pyrenean orogeny and plate kinematics. *Journal of Geophysical Research-Solid Earth*, *109*(B8). doi: ArtnB0810410.1029/2003jb002514

Sommaruga, A. (1999). Decollement tectonics in the jura foreland fold-and-thrust belt. *Marine and Petroleum Geology*, *16*(2), 111-134. doi: Doi10.1016/S0264-8172(98)00068-3

Stampfli, G. M., Mosar, J., Marquer, D., Marchant, R., Baudin, T., & Borel, G. (1998). Subduction and obduction processes in the swiss alps. *Tectonophysics*, *296*(1-2), 159-204. doi: Doi10.1016/S0040-1951(98)00142-5

Stock, J. D., & Montgomery, D. R. (1999). Geologic constraints on bedrock river incision using the stream power law. *Journal of Geophysical Research: Solid Earth*, *104*(B3), 4983–4993.

Stockmal, G. S., Beaumont, C., Nguyen, M., & Lee, B. (2007). Mechanics of thin-skinned fold-and-thrust belts: Insights from numerical models whence the mountains? inquiries into the evolution of orogenic systems: A volume in honor of raymond a. price. In J. W. Sears, T. A. Harms, & C. A. Evenchick (Eds.), (Vol. 433, p. 0). Geological Society of America. doi: 10.1130/2007.2433(04)

Stolar, D. B., Roe, G. H., & Willett, S. D. (2007). Controls on the patterns of

topography and erosion rate in a critical orogen. *Journal of Geophysical Research-Earth Surface*, *112*(F4). doi: ArtnF0400210.1029/2006jf000713

Stolar, D. B., Willett, S. D., & Roe, G. H. (2006). Climatic and tectonic forcing of a critical orogen. *SPECIAL PAPERS-GEOLOGICAL SOCIETY OF AMER-ICA*, *398*, 241.

Teixell, A., Labaume, P., Ayarza, P., Espurt, N., de Saint Blanquat, M., & Lagabrielle, Y. (2018). Crustal structure and evolution of the pyrenean-cantabrian belt: A review and new interpretations from recent concepts and data. *Tectonophysics*, *724*, 146-170. doi: 10.1016/j.tecto.2018.01.009

Thieulot, C. (2011). Fantom: Two- and three-dimensional numerical modelling of creeping flows for the solution of geological problems. *Physics of the Earth and Planetary Interiors*, *188*(1-2), 47-68. doi: 10.1016/j.pepi.2011.06.011

Thieulot, C., Steer, P., & Huismans, R. S. (2014). Three-dimensional numerical simulations of crustal systems undergoing orogeny and subjected to surface processes. *Geochemistry Geophysics Geosystems*, *15*(12), 4936-4957. doi: 10.1002/2014gc005490

Tsenn, M. C., & Carter, N. L. (1987). Upper limits of power law creep of rocks. *Tectonophysics*, *136*(1-2), 1-26. doi: 10.1016/0040-1951(87)90332-5

Tugend, J., Manatschal, G., Kusznir, N. J., Masini, E., Mohn, G., & Thinon, I. (2014). Formation and deformation of hyperextended rift systems: Insights from rift domain mapping in the bay of biscay-pyrenees. *Tectonics*, *33*(7), 1239-1276. doi: 10.1002/2014tc003529

Turcotte, D. L., & Schubert, G. (1982). *Geodynamics.* John Wiley New York.

Ueda, K., Willett, S. D., Gerya, T., & Ruh, J. (2015). Geomorphological-thermo-mechanical modeling: Application to orogenic wedge dynamics. *Tectonophysics*, *659*, 12-30. doi: 10.1016/j.tecto.2015.08.001

van der Beek, P., Van Melle, J., Guillot, S., Pecher, A., Reiners, P. W., Nicolescu, S., & Latif, M. (2009). Eocene tibetan plateau remnants preserved in the northwest himalaya. *Nature Geoscience*, *2*(5), 364-368. doi: 10.1038/Ngeo503

Vanderhaeghe, O., Medvedev, S., Fullsack, P., Beaumont, C., & Jamieson, R. A. (2003). Evolution of orogenic wedges and continental plateaux: insights from crustal thermal-mechanical models overlying subducting mantle lithosphere. *Geophysical Journal International*, *153*(1), 27-51. doi: DOI10.1046/j.1365-246X.2003.01861.x

Vogt, K., Willingshofer, E., Matenco, L., Sokoutis, D., Gerya, T., & Cloetingh, U. S. (2018). The role of lateral strength contrasts in orogenesis: A 2d numerical study. *Tectonophysics*, *746*, 549-561. doi: 10.1016/j.tecto.2017.08.010

Volkmer, J. E., Kapp, P., Guynn, J. H., & Lai, Q. Z. (2007). Cretaceous-tertiary structural evolution of the north central lhasa terrane, tibet. *Tectonics*, *26*(6). doi: ArtnTc600710.1029/2005tc001832

Wang, C. S., Dai, J. G., Zhao, X. X., Li, Y. L., Graham, S. A., He, D. F., . . . Meng, J. (2014). Outward-growth of the tibetan plateau during the cenozoic: A review. *Tectonophysics*, *621*, 1-43. doi: 10.1016/j.tecto.2014.01.036

Whipple, K. X., & Meade, B. J. (2004). Controls on the strength of coupling among climate, erosion, and deformation in two-sided, frictional orogenic wedges at steady state. *Journal of Geophysical Research-Earth Surface*, *109*(F1). doi: ArtnF0101110.1029/2003jf000019

Whipple, K. X., & Meade, B. J. (2006). Orogen response to changes in climatic and tectonic forcing. *Earth and Planetary Science Letters*, *243*(1), 218-228. doi: https://doi.org/10.1016/j.epsl.2005.12.022

Whipple, K. X., & Tucker, G. E. (1999). Dynamics of the stream-power river incision model: Implications for height limits of mountain ranges, landscape response timescales, and research needs. *Journal of Geophysical Research-Solid Earth*, *104*(B8), 17661-17674. doi: Doi10.1029/1999jb900120

Willett, S. D. (1999). Orogeny and orography: The effects of erosion on the

structure of mountain belts. *Journal of Geophysical Research-Solid Earth*, *104*(B12), 28957-28981. doi: Doi10.1029/1999jb900248

Willett, S. D., & Beaumont, C. (1994). Subduction of asian lithospheric mantle beneath tibet inferred from models of continental collision. *Nature*, *369*(6482), 642-645. doi: DOI10.1038/369642a0

Willett, S. D., Beaumont, C., & Fullsack, P. (1993). Mechanical model for the tectonics of doubly vergent compressional orogens. *Geology*, *21*(4), 371-374. doi: Doi10.1130/0091-7613(1993)021⟨0371:Mmftto⟩2.3.Co;2

Willett, S. D., & Brandon, M. T. (2002). On steady states in mountain belts. *Geology*, *30*(2), 175-178. doi: Doi10.1130/0091-7613(2002)030⟨0175:Ossimb⟩2.0.Co;2

Willett, S. D., Slingerland, R., & Hovius, N. (2001). Uplift, shortening, and steady-state topography in active mountain belts. *American Journal of Science*, *301*(4-5), 455-485. doi: DOI10.2475/ajs.301.4-5.455

Wilson, J. T. (1966). Did atlantic close and then re-open. *Nature*, *211*(5050), 676-&. doi: DOI10.1038/211676a0

Wobus, C. W., Hodges, K. V., & Whipple, K. X. (2003). Has focused denudation sustained active thrusting at the himalayan topographic front? *Geology*, *31*(10), 861-864. doi: Doi10.1130/G19730.1

Wolf, S. G., & Huismans, R. S. (2019). Mountain building or backarc extension in ocean-continent subduction systems - a function of backarc lithospheric strength and absolute plate velocities. *Journal of Geophysical Research: Solid Earth*, *0*(ja). doi: 10.1029/2018JB017171

Yi, Z. Y., Huang, B. C., Chen, J. S., Chen, L. W., & Wang, H. L. (2011). Paleomagnetism of early paleogene marine sediments in southern tibet, china: Implications to onset of the india-asia collision and size of greater india. *Earth and Planetary Science Letters*, *309*(1-2), 153-165. doi: 10.1016/j.epsl.2011.07.001

Yin, A., & Harrison, T. M. (2000). Geologic evolution of the himalayan-tibetan orogen. *Annual Review of Earth and Planetary Sciences*, *28*(1), 211-280. doi: 10.1146/annurev.earth.28.1.211

Yuan, X., Braun, J., Guerit, L., Rouby, D., & Cordonnier, G. (2019). A new efficient method to solve the stream power law model taking into account sediment deposition. *Journal of Geophysical Research: Earth Surface*, *0*(ja). doi: 10.1029/2018jf004867

Zhou, S. H., & Sandiford, M. (1992). On the stability of isostatically compensated mountain belts. *Journal of Geophysical Research-Solid Earth*, *97*(B10), 14207-14221. doi: Doi10.1029/92jb01091

Supporting Information for "Growth of collisional orogens from small and cold to large and hot - inferences from geodynamic models"

S. G. Wolf[1], R. S. Huismans[1], J.-A. Muñoz[2], M. Ellis Curry[3,4], P. van der Beek[3,5]

[1]Department of Earth Science, Bergen University, Bergen N-5007, Norway
[2]Geomodels Research Institute, University of Barcelona, Barcelona, Spain
[3]Université Grenoble Alps, CNRS, ISTerre, CS40700, 38058 Grenoble, France
[4]Department of Earth and Atmospheric Sciences, University of Houston, 77004 Texas, United States of America
[5]Insitut für Geowissenschaften, Universität Potsdam, 14476 Potsdam, Germany

Contents of this file

Introduction The supplementary material contains six additional models with small parameter variations of the models presented in the main text. Furthermore, this supplementary file includes the Fastscape surfaces and elevation profiles of models M5, M6, and M7 (Figs. S3, S4, S5), and animations of all models.

The first two additional models have the same setup as M1, but with velocity boundary conditions applied only on the left, respectively right side (Fig. S1). These models show that model evolution is independent of the absolute reference frame.

Supplementary models SM3 and SM4 are variations of M1, one with a higher convergence velocity of 3 cm/yr (SM3), and one with higher radioactive heat production in the upper and middle crust (SM4) (Fig. S2). SM3 shows plateau formation after greater amounts of convergence and with a thicker crust, and SM4 shows retro-Moho-flattening and thus plateau formation after less convergence and with a lower crustal thickness. Heat production in SM4 is higher in the upper and middle crust and zero in the lower crust $H_{UC,MC} = 1.63 \, \mu Wm^{-3}$, $H_{LC} = 0 \, \mu Wm^{-3}$. The values are chosen to initially create the same Moho temperature as in M1, and lead to a temperature increase at the base of the middle crust by 12 °C at model start.

Supplementary model SM5 is a variation of M5, with "medium" fluvial erodibility ($K_f = 1 \times 10^{-5} \, m^{0.2}/yr$, Figs. S6, S7). This model shows the influence medium fluvial erodibility on mountain belt growth. Overall model evolution is similar to M5. Greater erosional efficiency leads to enhanced exhumation in the model centre. Furthermore, foreland basins are already overfilled after ~30 Myr and the subsequent orogenic growth is delayed on average by 30 % to 40 %, creating an overall smaller orogen. Corresponding high sediment flux creates long thick-skinned thrust sheets once the orogen is large.

Supplementary model SM6 is a variation of M6, with "very high" fluvial erodibility ($K_f = 7.5 \times 10^{-5} \, m^{0.2}/yr$, Figs. S8, S9). This model shows the influence of very high fluvial erodibility on mountain belt growth. Overall model evolution is similar to M6. Very efficient surface processes lead to flux steady state between erosion and tectonic accretion of material once the orogen is 80 - 100 km wide. At steady state the orogen is perturbed by newly formed thrust sheets, which get subsequently removed. Hence, although the orogen roughly keeps its size and shape, orogen evolution is very dynamic.

The supplementary material also contains a diagram showing mountain belt evolution normalized to the S-point (Fig. S10).

Model animations (Files uploaded separately) Animations of all models can be found in the data repository. Models M1 - M4 show the whole modelled domain in the lower panel and a zoom inset in the upper panel. Both plots show the material colors (see legend in Fig. 2) and the temperature field displayed with isotherms: 350 °C, 550 °C, 1330 °C, 1500 °C in lower panel and 350 °C, 550 °C in zoom inset. The white, transparent overlay in the upper panel highlights strain-weakened shear zones.

Animations of Models M5, M6, M7, SM5, and SM6 show a zoom of the thermo-mechanical model with the surface process model on top. Material colors are according to the legend in Fig. 2 and the temperature isotherms are 100 °C, 350 °C, 550 °C, 700 °C, and 1330 °C.

Animation MS01: M1, reference model, no depletion of lithospheric mantle

Animation MS02: M2, 20 kg/m³ depletion of lithospheric mantle

Animation MS03: M3, 40 kg/m³ depletion of lithospheric mantle

Animation MS04: M4, No depletion of lithospheric mantle, 150 km extensional inheritance

Animation MS05: M5, No depletion of lithospheric mantle, with surface processes, low surface process efficiency

Animation MS06: M6, No depletion of lithospheric mantle, with surface processes, high surface process efficiency

Animation MS07: M7, No depletion of lithospheric mantle, with surface processes, with weak, shallow salt décollement

Animation MS08: SM5, No depletion of lithospheric mantle, with surface processes, medium surface process efficiency

Animation MS09: SM7, No depletion of lithospheric mantle, with surface processes, very high surface process efficiency
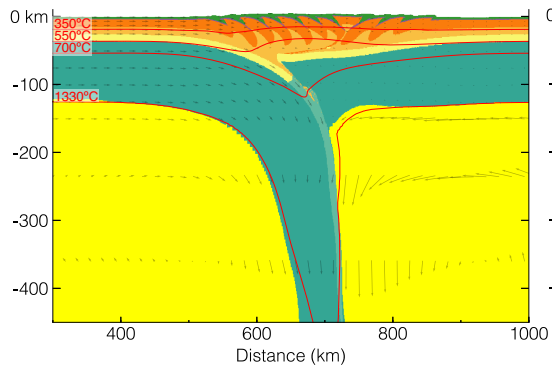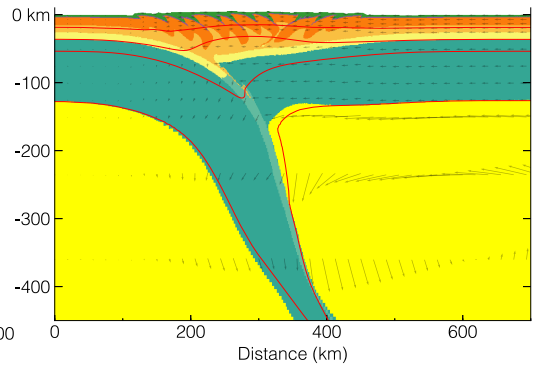
SM1: M1, velocity b.c. on left side

SM2: M1, velocity b.c. on right side

a) t = 40 Myr, Δx = 400 km

b) t = 40 Myr, Δx = 400 km

Figure S1. Models SM1 (M1_Left, a) and SM2 (M1_Right, b). The model setup is the same as in M1 with full velocity boundary conditions (b.c.) only applied on the left, respectively right side. Snapshots show material colors (see Fig. 2) with isotherms and quivers with length relative to local magnitude. t is model time, Δx is the amount of convergence. The models show that model evolution is independent of the kinematics of continent-continent collision.

SM3: Convergence velocity = 3 cm/yr

a) t = 10 Myr, Δx = 300 km

b) t = 23.33 Myr, Δx = 700 km
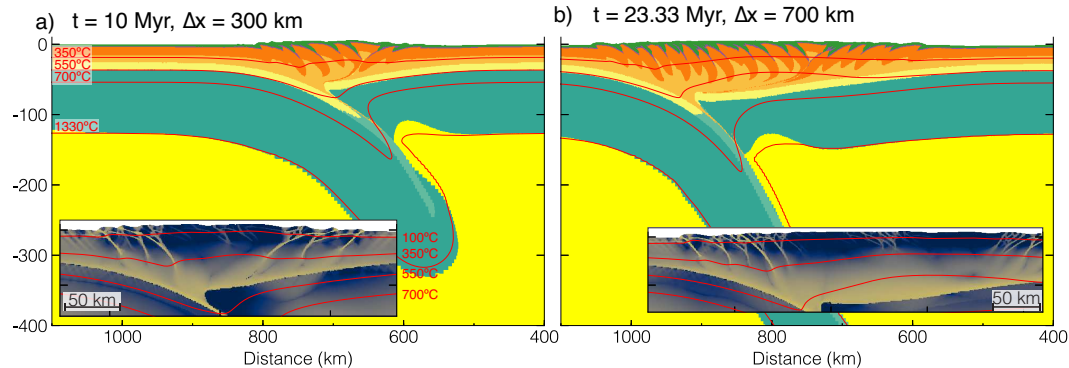
SM4: High heat production in upper/middle crust

c) t = 30 Myr, Δx = 300 km

d) t = 70 Myr, Δx = 700 km

Viscosity (Pa s)
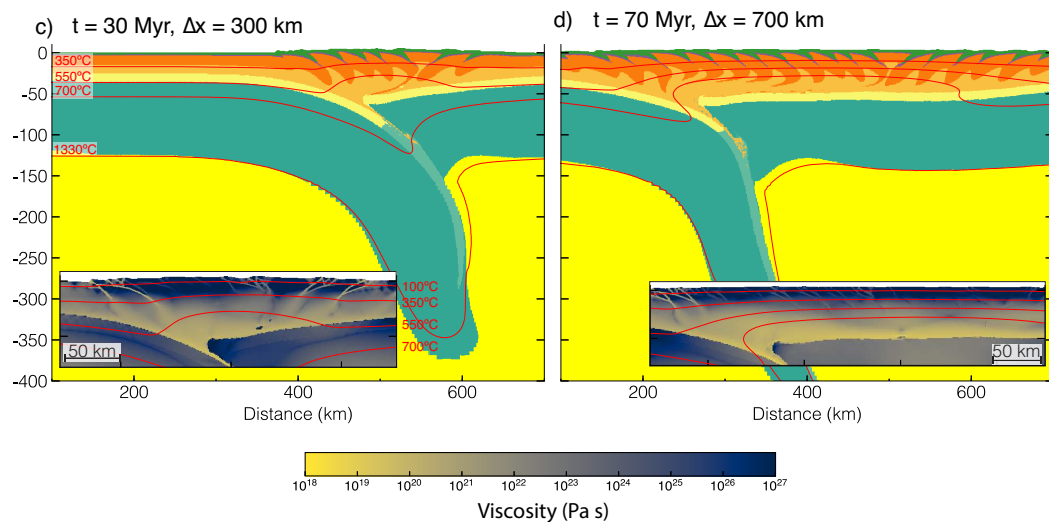
Figure S2.   Models SM3 (SMvel3, a, b) and SM4 (SMhighH, c, d). In SM3 the model setup is the same as in M1, but cumulative convergence velocity is 3 cm/yr instead of 1 cm/yr. SM4 has same model setup as M1, but different heat production in the crust. Heat production is higher in the upper and middle crust and zero in the lower crust. Initial Moho-temperature is the same as in M1, the temperature on the bottom of the middle crust is raised by 12 °C. Snapshots show material colors with isotherms. Zoom insets show viscosity field with logarithmic colormap and temperature isotherms of the crustal domain. t is model time, Δx is the amount of convergence. The models highlight that plateau formation is delayed by high convergence rates, and occurs earlier if radioactive crustal heat production is high.

M5: No depletion, with surface processes, low surface process efficiency

a)   t = 15 Myr, Δx = 150 km

b)   t = 30 Myr, Δx = 300 km

c)   t = 70 Myr, Δx = 700 km

d)   Legend
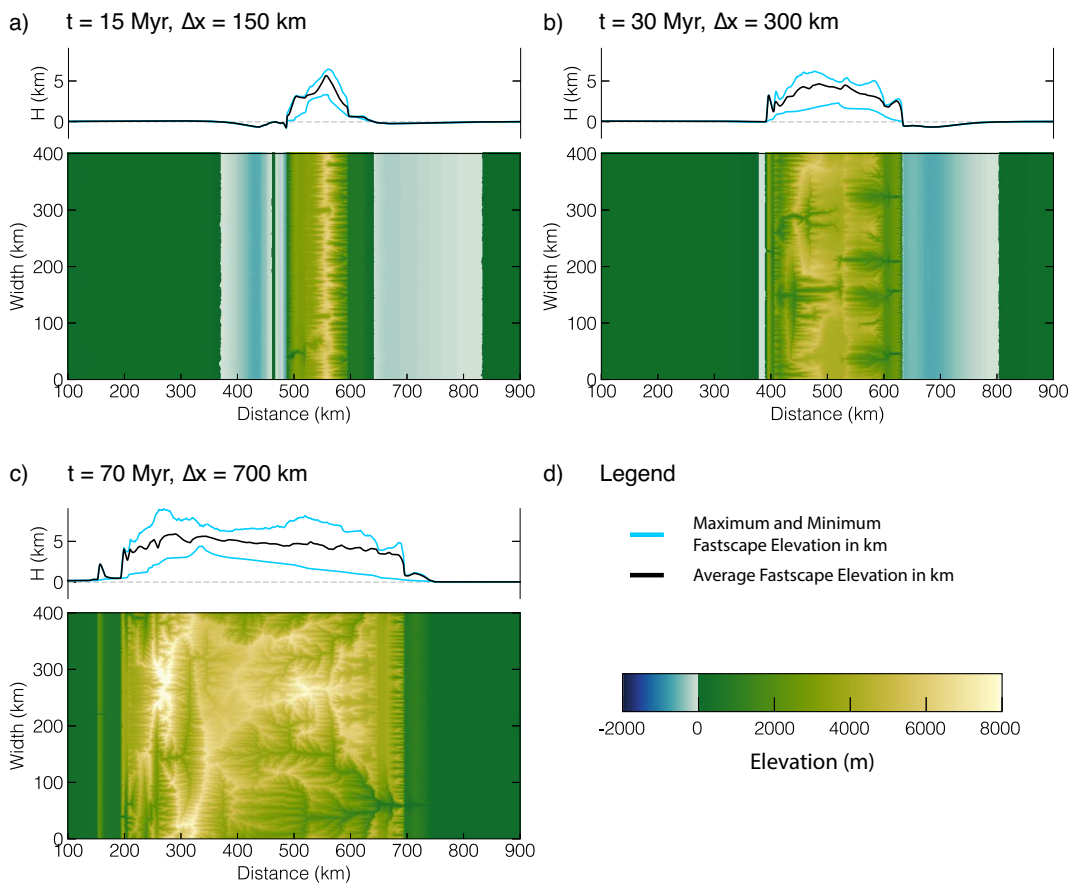
Figure S3. Model M5 without depletion of the lithospheric mantle, including a full coupling with surface processes ($K_f = 0.5 \times 10^{-5}\,\mathrm{m}^{0.2}/\mathrm{yr}$). (a-c) FastScape surface elevation in m and maximum, minimum and average surface elevation in km. t is model time, Δx is the amount of convergence. The snapshots correspond to Fig. 5 in the manuscript. (d) Legend with colorbar for a-c.

M6: No depletion, surface processes, high surface process efficiency

a)   t = 15 Myr, Δx = 150 km

b)   t = 30 Myr, Δx = 300 km

c)   t = 70 Myr, Δx = 700 km

d)   Legend

Maximum and Minimum
Fastscape Elevation in km

Average Fastscape Elevation in km

-2000   0   2000   4000   6000   8000
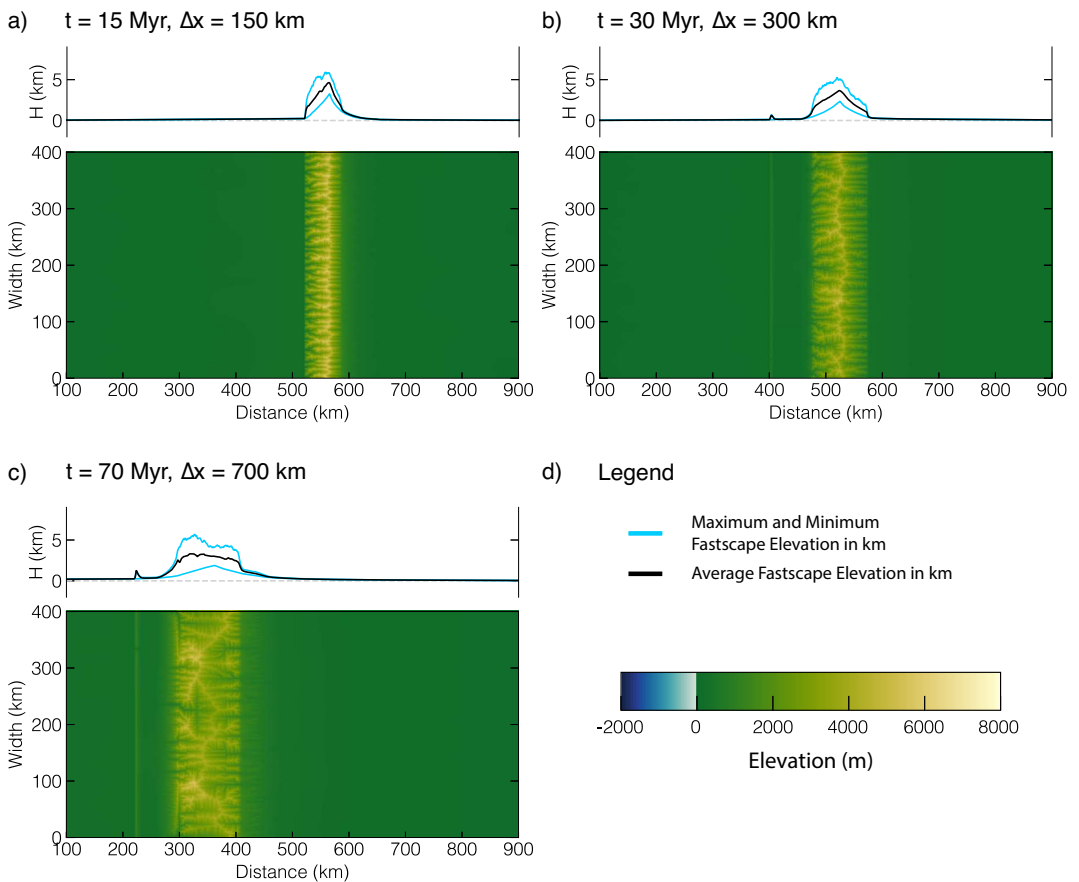
Elevation (m)

Figure S4. Model M5 without depletion of the litho-spheric mantle, including a full coupling with surface processes ($K_f = 5 \times 10^{-5}\,\mathrm{m}^{0.2}/\mathrm{yr}$). (a-c) FastScape surface elevation in m and maximum, minimum and average surface elevation in km. t is model time, Δx is the amount of convergence. The snapshots correspond to Fig. 7 in the manuscript. (d) Legend with colorbar for a-c.
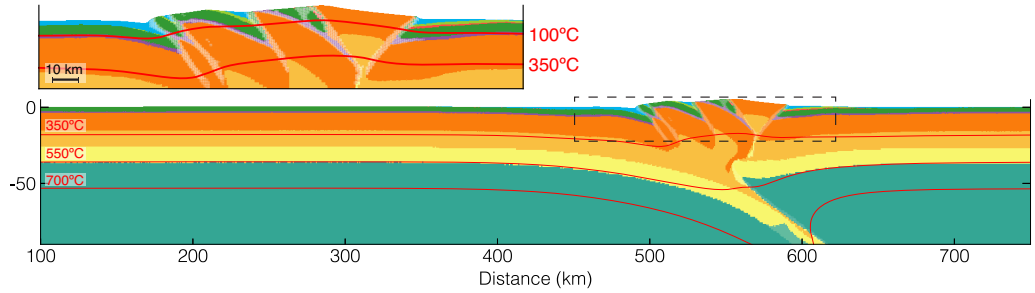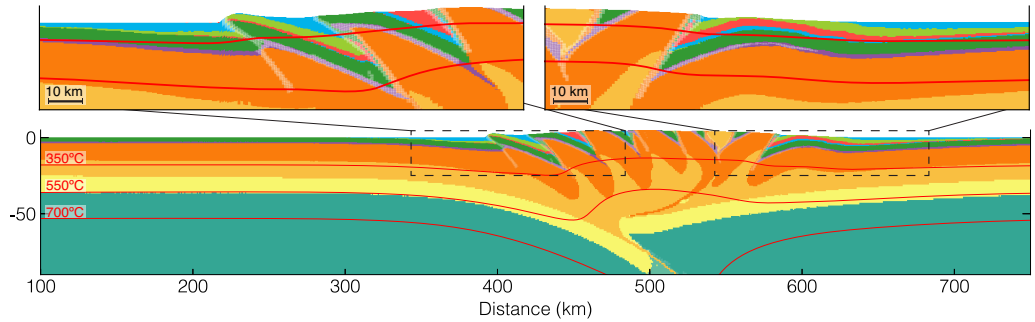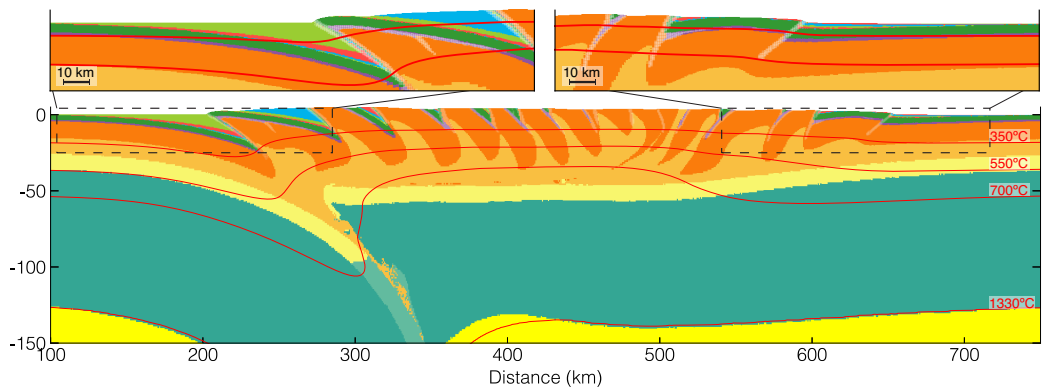
M7 (MSpDéc): No depletion, with surface processes, with weak décollement
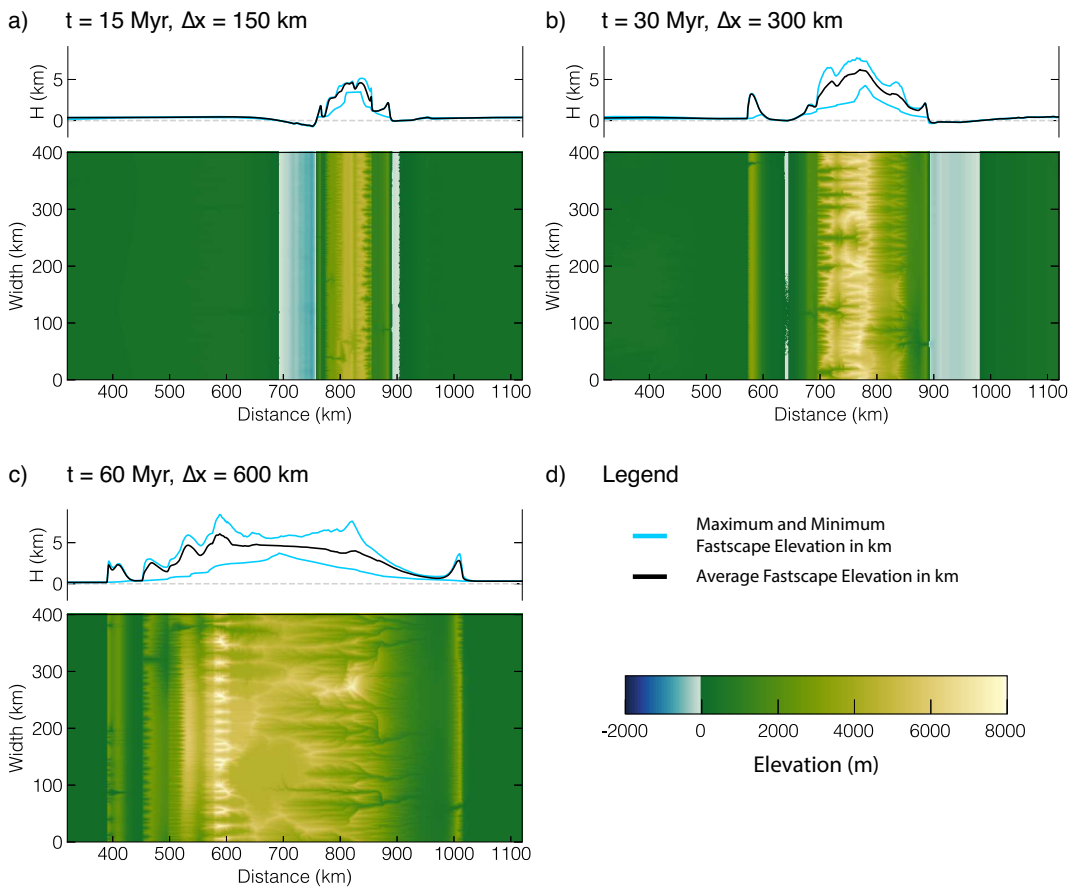
Figure S5. Model M6 without depletion of the lithospheric mantle, including a full coupling with surface processes ($K_f = 0.5 \times 10^{-5}\,\mathrm{m^{0.2}/yr}$), and a weak décollement horizon. (a-c) FastScape surface elevation in m and maximum, minimum and average surface elevation in km. t is model time, Δx is the amount of convergence. The snapshots correspond to Fig. 8 in the manuscript. (d) Legend with colorbar for a-c.
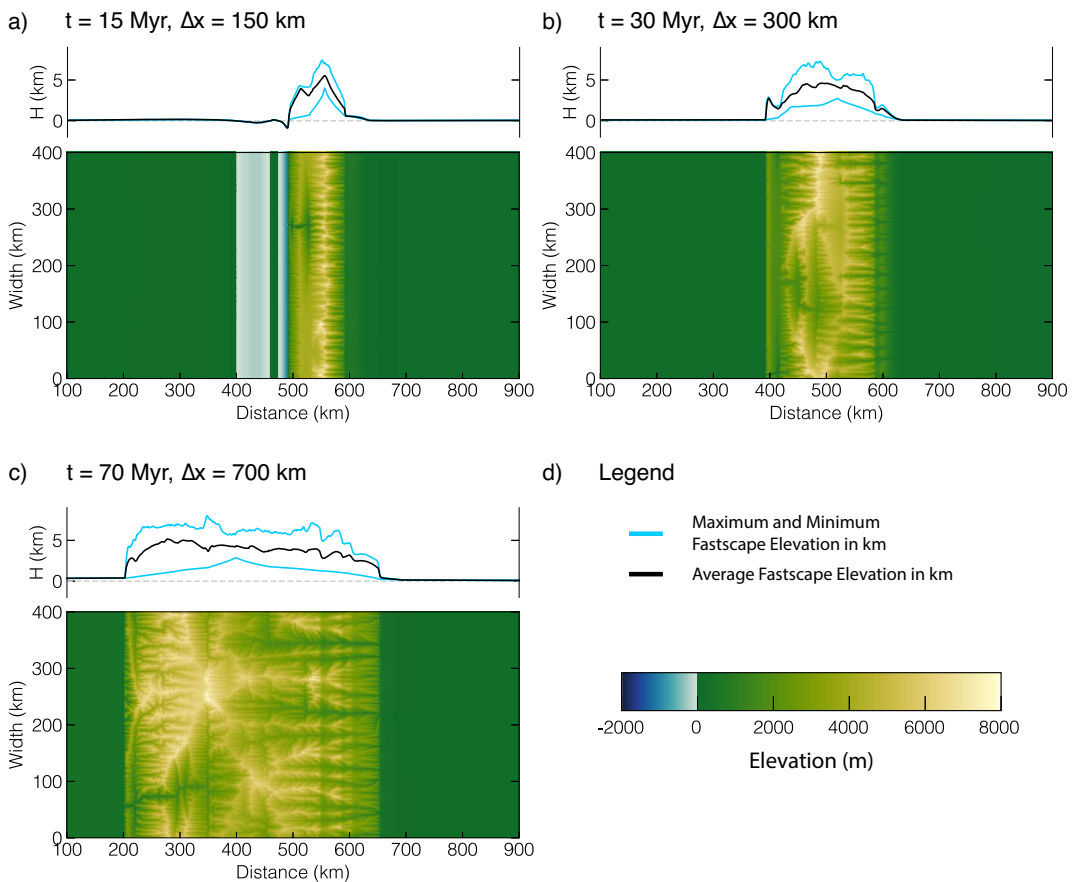
SM5: No depletion, surface processes, medium surface process efficiency

Figure S6. Model SM5 without depletion of the lithospheric mantle, including a full coupling with surface processes and medium fluvial erodibility ($K_f = 1 \times 10^{-5}\,\mathrm{m}^{0.2}/\mathrm{yr}$). (a-c) Material colors (see Fig. 2) with isotherms. t is model time, Δx is the amount of convergence. Zoom insets show close-up of crustal domains. The white overlay highlights strain-weakened shear zones.

SM5: No depletion, surface processes, medium surface process efficiency

Figure S7.   Model SM5 without depletion of the lithospheric mantle, including a full coupling with surface processes and medium fluvial erodibility ($K_f = 1 \times 10^{-5}\,\mathrm{m}^{0.2}/\mathrm{yr}$). (a-c) FastScape surface elevation in m and maximum, minimum and average surface elevation in km. t is model time, Δx is the amount of convergence. The snapshots correspond to Fig. S6. (d) Legend with colorbar for a-c.
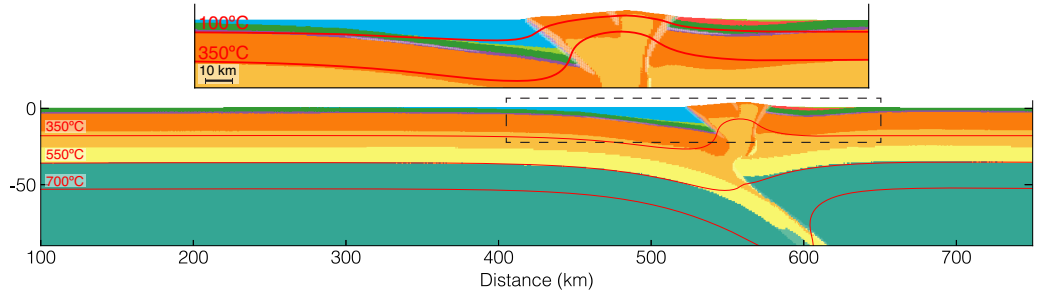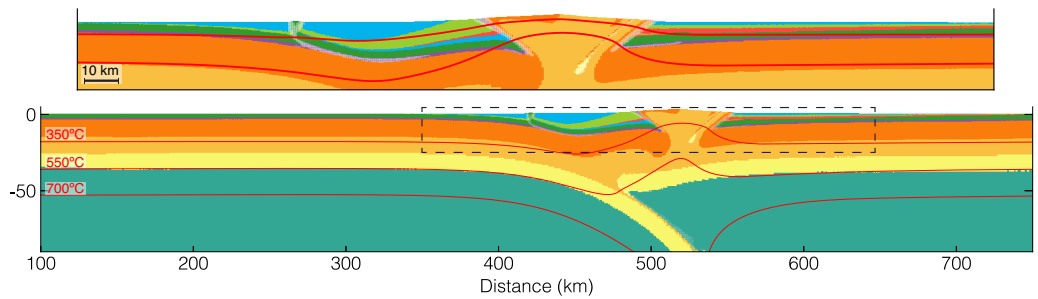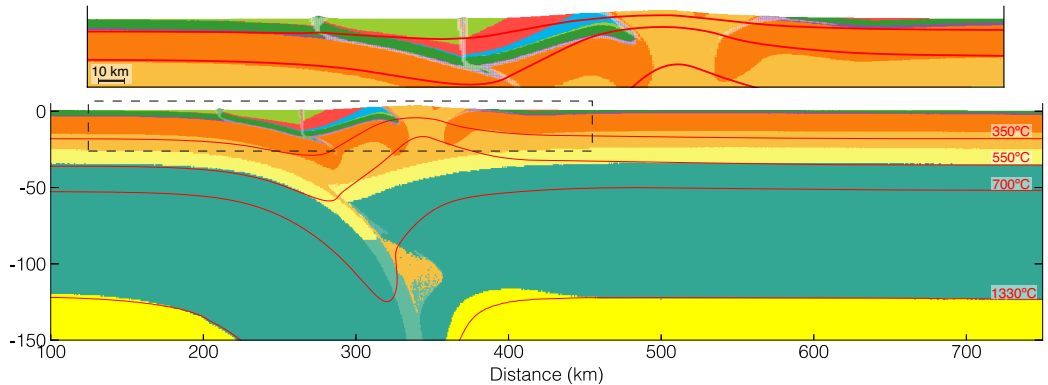
SM6: No depletion, with surface processes, very high surface process efficiency

a)   t = 15 Myr, Δx = 150 km

b)   t = 30 Myr, Δx = 300 km

c)   t = 70 Myr, Δx = 700 km

Figure S8.   Model SM6 without depletion of the lithospheric mantle, including a full coupling with surface processes and very high fluvial erodibility ($K_f = 7.5 \times 10^{-5}\,\mathrm{m}^{0.2}/\mathrm{yr}$). (a-c) Material colors (see Fig. 2) with isotherms. t is model time, Δx is the amount of convergence. Zoom insets show close-up of crustal domains. The white overlay highlights strain-weakened shear zones.

SM6: No depletion, with surface processes, very high surface process efficiency

a)   t = 15 Myr, Δx = 150 km

b)   t = 30 Myr, Δx = 300 km

c)   t = 70 Myr, Δx = 700 km

d)   Legend

Maximum and Minimum
Fastscape Elevation in km

Average Fastscape Elevation in km
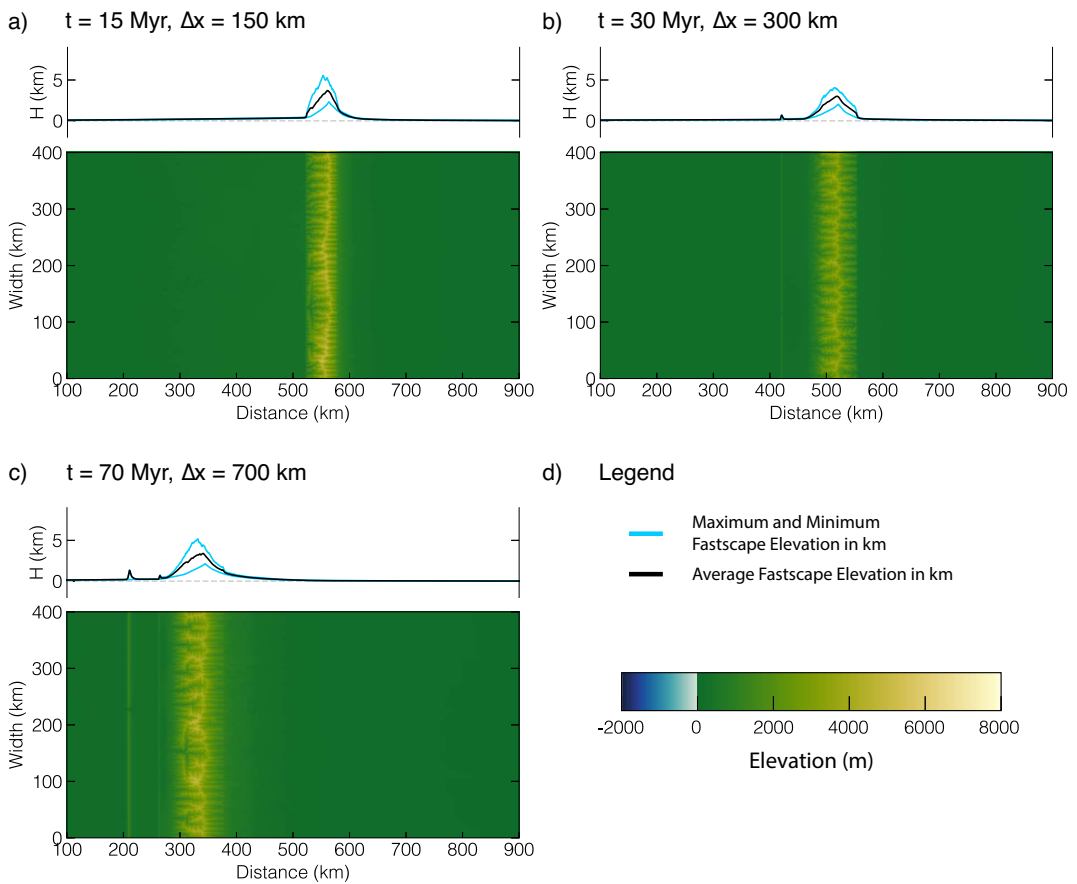
Elevation (m)

Figure S9.   Model SM6 without depletion of the lithospheric mantle, including a full coupling with surface processes and very high fluvial erodibility ($K_f = 7.5 \times 10^{-5}\,\mathrm{m}^{0.2}/\mathrm{yr}$). (a-c) FastScape surface elevation in m and maximum, minimum and average surface elevation in km. t is model time, Δx is the amount of convergence. The snapshots correspond to Fig. S8. (d) Legend with colorbar for a-c.
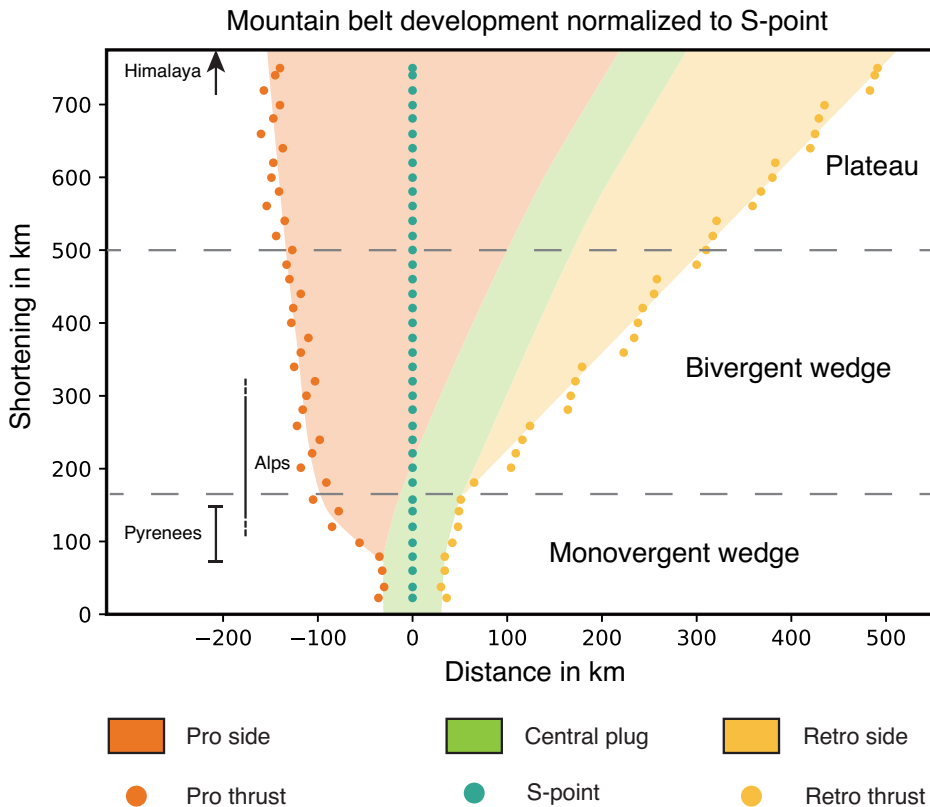
Figure S10. Evolution of shortening in models without surface processes normalised to S-point. Initial shortening creates a structurally monovergent wedge with deformation on the pro-side and the central, uplifted plug. After more than ≈ 150 km of shortening a structurally bivergent wedge forms, characterised by additional retro-side deformation. After more than 500 km of shortening a plateau flanked by wedges forms. With onset of retro-side shortening the orogen starts to migrate onto the retro-side. Note the jumps of the pro- and retro-thrusts. These correspond to formation of new thick skinned thrust sheets. See main manuscript for discussion about shortening estimates for the Pyrenees, Western Alps and Himalayas.

3 Synthesis

In this chapter I summarize the findings of the main body of this thesis, the four articles, which each pursue different aspects of the overarching main research question: What controls the evolution of mountain belts on Earth? In article one, I investigated mountain building and back-arc extension in ocean-continent subduction settings. For this study I created a set of geodynamic models to explain the parameter combinations that lead to either overriding plate extension, or shortening, and investigated the driving forces of model evolution. The second through fourth articles explored different aspects of mountain building during continent-continent collision. To explore the influence of surface processes on mountain building, I developed a coupling between a thermo-mechanical model with a surface process model. Inspired by the temperature-magnitude diagram of mountain building, I investigated whether orogenic growth from a small and cold to a large and hot orogen follows a typical distribution of shortening and structural style as a function of orogen size, and investigated its underlying controlling factors. The interaction between surface processes and tectonics, more specifically the controlling factors of topographic evolution of mountain belts during growth and decay, were the focus of the third and fourth article in this thesis. The fourth article builds on the results of the third, provides several additions, clarifications, and a scaling relationship linking surface processes to the tectonics of mountain building. The main body of each article were numerical models that I compared to different orogens on Earth, most notably the Pyrenees, Alps, Himalaya-Tibet, Andes, Southern Alps of New Zealand and Taiwan. In the subsequent section I consolidate the main findings and implications of this thesis, which is followed by an outlook section in which I propose future research questions and avenues.

3.1 Main findings and wider implications

Research in this thesis gives new insight into mountain building processes in different settings, and provides a new modelling tool linking tectonics, surface processes and stratigraphy. The main findings are illustrated in figures 3.1 to 3.3 and will be summa-

rized in the following 3 subsections.

3.1.1 Towards models integrating tectonics, surface processes and stratigraphy

In this thesis, I developed and used a coupling between a 2D thermo-mechanical model and a 2D surface process model. Both models are tightly coupled so that deposited sediments get deformed by tectonic movement. An additional stratigraphy routine based on a marker in cell approach tracks information about sediments deposited by the surface process model, and gives the possibility to link tectonics, surface processes and stratigraphy. Adding stratigraphic information from our models was beyond the scope of the research questions posed and answered in this thesis, and will be subject of further studies.

3.1.2 Overriding plate deformation in ocean-continent collision zones

Mountain building or back-arc extension in ocean-continent subduction settings is determined by plate velocities. Thereby, as a result of slab anchoring in the lower mantle, the absolute and not the relative plate velocities determine the overriding plate strain regime: Mountain building is promoted by high subduction velocity and when the overriding plate moves towards the trench. Extension is promoted when the overriding plate is not moving towards the trench (Fig. 3.1). Extension and shortening furthermore require removal of a weak back-arc lithospheric mantle. A strong back-arc lithosphere inhibits back-arc extension and leads to ablative overriding plate shortening which is not observed on Earth. Our force balance analysis provides driving and resisting forces for subduction during model evolution, and shows near equilibrium of forces. Near equilibrium supports the requirement of a weak overriding plate to deform it. Comparison of model results with the Andes and the Hellenic subduction zone supports modelling inferences.

Our results have wider implications for the understanding of subduction systems, as they provide a possible explanation for the minimum factors needed for overriding plate deformation in ocean-continent subduction systems. Especially the force-balance analysis provides a useful tool to understand the importance of different regions and processes during ocean-continent subduction systems.

Factors controlling overriding plate deformation during ocean-continent subduction
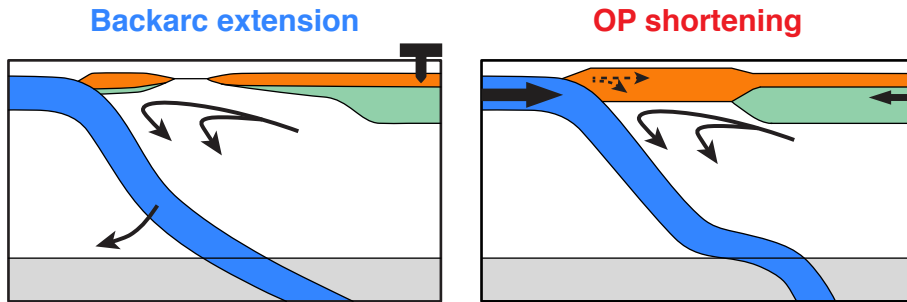

Figure 3.1: Sketch of an ocean-continent subduction zone with key processes influencing deformation of the overriding plate (OP). An overriding plate not moving towards the trench and weak lithospheric mantle promote backarc extension. Overriding plate movement towards the trench and a weak and removed lithospheric mantle promote overriding plate shortening.

3.1.3 The interplay between tectonics and surface processes during continent-continent collision

We find a relationship between orogen size and mountain belt style in terms of pro- versus retro-wedge deformation during continent-continent collision (Fig. 3.2): Small and cold orogens are expected to show localisation of deformation mainly on the pro-side and in inverted extensional structures. Increasing shortening leads to loading of the retro-plate, which additionally invokes deformation of the retro-side of the orogen. With further shortening, mountain belts are expected to form a large and hot plateau flanked by wedges. Large and hot orogens are furthermore expected to sit mainly on the retro-lithosphere as a result of underthrusting of the retro-mantle. This evolutionary sequence has been already observed in very early S-point models (e.g. Willett and Beaumont 1994; Vanderhaeghe et al. 2003). We provide additional insight through quantification of the evolutionary sequence and its underlying controls. The evolution from small to large is independent of slab pull of the subducting lithospheric mantle, and a result of internal crustal loading. Inherited weak extensional structures get reactivated during the initial stage of mountain building, but have only secondary control on large-scale mountain belt evolution. Surface processes active during mountain building create rock exhumation, fill foreland basins, and to first order delay orogenic growth. Deriving a force balance of thrust formation during orogenic growth, we explain thrust

**Typical evolutionary sequence of orogenesis during
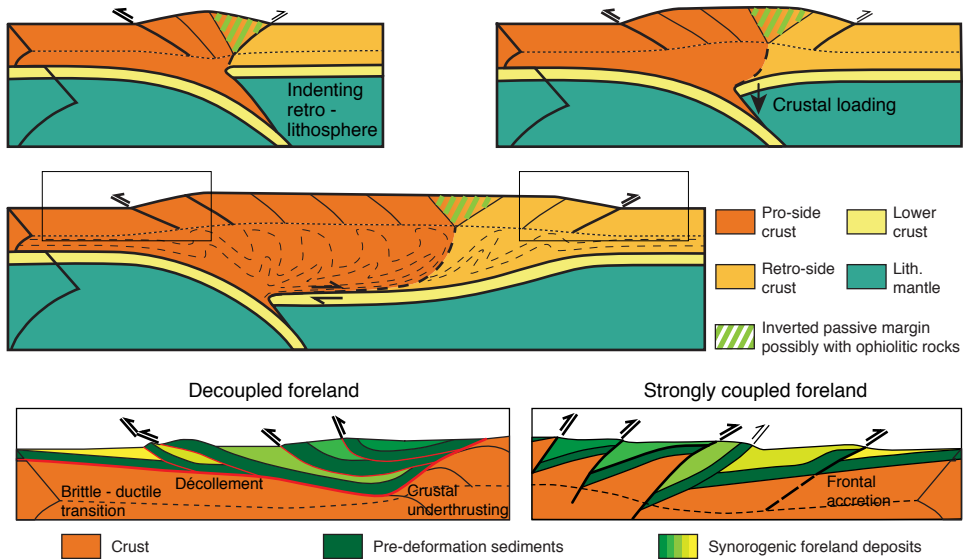continent-continent collision and contrasting structural styles**

Figure 3.2: Evolutionary sequence of orogenesis during continent-continent collision and contrasting structural styles depending on the existence of a weak décollement horizon.

spacing in orogens and the interaction between thin- and thick-skinned tectonics and the resulting structures. We propose that a reference thrust spacing is increased by syntectonic sedimentation and inherited weaknesses, and derive the combination of factors needed to generate thin-skinned foreland fold-thrust belts. Comparison of model results with the Pyrenees, Alps, and Himalayas shows first order applicability but also limitations of the presented model inferences.

Investigating the interaction between surface processes and tectonics during orogen growth, we can subdivide orogenic growth into two phases and classify orogens into 3 types. In phase 1, orogens primarily grow in height, until they have reached their maximum elevation controlled by the strength of the crust. Typically, phase 1 is over after around 50 km of plate convergence. In phase 2, orogens grow mainly in width but not height. Type 1 orogens are non-steady state orogens, characterized by several thrust-controlled longitudinal valleys, and low uplift and erosions rates. Type 2a orogens are at flux steady state, consist of several crustal-scale thrust sheets, reach similar heights as comparable type 1 orogens, and have thus a height controlled by crustal rheology. Type 2b orogens are also at flux steady state, but consist only of one crustal-scale thrust sheet, form a crustal monocline that is exhumed on the retro-shear zone, and do not form significant thrusts on the pro-side. Their width is limited by the width of the crustal thrust sheets, and their height is controlled by surface process efficiency. Typical for type 2 orogens are high uplift and erosion rates and rivers that cross active shortening features and flow pre-dominantly in transverse valleys in the orogen core. Hence, river topology seems to be an indicator for non-steady state.

To compare models to nature, we quantified the topology of river flow through a new-defined "longitudinality index" in models and natural orogens. We find that modelled steady state orogens have a low longitudinality index, comparable to river topology in the Southern Alps of New Zealand and Taiwan, while the Himalayan-Tibetan orogen, the Andes, and European Alps have longitudinality indices typical of non-steady state orogens. The characteristic absence of pro-side thrusting and orogenic structure of the Southern Alps of New Zealand furthermore indicate that they are a type-example of a type 2b orogen. We furthermore hypothesize that Taiwan could be a type 2a orogen.

Comparing stress and overpressure levels in the foreland crust to the gravitational potential energy generated by crustal thickening shows that the dynamics of thrust formation is to first order described by the Argand number Ar of the crust (Ellis et al. 1995). Furthermore, a scaling analysis shows that we can approximate the crustal
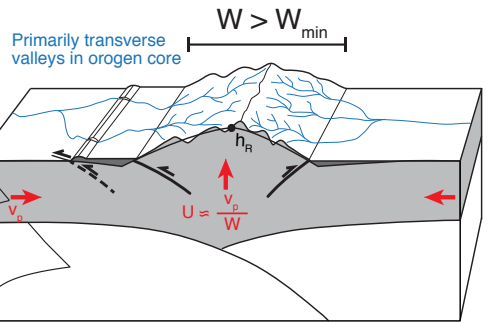
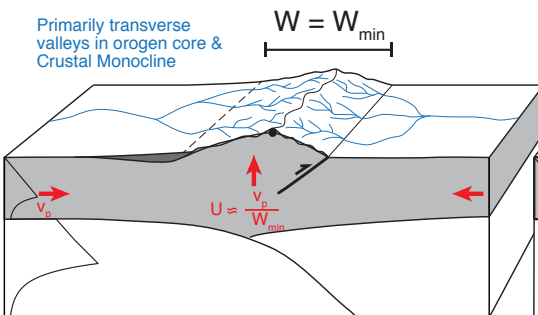## a) Topographic evolution of mountain belts
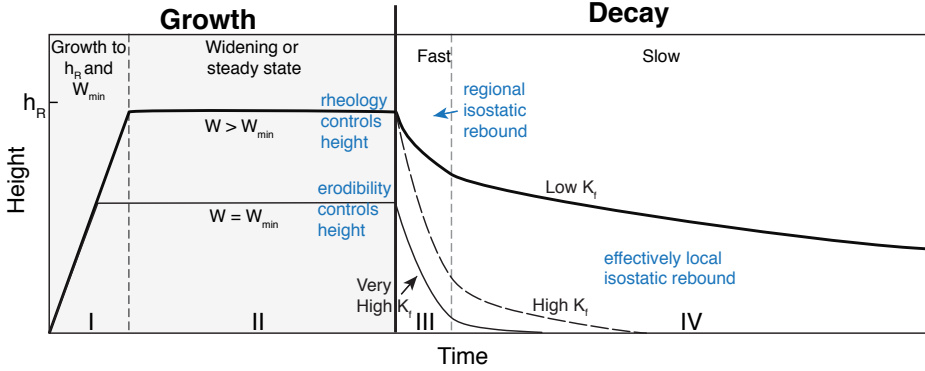
b) Growth Type 1
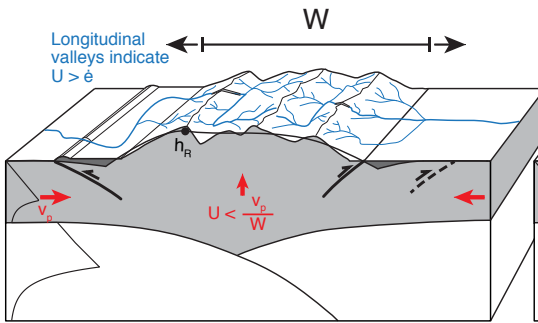
c) Growth Type 2a

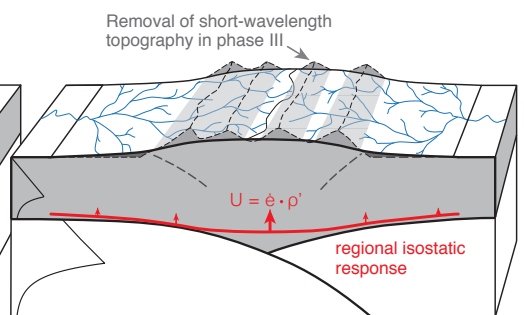## d) Growth Type 2b

e) Decay

Figure 3.3: (Caption on next page)

Figure 3.3: Typical topographic evolution of mountain belts through time (a), with associated block-diagrams of different orogen types during growth (b-d), and block-diagram describing orogenic decay (e). a) Mountain belt growth and decay can be subdivided into 4 phases. In phase I, orogens grow in height and width, until they have reached a maximum average height (h_R). In phase II, they only grow in width (type 1), and possibly reach steady state in which they on average keep their width (type 2a). In case fluvial erodibility is very high, orogens do not reach h_R in phase I, but still reach a minimum width (W_{min}) that corresponds roughly to the width of one crustal-scale thrust sheet plus a regional isostatic component (type 2b). Once shortening stops, short-wavelength topography is quickly removed in phase III. Effectively local-isostatic rebound and slow decay with a timescale dependent on surface process efficiency characterises phase IV. b) Type 1 orogens are characterised by several longitudinal valleys in the orogen core, and low uplift and erosion rates. c) Type 2a orogens are characterised by pre-dominantly transverse valleys in the orogen core, several crustal-scale thrust sheets ($W > W_{min}$), and high uplift and erosion rates. d) A crustal monocline, absence of significant pro-side thrusting, predominantly transverse valleys, high uplift and erosion rates, and $W = W_{min}$ are typical for type 2b orogens. e) Block-diagram showing different key-features of orogenic decay.

strength of orogens that are wider than one crustal-scale thrust sheet simply by knowing their average elevation. With the understanding that *Ar* provides essential information about orogen dynamics on Earth, we define a new non-dimensional number relating surface processes and tectonics during orogen growth. This new number, termed Beaumont number, *Be*, consists of the quotient of the crustal *Ar* and the uplift-erosion number N_E (Whipple and Tucker 1999; Willett 1999). Plotting the normalized orogenic widening rate and normalized orogenic height against *Be* gives a unique way to describe the efficiency of surface processes during mountain building, and allows computation of average fluvial erodibilities and crustal strength for orogens on Earth. Plotting several model sets into the *Be*-diagram, we create a reference template for mountain belts on Earth: Type 1 orogens are described by $Be > 0.5$, type 2a orogens have $Be \approx 0.5$, and type 2b orogens are characterised by $Be < 0.5$. Computing *Be* for the Southern Alps of New Zealand, Taiwan, and Himalaya-Tibet, a) shows that *Be* provides a simple and meaningful way to describe orogens on Earth, b) corroborates that these three orogens might be type-examples of the three orogen-types, and c) provides information about their crustal strength and average fluvial erodibility.

Our model inferences and analytical scaling relationships of growing orogens have wide implications for the interplay between tectonics, surface processes and especially climate. The inference that orogens wider than one crustal-scale thrust sheet have a

height controlled by rheology of the crust shows that we can infer crustal strength directly from orogen height. Inversely, changes towards higher or lower fluvial erodibility as a function of climate only have an effect on orogen height in the extreme case of very high fluvial erodibility and if orogens are already at the minimum orogen width. In case orogens are wider than one crustal-scale thrust sheet, climatic variations will not change orogen height, but potentially change orogen width. Our models furthermore provide the first consistent link between the dynamics of thrusting, erosion, and sedimentation during orogenesis.

3.1.4 The interplay between tectonics and surface processes during orogenic decay

With several models we show in paper three that orogenic decay is controlled by erosional efficiency and isostatic rebound in response to erosion. Once shortening stops, short-wavelength topography related to discrete thrust sheets and smaller than the wavelength of regional isostatic compensation is removed within few million years. Slow and long-term decay in the subsequent phase is determined by surface process efficiency and effectively local-isostatic rebound. Hence, during decay orogens seem to have a memory of their growth phase: Small and steady state orogens are quickly removed, large and non-steady state orogens live long. A characteristic decrease of fluvial erodibility during orogenic decay related to exhumation of less fractured rock (Molnar et al. 2007), and less erosive agents in streams (Egholm et al. 2013), indicates that long-lived orogenic topography is possibly the default behaviour for decaying orogens on Earth.

It is well known that orogenic decay is a function of erosional efficiency and isostatic rebound (Baldwin et al. 2003; Egholm et al. 2013). Our models and analysis provide additional insight that orogenic decay is potentially divided into two phases with distinct timescales and rebound characteristics.

3.2 Outlook

Throughout working on the relatively broadly posed research questions of this thesis, many further interesting questions and research avenues arose, either as continuation of the conducted research or as still unanswered topics. In general, these fur-
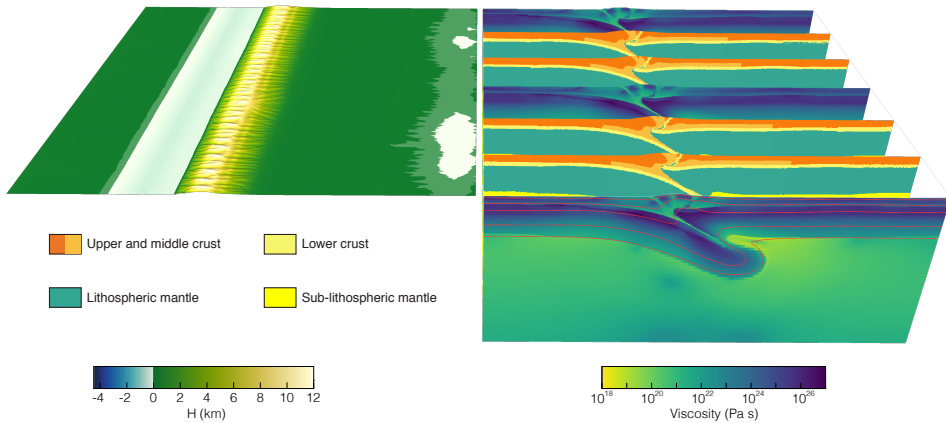
Figure 3.4: Snapshot of mountain building model created with 3D thermo-mechanical code pTatin3D coupled to surface process code FastScape. Slices on the right show material colours and viscosity fields of 3D thermo-mechanical model, surface on the right shows corresponding surface elevation. Red lines in viscosity plots on the model S-side are 100, 350, 550, 1000, 1330 °C temperature-contours. Both codes are fully coupled, deposited sediments have the same colour as the dark orange crust. The model is 1200 km wide and long, and 500 km deep. Uniform inflow of material on the W and E sides is balanced by outflow of material in the model bottom. Plate convergence creates consistent one-sided subduction and crustal-scale thick-skinned thrust sheets. Erosion exhumes the orogen core and creates a landscape with peaks higher than 12 km. High elevation and pre-dominantly transverse valleys indicate very high crustal strength and near-steady state.

ther questions can be subdivided into three categories: a) expansion to 3D thermo-mechanical modelling and coupling surface processes and tectonics in 3D, b) improve generic process-understanding of the interaction between tectonics, surface processes, and especially climate during mountain building in a ocean-continent subduction and continent-continent collision setting, and c) apply the developed modelling tools and generic process-oriented knowledge to specific mountain belts, i.e. try to reproduce the tectonic and landscape evolution of various mountain belts with thermo-mechanical-surface-process models.

In this thesis, I only presented 2D thermo-mechanical models coupled to the 2D surface process model FastScape in a T-coupling manner. A logical next step is to investigate mountain building coupled to surface processes in three dimensions. 3D thermo-mechanical modelling requires highly efficient, scalable codes and high performance computing with several thousands of CPUs. One such code, that almost linearly scales in speed with the amount of CPUs, is the 3D thermo-mechanically cou-

pled Arbitrary Eulerian-Lagrangian, Finite Element code pTatin3D (May et al. 2014, 2015). With the help of Dave May, I developed a coupling between pTatin3D and FastScape (Fig. 3.4), and building on the model setup of Duclaux et al. (2020), I created a continent-continent collision setup with several velocity boundary condition options. Furthermore, I installed, tested, and ran first models with the coupled code on several Norwegian HPC systems. Because of the linear scalability of pTatin3D, and new computing resources in Norway, this setup enables us to investigate mountain building (and extension) on an upper-mantle scale, with medium-high resolution in the crust of up to 500 to 1000 m in each spatial dimension.

This new modelling tool and the already developed 2D modelling tool presented in this thesis can answer many questions related to the interaction between surface processes and tectonics. Based on the results presented in paper 3 and 4, I propose to further investigate the interactions between surface processes, climate and mountain building. These investigations could follow the subsequent questions: First, what is a typical range of fluvial erodibilities and crustal strength on Earth? Although paper 4 already gave some insight into this question, positioning more mountain belts in the Be-diagram will give a better overview. Positioning orogens in the Be diagram requires, however, a) good data about the amount of sediment transported from the orogen during growth, or plate velocities through time, and b) active mountain belts, or good proxies for average paleoaltitude. These requirements make it challenging to find Be for instance for the European Alps, or the Andes. Second, do mountain belts change their Be as they grow, because rainfall or rainfall variability changes as the mountain belt gains elevation, i.e. do mountain belts move through the Be-plot during growth? Third, how do climatic perturbations influence the development of the different orogen types, and can we predict climatic signals from our models, similar to the experiments by Whipple and Meade (2006) and Whipple (2009)? Fourth, can we use the stratigraphy module that I developed in this thesis to get information about a typical evolutionary and climate-influenced stratigraphy during mountain building? Fifth, what are the influences of quaternary glaciations on mountain topography? One of the few, if not the only, type 2b orogen on Earth seem to be the Southern Alps of New Zealand, whose topography is heavily influenced by recent glaciations (e.g. Barrell 2011). Coupling the existing 2D thermo-mechanical-surface-process code with a code modelling glacier dynamics would be an interesting avenue to understand the impact of glaciations and climate on mountain building. This coupling could not only give insight into the formation of the Southern Alps, but also into a much more generic problem whether, and if yes, under which conditions glacial erosion limits topography

on Earth (e.g. Brozovic et al. 1997; Egholm et al. 2009).

One of the unexpected outcomes of the coupled tectonic-surface-process models presented in articles 3 and 4 is that landscape topology tracks information about flux steady state in orogens. I quantified valley longitudinality in mountain belt DEMs and modelled orogens, and found that there seems to be a good correspondence between orogens that have prominent longitudinal valleys in the core of the mountain belt and non-steady state growth. I propose to investigate this topic further, through in-depth investigation of prominent longitudinal valleys in several mountain belts on Earth.

The previously posed questions are relatively generic and more directed towards the geomorphological perspective of the developed models. The Pyrenees might be a perfect laboratory to investigate both the tectonic and landscape evolution of an orogen, using coupled 2D and 3D thermo-mechanical models. The Pyrenees are a relatively small orogen, which formed through inversion of a passive-margin and < 150 km of crustal shortening in the W (Muñoz 1992; Beaumont et al. 2000; Grool et al. 2018). The structural development (Muñoz 1992; Grool et al. 2018; Muñoz 2019), pre-extensional template (Roca et al. 2011; Garcés et al. 2020), palaeogeography (Garcés et al. 2020), and potential topographic evolution through time (Curry et al. 2019) are furthermore relatively well constrained. These constraints make the Pyrenees a fitting place to test thermo-mechanical-surface-process models. I propose to first investigate the influence of a laterally non-uniform extensional template with off-set rift basins on the structural evolution of the Pyrenees with 3D thermo-mechanical-surface-process models (Fig. 3.4). Second, I propose to model the topographic and exhumational evolution of the Pyrenees around the ECORS-profile, using constraints about topography from (Curry et al. 2019), structure from (Muñoz 1992, 2019), and exhumation history from (Curry et al., under revision in Geology). These two topics will give insight into the controlling factors of the tectonic and landscape evolution of the Pyrenees and potentially inform us about a typical evolution of K_f through the life of an orogen.

So far I only proposed further research questions related to continent-continent collision. Similarly, there are many possible research avenues to pursue for mountain building in an ocean-continent collision setting, specifically the Andes. There is a long-standing debate how much the strength of the subduction interface controls mountain building, and that there should be a link between high sediment volume in the interface and low interface strength (Lamb 2006; Pelletier et al. 2010). As sediment volume in the trench depends on erosion, and thus climate, there might be a potential link between orogen size, interface strength, and climate in the Andes (Lamb and Davis 2003). Us-

ing the ocean-continent subduction setup shown in this thesis, and the coupling with surface processes, we could investigate the link between climate and mountain building in the Andes and thereby also investigate the conclusion of Dielforder et al. (2020) that mountain height in ocean-continent subduction systems depends on plate interface strength. Besides the interaction of climate and plate interface strength, the Andes are also a great natural laboratory to investigate how pre-collisional extensional structures, and the interaction between thin- and thick-skinned tectonics influence mountain belt structure (Carrera et al. 2006; Iaffa et al. 2011; Carrera and Muñoz 2013). Building on the force balance in article 2 of this thesis, I propose to use 2D and also 3D models to investigate the structural controls of the Eastern flank of the central Andes.

References cited in the synthesis

Baldwin, J. A., Whipple, K. X., and Tucker, G. E. (2003). "Implications of the shear stress river incision model for the timescale of postorogenic decay of topography". In: *Journal of Geophysical Research-Solid Earth* 108.B3. DOI: Artn215810.1029/2001jb000550.

Barrell, D. J. A. (2011). "Chapter 75 - Quaternary Glaciers of New Zealand". In: *Developments in Quaternary Sciences*. Ed. by J. Ehlers, P. L. Gibbard, and P. D. Hughes. Vol. 15. Elsevier, pp. 1047–1064. DOI: https://doi.org/10.1016/B978-0-444-53447-7.00075-1.

Beaumont, C., Muñoz, J. A., Hamilton, J., and Fullsack, P. (2000). "Factors controlling the Alpine evolution of the central Pyrenees inferred from a comparison of observations and geodynamical models". In: *Journal of Geophysical Research-Solid Earth* 105.B4, pp. 8121–8145. DOI: Doi10.1029/1999jb900390.

Brozovic, N., Burbank, D. W., and Meigs, A. J. (1997). "Climatic limits on landscape development in the northwestern Himalaya". In: *Science* 276.5312, pp. 571–574. DOI: DOI10.1126/science.276.5312.571.

Carrera, N. and Muñoz, J. A. (2013). "Thick-skinned tectonic style resulting from the inversion of previous structures in the southern Cordillera Oriental (NW Argentine Andes)". In: *Geological Society, London, Special Publications* 377.1, pp. 77–100. DOI: 10.1144/sp377.2.

Carrera, N., Muñoz, J. A., Sabat, F., Mon, R., and Roca, E. (2006). "The role of inversion tectonics in the structure of the Cordillera Oriental (NW Argentinean Andes)". In: *Journal of Structural Geology* 28.11, pp. 1921–1932. DOI: 10.1016/j.jsg.2006.07.006.

Curry, M. E., van der Beek, P., Huismans, R. S., Wolf, S. G., and Muñoz, J. A. (2019). "Evolving paleotopography and lithospheric flexure of the Pyrenean Orogen from 3D flexural modeling and basin analysis". In: *Earth and Planetary Science Letters* 515, pp. 26–37. DOI: 10.1016/j.epsl.2019.03.009.

Dielforder, A., Hetzel, R., and Oncken, O. (2020). "Megathrust shear force controls mountain height at convergent plate margins". In: *Nature* 582.7811, pp. 225–+. DOI: 10.1038/s41586-020-2340-7.

Duclaux, G., Huismans, R. S., and May, D. A. (2020). "Rotation, narrowing, and preferential reactivation of brittle structures during oblique rifting". In: *Earth and Planetary Science Letters* 531. DOI: ARTN11595210.1016/j.epsl.2019.115952.

Egholm, D. L., Knudsen, M. F., and Sandiford, M. (2013). "Lifespan of mountain ranges scaled by feedbacks between landsliding and erosion by rivers". In: *Nature* 498.7455, pp. 475–+. DOI: 10.1038/nature12218.

Egholm, D. L., Nielsen, S. B., Pedersen, V. K., and Lesemann, J. E. (2009). "Glacial effects limiting mountain height". In: *Nature* 460.7257, pp. 884–7. DOI: `10.1038/nature08263`.

Ellis, S., Fullsack, P., and Beaumont, C. (1995). "Oblique Convergence of the Crust Driven by Basal Forcing - Implications for Length-Scales of Deformation and Strain Partitioning in Orogens". In: *Geophysical Journal International* 120.1, pp. 24–44. DOI: `DOI10.1111/j.1365-246X.1995.tb05909.x`.

Garcés, M. et al. (2020). "Paleogeographic and sedimentary evolution of the South Pyrenean foreland basin". In: *Marine and Petroleum Geology* 113. DOI: `ARTN10410510.1016/j.marpetgeo.2019.104105`.

Grool, A. R., Ford, M., Verges, J., Huismans, R. S., Christophoul, F., and Dielforder, A. (2018). "Insights Into the Crustal-Scale Dynamics of a Doubly Vergent Orogen From a Quantitative Analysis of Its Forelands: A Case Study of the Eastern Pyrenees". In: *Tectonics* 37.2, pp. 450–476. DOI: `10.1002/2017tc004731`.

Iaffa, D. N., Sabat, F., Muñoz, J. A., Mon, R., and Gutierrez, A. A. (2011). "The role of inherited structures in a foreland basin evolution. The Metan Basin in NW Argentina". In: *Journal of Structural Geology* 33.12, pp. 1816–1828. DOI: `10.1016/j.jsg.2011.09.005`.

Lamb, S. (2006). "Shear stresses on megathrusts: Implications for mountain building behind subduction zones". In: *Journal of Geophysical Research-Solid Earth* 111.B7. DOI: `ArtnB0740110.1029/2005jb003916`.

Lamb, S. and Davis, P. (2003). "Cenozoic climate change as a possible cause for the rise of the Andes". In: *Nature* 425.6960, pp. 792–797. DOI: `10.1038/nature02049`.

May, D. A., Brown, J., and Le Pourhiet, L. (2015). "A scalable, matrix-free multigrid preconditioner for finite element discretizations of heterogeneous Stokes flow". In: *Computer Methods in Applied Mechanics and Engineering* 290, pp. 496–523. DOI: `10.1016/j.cma.2015.03.014`.

May, D. A., Brown, J., and Pourhiet, L. L. (2014). "pTatin3D: High-Performance Methods for Long-Term Lithospheric Dynamics". In: *SC '14: Proceedings of the International Conference for High Performance Computing, Networking, Storage and Analysis*, pp. 274–284. DOI: `10.1109/SC.2014.28`.

Molnar, P., Anderson, R. S., and Anderson, S. P. (2007). "Tectonics, fracturing of rock, and erosion". In: *Journal of Geophysical Research-Earth Surface* 112.F3. DOI: `ArtnF0301410.1029/2005jf000433`.

Muñoz, J. A. (1992). "Evolution of a continental collision belt: ECORS-Pyrenees crustal balanced cross-section". In: *Thrust tectonics*. Springer, pp. 235–246.

— (2019). "Deformation and structure in the Northern Iberian margin (Pyrenees S.L.)" In: *The Geology of Iberia: A Geodynamic Approach*. Ed. by C. Quesada and J. Oliveira. Springer.

Pelletier, J. D., DeCelles, P. G., and Zandt, G. (2010). "Relationships among climate, erosion, topography, and delamination in the Andes: A numerical modeling investigation". In: *Geology* 38.3, pp. 259–262. DOI: `10.1130/g30755.1`.

Roca, E., Muñoz, J. A., Ferrer, O., and Ellouz, N. (2011). "The role of the Bay of Biscay Mesozoic extensional structure in the configuration of the Pyrenean orogen:

Constraints from the MARCONI deep seismic reflection survey". In: *Tectonics* 30. DOI: `ArtnTc200110.1029/2010tc002735`.

Vanderhaeghe, O., Medvedev, S., Fullsack, P., Beaumont, C., and Jamieson, R. A. (2003). "Evolution of orogenic wedges and continental plateaux: insights from crustal thermal-mechanical models overlying subducting mantle lithosphere". In: *Geophysical Journal International* 153.1, pp. 27–51. DOI: `DOI10.1046/j.1365-246X.2003.01861.x`.

Whipple, K. X. (2009). "The influence of climate on the tectonic evolution of mountain belts". In: *Nature Geoscience* 2.2, pp. 97–104. DOI: `10.1038/ngeo413`.

Whipple, K. X. and Meade, B. J. (2006). "Orogen response to changes in climatic and tectonic forcing". In: *Earth and Planetary Science Letters* 243.1, pp. 218–228. DOI: `https://doi.org/10.1016/j.epsl.2005.12.022`.

Whipple, K. X. and Tucker, G. E. (1999). "Dynamics of the stream-power river incision model: Implications for height limits of mountain ranges, landscape response timescales, and research needs". In: *Journal of Geophysical Research-Solid Earth* 104.B8, pp. 17661–17674. DOI: `Doi10.1029/1999jb900120`.

Willett, S. D. (1999). "Orogeny and orography: The effects of erosion on the structure of mountain belts". In: *Journal of Geophysical Research-Solid Earth* 104.B12, pp. 28957–28981. DOI: `Doi10.1029/1999jb900248`.

Willett, S. D. and Beaumont, C. (1994). "Subduction of Asian Lithospheric Mantle beneath Tibet Inferred from Models of Continental Collision". In: *Nature* 369.6482, pp. 642–645. DOI: `DOI10.1038/369642a0`.

uib.no